ELECTRONIC STRUCTURE DETERMINATION OF MODEL COMPLEXES OF [Mo-3Fe-4S] CLUSTERS AND METHOD DEVELOPMENT OF *IN SITU* REDUCTIVE AMINATION USING AMINE-BORANES

by

Bradley David Towey

A dissertation submitted in partial fulfillment
of the requirements for the degree

of

Doctor of Philosophy

in

Chemistry

MONTANA STATE UNIVERSITY
Bozeman, Montana

November 2014

©COPYRIGHT

by

Bradley David Towey

2014

All Rights Reserved

ACKNOWLEDGEMENTS

I would like to thank Dr. Tom Livinghouse, my advisor, for his support and assistance both inside and outside of the lab. He has been very influential and understanding while pushing me to become a better chemist. I also thank Dr. Rob Walker for his time and thoughtful critique of much of this research. In addition, I would like thank the rest of my committee members Dr. Joan Broderick, Dr. Trevor Rainey, and Dr. Richard Engel for their support, understanding, and guidance in helping me to persevere through all of the trials and tribulations of my graduate school experience. I am thankful for the support and incredible knowledge base I found in the past and present members of the Szilagyi and Livinghouse labs. Without the friendship and dedicated scholarship provided by these colleagues I would not be the scientist I am today.

I would like to express my gratitude towards my parents who have pushed and encouraged me to strive to be better, accomplish my goals, and to continually follow my dreams. Most importantly, I am forever grateful for my wife, Michelle Tigges, for her continual support, understanding, and nurturing through this process. Without her, graduate school would have been much more difficult.

TABLE OF CONTENTS

1. INTRODUCTION 1

Background 1
Nitrogenase 1
The Iron-Molybdenum Cofactor 2
Synthetic Biomimetic Model Complexes 5
X-ray Absorption Spectroscopy 9
Computational Theory and Application 11
Ab Initio Wavefunction Based Methods 11
Density Functional Theory 13
Basis Sets 15
Population Analysis 16
Time Dependent-Density Functional Theory 17
Reduction Amination 18
Research Directions 20

2. AN XAS INVESTIGATION OF A [Mo-3Fe-4S] CLUSTER 23

Introduction 23
Experimental Section 25
Sample Preparation 25
Sulfur K-edge X-ray Absorption Spectroscopy 26
XAS Data Normalization, Fitting, and Error Analysis 27
Results and Analysis 27
Analysis of S K, Mo L_{III} & L_{II}-edges of $MoFe_3S_4(dtc)_5$ 27
Analysis of Energy Positions of S K-edge XANES Features 29
Conclusions 35

3. QUANTIFIYING THE Mo-S BOND OF TETRATHIOMOLYBDATE COMPLEXES 38

Introduction 38
Experimental Section 42
Sample Preparation 42
Sulfur K-edge X-ray Absorption Spectroscopy 43
XAS Data Normalization, Fitting, and Error Analysis 43
Electronic Structure Calculations 45
Results and Analysis 47
Analysis of S K, Mo L_{III} & L_{II}-edges of MoS_4^{2-} 47
Ground State Orbital Composition 53
Excited State Energy Analysis 58

TABLE OF CONTENTS - CONTINUED

Intensity of S K-edge Spectral Features....60
Conclusions....65

4. QUANTIFICATION OF S MIXING OF DITHIOCARBAMATE LIGANDS IN TRANSITION METAL COMPLEXES....67

Introduction....67
Experimental Techniques and Computational Methods....76
Preparation of Compounds....76
Sulfur K-edge X-ray Absorption Spectroscopy....76
XAS Data Normalization and Fitting....77
Electronic Structure Calculations....78
Results and Analysis....80
Energy Positions of S K-edge Spectral Features....80
Na, Cu(II), Ni(II) dtc Complexes....80
Na, Fe(III), Mo(IV) dtc Complexes....83
Na, Fe(II), Zn(II) dtc Complexes....85
Calculated Ground State Orbital Energy Levels....87
Ground State Orbital Composition....93
Excited State Orbital Energy Levels....95
Intensity of the S K-edge Spectral Features....97
Discussion....100
$Zn_2(dtc)_4$....100
$Cu(dtc)_2$....100
$Ni(dtc)_2$....102
$Fe_2(dtc)_4$....102
$Fe(dtc)_3$....103
$Mo(dtc)_4$....104
Concluding Remarks....105

5. ELECTRONIC STRUCTURE DETERMINATION OF COPPER AND SODIUM DIETHYLDITHIOCARBAMATE COMPLEXES USING S K-EDGE X-RAY ABSORPTION SPECTROSCOPY AND DENSITY FUNCTIONAL THEORY....107

Introduction....107
Experimental Techniques and Computational Methods....111
Sample Preparation....111
Sulfur K-edge X-ray Absorption Spectroscopy....112
SSRL....112
CLS....112

TABLE OF CONTENTS - CONTINUED

ALS 113
SRC 114
XAS Data Normalization, Fitting, and Error Analysis 114
Shift and Scale (1) 114
Arctangent Fit to Shift and Scale (2) 115
Automated Data Reduction Protocol (ADRP, 3) 116
XANES Fitting 116
Error Analysis 118
Electronic Structure Calculations 119
Results and Analysis 121
Analysis of Energy Positions of XANES Features 121
Ground State Orbital Composition 123
Excited State Energy Analysis 128
Intensity of the S K-edge Spectral Features 132
Conclusions 137

6. REDUCTIVE AMINATION OF DIMETHYLHYDRAZONES USING AMINE-BORANE COMPLEXES 140

Introduction 140
Experimental Procedures 141
Materials and Methods 141
Synthesis of Amine-Boranes 142
Tert-butylamine borane 142
Diethylamine borane 142
Triethylamine borane 143
Pyridine borane 143
Morpholine borane 143
Synthesis of Hydrazones 144
2-Heptylidene-1,1-dimethylhydrazine 144
(E)-1,1-Dimethyl-2-(1-*p*-tolylethylidene)hydrazine 144
Synthesis of Hydrazines: General Procedure for 1,2-Reductions of Hydrazones 145
2-Heptyl-1,1-dimethylhydrazine (**18**) 145
2-Benzyl-1,1-dimethylhydrazine (**20**) 145
Synthesis of Hydrazines: General Procedure for *In Situ* 1,2-Reductions of Hydrazones 145
2-Heptyl-1,1-dimethylhydrazine (**18**) 145
1,1-Dimethyl-2-phenethylhydrazine (**19**) 146
2-Benzyl-1,1-dimethylhydrazine (**20**) 147
1,1-Dimethyl-2-(1-*p*-tolyethyl)hydrazine (**22**) 147

TABLE OF CONTENTS - CONTINUED

2-(Heptan-2-yl)-1,1-dimethylhydrazine (**21**).....148
Results and Discussion.....149
Conclusion.....152

7. CONCLUSION.....153

Outlook.....155

REFERENCES CITED.....157

APPENDICES.....172

APPENDIX A: Supporting Information for Chapter 3.....173
APPENDIX B: Supporting Information for Chapter 4.....177
APPENDIX C: Supporting Information for Chapter 5.....198
APPENDIX D: NMRs from Chapter 6.....209

LIST OF TABLES

Table Page

1.1: Production (%) of NH_3 from NH_2NH_2 and C_2H_4 from the Catalytic Reduction by various $MoFe_3$-Carboxylate Cubanes Using $CoCp_2$ as the Reducing Agent and Lut•HCl as the Source. Reduction of NH_2NH_2 ([NH_2NH_2]:[catalyst] = 100:1).[40] Reduction of C_2H_2 ([C_2H_2]:[catalyst] 20:1).[41] 7

2.1: Energy of S K-edge Features of Free Ligands and $MoFe_3S_4(dtc)_5$ 32

3.1: The fit areas of the different MoS_4^{2-} salts of the e and t_2 orbitals in units of eV 62

3.2: The determined S character (e^-/hole) from the fits in the Table 3.1 using the transition dipole integral of 8.31 eV.[87] 63

3.3: Extracted S character (e^-/hole) using transition dipole integrals tuned to QCISD calculations 64

4.1: EPR results from various studies 70

4.2: Distances in in Å between different atoms in the crystal structures from Figure 4.1 74

4.3: Postulated S K-edge peak positions in eV 87

4.4: Energy Decomposition Analysis for Zn/Cu/Ni dithiocarbamate complexes (in eV) as implemented in ADF 91

4.5: Numerical fitting results corresponding to pre-edge features from Figure 4.13 98

4.6: Quantitative Analysis of Cu(II), Ni(II), Fe(III), Mo(IV) dtc compounds 99

5.1: Comparison of S character using B3LYP and B(38HF)P86 functionals using different population analyses of $Cu(dtc)_2$ and Na(dtc) 125

5.2: TD-DFT S K-edge excitations, oscillator strengths, excitation energies and LUMOs populated (>10%) of $Cu(dtc)_2$ and Na(dtc) 131

LIST OF TABLES – CONTINUED

Table Page

5.3: Summary of $Cu(dtc)_2$ normalizations, areas, complex transition dipole integrals, and ligand transition dipole integrals 133

5.4: S character per hole of $Cu(dtc)_2$ rising edge π* feature using SSRL PIPS FY 136

5.5: Summary of Na(dtc) normalizations, areas, and per hole hole covalencies of the S-C-N π* feature 137

6.1: Reduction of dimethylhydrazones from different amine-boranes in HCl/MeOH.....149

6.2: Reduction of dimethylhydrazones using 3 equivalents of *tert*-butylamine borane.....151

LIST OF FIGURES

Figure Page

1.1: Structural representation of the nitrogenase MoFe-Fe protein complex from *Azotobacter vinelandii* stabilized by AlF_4^-.[5] The transparent region represents one half of the catalytic complex and illustrates the MgATP binding sites, and the electron transfer pathway from the [4Fe-4S] cluster of the Fe protein to the FeMo-cofactor active site via the P cluster intermediate. This image was generated using the Protein Data Bank file 1N2C.....3

1.2: $MoFe_3S_4$ clusters are structural motifs of FeMo-co. The overlay of the [Mo-3Fe-4S] cluster with FeMo-co shows small deviations as determined by Lee and Holm.[19].....6

1.3: The different ligand environments around the Mo site of different $MoFe_3S_4$ cubanes.[40].....8

1.4: An example of an S K-edge XAS spectrum depicting the XANES and EXAFS regions. In addition, the XANES region is broken into the pre-edge and rising edge features.....10

1.5: Schematic demonstration of theoretically converging series of *ab initio* wavefunction methods.....13

1.6: The relationship of mixing HF exchange with GGA functionals.....15

1.7: Potential mechanistic pathways for reductive amination 18

1.8: Sodium cyanoborohydride reduction of a dimethylhydrazone.....19

2.1: The crystal structure of $MoFe_3S_4(dtc)_5$ (Cambridge Crystallographic Database Code JALDOP).[83].....23

2.2: The S K, Mo L_{III} and L_{II}-edges of the $MoFe_3S_4(dtc)_5$ cluster.....28

2.3: The Mo L_{III} and L_{II}-edges expanded of $MoFe_3S_4(dtc)_5$. The normalized intensity is based on the S K-edge and not the L_{III} and L_{II}-edges 29

LIST OF FIGURES – CONTINUED

Figure Page

2.4: (A) The S K-edge XANES, (B) the 1st derivative, and (C) the 2nd derivative plots of $MoFe_3S_4(dtc)_5$ along with the dtc and S^{2-} free ligands....30

2.5: An interpretation of the S K-edge XANES region of the $MoFe_3S_4(dtc)_5$ cluster....34

2.6: A second interpretation of the S K-edge XANES region of the $MoFe_3S_4(dtc)_5$ cluster....35

3.1: The S K, Mo L_{III} and L_{II}-edges of $(PPh_4)_2MoS_4$ using EY (blue) and FF (red) detection methods normalized to S at 2490 eV....48

3.2: The normalized Mo L_{III}-edge of $(PPh_4)_2MoS_4$ from both detection methods (EY-blue, FF-red). The spectra were normalized to one at 2540 eV. The inset is the 2nd derivative spectrum of the EY detection method....49

3.3: (A) The S K-edge XANES using FF, (B) the 1st derivative, and (C) the 2nd derivative of $(PPh_4)_2MoS_4$ along with the Na_2S ligand....51

3.4: The S K-edge XANES of $(PPh_4)_2MoS_4$ (black), Na_2MoS_4 (red), and $(NH_4)_2MoS_4$ (blue) using FF detection....52

3.5: The per hole S character determined using QCISD/AIM calculations compared to the number of basis functions used for MoS_4^{2-}. The S composition of the e orbitals are in blue, the t_2 orbitals are in red, and the total d-orbital contribution is in black....54

3.6: The per hole S character determined using different functionals with the AIM population analysis of MoS_4^{2-}. The S composition of the e orbitals are in blue, the t_2 orbitals are in red, and the total d-orbital contribution is in black....56

3.7: The molecular orbital picture generate from BP86/def2-TZVP for MoS_4^{2-}....57

LIST OF FIGURES – CONTINUED

Figure Page

3.8: The TD-DFT S K-edge calculations using BP86 (top left), B3LYP (top right), TPSS (bottom left) and TPSSh (bottom right) functionals using the def2-TZVP basis set for MoS_4^{2-} 59

3.9: The TD-DFT S K-edge calculations using BP86 of the crystalline environment 7 Å away for Na_2MoS_4 (left) and 5 Å away for $(NH_4)_2MoS_4$ (right) 60

3.10: An example of an S K-edge XANES fit for the extraction of the S 3p contribution from the MoS_4^{2-} e and t_2 orbitals.....61

4.1: The crystal structures of $Ni(dtc)_2$ (top left), $Cu(dtc)_2$ (middle left), $Zn_2(dtc)_4$ (bottom left), $Fe_2(dtc)_4$ (top right), $Fe(dtc)_3$ (middle right), and $Mo(dtc)_4$ (bottom right) 73

4.2: Energy position analysis of the XANES region of the normalized S K-edge spectra (A), first derivative spectra (B), and second derivative spectra (C) of Na(dtc), $Ni(dtc)_2$, and $Cu(dtc)_2$ 82

4.3: Energy position analysis of the XANES region of the normalized S K-edge spectra (A), first derivative spectra (B), and second derivative spectra (C) of Na(dtc), $Fe(dtc)_3$, and $Mo(dtc)_4$ 84

4.4: Energy position analysis of the XANES region of the normalized S K-edge spectra (A), first derivative spectra (B), and second derivative spectra (C) of Na(dtc), $Fe_2(dtc)_4$, and $Zn_2(dtc)_4$ 86

4.5: $Ni(dtc)_2$ d-manifold orbitals. The orbitals were generated from BP86/def2-TZVP. Notice the back bonding of the x^2-y^2 orbital into the C-N σ orbital 88

4.6: The MOs of $Ni(dtc)_2$ starting from the free ligand, two ligands around a 2+ point charge, and on the far right the ligands chelating onto Ni generated from ADF using BP86/TZ2P 89

LIST OF FIGURES – CONTINUED

Figure Page

4.7: The MOs of $Cu(dtc)_2$ starting from the free ligand, two ligands around a 2+ point charge, monomer complex of both spins, and also the $Cu_2(dtc)_4$ dimer computed in ADF using BP86/TZ2P 90

4.8: The MOs of the crystal structure of room temperature $Fe(dtc)_3$ starting from the free ligand, three ligands around a 3+ point charge, monomer complex of both spin 1/2 and 5/2 states generated from ADF using BP86/TZ2P 92

4.9: The MOs of $Mo(dtc)_4$ starting from the free ligand (left), four ligands around a 4+ point charge (middle), and on the far right the $Mo(dtc)_4$ generated from ADF using BP86/TZ2P.....93

4.10: The AIM per hole S character of transition metal dtc complexes using def2-TZVP basis set and B3LYP functional for all the complexes except for $Cu(dtc)_2$, for which the B(38HF)LYP functional was used.....94

4.11: TD-DFT of $Cu(dtc)_2$ (left) and $Ni(dtc)_2$ (right) of the M-S, π^*, and σ^* transitions computed in ORCA compared to their respective S K-edge XAS spectrum.....95

4.12: TD-DFT calculated in ORCA of Fe-S and π^* for $Fe(dtc)_3$ containing 57 % spin 5/2 and 43% spin 1/2 (left) and the Mo-S, π^*, and σ^* for $Mo(dtc)_4$ (right) 96

4.13: The M-S and the π^* fits of $Ni(dtc)_2$ (green), $Cu(dtc)_2$ (blue) on the left, $Fe(dtc)_3$ (brown), and $Mo(dtc)_4$ (purple) on the right 97

5.1: The crystal structure of $Cu(dtc)_2$ dimer from the Cambridge Crystallographic Database Code CETCAM12 111

5.2: Data treatment 2 by fitting an arctangent function to shift and scale data (A), subtracting the data (B), subtracting the pre-edge linear fit (C), and normalization (D) 115

LIST OF FIGURES – CONTINUED

Figure Page

5.3: Energy position analysis of the XANES region of the normalized S K-edge spectra (A), first derivative spectra (B), and second derivative spectra (C) of Na(dtc) and $Cu(dtc)_2$ 122

5.4: MO diagram of Na(dtc) and $Cu(dtc)_2$ generated from B(38HF)P86/def2-TZVP. Mulliken symbols derived assuming C_{2v} symmetry for Na(dtc) and D_{2h} for $Cu(dtc)_2$.....123

5.5: Per hole S character in the first three LUMOs of $Cu(dtc)_2$ with different basis sets and population analyses using the B(38HF)P86 functional.....126

5.6: Per hole S character in the LUMO of Na(dtc) using different basis sets and population analyses with the B(38HF)P86 functional.....127

5.7: Ground state S K-edge simulation of $Cu(dtc)_2$ (left) and Na(dtc) (right) using B(38HF)P86/def2-TZVP/AIM. The line widths range from 0.8 (light blue), 1.0 (brown) and 1.2 (purple) eV. An arctangent function was used to simulate the edge jump at 2474.4 eV.....128

5.8: TD-DFT S K-edge simulation of $Cu(dtc)_2$ using B3LYP (left) and B(38HF)P86 (right). The line widths vary from 0.8 (light blue), 1.0 (brown) and 1.2 (purple) eV. An arctangent function was used for the edge jump at 2474.4 eV.....129

5.9: Calculated S K-edge of Na(dtc) using B3LYP (left) and B(38HF)P86 (right). The line widths range from 0.8 (light blue), 1.0 (brown), and 1.2 (purple) eV. The edge jump was mimicked with an arctangent function at 2474.3 eV.....130

5.10: Ground state fit of $Cu(dtc)_2$ that utilizes one peak for the Cu-S bond, two fits for the S-C-N π^* orbitals, and one fit for the C-S σ^* 135

LIST OF FIGURES – CONTINUED

Figure Page

6.1: The hydrazines synthesized were
18) 2-heptyl-1,1-dimethylhydrazine,
19) 1,1-dimethyl-2-phenethylhydrazine,
20) 2-benzyl-1,1-dimethylhydrazine,
21) 2-(heptan-2-yl)-1,1-dimethylhydrazine, and
22) 1,1-dimethyl-2-(1-*p*-tolylethyl)hydrazine.....141

B.1: $Cu(dtc)_2$ and Na(dtc).....179

B.2: $Ni(dtc)_2$ and Na(dtc).....180

B.3: $Fe(dtc)_3$ and Na(dtc).....181

B.4: $Mo(dtc)_4$ and Na(dtc).....182

C.1: Shift and scale workups of $Cu(dtc)_2$ at SSRL (A), ALS (B), CLS (C), and SRC (D).....199

C.2: Arctangent fit to shift and scale workups of $Cu(dtc)_2$ at SSRL (A), ALS (B), CLS (C), and SRC (D).....200

C.3: ADRP workups of $Cu(dtc)_2$ at SSRL (A), ALS (B), CLS (C), and SRC (D).....201

C.4: Shift and scale workups of Na(dtc) at SSRL (A), CLS (B), and SRC (C).....202

C.5: Arctangent fit to shift and scale of Na(dtc) at SSRL (A), CLS (B), and SRC (C).....203

C.6: ADRP workups of Na(dtc) at SSRL (A), CLS (B), and SRC (C).....204

C.7: Calculated S K-edge of $Cu(dtc)_2$ (left) and Na(dtc) (right) using B(30HF)P86/def2-TZVP. The line widths range from 0.8 (light blue), 1.0 (brown), and 1.2 (purple) eV. The edge jump was mimicked with an arctangent function.....204

LIST OF FIGURES – CONTINUED

Figure Page

C.8: Ground state fit of Na(dtc) collected from SSRL that utilizes one peak for the S-C-N π* and C-S σ* orbitals, and a user defined function to fit the edge jump and neighboring EXAFS features 205

D.1: ^{1}H NMR of 2-heptylidene-1,1-dimethylhydrazine 210

D.2: ^{13}C NMR of 2-heptylidene-1,1-dimethylhydrazine 211

D.3: ^{1}H NMR of 2-heptyl-1,1-dimethylhydrazine (**18**) 212

D.4: ^{13}C NMR of 2-heptyl-1,1-dimethylhydrazine (**18**) 213

D.5: ^{1}H NMR of 1,1-dimethyl-2-phenethylhydrazine (**19**) 214

D.6: ^{1}H NMR of 2-benzyl-1,1-dimethylhydrazine (**20**).....215

D.7: ^{1}H NMR of 2-(heptan-2-yl)-1,1-dimethylhydrazine (**21**) 216

D.8: ^{13}C NMR of 2-(heptan-2-yl)-1,1-dimethylhydrazine (**21**) 217

D.9: ^{1}H NMR of (*E*)-1,1-dimethyl-2-(1-p-tolylethylidene)hydrazine 218

D.10: ^{1}H NMR of 1,1-dimethyl-2-(1-*p*-tolylethyl)hydrazine (**22**).....219

D.11: ^{13}C NMR of 1,1-dimethyl-2-(1-*p*-tolylethyl)hydrazine (**22**) 220

D.12: ^{1}H NMR of *tert*-butylamine borane 221

D.13: ^{1}H NMR of diethylamine borane 222

D.14: ^{1}H NMR of triethylamine borane.....223

D.15: ^{1}H NMR of pyridine borane.....224

D.16: ^{1}H NMR of morpholine borane.....225

ABSTRACT

In nature, bacteria are able to convert inert nitrogen gas to ammonia using the iron molybdenum-cofactor of the nitrogenase enzyme. Even though the crystal structure and the magnetic coupling of the iron molybdenum-cofactor cluster have been elucidated, the bonding site(s) and the mechanism of the reduction are not understood. The reactivity towards nitrogenase substrates of the iron molybdenum-cofactor from synthetic [Mo-3Fe-4S] biomimetic models has previously been examined, but these models are limited to reducing N,N single and double bonds, protons, acetylene, and acetonitrile. The reactivity of these clusters is dictated by their electronic structure, which is tuned by the chelating ligands. To study the ligand donations, a simpler cluster with a homoleptic ligand environment, the $MoFe_3S_4(S_2CNEt_2)_5$ complex, was synthesized and analyzed with S K-edge X-ray absorption spectroscopy. The S K-edge is convoluted due to the different sulfur environments and only plausible assignments could be inferred based on Slater's rules for effective oxidation states. Iron sulfide bonds have been characterized using S K-edge X-ray absorption spectroscopy, however, little is known regarding molybdenum sulfide bonding. The tetrahedral MoS_4^{2-} compound was utilized to understand the Mo-S bonding with X-ray absorption spectroscopy in conjunction with computational methods. The terminal sulfides of MoS_4^{2-} donate approximately five electrons to the formally +6 charge on the Mo center. Since the charge delocalization of transition metal dithiocarbamate complexes have not been studied extensively, the experimental electronic structure of Zn(II), Cu(II), Fe(II), Fe(III), and Mo(IV) dithiocarbamate complexes were examined. The dithiocarbamate ligands exhibit classical bonding in which the ionic character increases with increasing positive charge on the metal. Piecing these models together, the $MoFe_3S_4(S_2CNET_2)_5$ cluster contains a covalent [Mo-3Fe-4S] core with ionic dithiocarbamate ligands surrounding and stabilizing the cluster. The last part of this thesis is the development of a new method for reductive amination of dimethylhydrazones to dimethylhydrazines using amine-boranes. Conventionally, the C=N bond is reduced with toxic or less selective reducing agents. A potent, and easy to handle *tert*-butylamine borane was used and prepared *in situ* towards the synthesis of dimethylhydrazines containing different functionalities in high yields.

CHAPTER 1

INTRODUCTION

Background

The focus of this thesis is to further the understanding of the chemical bonding of the iron molybdenum-cofactor (FeMo-co) of nitrogenase. To understand the chemical bonding of FeMo-co at a fundamental level, biomimetic model systems were synthesized and characterized in order to be analyzed with X-ray absorption spectroscopy (XAS), and validated with density functional theory (DFT) and *ab initio* wavefunction (WFN) methods. The last part of this thesis is the development of new, cost effective, and potentially less toxic methods for the reductive amination of asymmetrical dimethylhydrazones. The reduction of asymmetrical dimethylhydrazones is necessary in obtaining dimethylhydrazines. One important utility for the use of dimethylhydrazine molecules is that they are precursors towards the syntheses of nitrogen containing heterocycles via metalloamination. Metalloamination is a process that adds a N-metal bond across a carbon-carbon double or triple bond. Small organic substrates were synthesized and characterized for the synthesis of asymmetrical dimethylhydrazines.

Nitrogenase

Nitrogen is a vital component for all living organisms as it is incorporated into proteins, amino acids, nucleic acids, and many other biomolecules.[1,2] The largest source of nitrogen is in the atmosphere and is mostly composed of dinitrogen. Dinitrogen

however, is not bioavailable to organisms due to the relatively inert and strong N≡N triple bond. Biological nitrogen fixation (reduction) is made possible by microorganisms called diazotrophs using the nitrogenase enzyme to yield ammonia. Approximately 60% of the ammonia produced is through biological nitrogen fixation. The other 40% of ammonia produced is through the industrial Haber-Bosch process, which requires an iron based catalyst, H_2, and high pressures and temperatures.[1] There are three forms of the active site of the enzyme and they include Mo, V, and Fe cofactors.[3] The Mo-dependent enzyme is the most active and the most studied, and its active site contains the iron-molybdenum cofactor (FeMo-co). The enzyme consists of two metalloproteins called the Fe-protein and the MoFe-protein.[4] The Fe-protein delivers electrons sequentially to the MoFe protein where the substrate binds via a MgATP driven process to yield two equivalents of ammonia as shown below:[1]

$$N_2 + 8H^+ + 8e^- + 16MgATP + H_2O \rightarrow 2NH_3 + H_2 + 16MgADP + 16Pi \qquad (1.1)$$

The Iron-Molybdenum Cofactor

The FeMo-co is a complex iron sulfur cluster, and is located in the MoFe-protein. Figure 1.1 shows the crystal structure of the Fe and MoFe protein along with the embedded FeMo-co from *Azotobacter vinelandii* stabilized by $A1F_4^-$. The nitrogenase from *Azotobacter vinelandii* is the best characterized of all the nitrogenases.[5]

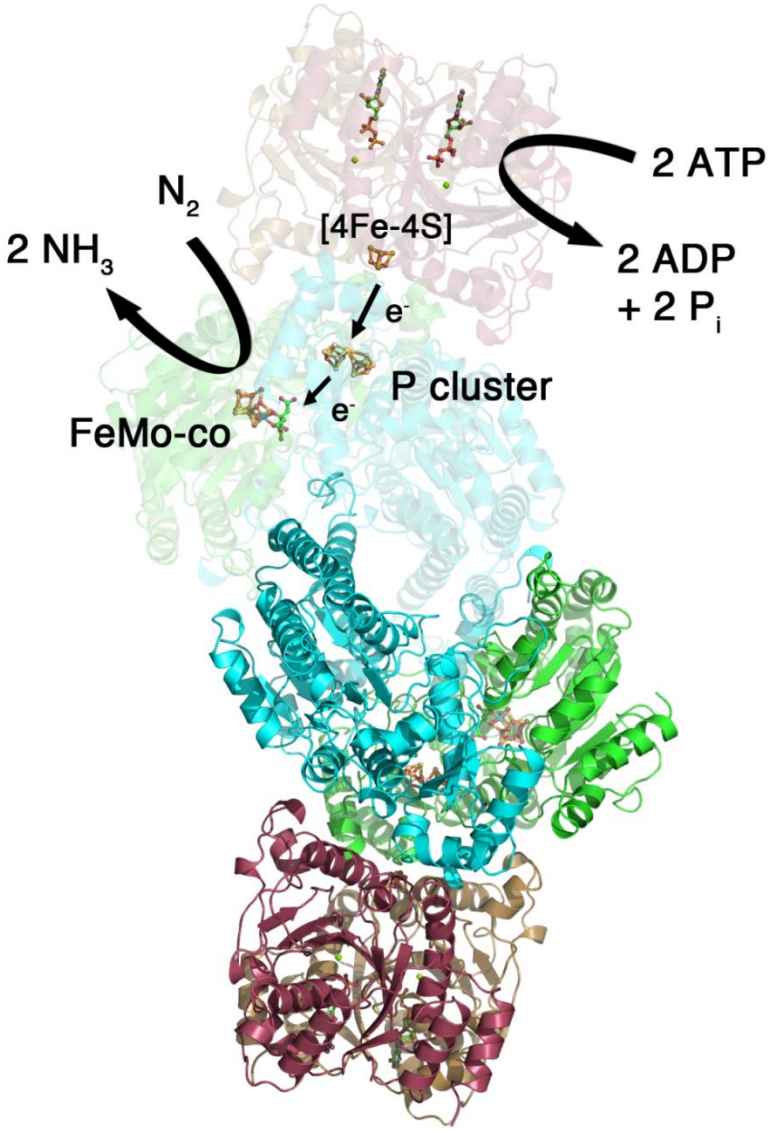


Figure 1.1: Structural representation of the nitrogenase MoFe-Fe protein complex from *Azotobacter vinelandii* stabilized by AlF_4^-.[5] The transparent region represents one half of the catalytic complex and illustrates the MgATP binding sites, and the electron transfer pathway from the [4Fe-4S] cluster of the Fe protein to the FeMo-cofactor active site via the P cluster intermediate. This image was generated using the Protein Data Bank file 1N2C.

FeMo-co is composed of [Mo-7Fe-9S-C] cluster as determined from x-ray diffraction with an atomic resolution of (1.0 Å),[6] x-ray emission spectroscopy,[7] and DFT modeling.[8] An R-homocitrate is coordinated to Mo through the 2-hydroxy and 2-carboxyl

groups along with an imidazole of His442 bonding through the N atom. Three different forms of the FeMo-co have been structurally characterized from isolated MoFe-protein: resting (FeMo-co^{N}), one-electron reduced (FeMo-co^{Red}), and one-electron oxidized (FeMo-co^{Ox}).[4] The Mo center is diamagnetic with a formally a +IV ($4d^2$) oxidation state as determined from electron nuclear double resonance,[9] and supported by X-ray absorption spectroscopic measurements in all three forms.[10,11] FeMo-co^{N} has a $S_t = 3/2$ EPR signal, where FeMo-co^{Red} is EPR silent with $S_t \geq 1$ integer spin. FeMo-co^{Ox} is diamagnetic at 4 K, however a low lying excited state of $S_t \geq 1$ state is populated from 240-320 K.[12] The midpoint potential for reduction of FeMo-co^{Ox} to FeMo-co^{N} is -42 mV,[13] while that for the reduction of FeMo-co^{N} to FeMo-co^{Red} is -465 mV.[4] A DFT study by Harris and Szilagyi used spectroscopically calibrated functionals and basis sets to determine the spin coupling, iron oxidation states, and ligand protonation states, along with uncovering the identity of the interstitial atom before experimental verification.[8] The oxidation state of FeMo-co^{N} was best defined as [Mo^{IV}-$2Fe^{II}$-$5Fe^{III}$-$9S^{2-}$-C^{4-}] as well as a protonated R-homocitrate ligand. Additionally, all nine sulfurs are antiferromagnetically coupled to the weak field irons.[8]

Despite the advances in the geometric and electronic understanding of FeMo-co, it still remains unclear where N_2 fixation occurs. The reduction can take place on the Mo atom, or the "6iron belt" of the FeMo-co.[1,14] Biomimetic models of FeMo-co have been synthesized in an attempt to understand its biosynthesis and the biomolecular mechanism of nitrogen fixation.

Synthetic Biomimetic Model Complexes

Many [Mo-3Fe-4S] biomimetic models of the iron molybdenum-cofactor (FeMo-co) have been synthesized to understand the biological synthesis and mechanistic understanding of the reduction of dinitrogen. There are a few different systems that are capable of catalytically or stoichiometrically fixing dinitrogen at a monometallic center using Mo and W.[15-18] However, these catalysts use non-biological ligands and chemical conditions that are different than active nitrogenase enzymes.[1] Despite the non-biological ligands and conditions, the catalytic reduction of N_2 at a single Mo site demonstrates that the binding site of N_2 could be the Mo site in the FeMo-co cluster. Even though the FeMo-co has never been synthesized, there are many biomimetic models that are both catalytic and structural analogues of the FeMo-co.[19] [Mo-3Fe-4S] biomimetic models are close structural analogues because the bond distances of the distal atoms to Mo are nearly identical.[19] The Holm[19-30] and Coucouvanis'[31-40] groups have synthesized many biomimetic models of the FeMo-co. Figure 1.2 depicts the structural similarities of the FeMo-co and [Mo-3Fe-4S] clusters. The Coucouvanis group has examined the reactivity of theses clusters and showed that some clusters are able to reduce a few of the same substrates as the FeMo-co.[40-43]

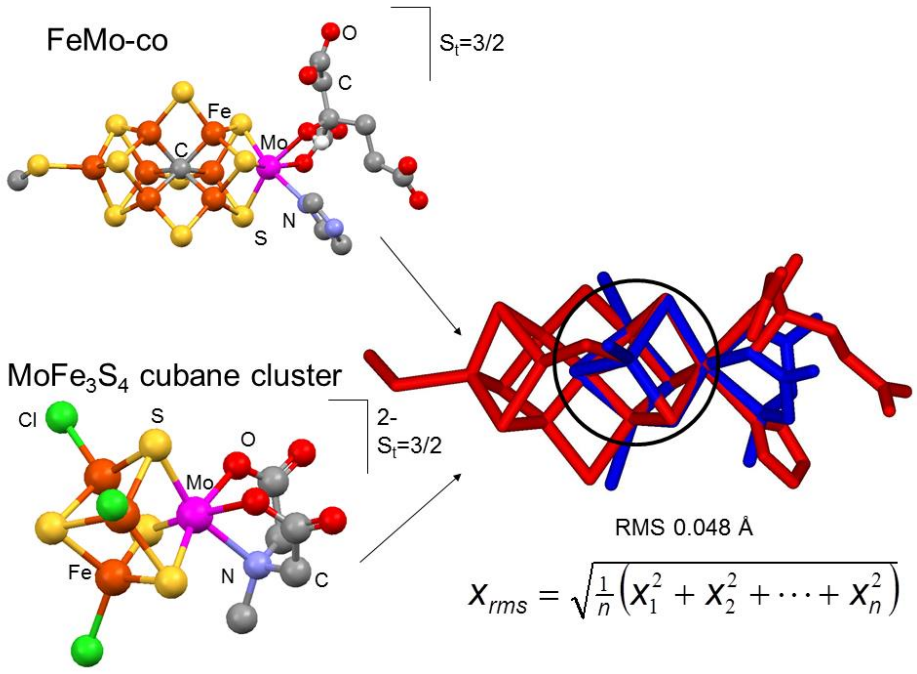


Figure 1.2: $MoFe_3S_4$ clusters are structural motifs of FeMo-co. The overlay of the [Mo-3Fe-4S] cluster with FeMo-co shows small deviations as determined by Lee and Holm.[19]

Table 1.1 summarizes the reactivity of the clusters that are depicted in Figure 1.3. One compound in particular, $[MoFe_3S_4(Cl_4\text{-cat})(MeCN)]^{2-}$ (**9**), catalytically reduced hydrazine, *cis*-dimethyldiazene, acetonitrile, and acetylene all at the Mo site.[40-43] Additionally, Coucouvanis' experimental reductions of hydrazine and acetylene (Table 1.1) were influenced by the ligand environment around the cluster.[40] The reactivity of the $[MoFe_3S_4Cl_3(Hcit)]^{3-}$ (**1**) is the highest in terms of NH_3 production (98 % conversion) and second in ethylene production.[40,41] However, both **1** and **9** are capable of quantitative (100%) reduction of hydrazine with smaller hydrazine to catalyst ratios.[42] Compounds **1**, **2**, **4**, **5**, **7**, and **8** are easily protonated to allow for dissociation from the Mo, allowing the

Table 1.1: Production (%) of NH_3 from NH_2NH_2 and C_2H_4 form C_2H_2 from the Catalytic Reduction by various $MoFe_3$-Carboxylate Cubanes Using $CoCp_2$ as the Reducing Agent and Lut•HCl as the Proton Source. Reduction of NH_2NH_2 ([NH_2NH_2]:[catalyst] = 100:1).[40] Reduction of C_2H_2 ([C_2H_2]:[catalyst] 20:1).[41]

	Cubane Catalyst	% NH_3[a]	% C_2H_4[b]
1	$[MoFe_3S_4Cl_3(Hcit)]^{3-}$	98	60
2	$[MoFe_3S_4Cl_3(H_2cit)]^{2-}$	95	N/A
3	$[(MoFe_3S_4Cl_3)_2(\mu\text{-}ox)]_4^-$	85	N/A
4	$[MoFe_3S_4Cl_3(mida)]^{2-}$	79	N/A
5	$[MoFe_3S_4Cl_3(Hcmal)]^{2-}$	78	N/A
6	$[MoFe_3S_4Cl_3(tla)]^{2-}$	71	N/A
7	$[MoFe_3S_4Cl_3(Hnta)]^{2-}$	65	N/A
8	$[MoFe_3S_4Cl_3(tdga)]^{2-}$	65	N/A
9	$[MoFe_3S_4Cl_3(Cl_4\text{-}cat)(CH_3CN)]^{2-}$	61	70
10	$[MoFe_3S_4Cl_3(Cl_4\text{-}cat)(im)]^{2-}$	48	N/A
11	$[MoFe_3S_4Cl_4(dmpe)]^-$	14	N/A
12	$[Fe_4S_4Cl_4]^{2-}$	7	25
13	recovered cubane[c]	N/A	60
14	$[MoFe_3S_4Cl_3(Cl_4\text{-}cat)(CN)]^{3-}$	N/A	22
15	$[(CO)_3MoFe_3S_4Cl_3]^{3-}$	N/A	24
16	$[(CO)_3MoFe_3(p\text{-}S_4\text{-}C_6H_4\text{-}Cl_3)]^{3-}$	N/A	21
17	blank	N/A	2

a) Experimental values after 12 hours. b) Experimental values after 24 hours. c) The recovered cubane is the active catalyst recovered in the form of $[CoCp_2][(MoFe_3S_4Cl_3(Cl_4\text{-}cat)(DMF)]$.[41]

substrate to bind to the Mo and thus potentially mimicking the homocitrate ligand on the FeMo-co.[40] In addition, these polycarboxylate ligands may allow for transfer of a proton to the bound substrate and stabilization of the protonated substrate from hydrogen bonding to the ligands on Mo.[41] Other compounds such as $[MoFe_3S_4Cl_3(mida)]^{2-}$, are better structural mimics of the FeMo-co, but their reactivity toward NH_3 is not as high as a few of the other $MoFe_3S_4$ cubanes. The $Fe_4S_4Cl_4^{2-}$ cluster cannot reduce hydrazine, unlike a heterometal cubane.[40] However, the $Fe_4S_4Cl_4^{2-}$ cluster can reduce acetylene, demonstrating the iron atom's potential for binding other nitrogenase substrates.[41]

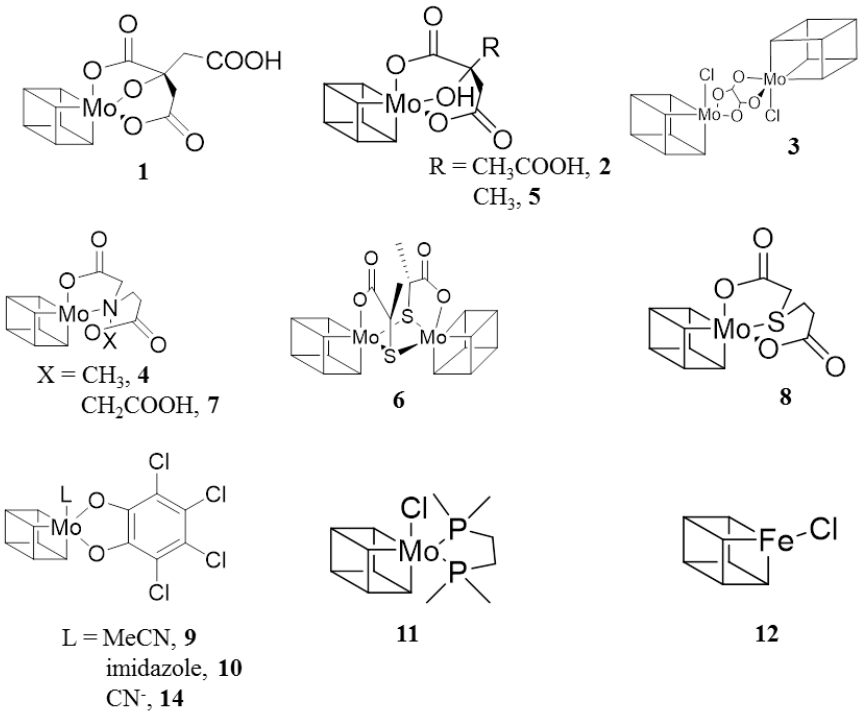


Figure 1.3: The different ligand environments around the Mo site of different $MoFe_3S_4$ cubanes.[40]

The Coucouvanis group also demonstrated that certain ligands are capable of inhibiting substrate reduction.[40,41] When the reduction of hydrazine in a CO atmosphere was conducted, it was unclear whether CO binds to the Fe or Mo sites.[40] Either way, CO irreversibly binds to the cluster and inhibits substrate (hydrazine and acetylene) reduction.[40,41] Additionally, substrate reduction is somewhat inhibited by the presence of phosphine ligands on the molybdenum site, which either shows that the substrate is competing with these ligands, or the phosphine ligands perturb the electronic structure of the metals in the cluster.[40,41] Even though [Mo-3Fe-4S] clusters demonstrate catalytic activity towards different nitrogenase substrates, the clusters still cannot bind N_2.

The [Mo-3Fe-4S] structural analogues mimic the structural, spin and oxidation states of FeMo-co, but cannot reduce dinitrogen. The tuning of the ligand environment from the Coucouvanis' group shows that the electronic structure is very important to the reactivity of these clusters. Few studies have been carried out to clarify the reasons for the limitation of the reactivity of the [Mo-3Fe-4S] clusters. Due to the complicated electronic structure possessed by these clusters, a simpler cluster was desired that contains a homoleptic environment surrounding the [Mo-3Fe-4S] cluster. One family of such clusters is stabilized and completely complexed by dithiocarbamate ligands. The synthesis and the S K-edge spectrum of $MoFe_3S_4(S_2CNEt_2)_5$,[44] where $S_2CNEt_2^-$ is the diethyldithiocarbamate (dtc) anion is discussed further in Chapter 2.

X-ray Absorption Spectroscopy

XAS is an experimental technique to electronically and geometrically characterize molecules or metal complexes. XAS experimentally probes electronic structural properties such as ligand-to-metal donation and ligand-metal effective nuclear charge (Z_{eff}). A typical XAS spectrum is broken up into two different regions: the X-ray absorption near-edge structure (XANES) and the extended X-ray absorption fine structure (EXAFS—see Figure 1.4). XANES experimentally defines the frontier molecular orbitals and thus provides information about metal and ligand oxidation states, metal-ligand bond covalencies, and ligand field splitting.[45] Furthermore, the XANES region is broken into two parts: the pre-edge and rising edge regions as depicted in Figure 1.4. The higher energy EXAFS region contains geometric structural information in the

form of a radial distribution of atoms around the absorber. The two types of excitations probed in this thesis are the K-edge and L-edges. The K-edge is an excitation that

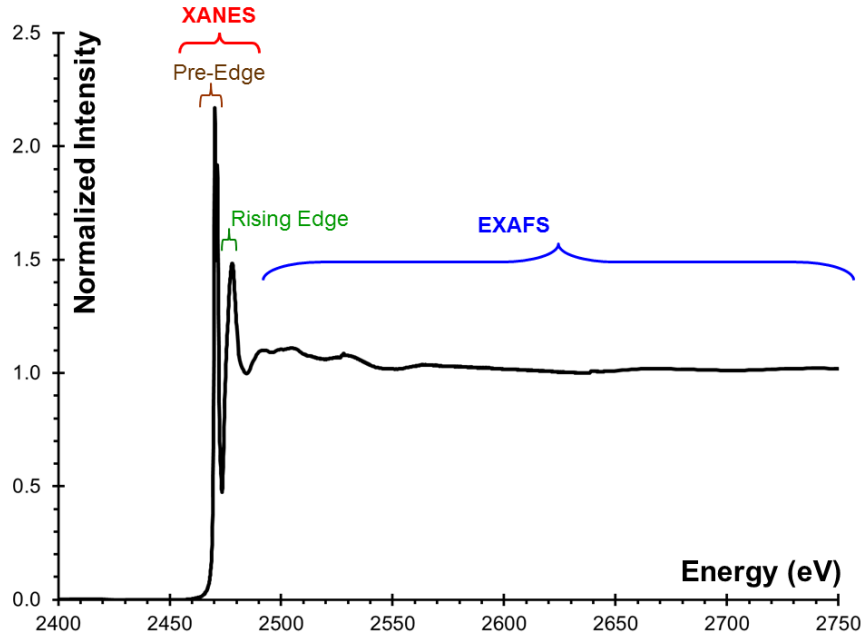


Figure 1.4: An example of an S K-edge XAS spectrum depicting the XANES and EXAFS regions. In addition, the XANES region is broken into the pre-edge and rising edge features.

originates from a 1s core electron of the absorbing atom to bound states, and eventually, the continuum. The ligand K-edge probes the 1s core orbital electron excitations to low-lying LUMO orbitals. Intensities of the peaks in the XANES region are proportional to ligand character in the frontier orbitals. The greater the ligand (np)-to-metal (nd) donation, the more intense the pre-edge features become due to the greater ligand character in the metal d-orbitals. The rising edge region probes the excitation from the 1s core to the unfilled (n+1)p ligand orbital. Changes in the rising edge position reflect differences in Z_{eff}. A higher rising-edge energy position is due to an oxidized ligand. The L-edge is an excitation from n = 2 shell, where the L_I-edge is an excitation from the 2s

orbital to the continuum and L_{II} and L_{III}-edges correspond to the excitation from the 2p orbitals with J = 1/2 and 3/2 ground state quantum values, respectively. The metal L_{III} and L_{II}-edges region probes the metal 2p to 3d, 4s, 4d, 5s, etc. transitions, where the energy position of pre-edge features are dictated by Z_{eff} and the ligand field splitting of the metal atom. The intensity of the pre-edge region is proportional to the amount of metal character in the frontier orbitals. A shift of the peak position to higher energy indicates that the metal is oxidized.

Computational Theory and Application

Computational theory was utilized to support and complement experimental interpretations of XAS data. As the field of computational chemistry continues to advance, new methodologies are being developed that more accurately models experimental results. Discussed below are two of the most relevant *ab initio* wavefunction and density functional theory based methods that are utilized in the field of bioinorganic and inorganic chemistries.

Ab Initio Wavefunction Based Methods

Ab initio wavefunction theory based methods utilize the Hartree Fock (HF) approximation where the assumption is that the electrons move independently in an average field of each other. If the HF limit is achieved with an infinitely large basis set, then the energy error or the electron correlation energy ($E_{corr)}$ is determined by equation 1.2.

$$E_{corr} = E - E_{HF} \qquad (1.2)$$

where E is the true energy of the system and the E_{HF} is the energy associated with the HF limit. The exact total energy Hamiltonian of a system is expressed in equation 1.3 by taking into account all of the kinetic (T) and potential energy (V) contributions.

$$H = T^{electron} + T^{nuclear} + V^{nuc/nuc} + V^{elec/elec} \quad (1.3)$$

However, the total energy Hamiltonian is not solvable. Using the Born-Oppenheimer approximation, the nuclear part of the Hamiltonian can be separated from the electronic, rendering equation 1.4.

$$H = -\frac{h^2}{4\pi m_e}\sum_i^{electrons}\nabla_i^2 - \frac{e^2}{4\pi\varepsilon_0}\sum_i^{electrons}\sum_A^{nuclei}\frac{Z_A}{r_{iA}} + V^{HF} \quad (1.4)$$

This electronic Hamiltonian is now solvable using the HF approximation. The V^{HF} term takes into account the exchange and repulsion between pairs of elections as expressed in equation 1.5

$$V^{HF} = 2J_{\mu v} - K_{\mu v} \quad (1.5)$$

where J is the Coulomb and K is the exchange integrals between the electrons, while μ and v are basis functions. However, electron-electron correlation is not taken into account. Post-HF methods allow for more complete treatments of the correlation energy of the system by approaching the complete configuration interaction limit (full CI). With an infinite basis set size and full CI treatment, the exact solution of the Schrödinger equation can be determined. Figure 1.5 illustrates how increasing basis set size and adding more electronic correlation increases the accuracy of the energy. Unfortunately, this is very impractical for molecules larger than a few atoms due to the high computational costs associated with these calculations.[46,47]

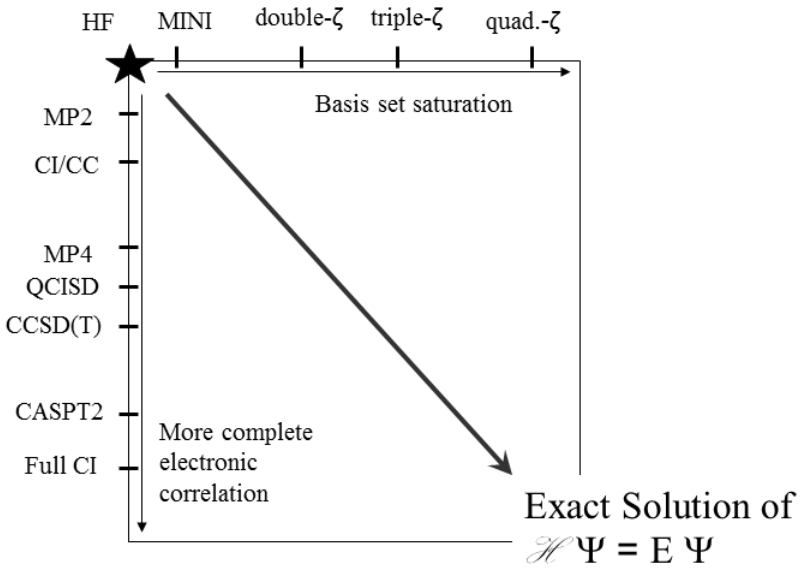


Figure 1.5: Schematic demonstration of theoretically converging series of *ab initio* wavefunction methods

Density Functional Theory

Density functional theory is a different computational technique that calculates the energy of the system as a functional of the electron density. The electron density is a function with only three variables: the x, y, and z positions of the electrons as seen in equation 1.6:

$$\text{Energy} = F[\rho(x,y,z)] \qquad (1.6)$$

where $\rho(x,y,z)$ is the electron density and F is a functional. Density functional theory based methods approximates the exchange and correlation through the functionals of the electron density. DFT utilizes considerations from the Hohenberg-Kohn theorem[48], and the Kohn-Sham equations.[49] DFT separates the electronic energy into four different terms as shown in equation 1.7:

$$E(\rho) = E^{T}(\rho) + E^{V}(\rho) + E^{J}(\rho) + E^{XC}(\rho) \qquad (1.7)$$

where E^T is the kinetic energy, E^V is the electron-nuclear potential energy, E^J is the electron-electron repulsion, and E^{XC} is the exchange-correlation term. Unlike the *ab initio* WFN based calculations described above, DFT approximates the amount of exchange and correlation of the system depending on the functional used. Each functional provides differing amounts of E^X and correlation E^C that is utilized in the E^{XC} term in equation 1.7. Advances in DFT went from early Xα and Slater-exchange to the local density approximation (LDA) to the utilization of the Kohn-Sham first derivative-corrected generalized gradient approximation (GGA), and second derivative-corrected functionals (meta-GGA).[50] The LDA, GGA, and meta-GGA functionals make up the first three rungs of "Jacob's ladder".[51,52] The higher rungs of Jacob's ladder incorporate more complex electron interactions of the density. However, their application to coordination complexes is limited for realistically sized models, and their accuracy is not guaranteed. An alternative approach proposed by Becke is to incorporate hybrid exchange functionals that mixes exact nonlocal HF exchange and pure GGA or meta-GGA functionals.[53,54] This mixing is a useful technique that allows for empirical tuning of the functional towards the experimentally observed electronic structure.[55] Figure 1.6 graphically depicts the conceptual relationship of the vary amount of HF exchange in density functionals and their relative position to HF theory. GGA functionals such as BP86[56,57] often lead to an overly covalent description of the ground state electronic structure, whereas empirically derived functionals such as B3LYP[54] can improve accuracy for coordination complexes. Unfortunately, there is no single known functional that accurately models all transition

metal complexes. The advantage to using DFT over *ab initio* WFN methods is that DFT scales to the 3rd power, and is therefore, less computationally expensive.

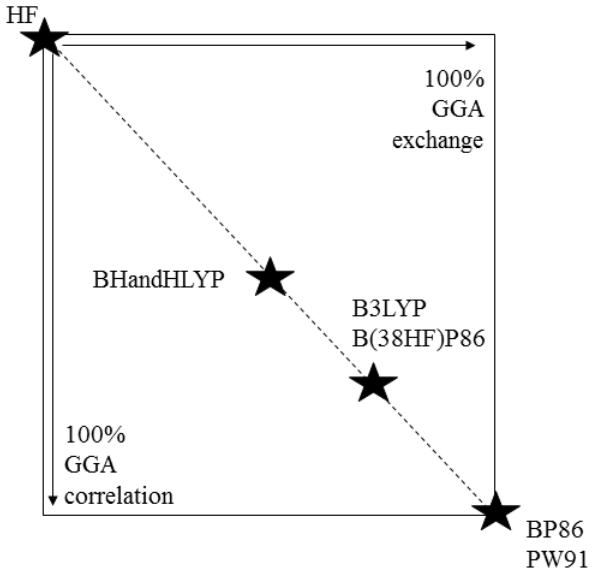


Figure 1.6: The relationship of mixing HF exchange with GGA functionals.

Basis Sets

A very important input parameter in both DFT and *ab initio* WFN calculations are the size and quality of the basis set. There are different types utilized in this thesis: Slater-type orbitals (STO) and Gaussian-type orbitals (GTO). STOs are generally more chemically meaningful due to the hydrogen-like radial distribution and the correct cusp behavior of the orbital. However, STOs are more computationally expensive compared to GTOs. The use of *ab initio* WFN theory to determine the basis set quality and how well it approaches the saturation limit is very beneficial. Once the basis set saturation limit is achieved, larger basis sets would only slightly improve the electronic structure while increasing the computational cost.[46,47]

Population Analysis

Once the ground state energy has been determined using either *ab initio* WFN or DFT, it is necessary to break the total electron density into its atomic or molecular orbital fragments. The population analyses described in this thesis are the Mulliken population analysis (MPA),[58] Weinhold's Natural population analysis (NPA),[59] Löwdin population analysis,[60] and Bader's Quantum Theory of "Atoms in Molecules" (AIM).[61] The MPA is standard in most quantum chemical programs. It partitions the total density equally amongst atoms in the molecule with respect to the basis function overlap. Due to the bond polarity associated with coordination complexes, MPA does not yield chemically reasonable bonding descriptions of metal ligand bonds. Another pitfall of MPA is that it is largely basis set dependent. The NPA method partitions the density based on orthonormal natural atomic orbitals. The electron density is fit to the core orbitals, at two electrons each. The valence orbitals are then filled with occupations close to two electrons per orbital. The Rydberg orbitals are filled with the left over electron density that was not used in the valence orbitals. NPA has resolved the basis set dependence issues experience from MPA. In addition, NPA has been implemented successfully for coordination complexes using a proper description of the valence set of atomic orbitals.[62,63] The Löwdin population analysis transforms atomic orbital basis functions into orthonormal basis functions allowing the MO coefficients to transform to give a representation of the wavefunction using the new basis set. The Löwdin technique however, does not account for differences in electronegativity of different atoms, and is computationally more expensive than MPA. AIM examines the topology of the electron

density of the molecule of interest. AIM creates spatial partitions of the atoms whose boundary conditions are defined by the zero flux surface of the electron density. The electron density is integrated inside this zero flux boundary to determine the total charge of the atom in the associated space. AIM is the most chemically reasonable method since it does not contain any orbital-based constraints. It also accounts for electronegativity differences, and is relatively basis set insensitive.[64,65] AIM is the most rigorous, and therefore, it is computationally the most expensive method. AIM also does not provide individual orbital contribution from the determined atomic density.

Time Dependent-Density Functional Theory

Time dependent density functional theory (TD-DFT) is an extension of DFT and allows for the simulation of energies of excited states of isolated systems from valence or core excitations. If a molecule is subjected to a linear electric field that fluctuates, then the frequency-dependent polarizability is closely approximated by:[47]

$$\langle \alpha \rangle_{\omega} = \sum_{i \neq 0}^{\text{states}} \frac{|\langle \Psi_0 | \mathbf{r} | \Psi_i \rangle|^2}{\omega - (E_i - E_0)} \qquad (1.8)$$

where $<\alpha>_{\omega}$ is the frequency-dependent probability of a transition, **r** is the one dimensional position vector, and ω is the frequency of the fluctuation. The numerator in the sum is the transition dipole moment, while denominator contains both the frequency and the energies of the excited and ground states. The derived excitations are simply the poles of the response function when the denominator approaches zero because the frequency matches the difference in energy of the excited and ground states. TD-DFT has been developed and implemented over the last 10 years to simulate a number of different XAS spectra at the ligand K, metal K, and metal L-edges.[66-73]

Reductive Amination

The reduction of carbon-nitrogen π-systems to saturated derivatives have been part of synthetic chemist's repertoire since the introduction of lithium aluminum hydride ($LiAlH_4$, LAH) and sodium borohydride ($NaBH_4$) in the 1940's.[74,75] Figure 1.7 illustrates mechanistic possibilities of the reduction of the carbon-nitrogen π-system where activation via protonation or complexation occurs prior to hydride transfer to the electrophilic carbon.

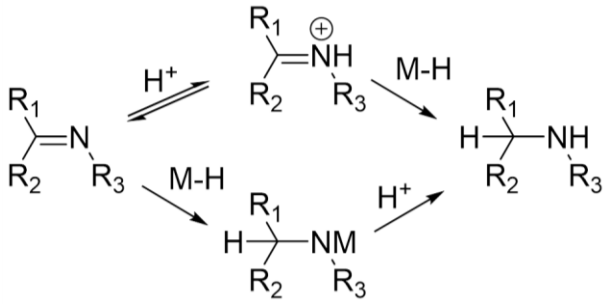


Figure 1.7: Potential mechanistic pathways for reductive amination.

New reducing agents were needed with different properties and selectivities as the complexity of molecules grew. Alterations of the metal hydride species were usually made by replacing one or more hydrogens with other functionalities or replacing the counter cations. A few popular examples include sodium bis(2-methoxyethoxy)aluminumhydride (Red-Al), diisobutyl aluminum hydride (DIBALH), sodium cyanoborohydride ($NaBH_3CN$) and lithium triethylborohydride ($LiEt_3BH_3$, superhydride).[74,75] Neutral boranes are also commonly used, although they are generally employed in the form of a solvate or an amine complex. Common examples include

dimethylsulfide borane ($Me_2S•BH_3$) tetrahydrofuran borane ($THF•BH_3$), pyridine borane, diphenylamine-borane ($Ph_2NH•BH_3$), etc.[74,75]

The Livinghouse lab recently used LAH for the reductions of unsymmetrical dimethylhydrazines for their application in metalloamination.[76] However, LAH is a very potent reducing agent, capable of further reducing carbonyls, or other susceptible functional groups that are present.[77] For example, the styrene functional group of the dimethylhydrazone shown in Figure 1.8 was subjected to further reduction in the presence of LAH. Therefore, $NaBH_3CN$ was utilized for its selectivity and facile reduction of C=N π-systems.[74,75,78] It was successfully utilized in the reduction of the dimethylhydrazone in Figure 1.8 at 85% yield.

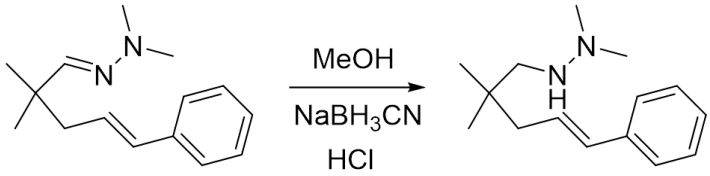


Figure 1.8: Sodium cyanoborohydride reduction of a dimethylhydrazone.

Due to the expense and toxicity of $NaBH_3CN$, a new reducing agent was desired for the selective reduction of the C=N π-system that is cheaper and less toxic for large scale reactions. Amine-boranes have been used as a worthy substitute for cyanoborohydrides for the reduction of hydrazones.[77,79-82] However, many of the commercial amine-boranes are expensive. Therefore, we investigated the possibility of designer amine-borane prepared *in situ* that were potent enough to reduce the C=N bond of hydrazones in Chapter 6.

Research Directions

In order to understand how the ligand contributions affect the reactivity of biomimetic models of FeMo-co, a simpler system, $MoFe_3S_4(dtc)_5$ was chosen due the homoleptic ligand environment surrounding the cubane. The experimental electronic structure was examined utilizing the S K and Mo L_{III} and L_{II}-edges in Chapter 2. Since both types of Na(dtc) and Na_2S free ligands are S based, they were compared along with the $MoFe_3S_4(dtc)_5$ cluster. The Mo L-edges lay shortly after the S K-edge EXAFS region, and were also examined qualitatively. Tentative assignments to the S K-edge spectrum of the $MoFe_3S_4(dtc)_5$ cluster are discussed based on the Slater's rules for effective oxidation states.

Due to the complexity of the $MoFe_3S_4(dtc)_5$ cluster discussed in Chapter 2, Chapter 3 examines the Mo-S bond using the simple MoS_4^{2-} anion. S K-edge XAS was collected for three different salts of the MoS_4^{2-} compound for comparison. Wavefunction calculations were carried out to determine the basis set saturation limit with regards to S character in the e and t_2 orbitals, and also utilized in the interpretation of the extracted experimental S character. A complete analysis of various GGA, hybrid-GGA, meta-GGA, and meta-hybrid-GGA functionals utilizing a diverse set of exchange correlation functionals were carried out using a saturated basis set. In addition, the S K-edge spectra were also simulated using TD-DFT calculations.

Similar to Chapter 3, Chapter 4 investigates the dtc ligand bonding using different transition metals in regard to the $MoFe_3S_4(dtc)_5$ complex. The transition metals examined in this chapter were Zn(II), Cu(II), Ni(II), Fe(II)/Fe(III), and Mo(IV) all coordinated to

two or more dtc ligands. The S K-edge XAS dipole integrals were developed based on the effective oxidation state of the sulfur in the complexes. The experimental S 3p character was determined using the new S K-edge dipole integrals and correlated with popular literature functionals that have been utilized for similar systems using a saturated basis set. In addition, the excited spectra were simulated with TD-DFT to reproduce the S K-edge excited state.

Chapter 5 delves deeper into the detector dependence and error associated with S K-edge XAS of $Cu(dtc)_2$. $Cu(dtc)_2$ has been studied extensively with electron paramagnetic resonance due to the d^9 electronic configuration of Cu(II). Using the experimental bonding parameters, the covalency of the semi-unoccupied molecular orbital was derived for this system. The Cu-S σ* peak area was measured at various beamlines, utilizing different detectors and detection methods to correlate the error in the transition dipole integral. The application of the transition dipole was applied to extracting the experimental S character from both the Na(dtc) free ligand and the $Cu(dtc)_2$ complex for the rising edge that corresponded to the S-C-N π* orbital(s). The ground state and excited state electronic structures were also investigated and correlated to the experimental electronic structure for Na(dtc) and $Cu(dtc)_2$ computationally.

Chapter 6 takes a step back from spectroscopy and theory and focuses on new method development for the reduction of the unsaturated C,N double bond. Instead of using the highly toxic, and costly sodium cyanoborohydride reducing agent, we investigated the reactivities of amine-boranes towards reductive the amination of dimethylhydrazones. The Livinghouse group has shown that the corresponding

dimethylhydrazines are excellent reagents for facile intramolecular metalloamination of nitrogen containing heterocycles using organo-zinc reagents.[76] The importance of nitrogen containing heterocycles cannot be understated, especially in regards to the pharmaceutical industry. Different amine-boranes were synthesized to compare their reactivity and towards 2-heptylidene-1,1-dimethylhydrazine and 2-benzylidene-1,1-dimthylhydrazine. The best amine-borane was determined based on reactivity time and feasibility of the workup. Once the optimal reaction conditions were determined, multiple dimethylhydrazones containing different functionalities were reduced *in situ*, thus demonstrating the applicability of the designer amine-boranes in regards to the reduction carbon-nitrogen π system.

CHAPTER 2

AN XAS INVESTIGATION OF A [Mo-3Fe-4S] CLUSTER

Introduction

The electronic structure of [Mo-3Fe-4S] clusters are complicated due to the different bonding modes and the magnetic coupling exhibited in the cluster.[24] In an effort to analyze the experimental electronic structure and bonding of a [Mo-3Fe-4S] cluster, a simple cluster was desired, which contained a homoleptic environment surrounding the cubane of the cluster. Therefore, the effect of ligand covalency of both the terminal and bridging sulfides in the cluster could be examined. One family of such clusters is stabilized and completely complexed by diethyldithiocarbamate (dtc) ligands. Figure 2.1 displays the crystal structure of $MoFe_3S_4(dtc)_5$ from Qui-Tian, L. *et al*.[83]

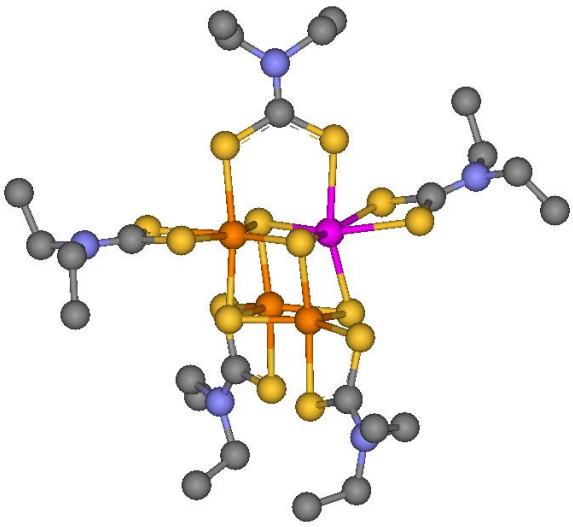


Figure 2.1: The crystal structure of $MoFe_3S_4(dtc)_5$ (Cambridge Crystallographic Database Code JALDOP).[83]

The dtc anion contains a -1 charge delocalized between an S-C-S bond moiety, which stabilizes the [Mo-3Fe-4S] core enabling it to achieve the high oxidation state of +5.[44] Two of the three irons are five coordinate, while the other iron is hexa-coordinate. All the irons are in the +3 oxidation state and are high spin according to liquid nitrogen temperature Mossbauer experiments.[44] Since the cluster has an overall neutral charge, the Mo is therefore in the +4 oxidation state. The bidentate nature of the dtc ligand allows for the cluster to spontaneously assemble in a one pot reaction mixture.[44] Four dtc ligands bind to an individual metal center, while the other dtc ligand bridges the Fe and Mo sites.

The reactivity of the FeMo-co and biomimetic [Mo-3Fe-4S] cluster models are linked directly to their electronic structures.[8,43,45] X-ray absorption spectroscopy (XAS) directly probes the experimental electronic structure and has been utilized to analyze the blue-copper protein plastocyanin,[84,85] different types of iron sulfur clusters,[86-88] and many different types of biomimetic models related to protein active sites.[45] Extracted FeMo-co has been examined at the S K- and Mo L_{III} and L_{II}-edges back in 1988.[10] The Mo L_{III} and L_{II}-edges supported the electron nuclear double resonance interpretation of the effective of oxidation state of Mo to be +4 in the oxidized and semi-reduced forms.[9] The +4 oxidation state of FeMo-co is the same oxidation state exhibited by the $MoFe_3S_4(dtc)_5$ clusters.[44] Additionally, since the crystal structure of FeMo-co was not known at the time, the authors compared different ligand environments around Mo using biomimetic models on the effective oxidation state of the Mo site.[9] Their results indicated that both S and O atoms were bonded to Mo, not just an all S or an all O environment. Another significant result from the Cl K-edge of the FeMo-co was that Cl^- was not present in the structure.[9]

The utilization of ligand K-edge XAS towards the Fe-S clusters has been successful in the understanding of the bond covalency and the magnetic structure of $[Fe_2S_2]^{+}$ versus $[Fe_4S_4]^{2+}$ clusters.[86,87] Solomon *et al.* determined that the iron's effective oxidation state increased when going from the dimer to the tetramer.[86] This is due to the decrease in the sulfide covalency from μ_2 to μ_3 bridging sulfide ligand. The increase in the effective charge of the iron meant that the terminal ligands donated more electron density, thus increasing their bond covalency. The measure of the effective oxidation state for sulfur is defined as the transition from the S 1s→4p orbital. The more oxidized the sulfur atom in a molecule/ligand, the deeper the S 1s orbital shift to lower energy with respect to the S 4p orbitals due to the increase in the effective nuclear charge.[86]

Due to the complexity of experimental S K-edge spectrum of FeMo-co and its complicated magnetic coupling determined by density functional theory calculations, a simpler heteronuclear cubane was examined. The S K, Mo L_{III} and L_{II}-edge XAS spectrum was measured and utilized in an effort to better understand the effects of sulfide and the dtc ligands to electronic structure of the [Mo-3Fe-4S] cubane of $MoFe_3S_4(dtc)_5$. In addition, the $MoFe_3S_4(dtc)_5$ cluster was compared to the free ligand salts of Na_2S and Na(dtc) to aide in the interpretation of the S K-edge spectrum.

Experimental Section

Sample Preparation

The $MoFe_3S_4(dtc)_5$ cluster[44] and Na_2S[89] were synthesized according to literature procedures. Na(dtc) was purchased from Fisher Scientific and dehydrated under vacuum

for 3 hours. This procedure led to the disappearance of the OH stretch in the FT-IR spectrum at 3000-3700 cm^{-1} and assumed suitably pure.

Sulfur K-edge X-ray Absorption Spectroscopy

All measurements were collected at beamline 4-3 of the Stanford Synchrotron Radiation Lightsource under storage ring (SPEAR 3) condition of 300-80 mA current and 3 GeV energy. BL 4-3 has a 20-pole, 2.0 T Wiggler beamline equipped with a liquid N_2 cooled Si(111) double-crystal monochromator. All XAS measurements were carried out at room temperature and the samples were prepared in a nitrogen or argon gas filled gloveboxes. Repeated measurements of the same samples did not reveal any significant variation among data sets from the different collection periods. The solid samples were ground with boron nitride and pasted onto a Kapton tape. The only exception to this was $MoFe_3S_4(dtc)_4$, which had a low concentration of sulfur and yielded the highest intensity for the Mo L_{III}- and L_{II}-edges. Any excess sample was scraped off from the tape to minimize the distortion of peak intensities due to self-absorption effects. The sample cell was protected with a few μm thick Mylar polypropylene window to eliminate possible sample degradation due to oxidation or exposure to moisture. The beamline was optimized to maximize incident beam intensity at the high energy end of the scan. Fluorescence detection methods utilized were the Lytle or a nitrogen gas purged and a passivated implanted planar silicon detector (PIPS, CANBERRA).

XAS Data Normalization, Fitting, and Error Analysis

All data was background subtracted and normalized using the Automated Data Reduction Protocol (ADRP) developed by D. Gardenghi.[90] All the S K-edge data was averaged and calibrated to sodium thiosulfate pentahydrate at 2472.02 eV. ADRP consists of three steps to analyze the XAS data: (1) baseline subtraction, (2) background correction, and (3) normalization. The baseline subtraction and background subtraction are performed in a single step. The background is fit with a smooth second-order polynomial, that is then subtracted from the spectrum. Normalization of the data was accomplished by fitting a flattened second-order polynomial to the post edge region. For $MoFe_3S_4(dtc)_5$, the second-order polynomial was fit after the Mo L_{II}-edge. All the spectra were normalized through a fit spline function to 1.0 at 2490 eV. The error introduced by data reduction and normalization procedures was at most 3% in the peak amplitudes.

Results and Analysis

Analysis of S K, Mo L_{III} & L_{II}-edges of $MoFe_3S_4(dtc)_5$

Figure 2.2 shows two overlapping edges—the S K and Mo L_{III} and L_{II}-edges for the $MoFe_3S_4(dtc)_5$ cluster. Molybdenum has core excitations that occur shortly after the S K-edge. The peak at ~2525 eV corresponds to the Mo $2p_{3/2}\rightarrow 4d$ transition, and the peak at ~2638 eV is the Mo $2p_{1/2}\rightarrow 4d$ transition.

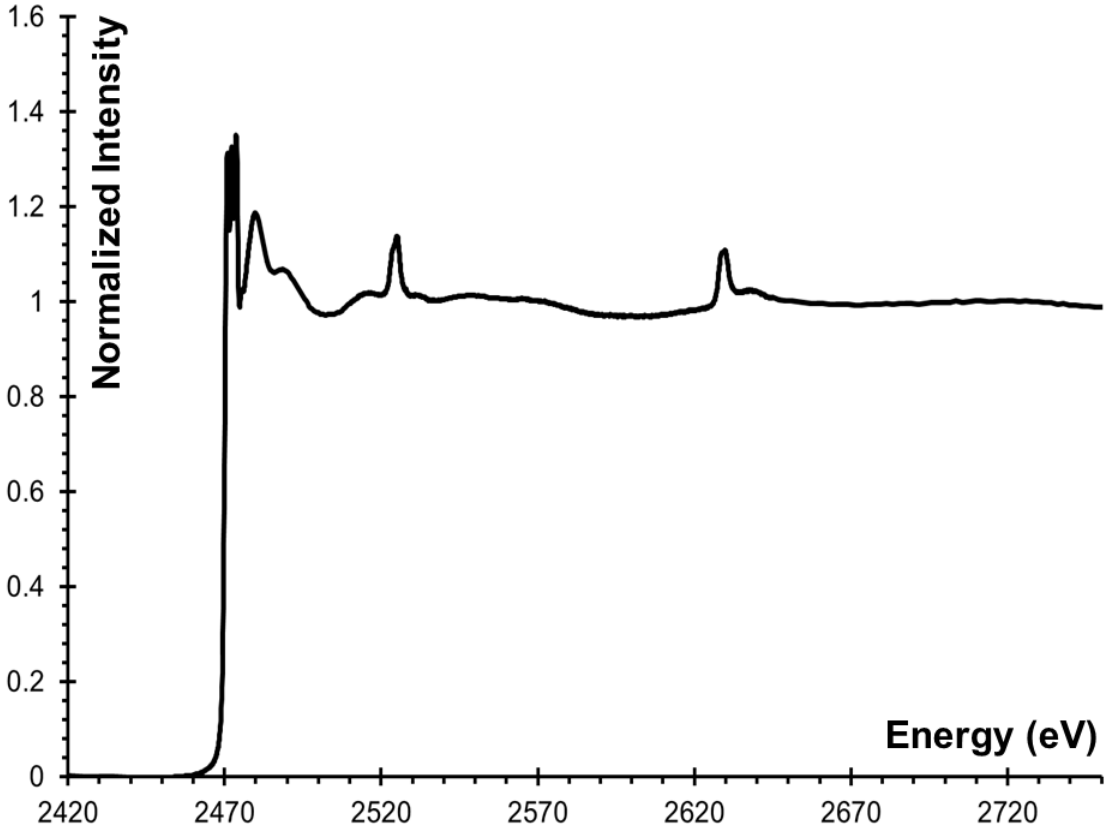


Figure 2.2: The S K, Mo L_{III} and L_{II}-edges of the $MoFe_3S_4(dtc)_5$ cluster.

Both the Mo L_{III} and L_{II}-edges both contain two peaks corresponding to transitions from the 2p orbitals to the empty Mo 4 d-orbitals. The hexa-coordinate Mo has two features seen in the Mo L_{III} and L_{II}-edges that correspond to excitations to low lying unoccupied orbitals. The asymmetry of the Mo L-edges is consistent with extracted FeMo-co where the lower energy feature is a shoulder to the slightly higher energy peak.[10] As seen in Figure 2.3, the oscillatory S K-edge EXAFS complicates the Mo L-edges and no further examination of these edges was taken.

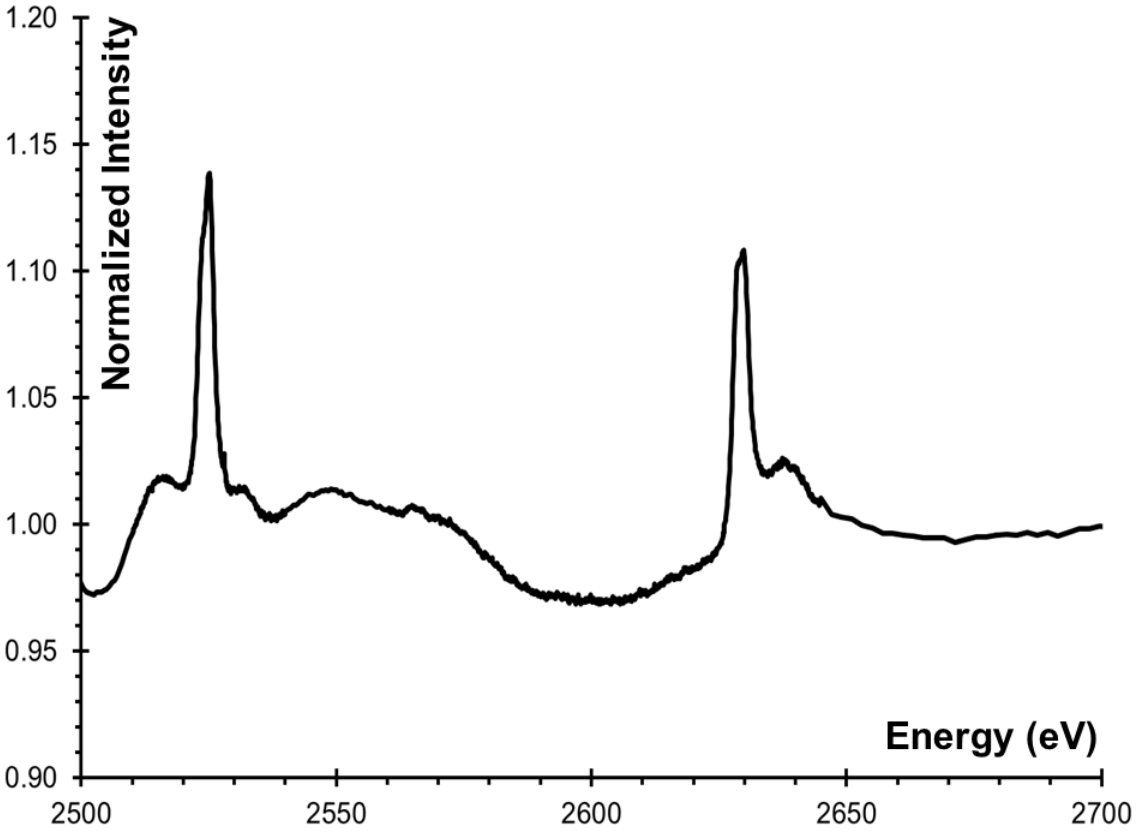


Figure 2.3: The Mo L_{III} and L_{II}-edges expanded of $MoFe_3S_4(dtc)_5$. The normalized intensity is based on the S K-edge and not the L_{III} and L_{II}-edges.

Analysis of Energy Positions of S K-edge XANES Features. Figure 2.4 displays the S K-edge XANES region, the first derivative, and second derivative plots of Na(dtc), Na_2S, and the $MoFe_3S_4(dtc)_5$ cluster from Figure 2.2. Our interpretation of the edge jump is the first derivative peak (inflection point) after the most intense feature (white line), which corresponds to Z_{eff} of the sulfur. This is the lower estimate of the edge position, but this assignment is ambiguous for ligands other than sulfides. The free ligand spectrum of Na_2S contains only one dipole allowed transition, which is the S 1s → 4p due to the filled valence shell of S^{2-}.[62] This transition is located at 2471.6 eV. At higher energies, the electron is ejected into the continuum and the two intense features at 2472.3 and

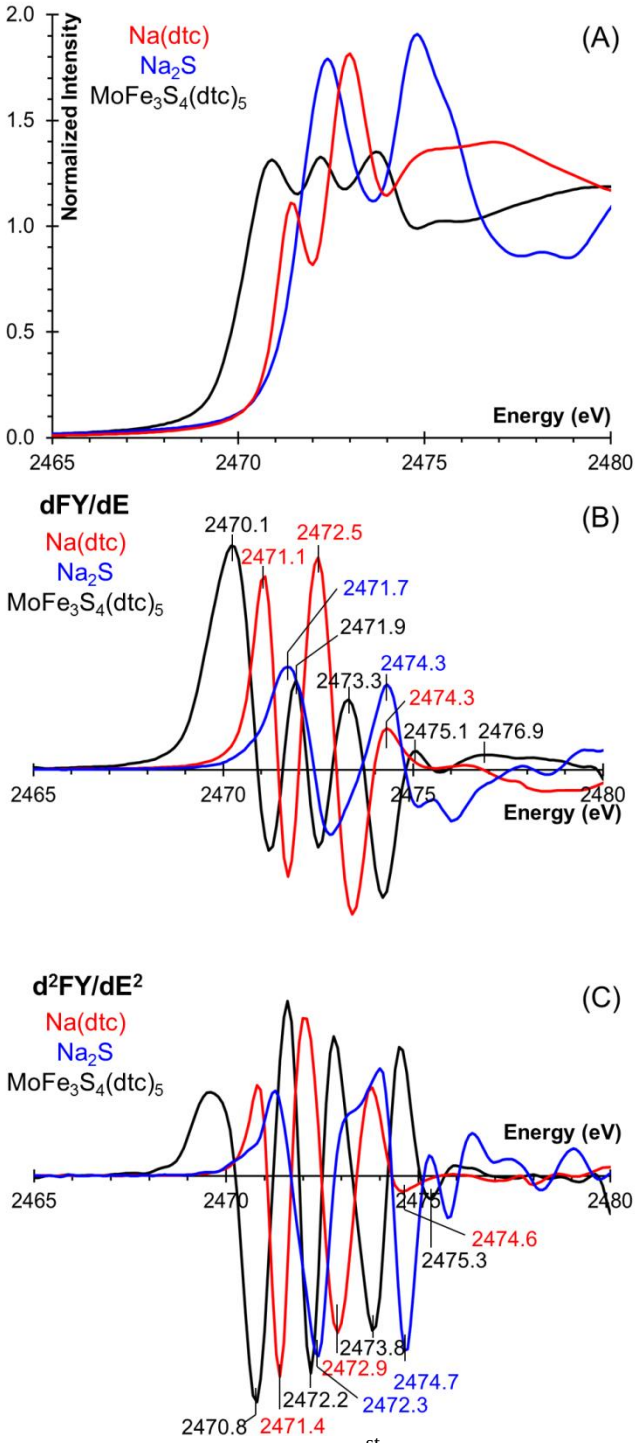


Figure 2.4: (A) The S K-edge XANES, (B) the 1st derivative, and (C) the 2nd derivative plots of $MoFe_3S_4(dtc)_5$ along with the dtc and S^{2-} free ligands.

2474.7 eV are part of the EXAFS region. For the Na(dtc), the pre-edge feature corresponds to the transition to the S-C-N π* which is the lowest unoccupied molecular orbital (LUMO). The most intense feature for the dtc ligand corresponds to the transition to the S-C σ* orbital. The estimated S 4p peak position is at 2474.3 eV for the dtc ligand, which is higher in energy compared to Na_2S. The increase in energy is due to the differences in Z_{eff} of the two ligands. Sulfide has a formal -2 charge compared to dtc whose formal charge is -1, which corresponds to ΔE of 2.6 eV. The lower the Z_{eff} associated with the absorbing species, the lower the energy of the transition.

In regards to the [Mo-3Fe-4S] complex, it is very difficult to assign the peaks corresponding to the metal sulfide, and the metal dtc transitions. Additionally, the transitions to the S-C-N π* and S-C σ* orbitals that are localized to the dtc ligand are ambiguous. Since there are 14 different sulfur environments, there should be 14 different S 4p transitions since there should be 14 different effective oxidation states of sulfur. Table 2.1 summarizes the peak and edge positions for the Na(dtc), Na_2S, and $MoFe_3S_4(dtc)_5$ complexes. Two edge positions are listed in Table 2.1 for the $MoFe_3S_4(dtc)_5$ cluster due to the ambiguity of the S 4p peak(s). As discussed above, the large energy difference of the free sulfide and dtc S 4p transitions could potentially account for two these positions in the [Mo-3Fe-4S] cluster. If this is the case, then the S 4p positions would be located at 2475.1 eV for the μ3 sulfides, and 2476.9 eV for the dtc ligands. The energy difference would then be 1.8 eV. The decrease in the ΔE is congruent with the decrease in the energy spacing of the high lying Rydberg orbitals just before the continuum.

Table 2.1: Energy of S K-edge Features of Free Ligands and $MoFe_3S_4(dtc)_5$.

	Pre/Rising Edge Feature(s) eV	Estimated Edge Position eV[b]
Na(dtc)	2471.4 2472.9	2474.3
Na_2S[a]	-	2471.7
$MoFe_3S_4(dtc)_5$	2470.8 2472.2 2473.8 2475.3	2475.1 2476.9

a) Na_2S is defined as on S 1s→4p transition and the features observed in Figure 2.4 (A) are EXAFS. b) The edge position is defined as the first local maxima of the first derivative after the white line.

The intensity of the normalized spectrum in Figure 2.4 (A) of the $MoFe_3S_4(dtc)_5$ cluster is proportional to the amount of S character in the chemical bonds. The lower normalized intensity is indicative of a more ionic complex. The [Mo-3Fe-4S] cubane is typically covalent due to the $\mu 3$ sulfides. The higher covalency would result in larger pre-edge features where there is more electron donation to the irons and the molybdenum site. The five dtc ligands must have a stabilizing effect on the metal ions, presumably through ionic bonding. Since there are 2.5 times as many sulfurs from the five dtc ligands than the four sulfides, then the normalized intensity of the spectrum would be suppressed. As discussed in the Introduction, Solomon *et al.* hypothesized that systems $\mu 3$ ligands donate less electron density to the metals, forcing the mono-dentate terminal ligands to donate more electron density to the metal sites.[86] However, since dtc is a bi-dentate ligand, the two sulfurs contribute less electron density per sulfur to the metal sites as

opposed to a thiolate ligand thus lowering the intensity of S K-edge features associated with dtc binding.

There are 14 different sulfur environments contributing simultaneously to this spectrum—four sulfides and ten sulfurs from the five dtc ligands. This means there are 14 different pre-edge and edge features superimposed on each other. Of the four sulfides, there are three in different chemical environments. Similarly, of the five dtc ligands, three of them are also in three different chemical environments. Due to the complexity of the spectrum, only hypothetical assignments can be inferred based on Slater's rules for effective oxidation states. The Z_{eff} is greater for Fe(III) than Mo(IV) at 6.60 vs 5.65, respectively. The dtc anion has a larger Z_{eff}, when compared to the sulfide anion, which is due to the lower associated charge on the ligand. Figure 2.5A shows one such possible assignment with the first rising edge spectral feature assigned to the coordination of Fe(III)-S bond. The next feature could then be the Mo(IV)-S bonding contribution. Then the last feature could be due to both the Fe(III)-dtc and Mo(IV)-dtc bonds. If that is the case, then we cannot assign the S-C-N π^* and the S-C σ^* of the dtc ligand in addition to the S 4p transition.

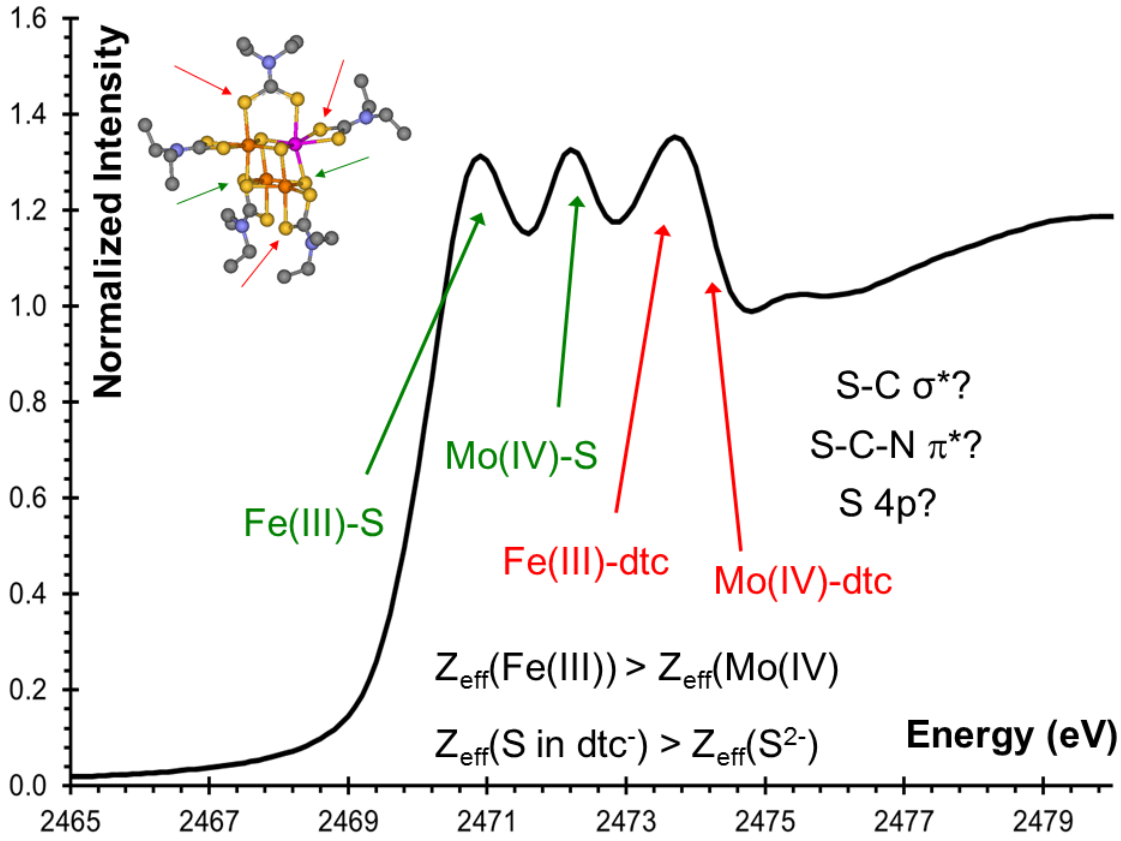


Figure 2.5: An interpretation of the S K-edge XANES region of the $MoFe_3S_4(dtc)_5$ cluster.

Another interpretation of the S K-edge is given in Figure 2.6. The lowest energy feature could correspond to both the Fe(III)-S and Mo(IV)-S bonds. The next subsequent peak higher in energy could then be the Fe(III)-dtc bond. The last intense feature could be two features corresponding to the Mo(IV)-dtc bond and the S-C-N π* orbitals. The S-C σ* could then be the small feature at 2475.3 eV. These interpretations assume that the ligand-metal bonds correspond to a single transition in the S K-edge XANES region. This assumption may not be valid based on the d-orbital splitting of the three irons and the molybdenum atom. Due to the current resolving power of this technique, making absolute assignments is rather difficult.

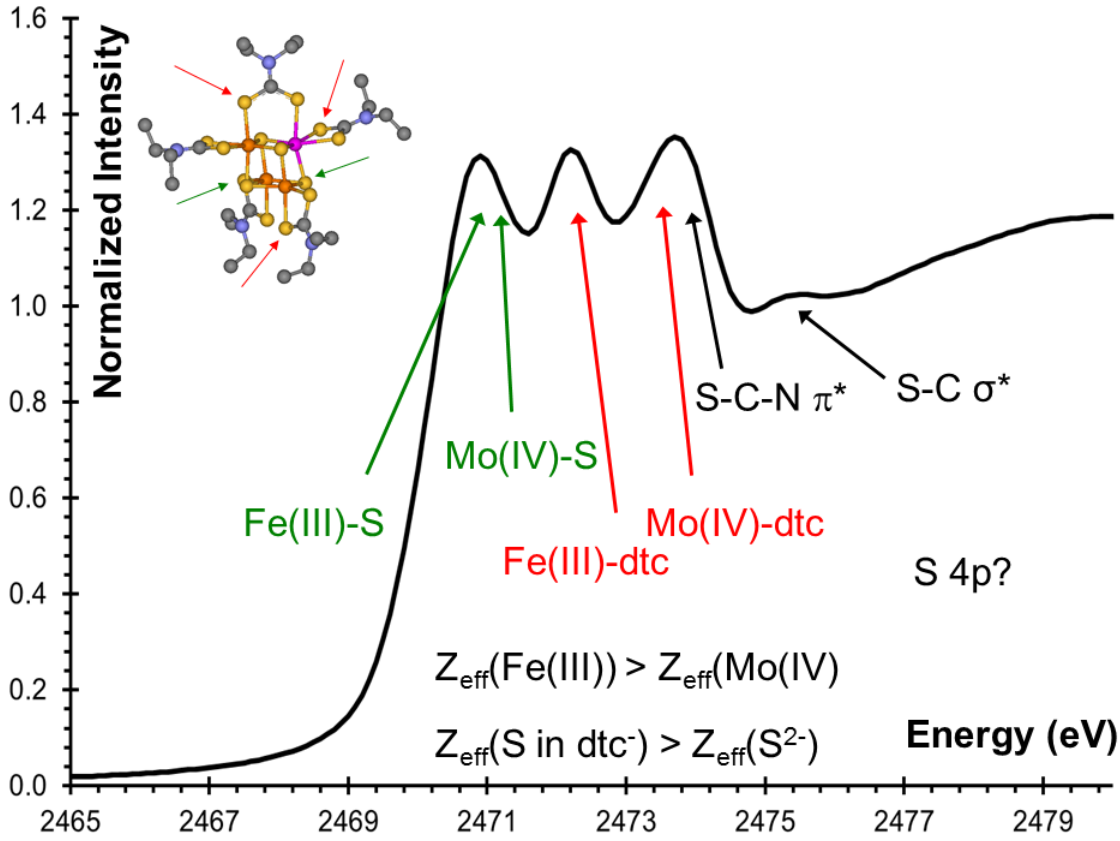


Figure 2.6: A second interpretation of the S K-edge XANES region of the $MoFe_3S_4(dtc)_5$ cluster.

Conclusions

The S K Mo L_{III} and L_{II}-XAS data was gathered for the $MoFe_3S_4(dtc)_5$ cluster, and possible transition assignments were postulated based on its theorized electronic structure. The Mo L_{III} and L_{II}-edges are comprised of two transitions to low lying unoccupied orbitals. There are 14 different sulfur environments present in this cluster, thus convoluting the S K-edge spectrum. When comparing the free ligands, there is a large difference in the effective oxidation states of the Na_2S and Na(dtc). The complexation of these two ligands in the $MoFe_3S_4(dtc)_5$ cluster could lead to two

different prominent edge positions in the XANES S K-edge spectrum. In addition, the S K-edge of the dtc free ligand contains the transition to the S-C-N π* and S-C σ* orbitals. The transitions associated with the metal sulfide and metal dtc bonding could not be identified. Numerous interpretations of the S K-edge XANES region can be made based on the Slater's rules for effective oxidation states. Furthermore, the transitions to the S-C-N π* and S-C σ* orbitals were either not resolvable, or took on a different shape that could not be discerned from the other features. Therefore, no absolute assignments corresponding to the S K-edge XANES region can be confirmed for the $MoFe_3S_4(dtc)_5$ cluster. Complementary electronic structure measurements, such X-ray emission spectroscopy, could provide further insight into the deconvolution of the S K-edge XANES region of the $MoFe_3S_4(dtc)_5$ cluster. The amplitude of the peaks associated with the $MoFe_3S_4(dtc)_5$ cluster are not intense as compared to the Na_2S and Na(dtc) spectra, signifying higher degree of ionic bonding present in this system. This is a reasonable conclusion based on the number of sulfurs involved in bonding, thus reducing the covalent character per sulfur. The complexity and ambiguity of the S K-edge spectrum of this cluster is probably why other [Mo-3Fe-4S] cluster single cube clusters were never published. The $MoFe_3S_4(dtc)_5$ cluster was not examined computationally due to the size of the cluster and potentially complicated magnetic coupling.

In order to understand the effects these free ligands have to the iron and molybdenum sites experimentally, simpler models were examined in the following chapters. The Fe-S bonding models and protein sites have already been examined extensively in literature,[86-88] so in order to characterize the Mo-S bonds, the MoS_4^{2-}

system was examined. Additionally, the development of the dtc ligand using XAS through a series of transition metal including Fe(II)-dtc, Fe(III)-dtc and Mo(IV)-dtc were examined.

CHAPTER 3

QUANTIFYING THE Mo-S BOND OF TETRATHIOMOLYBDATE COMPLEXES

Introduction

The Mo-S bond is an important function for molybdoenzymes such as FeMo-co that leads to stability and reactivity at the Mo site.[91] The Mo-S bond of the $MoFe_3S_4(dtc)_5$ cluster is also important as discussed in Chapter 2. A simple model system to use for the study of the Mo-S bond is the MoS_4^{2-} anion.[91] MoS_4^{2-} is used in the syntheses of $MoFe_3S_4$ clusters and other biomimetic models as the starting material.[20,25,26,91] All the sulfides are terminal and their electronic contributions are equal to the Mo in the MoS_4^{2-} system. The Mo has a formal oxidation state of +6 corresponding to a d^0 electronic configuration, and each of the four sulfides has -2 formal charge. The ideal geometry for MoS_4^{2-} complexes is T_d. The lowest unoccupied molecular orbitals are the e and t orbitals utilizing crystal field theory.

To analyze the quantitative ground state information pertaining to sulfur base ligands, no other experimental technique other than X-ray absorption spectroscopy (XAS) yields comparable electronic and geometric structural information from core orbital excitations. The quantitative analysis of the X-ray absorption near edge structure (XANES) region of the S K-edges has been well defined for μ-sulfides in di- and tetra-nuclear Fe-S clusters.[86,87] The peak areas (D_0) in S K-edge XANES region are proportional to the electric dipole allowed transitions from the S 1s→3p orbitals, and are weighted by the amount of S 3p character, α^2, governed by equation 3.1. Equation 3.1

also shows that the area of the pre-edge features is also dependent on the transition dipole integral (I(S 1s→3p), eV/hole), the number of electron holes probed in the molecular orbitals (h), the number of absorbing atoms (n), and the 1/3 ratio is the x, y, and z dependence of the transition dipole expression.[92]

$$D_0 = \frac{1}{3}\alpha^2 \frac{h}{n} I(S\ 1s \rightarrow 3p) \quad (3.1)$$

To quantify the S 3p character for a specific S based ligand, its transition dipole must be determined by independent techniques. The dipole integrals for μ-sulfides were determined in literature using X-ray photoelectron spectroscopy of $KFeS_2$ to be 210% of the four sulfides contributing to one iron site.[87] Therefore, 0.42 e^- is contributed to each hole in the iron d^5 high spin manifold per sulfide. The corresponding I(S 1s→3p) was determined to be 8.31 eV. This dipole integral was then applied to other 2Fe-2S model compounds and the oxidized and reduced forms of the Rieske protein.[87] This dipole integral was also incorporated as an additional data point in Queen *et al.*[93] analysis of S K-edge dipole integrals in the determination of transition dipole integrals based only on the edge position.

The S K-edge XANES region of the $(NH_4)_2MoS_4$ and $(PPh_4)_2MoS_4$ salts have been collected and analyzed previously by Wittneben *et. al.*[94] and Müller *et. al.*[95] The S K-edge spectrum by Müller *et. al.* of $(PPh_4)_2MoS_4$ contains two intense transitions that correspond to the terminal sulfide mixing into the e and t_2 orbitals (assuming T_d symmetry) of the Mo 4d-orbitals at 2468.4 and 2469.5 eV respectively.[95] The feature at 2468.4 eV corresponds to the π^* antibonding orbitals with e symmetry, while the peak at 2469.5 eV corresponds to σ^* and π^* antibonding orbitals that have t_2 symmetry.[95]

Wittneben *et. al.* spectrum of $(NH_4)_2MoS_4$ was published in 1989 and shows a one broad, intense peak corresponding to the transitions to the e and t_2 orbitals.[94] Moving higher in energy, the peak positions in Müller *et. al.* at 2473.7 and 2476.1 eV are ambiguously assigned as the S 1s→4s and the S 1s→4p transitions.[95] However, the transition at 2473.7 eV could also be the S 1s→4p transition while the peak at 2476.1 eV is the S→Mo charge transfer process.[95] The splitting of the Mo 4 d-orbitals from the XANES spectrum from the difference between the two peaks is 1.1 eV. In comparison, the difference of the first and second main bands in UV-Vis measurements results in a d-orbital splitting of 1.24 eV.[95,96] Conversely, the MoS_4^{3-} anion also displays the same d manifold splitting of 1.1 eV from ligand field splitting measurements.[95] The slight difference of the MoS_4^{3-} anion energy splitting is due to the direct measurement of the electronic transition from the e to the t_2 orbitals since there is one d-electron.

The computational electronic structure of the MoS_4^{2-} has been studied more extensively in literature.[91,94,95,97-99] In support of their S K-edge measurements, Wittneben *et. al.* calculated the energy splitting of the seven highest occupied and six lowest unoccupied orbitals using Xα calculations.[94] In their calculation, they show that an a_1 orbital splits the e and t_2 orbitals. This is not observed spectroscopically from XANES spectrum determined by Müller *et. al.*[95] The Xα calculations conducted by Müller *et. al.* show that the a_1 orbital lies higher in energy above the t_2 orbitals. Using charge-partitioning methods that included the inner and outer sphere charges, the amount of S and Mo character were calculated for both the e and t_2 antibonding orbitals. Using this method, the e and t_2 orbitals contain 60% and 45% Mo character, respectively.[95] The

amount of S character is obtained by simply subtracting the percent metal character from 100%. Thus, the S character is 40% and 55% in the e and t_2 orbitals respectively. The large calculated S character is consistent with the intense pre-edge features in the XANES spectrum, and indicates a very covalent Mo-S bond. According to this calculation, the overall Mo-S bond exhibits a very covalent, yet classical bonding description, where the metal contribution is higher than the sulfur contributions. Similarly, the calculations by Bernholc and Stiefel on the MoS_4^{2-} anion show that there is higher sulfur contribution than molybdenum in the t_2 orbitals,[91] which supports Müller *et. al.* calculations. The population analysis by Jostes *et al.* computed 58% and 45% Mo character in the e and t_2 orbitals, respectively.[99] However, they calculated Mo 5p mixing into the 4 d-orbitals. Likewise, the amount of the S 3p character they calculated was 42% and 40%.[99] The comparison of their calculations to their magnetic circular dichroism experiments showed that their calculation had insufficient parameters, including basis set size that was utilized to describe the electronic structure.[99] The Mo 4d-orbital splitting was determined to be 1.4 eV from Xα calculations, which is comparable to the XANES measurements of 1.1 eV.[95] The computational electronic structure can give a reasonable bonding picture while over or underestimating the ligand contributions in metal ligand bonds. This demonstrates the need to validate computational models with experimental measurements.

Along with the S K-edge, the Mo K-edge has been examined of the MoS_4^{2-} anion. The metal K-edge is sensitive to the effective oxidation state. The formal charges of molybdenum can range from 0-6. Manthiram *et. al.* conducted a thorough study

measuring the Mo K-edge of a number of molybdenum compounds and the corresponding chemical shifts was compared to the effective atomic charge in parabolic relationship.[100] For $(NH_4)_2MoS_4$, the effective oxidation was determined to be +1.49 on Mo, which is much lower from its formal oxidation state of +6.[100]

Even though Müller *et. al.* and Wittneben *et. al.* examined the S K-edge of MoS_4^{2-}, they did not attempt to extract the S 3p character associated in bonding since the technique had not yet been developed for the S K-edge.[88] The sulfur contribution determined from the S K-edge should correspond to the Mo effective oxidation state from the Mo K-edge measurements by Manthiram *et. al.* The aim of this study is understand the Mo-S bonding experimentally using the S K-edge XANES region. To this end we developed a new transition dipole integral, I(S 1s→3p), for terminal sulfides to extract the experimental sulfur character using complementary *ab initio* WFN methods. To study the electronic structure, the S K-edge spectra for Na_2MoS_4, $(NH_4)_2MoS_4$, and $(PPh_4)_2MoS_4$ salts were collected and analyzed.

Experimental Section

Sample Preparation

The $(NH_4)_2MoS_4$ was purchased from Sigma Aldrich and used without further purification. The Na_2S,[89] Na_2MoS_4,[97] and $(PPh_4)_2MoS_4$[101] salts were synthesized according to literature procedures.

Sulfur K-edge X-ray Absorption Spectroscopy

All measurements were collected at beamline 4-3 of the Stanford Synchrotron Radiation Lightsource under storage ring (SPEAR 3) condition of 300-80 mA current and 3 GeV energy. BL 4-3 has a 20-pole, 2.0 T Wiggler beamline equipped with a liquid N_2 cooled Si(111) double-crystal monochromator. All XAS measurements were carried out at room temperature and the samples were prepared in a nitrogen or argon gas filled gloveboxes. Repeated measurements of the same samples did not reveal any significant variation among data sets from the different collection periods. The solid samples were ground with boron nitride and pasted onto a Kapton tape. Excess sample was removed from the tape to minimize the distortion of peak intensities from self-absorption effects. The sample cell was protected by a few μm thick Mylar polypropylene window to eliminate possible sample degradation from air. The beamline was optimized to maximize the incident beam intensity at the high energy end of the scan. The data presented were either collected with partial electron yield (EY) or fluorescence (FF) detection methods. Partial electron yield was collected using a multi-element Lytle (EXAFS Co) detector equipped with nickel grid at a 45 V collector potential. Fluorescence detection methods utilized were the Lytle or a nitrogen gas purged and a passivated implanted planar silicon detector (PIPS, CANBERRA).

XAS Data Normalization,
Fitting, and Error Analysis

All data was background subtracted and normalized using the Automated Data Reduction Protocol (ADRP) developed by D. Gardenghi,[90] and calibrated to sodium

thiosulfate pentahydrate at 2472.02 eV. ADRP consists of three steps to analyze the XAS data: (1) baseline subtraction, (2) background correction, and (3) normalization. The baseline subtraction and background subtraction are performed in a single step. The background is fit with a smooth second-order polynomial, that is then subtracted from the spectrum. Normalization of the data was accomplished by fitting a flattened second-order polynomial to the post edge region. The second-order polynomial was fit before the Mo L_{III}-edge from 2485 to 2520 eV for MoS_4^{2-} samples. All the S K-edge spectra were normalized through a fit spline function to 1.0 at 2490 eV. The error introduced by data reduction and normalization procedures was at most 3% in the peak amplitudes. The Mo L_{III}-edge spectrum was normalized for all three complexes by taking the normalized the S K-edge data and shifting the spectrum to 0 at 2515 eV and to 1 and 2540 eV.

The normalized data were fit using Peak Fit v4.12 (SeaSolve), and employed the following common protocol. The free ligand, Na_2S, was used to fit the S 4p as a single transition using the Gaussian+Lorentzian Amplitude Function in Peak Fit with the Gaussian/Lorentzian mixing ratio held constant at 0.5. The edge jump was simulated as a Lorentzian ascending curve was normalized to one. The user defined function was used to as the background for the MoS_4^{2-} anion. The user defined function was used to subtract the edge-jump at 2474 eV. After the subtraction of the free ligand spectrum without the edge jump, the remaining peak intensities were refit. In order to avoid unreasonable distortion and large variations in intensities for ill-resolved features, additional fits were obtained in consecutive steps by gradually allowing for the amplitudes, energy positions, line-widths, and lastly allowing the Gaussian/Lorentzian mixing ratio to deviate from the

pseudo-Voigt line. The final fits for the Mo-S peaks were obtained by relaxing all fit parameters except the Gaussian/Lorentzian mixing which was held at 0.5 and the linewidths were shared between peaks that were interpreted as single transitions. Only chemically reasonable fits were considered.

Electronic Structure Calculations

The crystal structure of Na_2MoS_4 was obtained from *George et. al.*[97] The crystal structure contains C_s symmetry. The MoS_4^{2-} was symmetrized in ChemCraft to T_d by taking the average distances of the four Mo-S bonds and adjusting each bond length to 2.178 Å. Crystallographic coordinates are available in Appendix A. All ground state electronic structure calculations were computed in Gaussian09 Revision C.02.[102] The LANL2DZ,[103-105] def2-SV(P),[106] def2-SVP,[106] def2-SVPD,[106] def2-TZVP,[106] def2-TZVPD,[106] def2-TZVPP,[106] def2-TZVPPD,[106] def2-QZVP,[106] def2-QZVPD,[106] def2-QZVPP,[106] def2-QZVPPD,[106] and cc-pVTZ-DK,[107,108] aug-cc-pVTZ-DK,[107,108] and aug-cc-pVTZ-DK Diffuse[107,108] basis sets from the EMSL basis set exchange[109,110] were utilized for the description of the electronic ground state structure. These basis sets were employed in *ab initio* WFN methods using QCISD, and basis set saturation occurs with the def2-TZVP basis set. In addition to WFN calculations, density functional theory (DFT) calculations were also computed using a wide range of representative exchange and correlation density functionals that were chosen according to the rungs of Perdew's ladder of functionals.[51,52] The functionals from the generalized gradient approximation rung that were used are BP86,[56,57] BLYP,[57,111] mPW,[112] OLYP,[111,113,114] PBE,[50] and PW91.[115,116] The next rung up the ladder representing the metaGGA functionals that were

employed are M0-6L,[117] TPSS,[52] and TPSSLYP1W.[118] Hybrid functionals were utilized as a bridge between these two rungs as they incorporate Hartree-Fock exchange and ionic character into GGA and meta-GGA functionals. The Hybrid GGA functionals used in this study were B1LYP,[56,119] B3LYP,[54,111] BHandHLYP,[53,111] MPW1k,[120] mPW1PBE,[50,112] MPW3LYP,[121] MPWLYP1M,[122] and O3lYP.[111,123] The M06,[124] M06-2x,[124] M06-HF,[125,126] and TPSSh[52] functionals were employed as the hybrid meta-GGA functionals. The employment of the polarizable dielectric environment[127-132] in Gaussian09 using acetonitrile with a dielectric constant of 35.6 and a solvent radius of 1.81 Å with both the BP86 functional and QCISD electronic correlation showed negligible change in the electronic structure when compared to a gas phase calculation. Therefore, the electronic structure calculations were performed in the gas phase to minimize computational costs. Population analysis was conducted in Gaussian using "Atoms-in-Molecules"[64,133-135] from the AIMAll program.[136]

TD-DFT calculations were conducted to simulate the S K-edge pre-edge region of the XAS spectra using both Amsterdam Density Functional Theory (ADF) 2012[137-139] and ORCA quantum chemistry program package 2.8.0.[140] In ORCA, the S 1s orbitals were localized since they are symmetry equivalent in the MoS_4^{2-} molecules. Only excitations were computed from the localized S 1s orbital were allowed. The excitation energies were corrected by a constant to line up the calculated spectra with the experimental spectra. The TD-DFT calculations were performed using BP86, B3LYP, TPSS, and TPSSh functionals. The RIJCOSX approximation was employed for hybrid functionals.[141-143] Standard integration grids and a conductor like screening model

(COSMO)[128,144-146] using acetonitrile were also utilized. In addition, only the def2-TZVP basis set was utilized along with the Zero Order Regular Approximation (ZORA),[147,148] which uses uncontracted Gaussian basis sets. In ADF, the TD-DFT calculations were conducted using BP86/TZ2P[149] with COSMO (acetonitrile), and ZORA on the crystal structures 7 and 5 Å away from the MoS_4^{2-} anion for $(NH_4)_2MoS_4$ and Na_2MoS_4, respectively. The excitations were calculated from all four sulfurs.

Results and Analysis

Analysis of the S K, Mo L_{III} & L_{II}-edges of MoS_4^{2-}

The S K and Mo L_{III} and L_{II}-edges of $(PPh_4)_2MoS_4$ are shown in Figure 3.1 for both EY and FF detection methods. The partial electron yield detection method has more intense features than using fluoresce detection method at all three edges. In fluoresce XAS, self-absorption occurs from the sample bulk absorbing the emitted radiation from neighboring molecules, thereby suppressing the signal. Partial EY is more intense because it measures the current, not the radiation, produced during a measurement. Since EY is measuring the ejected electrons from the sample, it is a surface technique because only the electrons near the surface are able to escape (0-10 Å).[150] Therefore, EY gives a more accurate reading of the peak intensities than fluorescence detection methods if there is little surface contamination. The spectra in Figure 3.1 were normalized to one in the S K-edge at 2490 eV. This accounts for why the two spectra are nearly identical at the S K post-edge/Mo L_{III} pre-edge region, but split moving towards higher energy. When the Mo

L_{III}-edge is normalized using these two detection techniques (Figure 3.2), the intensities of these peaks are nearly equivalent. The Mo L_{III}-edge occurs at approximately 2525 eV,

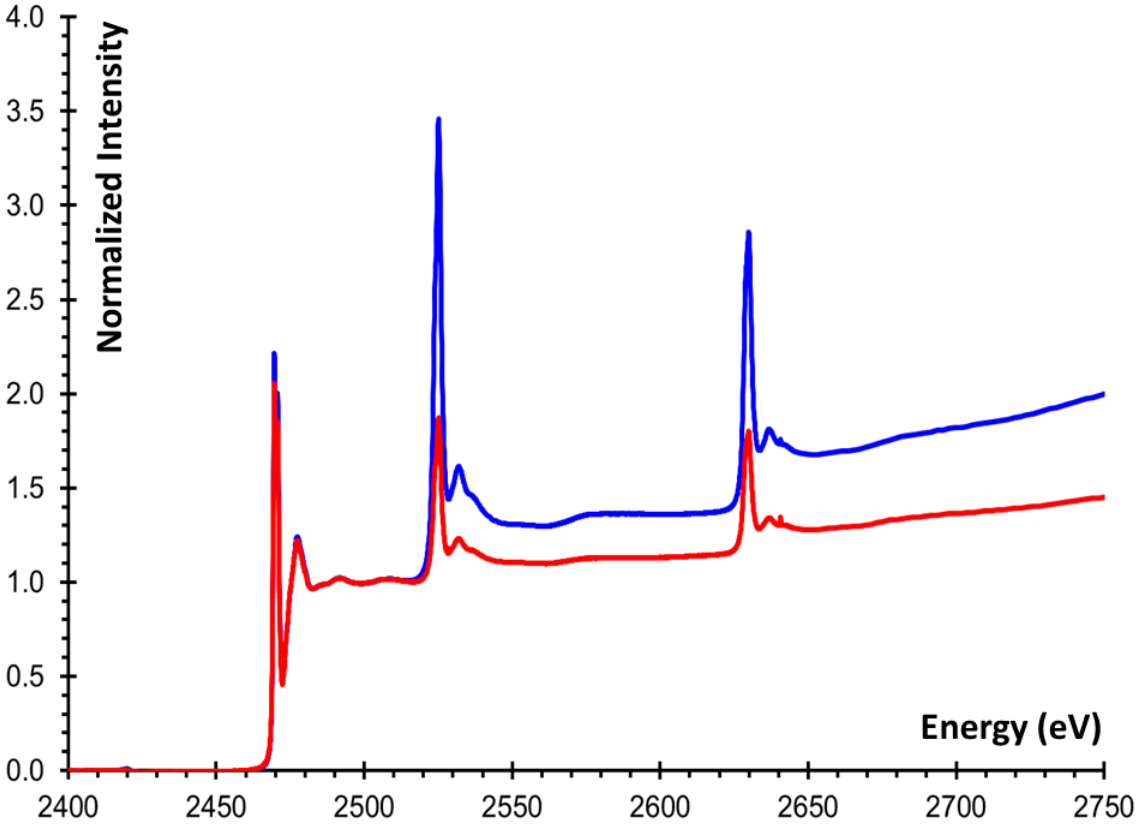


Figure 3.1: The S K, Mo L_{III} and L_{II}-edges of $(PPh_4)_2MoS_4$ using EY (blue) and FF (red) detection methods normalized to S at 2490 eV.

which corresponds to the Mo $2p_{3/2} \rightarrow 4d$ transition. Similarly, the Mo L_{II}-edge in this spectrum is located around 2630 eV for the Mo $2p_{1/2} \rightarrow 4d$ transition. The intense feature in the Mo L_{III} and L_{II}-edges both contain two peaks corresponding to transitions from the 2p orbitals to the empty Mo 4 d-orbitals. The normalized Mo L_{III}-edge is displayed in Figure 3.2. Based on tetrahedral symmetry, these excitations are probing the e and t_2 orbitals. Using the Mo L_{III}-edge, the d-orbital splitting is 1.4 eV, which is the same as its

UV-Vis spectrum using the charge transfer bands.[95] Lying higher in energy is the transition to the Mo 5s orbital. The Mo 5s orbital is just below the continuum and does not contribute to Mo-S bonding. It is analogous to the S 4p transition in the S K-edge. The Mo L-edges are more intense for the MoS_4^{2-} anion than the $MoFe_3S_4(dtc)_5$ complex in Chapter 2. Therefore, the S EXAFS does not significantly interfere with the Mo L-edges. The higher intensity results in more Mo character in the Mo-S bond of the e and t_2 orbitals when compared to the $MoFe_3S_4(dtc)_5$ Mo L-edges.

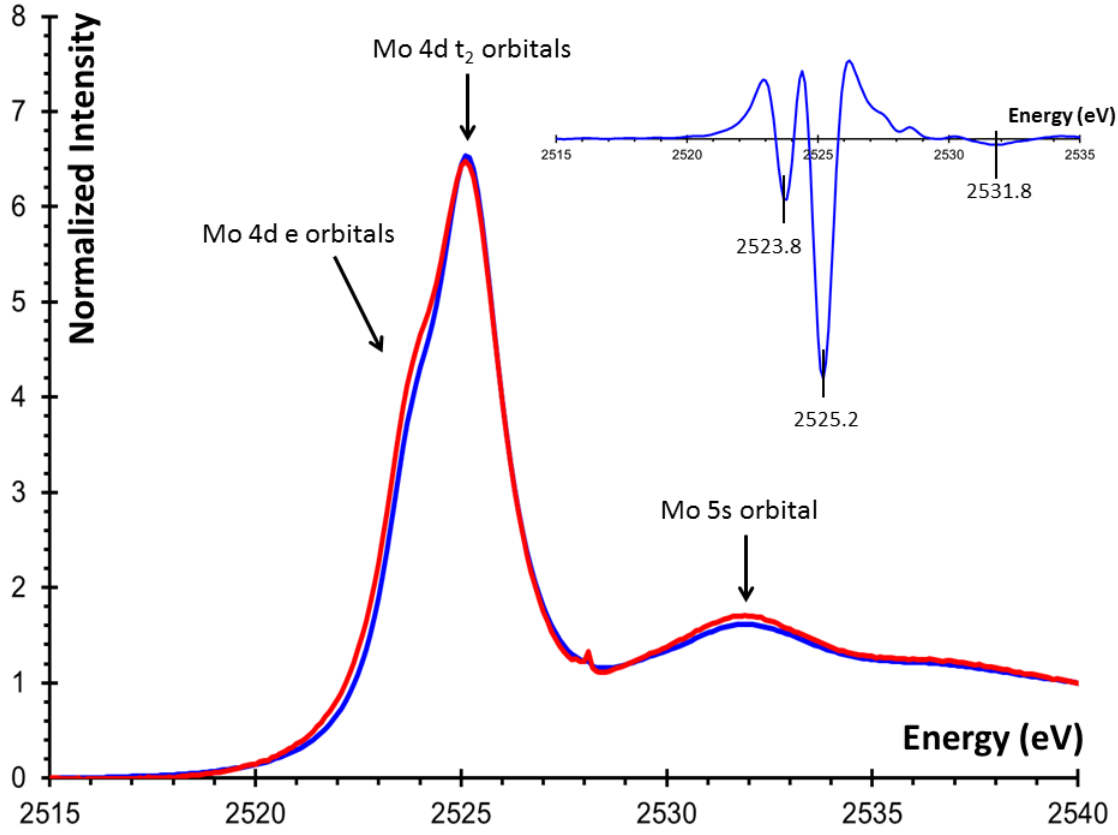


Figure 3.2. The normalized Mo L_{III}-edge of $(PPh_4)_2MoS_4$ from both detection methods (EY-blue, FF-red). The spectra were normalized to one at 2540 eV. The inset is the 2nd derivative spectrum of the EY detection method.

The comparison of the S K-edge, the first and second derivative plot of the Na_2S free ligand spectrum and $(PPh_4)_2MoS_4$ are displayed in Figure 3.3. In Figure 3.3A, the $(PPh_4)_2MoS_4$ compound pre-edge features are lower in energy than the S 4p transition in Na_2S. The lower the energy of the sulfur species, the lower the Z_{eff} associated on the sulfur. The two intense features of $(PPh_4)_2MoS_4$ are the terminal sulfides 3p-orbitals mixing with the empty Mo 4d-orbitals. Since MoS_4^{2-} is tetrahedral, the peaks at 2469.6 eV and 2470.7 eV are the sulfide contribution to the e and t_2 Mo 4d-orbitals. Müller *et al*. S K-edge peaks for the e and t_2 orbitals were 2468.4 and 2469.5 eV, respectively.[95] The difference in the energy positions is because the spectra in Figure 3.3A were calibrated to sodium thiosulfate and while Müller *et al*. data was not calibrated. The ΔE of the e and t_2 of the S K pre-edge features is congruent with Müller *et al*. data of 1.1 eV.[95] The quantitative estimate of the S 4p cannot be established due to the plateau of the 1st derivative spectrum of $(PPh_4)_2MoS_4$. Since the S 4p cannot be accurately estimated, the extraction of the sulfur covalencies developed by Queen *et al.* cannot be performed.[93] The S K and Mo L-edges show different energy level splitting due to the different origins of excitations. The S K-edge has a higher resolving power due to the longer core hole lifetime than the Mo L-edges since the Mo L-edges are higher in energy. According to Heisenberg's uncertainty principle, the higher the energy of the edge, the shorter the core hole lifetimes and correspondingly the broader the experimental linewidth. Therefore, the S K-edge analysis is the focus for the remainder of this study.

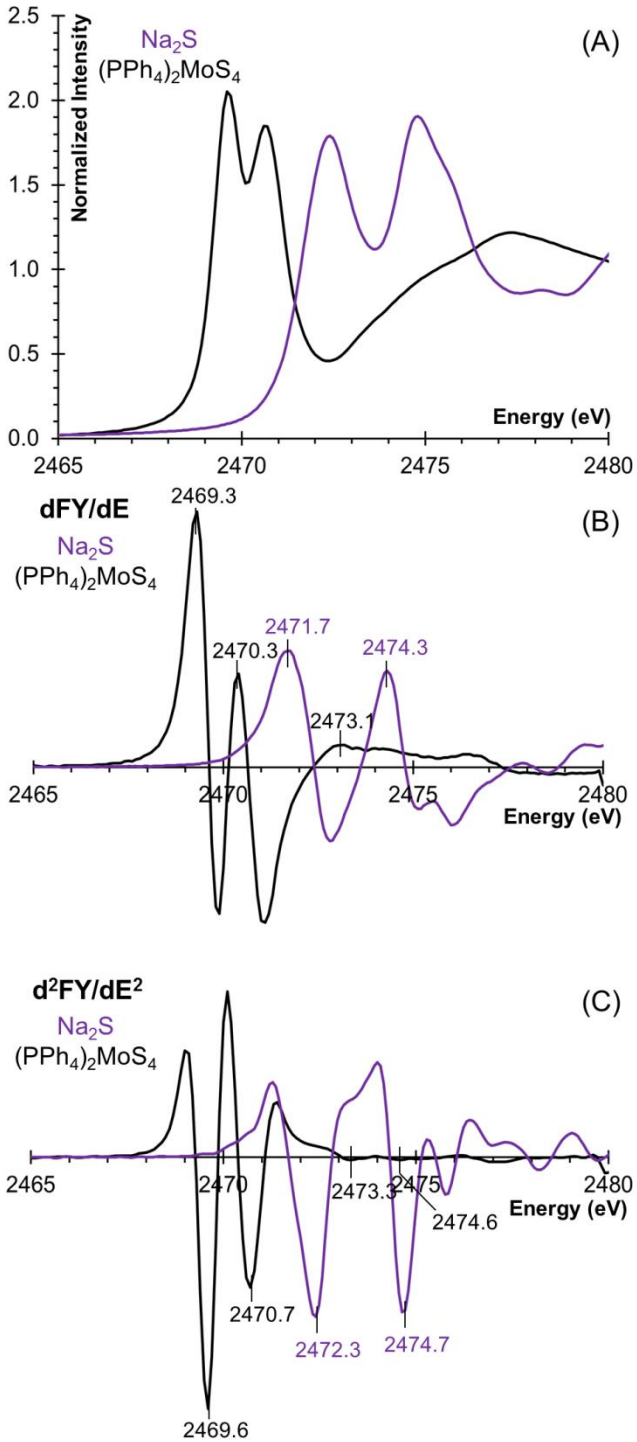


Figure 3.3: (A) The S K-edge XANES using FF, (B) the 1st derivative, and (C) the 2nd derivative of $(PPh_4)_2MoS_4$ along with the Na_2S ligand.

In addition to the phosphonium salt of the tetrathiomolybdate anion, the sodium and ammonium salts were also examined with S K-edge XAS. Figure 3.4 shows the overlay of the XANES region for the three different salts. There are a few surprising

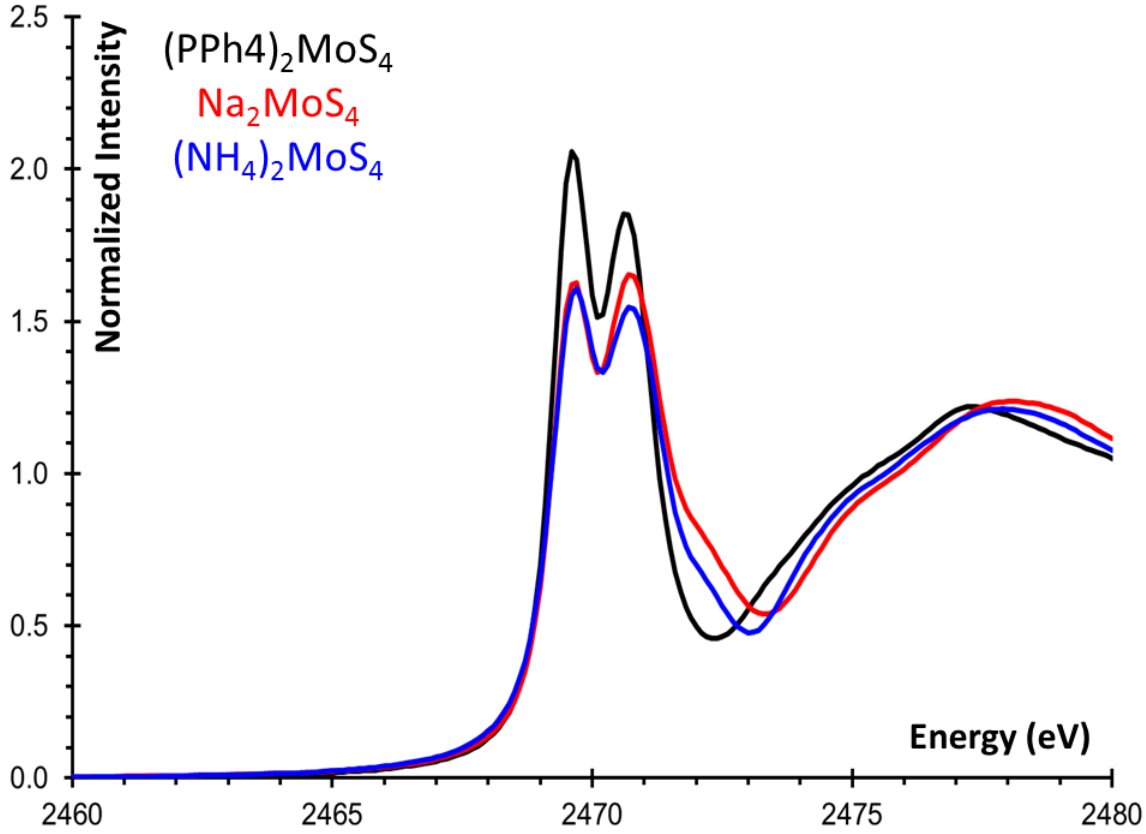


Figure 3.4: The S K-edge XANES of $(PPh_4)_2MoS_4$ (black), Na_2MoS_4 (red), and $(NH_4)_2MoS_4$ (blue) using FF detection.

differences between these thee salts. First, is the difference in normalized intensities between the three salts, with the phosphonium salt having the most intense pre-edge features. The second difference between the spectra is the shoulder after the 2470.7 eV peak observed for the sodium and ammonium salts at approximately 2472.1 eV. Another difference between these three spectra is that the rising-edge/edge features do not overlay

as well as the beginning of the transition to the e orbitals. The differences in the pre-edge edge region are influenced by their geometric structure, along with the crystal structure. The phosphonium cation is very large in comparison to the ammonium and sodium cations. The size and rigidity of the phosphonium salt encapsulates the MoS_4^{2-} anion allowing it to assume the tetrahedral structure with no other influences from other molecules, similar to crystal structure of $(PPh_4)_2MoSe_4$.[151] The ammonium and sodium salts are small and there is the possibility for weak bonding interactions between the MoS_4^{2-} anion and the cations.

Ground State Orbital Composition

Ab initio WFN calculations were used to model the ground state of the MoS_4^{2-} due to the discrepancy discussed in the Introduction of the Mo-S contributions. Wavefunction calculations were carried out using QCISD electronic correlation to see how the bonding description changes as larger basis sets are incorporated. The larger the basis set used, the closer the approximation is to the exact solution of the Schrödinger equation. This serves as an excellent reference point for DFT calculations. Figure 3.5 shows the QCISD/AIM analysis of the sulfur contribution to the e and t_2 orbitals to the Mo 4d-orbitals.

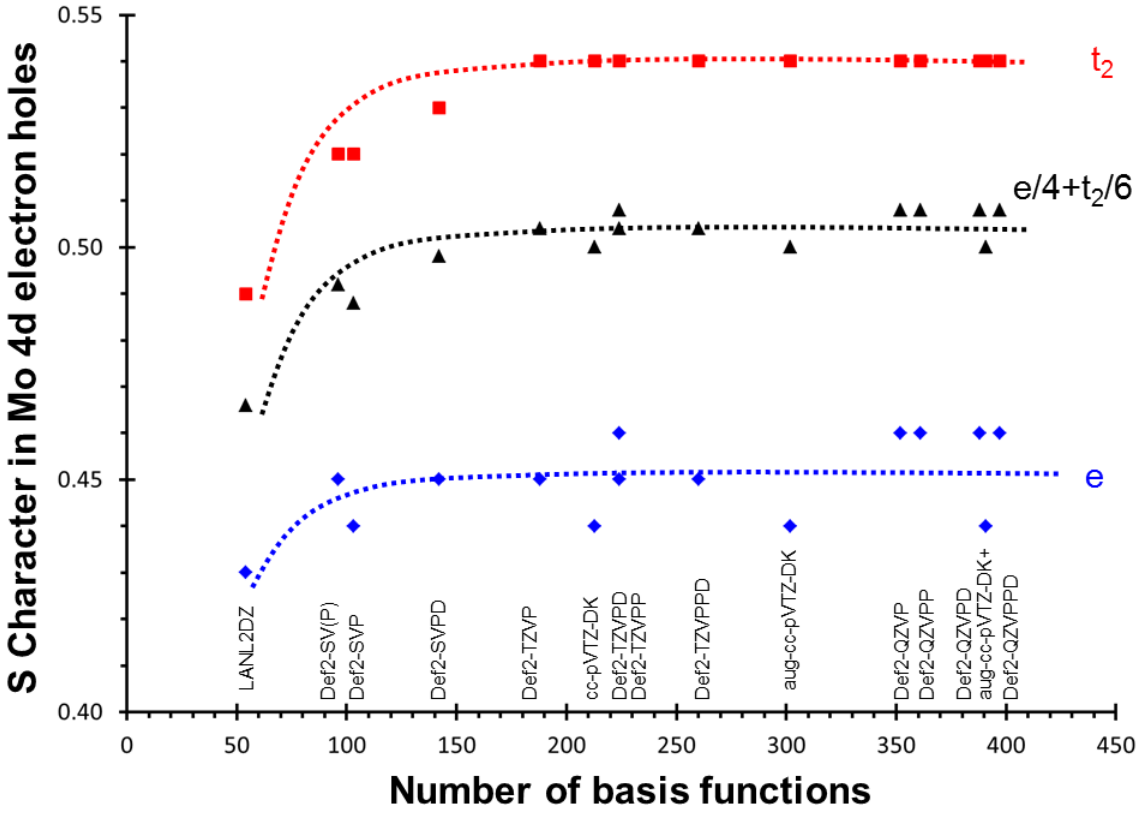


Figure 3.5: The per hole S character determined using QCISD/AIM calculations compared to the number of basis functions used for MoS_4^{2-}. The S composition of the e orbitals are in blue, the t_2 orbitals are in red, and the total d-orbital contribution is in black.

The QCISD/AIM calculations in Figure 3.5 show the increase in sulfur contribution for basis sets with less than 188 basis functions. Basis set saturation of the sulfur contribution occurs at 188 basis functions and corresponds to def2-TZVP. Interestingly, there are small oscillations in the amount of sulfur character in the e orbitals between 0.44-0.46 e^-. The t_2 orbitals plateau at 0.54 e^- for all basis sets larger than 188 basis functions (def2-TZVP). These QCISD results are consistent with Müller *et al.*[93] and Bernholc and Stiefel[91] bonding description. Although, the QCISD calculations indicate that the e orbitals contain more sulfur character than Müller *et al.* Xα calculations.[95] The bonding

picture using QCISD/def2-TZVP/AIM for S is 0.45 e^-/hole and 0.54 e^-/hole in the e and t_2 orbitals, respectively. This yields a total sulfur contribution of 0.504 e^-/hole in the Mo 4d-orbitals. The 0.504 e^-/hole sulfur contribution effectively brings the oxidation state of Mo to +1. The Mo K-edge study of Mo based compounds determined that the effective charge is +1.49 experienced by Mo in $(NH_4)_2MoS_4$.[100] As observed from Figure 3.4, the normalized intensity indicates that there is less S contribution as compared to $(PPh_4)_2MoS_4$, where the MoS_4^{2-} anion is completely shielded and undisturbed from neighboring molecules. Therefore, the Mo-S bonding picture is not as covalent for $(NH_4)_2MoS_4$ as it would be for $(PPh_4)_2MoS_4$. The QCISD calculations are most likely only applicable to the $(PPh_4)_2MoS_4$ salt.

DFT calculations were also conducted to compare to the reference QCISD calculations using the def2-TZVP basis set, since it is the smallest basis set that accurately describes the Mo-S contributions as seen in Figure 3.5. The use of DFT calculations along with def2-TZVP is advantageous because of the lower computational costs associated with DFT when compared to WFN *ab initio* computations. Figure 3.6 examines a comprehensive list of functionals used to compute the sulfur contribution in the Mo 4d-oribtals. Figure 3.6 clearly shows that the functionals tested do not compare to

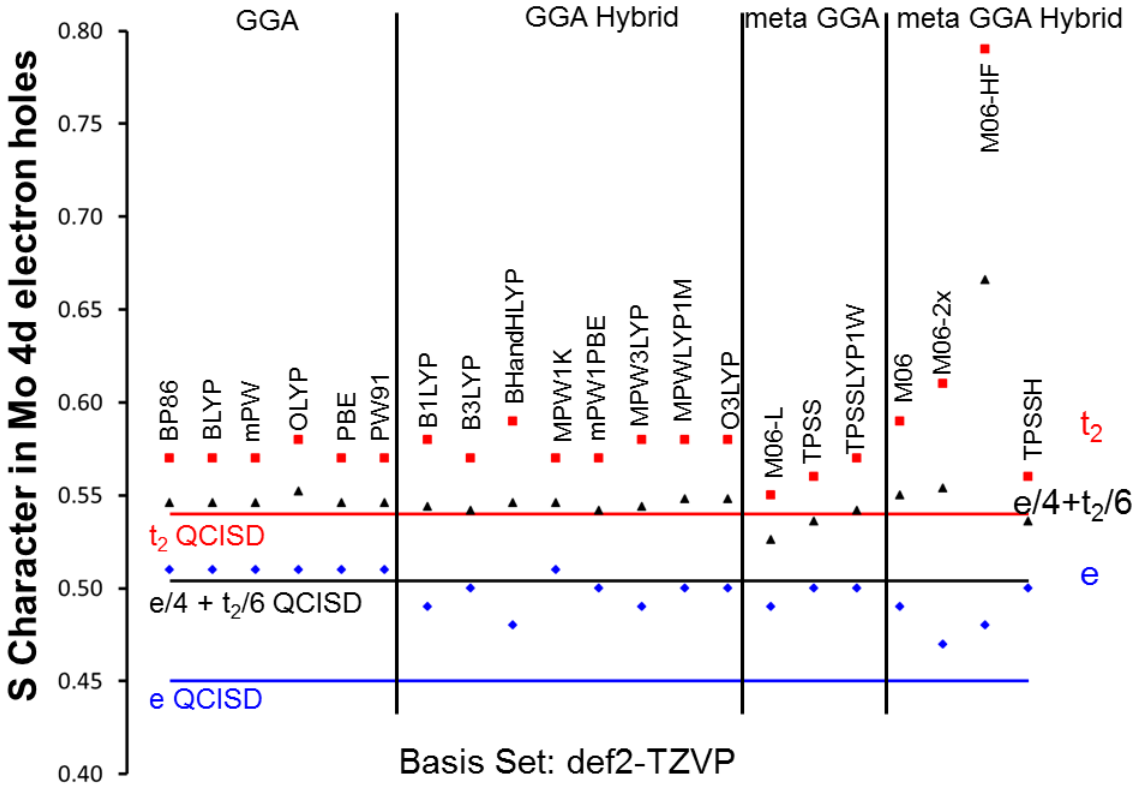


Figure 3.6: The per hole S character determined using different functionals with the AIM population analysis of MoS_4^{2-}. The S composition of the e orbitals are in blue, the t_2 orbitals are in red, and the total d-orbital contribution is in black.

the QCISD reference calculation. All the functionals tested yielded too much sulfur mixing into the Mo 4d-orbitals. All the functionals give similar sulfur bonding contributions with the exception of the M06 based functionals. Historically, DFT has been shown to produce an overly covalent bonding description for coordination complexes.[93] It appears that DFT has trouble with the high negative charge associated on the terminal sulfides. This bonding picture is unreasonable because the Mo is effectively reduced to $Mo^{0.5}$, which is not chemically feasible. The energy splitting of the MoS_4^{2-} was typically calculated at 1.1 eV for most functionals as seen for example in Figure 3.7. This is consistent with the S K-edge splitting in Figure 3.3C. Figure 3.7 also shows the

orbital picture of MoS_4^{2-} anion determined by BP86/def2-TZVP. The bonding picture shows large orbital mixing of all the sulfides with the Mo site. There is also a large amount of Mo contribution in these orbitals, which is consistent with the observed intensity in the Mo L-edge spectrum. In addition, the next orbital above the t_2 orbitals is the a_1 orbital of the Mo 5s as determined by DFT. This illustrates that low lying Mo orbitals do not contribute in bonding to the Mo 4d-orbitals. While the relative energies are accurately model by DFT of the S K-edge XAS spectrum, the bonding description of the Mo-S bond is not reproduced by DFT.

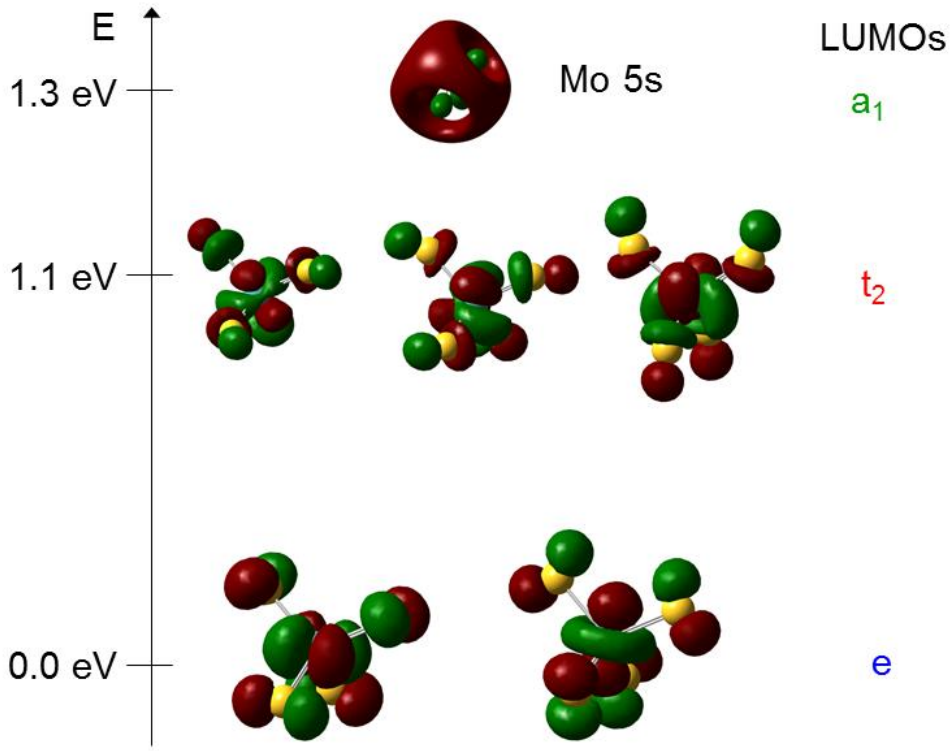


Figure 3.7: The molecular orbital picture generated from BP86/def2-TZVP for MoS_4^{2-}.

Excited State Energy Analysis

TD-DFT calculations were performed with MoS_4^{2-} to simulate the S K-edge spectrum with the def2-TZVP basis set. There are three dipole allowed transitions allowed from the S 1s orbitals in the S K-edge spectrum using T_d symmetry to describe the MoS_4^{2-} anion. The localized S 1s orbitals have an irreducible representation of $a_1 + t_2$, and there is one symmetry allowed excitation from this irreducible representation to the e set of the Mo 4d-orbitals. Similarly, there are two electric dipole allowed transitions to the t_2 orbitals. These transitions occur because the S 3p orbitals' irreducible representation has the same Mulliken symbols as the Mo d-orbitals (e and t_2). To model the S K-edge spectrum the BP86, B3LYP, TPSS, and TPSSh functionals were used as a representative case from GGA, metaGGA, Hybrid, and Hybrid metaGGA type of functionals. The spectra generated from the TD-DFT calculations are displayed in Figure 3.8. Figure 3.8B is the most accurate description of the excited state spectrum of the S K-edge as seen by the relative intensities determined by the oscillator strengths of the transitions to the e and t_2 orbitals. The first five excitations are the electric dipole allowed transitions to the Mo 4d orbitals. The splitting of these excitations reproduces the experimental splitting of the e and t_2 features. The sixth excitation is insignificant and does not contribute to the spectrum. The next three excitations correspond to transitions to higher lying S p-orbitals, are most likely the S 4p-orbitals. Bound states are no longer probed after the S 4p-orbials and further excitations result in photoelectrons that contribute to the EXAFS region. The splitting between the pre-edge and rising edge is smaller compared to the experimental S K-edge spectrum with the TPSSh functional

coming the closest to reproducing the splitting. The excitations to the t_2 orbitals are nearly degenerate, while the B3LYP functional displays the greatest splitting between the excitations.

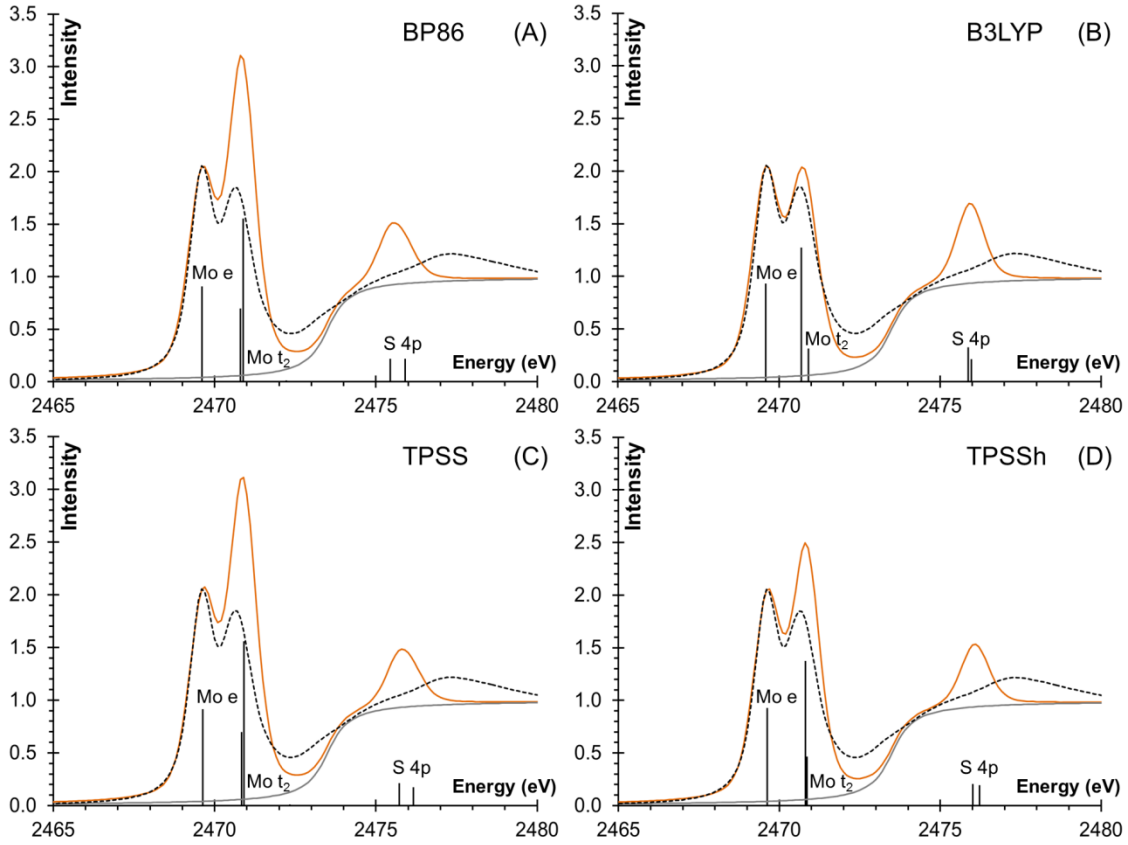


Figure 3.8: The TD-DFT S K-edge calculations using BP86 (top left), B3LYP (top right), TPSS (bottom left) and TPSSh (bottom right) functionals using the def2-TZVP basis set for MoS_4^{2-}.

The differences in the S K-edge spectra attributed in Figure 3.4 were examined with TD-DFT. The surrounding crystalline environment within 7 and 5 Å away of the MoS_4^{2-} anion for the Na^+ and NH_4^+ systems was investigated to see if there were higher laying sulfide-cation bonds in the respective structures. As Figure 3.9 depicts, there are sulfide-cation interactions present in the crystalline environment for the Na_2MoS_4 and

$(NH_4)_2MoS_4$ systems. Although the results in Figure 3.9 show the influence of the cations in the S K-edge spectrum, the accuracy of the splitting in the calculations is not reproduced. The reason for this could be due to the relatively small cavity around the MoS_4^{2-} anion. The overall charge of the calculated modeled system, incorporating the nearby cations, was +5 and +9 for Na_2MoS_4 and $(NH_4)_2MoS_4$, respectively. This large charge imbalance could lead to the inaccurate splitting observed in Figure 3.9.

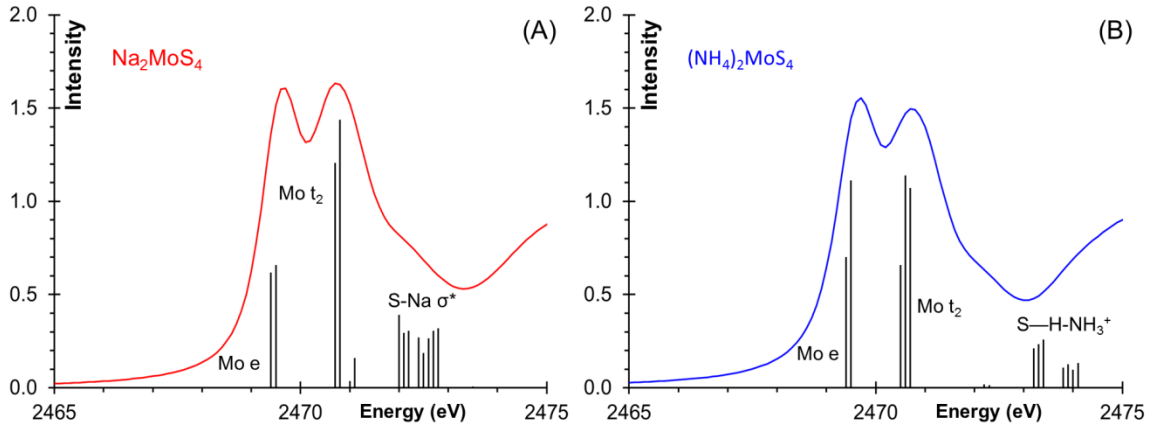


Figure 3.9: The TD-DFT S K-edge calculations using BP86 of the crystalline environment 7 Å away for Na_2MoS_4 (left) and 5 Å for $(NH_4)_2MoS_4$ (right).

Intensity of S K-edge Spectral Features

The fit areas of the S K-edge pre-edge features were extracted from the normalized data. Several fits were performed for each compound, and Figure 3.10 shows an example of a chemically reasonable fit of the S K-edge XANES region of the $(PPh_4)_2MoS_4$ compound. Table 3.1 displays the fits of the three different MoS_4^{2-} salts

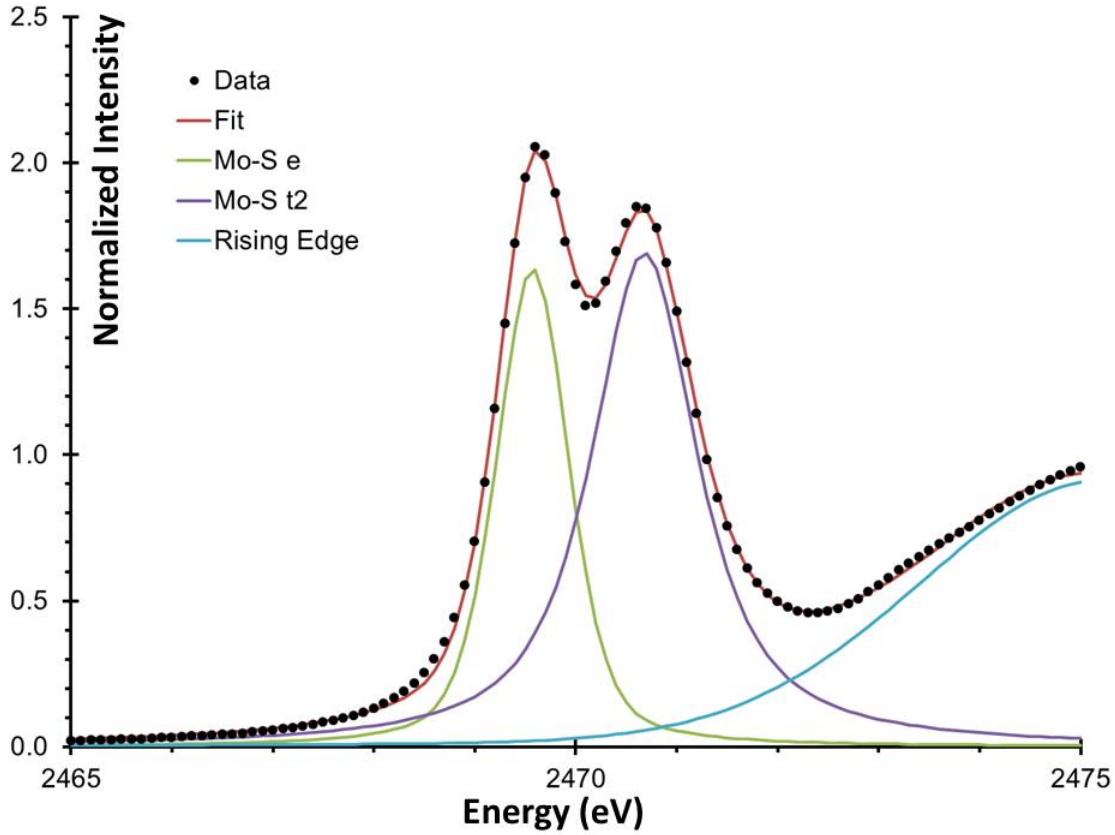


Figure 3.10: An example of an S K-edge XANES fit for the extraction of the S 3p contribution from the MoS_4^{2-} e and t_2 orbitals.

attributed to the e and t_2 orbitals along with the corresponding detection method. The phosphonium salt has the largest area associated with these transitions, and will therefore have the largest covalency according to equation 3.1. The TD-DFT results indicate the presence of sulfide-cation interactions, which would explain the reduction of the fit areas of the Na^+ and NH_4^+ compounds. The TD-DFT results in Figure 3.8 show the broken

Table 3.1: The fit areas of the different MoS_4^{2-} salts of the e and t_2 orbitals in units of eV.

$[MoS_4]^{2-}$ Salt	Detector	D_0 Mo-S e	D_0 Mo-S t_2	D_0 Mo-S Total
NH_4^+	FF	1.57 ± 0.05	2.70 ± 0.06	4.27 ± 0.04
PPh_4^+	FF	1.76 ± 0.03	3.14 ± 0.04	4.90 ± 0.04
Na^+	FF	1.46 ± 0.03	2.61 ± 0.04	4.07 ± 0.04
NH_4^+	EY	1.70 ± 0.03	3.01 ± 0.05	4.72 ± 0.05
PPh_4^+	EY	1.83 ± 0.03	3.30 ± 0.03	5.12 ± 0.03
Na^+	EY	1.69 ± 0.03	3.01 ± 0.03	4.71 ± 0.03

degeneracy of the excitations to the t_2 orbitals. If the excitations were degenerate then the t_2 peak would have to be fit as a pseudo-Voigt line. Therefore, the Mo-S t_2 feature was treated as "envelope" of transitions and the peak could vary from the idealized pseudo-Voigt line. This is observed for the purple peak (t_2) in Figure 3.10 where it adds more Lorentzian mixing into the peak to fit the data. The peak ratio of the fits of the e and t_2 orbitals is ~0.56, which is close to the ratio of QCISD/AIM S character of 0.55. This indicates the chemical feasibility of the fits in Table 3.1.

The amount of S 3p mixing with Mo using the literature transition dipole integral for sulfides of 8.31 eV[87] was determined using equation 3.1. Using this transition dipole integral, Table 3.2 shows the amount of S character using the fits from Table 3.1.

Table 3.2: The determined S character (e^-/hole) from the fits in Table 3.1 using the transition dipole integral of 8.31 eV.[87]

$[MoS_4]^{2-}$ Salt	Detector	Mo-S e α^2	Mo-S t_2 α^2	Mo-S Total α^2
NH_4^+	FF	0.57 ± 0.02	0.65 ± 0.01	0.62 ± 0.01
PPh_4^+	FF	0.64 ± 0.01	0.76 ± 0.01	0.71 ± 0.01
Na^+	FF	0.53 ± 0.01	0.63 ± 0.01	0.59 ± 0.01
NH_4^+	EY	0.62 ± 0.01	0.72 ± 0.01	0.68 ± 0.01
PPh_4^+	EY	0.66 ± 0.01	0.79 ± 0.01	0.74 ± 0.01
Na^+	EY	0.61 ± 0.01	0.72 ± 0.01	0.68 ± 0.01

The sulfur covalency displayed in Table 3.2 is chemically unfeasible as determined by QCISD calculations and the earlier Mo K-edge study that included the $(NH_4)_2MoS_4$ salt. The Mo in the $(NH_4)_2MoS_4$ complex would have an effective oxidation state of 0. In fact, all of the covalencies are unrealistically high, which results in an effective oxidation state of +0/$^-$1 on Mo. One reason for the discrepancy is that the transition dipole integral was determined using fluorescence detectors and not electron yield. Therefore, the data associated with the EY cannot be interpreted using the 8.31 eV sulfide dipole integral.[87] The 8.31 eV transition dipole integral was developed for bridging sulfides, which exhibits different bonding properties than with terminal sulfides.[87] The method of extracting the sulfur character from any system that contains a metal-sulfur bond cannot be used in this study either. The first derivative spectrum in Figure 3.3B exhibits the plateau after the white line, which results in an ambiguous assignment of the S 4p transition necessary for the extraction of the sulfur character.

A new experimental expression for the sulfur transition dipole integral was developed for terminal sulfides using QCISD for the extraction of S 3p character for the

ammonium and sodium salts. The MoS_4^{2-} anion in $(PPh_4)_2MoS_4$ system is the most innocent since it doesn't interact with the surrounding cations. Therefore, the QCISD sulfur character along with the corresponding peak areas of $(PPh_4)_2MoS_4$ for both FF and EY detection methods were used to develop the S I(S 1s→3p) for terminal sulfides. The transition dipole integrals determined from the QCISD calculations were 11.7 eV for FF, and 12.2 eV for EY detection methods. Table 3.3 summarizes the results for all the salts with the application of these new transition dipole integrals. The results in Table 3.3

Table 3.3: Extracted S character (e^-/hole) using transition dipole integrals tuned to QCISD calculations.

$[MoS_4]^{2-}$ Salt	Detector	I^C	Mo-S e α^2	Mo-S t_2 α^2	Mo-S Total α^2
NH_4^+	FF	11.7	0.41 ± 0.01	0.47 ± 0.01	0.44 ± 0.01
PPh_4^+	FF	11.7	0.46 ± 0.01	0.54 ± 0.01	0.50 ± 0.01
Na^+	FF	11.7	0.38 ± 0.01	0.45 ± 0.01	0.42 ± 0.01
NH_4^+	EY	12.2	0.44 ± 0.01	0.52 ± 0.01	0.46 ± 0.01
PPh_4^+	EY	12.2	0.47 ± 0.01	0.57 ± 0.01	0.50 ± 0.01
Na^+	EY	12.2	0.44 ± 0.01	0.52 ± 0.01	0.46 ± 0.01

indicate that the electron density donated to the Mo 4d-orbitals is about 4.5 e^-, giving Mo an effective oxidation state of +1.5. An effective oxidation state of +1.5 is congruent with Mo K-edge for $(NH_4)_2MoS_4$ having a charge of +1.49.[100] The sodium salt displays similar charge donation. These results reveal the non-innocence of the cations due to the lower sulfide contribution to the Mo 4d-orbitals. The EY results show the least variation and are the most reliable. This demonstrates the effect of self-absorption has on the peak intensity in FF detection.

The experimental electronic structure of MoS_4^{2-} was extracted using equation 3.1 for determining the amount of S 3p mixing with Mo using Fermi's Golden Rule for electric dipole allowed transitions. The sulfide donation to the e orbitals forms a classical, very covalent bond. However, the sulfide contribution to the t_2 orbitals exhibits inverted bonding. Inverted bonding occurs when the MO contains more ligand character than metal character. Due to the short inter-ligand S…S distances (3.556 Å), there is significant ligand-ligand repulsion between the sulfides resulting in more destabilized donor ligand orbitals than the empty Mo 4d-orbitals. This destabilization results an inverted bonding description containing predominately sulfur character in the antibonding valence orbitals. Oxidation of the MoS_4^{2-} anion occurs via the extraction of an electron from the t_2 orbital, which contains more sulfur character. In the presence of O_2, the sulfides are slowly oxidized, eventually forming sulfates, and consequently, eventually forming the MoO_4^{2-} species.

Conclusions

The electronic structure of the MoS_4^{2-} has been analyzed using S K-edge XAS with the aide of WFN, DFT, and TD-DFT calculations. The tetrahedral MoS_4^{2-} anion exhibits two intense features in the S K-edge XANES region. These features correspond to excitations to the e and t_2 orbitals of the Mo 4d-orbitals due to S 3p mixing. In addition, the ammonium and sodium salts exhibit bonding interactions with the MoS_4^{2-} anion as indicated by the presence of the shoulder after the t_2 peak at ~2472.1 eV. The Mo L-edges also exhibit the splitting of the empty Mo 4d-orbitals, albeit with less

resolving power than the S K-edge. The *ab initio* WFN calculations using QCISD electronic correlation show a basis set saturation with def2-TZVP with 0.45 e^-/hole and 0.54 e^-/hole in the e and t_2 orbitals, respectively. Comparison of the *ab initio* WFN calculations to DFT indicates that DFT produces an overly covalent bonding description of the Mo-S bond. The TD-DFT calculations qualitatively reproduce the S K-edge XANES spectrum with the B3LYP functional. The TD-DFT calculations show that the peak corresponding to the t_2 transition is made up of two transitions that are not degenerate. In addition, TD-DFT shows the excitations to the non-innocent cations of the ammonium and sodium ions in the crystal lattice. The experimental sulfur character was extracted using new transition dipole integrals in collaboration with QCISD calculations for both EY and FF detection methods. The experimental S character of $(NH_4)_2MoS_4$ was consistent with the interpretation of Mo K-edge effective charge on the Mo of 1.5. The ammonium and sodium complexes exhibit lower S character due to the interactions of MoS_4^{2-} with its respective cations. The sodium-sulfide interaction forms a weak bond thus lowering the amount of electron density donated to the formally empty Mo d-manifold. The ammonium cation is also non-innocent in that electron density from the sulfides is lost due to hydrogen bonding. The bonding description reveals that the Mo-S bond to the e orbitals exhibit classical bonding. Conversely, the t_2 bond contains more sulfur than molybdenum character leading to an inverted bonding picture.

CHAPTER 4

QUANTIFICATION OF S MIXING OF DITHIOCARBAMATE LIGANDS IN TRANSITION METAL COMPLEXES

Introduction

An important S-compound that lies between the most reduced and most oxidized forms of sulfur ligands is the family of dialkyldithiocarbamates.[152] Diethyldithiocarbamate (dtc) ligands are a form of 1,1-dithio ligands where a wide range of chemistry has been developed that incorporates these ligands. Dtc transition metal complexes are used in inorganic analysis, they can separate metal ions in HPLC and GC chromatography, used as rubber vulcanization accelerators, fungicides and pesticides.[152] Additionally, dtc complexes have been shown to be inhibitors of many types of cancer cells *in vitro* and *in vivo*.[153]

The chemical reactivity of these dtc complexes is due to its ground state electronic structure. X-ray absorption spectroscopy (XAS) is a valuable technique for extracting quantitative ground state information from core orbital excitations. One of the most successful elements for ligand K-edge XAS is sulfur due to its biological and chemical relevance. There is no other experimental technique other than XAS, which can give comparable electronic and geometric structural information for S-containing compounds. The quantitative X-ray absorption near-edge spectroscopic analysis of S K-edges has been determined and is well defined for sulfide,[87] thiolate,[88] dithiolenes[62] and for oxidized sulfur compounds such as MetSO and $MetSO_2$ ligands.[154,155] Dtc is a unique

ligand as it bridges formally the thiolates and thioethers with regards to formal charge.

At the S K-edge, electric dipole allowed features are proportional to the amount of S 3p character in the unoccupied or half-filled molecular orbitals. The intensity of these features is correlated to the covalency as expressed in equation 4.1:[92]

$$D_0 = \frac{1}{3}\alpha^2\frac{h}{n}I(S1s\rightarrow 3p) \qquad (4.1)$$

In equation 4.1, h stands for the number of electron holes in the probed unoccupied orbitals, n is the numbers of absorbing atoms, the 1/3 ratio is the x, y, and z dependence of the transition dipole expression and the I(S 1s→3p) is the transition dipole integral (eV/hole). To quantify covalency for a specific S based ligand, its transition dipole must be determined by independent experimental techniques. The dipole integrals for S^{2-}, SR^{-}, and dithiolenes were determined in literature using X-ray photoelectron spectroscopy[87] and electron paramagnetic resonance (EPR).[87,92,156]

Prior to Queen *et al.*,[93] transition dipole integrals could not successfully be applied to the dtc complexes and the free ligand. The transition dipole integral for $Cu(dtc)_2$ was determined using the fit areas of the S K-edge of $Cu(dtc)_2$ in conjunction with literature EPR data. This methodology was employed when dipole integrals were first being developed in the Cl K-edge.[92] The D_{4h} bis(creatininium)$CuC1_4$ superhyperfine structure was analyzed with EPR, and subsequently, correlated the bond covalency to the intensity of the pre-edge feature in the Cl K-edge.[92] Once the dipole integral for Cl^{-} was determined, it was applied to other transition metal chloride complexes to derive the amount of Cl 3p character in those complexes.[157,158]

EPR is a technique that can provide an experimental estimate of the metal-ligand

bond covalency by measuring the compounds' ground state properties. There have been many studies on the EPR of $Cu(dtc)_2$, however, only the studies that determined the bonding parameters of the $Cu(dtc)_2$ were considered for this chapter.[159-163] There were two ways EPR data was gathered for $Cu(dtc)_2$: in solution, or doped in a diamagnetic single crystal lattice. Common host lattices used are $Ni(dtc)_2$ and $Zn(dtc)_2$. The $Cu(dtc)_2$ monomer adapts to the coordination environment of the host molecule of Ni(II), but maintains the same geometry as the $Cu_2(dtc)_4$ when doped in $Zn_2(dtc)_4$.[161] The molecular geometry of $Cu(dtc)_2$ doped in $Ni(dtc)_2$ is square planar, but square pyramidal in $Zn_2(dtc)_4$. This corresponds to different g-factor (g) and metal hyperfine values (A) depending on the symmetry of the host guest molecule.[161] In Table 4.1, the lower A values shown from the $Zn_2(dtc)_4$ lattice is a result of 4s mixing into the 3d orbitals due to the reduction of symmetry from square planar to square pyramidal.[161] When dissolved in a non-coordinating solution, the $Cu(dtc)_2$ is a monomeric containing square planar geometry and D_{2h} symmetry with respect to the copper and four sulfurs. However, when dissolved in a coordinating solvent, the A values become similar to those determined from the $Zn_2(dtc)_4$ lattice.

Table 4.1: EPR results from various studies.

Solution/Lattice	g‖	g⊥	A‖	A⊥	α^2 (%)	Ref
60% pyridine:40% chloroform	2.121	2.040	140.3	26	44	160
60% pyridine:40% chloroform[a]	2.098	2.035	159.5	41.5	41	160
Zn	2.107	2.029	143	20	42	161
Zn	2.1085	2.023	147.2	N/A	49.6	163
Ni	2.084	2.023	160	40	46	161
Ni	2.084	2.023	159	39	55[b]-72[c]	162
Ni	2.087	2.023	154	35	47	159

α^2 is the sigma bond covalency of the dtc^- ligand determined by subtracting the Cu^{2+} contribution by 100%. a) Savino and Bereman used these same values and determined α^2 of 0.47 e^- per hole.[164] b) $\langle r^3 \rangle$ value from Hurd and Coodin[165] and c) Morton.[166]

The final bonding parameters determined are derived from the g and A values. As seen in Table 4.1, the g and A values are consistently determined from the various groups and material phases. However, ambiguity arises when approximations are made to arrive at the bonding parameters. These approximations include the spin overlap integral, $\langle r^3 \rangle$ for sulfur, and the interpretation of UV-Vis excitations, which can be seen in the papers from Table 4.1. The overlap integral is determined empirically and ranges in the literature from 0.005 to 0.3, and is a result of the Cu and the hybridization of the ligand orbitals.[159,160,163] There was not a consistent overlap integral used between authors and we will trust the authors' interpretations. The overlap integral makes a profound impact as it directly affects α^2. There are two different $\langle r^3 \rangle$ used for sulfur by Morton (4.85 a.u.)[166] and Hurd and Coodin (6.14 a.u.).[165] Kirmse and Solovev were able to see the ^{33}S hyperfine coupling and showed the variability of α^2 by using both Morton, and Hurd and Coodin $\langle r^3 \rangle$ values as displayed in Table 4.1.[162] Schmitt and Maki examined $Ni(mnt)_2^-$

with EPR and used a modified form of Morton's value by a linear interpolation between the S and the monoanion Ni(mnt)$^-$ complex.[167] They arrived 4.61 a.u. for $<r^3>$, which gave an average S covalency in the Ni(III) complex of 0.55 e$^-$ per hole.[167] Due to this large variability and chemical unreasonable bond covalencies, the results from Kirmse and Solovev were not considered in this study.

Many EPR studies apply the same theoretical treatment of the first five LUMOs that was developed by Maki and McGarvey for copper bis-acetylacetonate complexes, which is comprised of a D_{4h} symmetry and $3d^1$ electron holes.[168] Maki and McGarvey also determined the expressions of g||, g⊥, A||, and A⊥ in equations 3-6 in the reference.[168] The theoretical treatment and the equations for of g||, g⊥, A||, and A⊥ were utilized by Pettersson and Vänngård,[159] Reddy and Rinivasan,[163] Gersmann and Swalen,[160] and Weeks and Fackler.[161] Yet, Gersmann and Swalen use an approximation for α^2 that does not require the UV-Vis excitation energies developed by Kivelson and Neiman.[160,169] However, Weeks and Fackler,[161] and Kuska and Rogers[170] show that this approximation is not valid. Based on the results from Table 4.1, only the α^2 values from Weeks and Fackler,[161] Savino and Bereman,[164] and Pettersson and Vänngård[159] for the $Ni(dtc)_2$ host lattice and non-coordinating solution were considered. Even though there is ambiguity for the determination of the bonding parameters, Weeks and Fackler tabulate different bonding parameters with an average spin density of 0.54 on the Cu(II) center.[161] Since, 95% of the electron density lies between the Cu and four sulfur atoms, the determination of the S character of the b_{1g} semi-occupied molecular orbital (SUMO) is 0.47 e$^-$ per hole. The σ bond covalency is between 0.40-0.50 S character, which 0.47 e$^-$

per hole average is in the middle of this range.[161] The 0.47 e^- per hole sulfur character was applied to S K-edge of $Cu(dtc)_2$ to determine the transition dipole integral from the S 1s→3p. $Cu(dtc)_2$ provided an additional data point in the transition dipole integral curve for XAS evaluation of the ground state electronic structure.[93] Equations 4.2-4.4 derived by Queen *et al.*[93] were utilized to determine the complex dipole integrals for Cu(II), Ni(II), Fe(III), and Mo(IV) dtc compounds.

$$\text{slope} = 3.2(\Delta E^{L\rightarrow m})^2 + 2.3 \quad (4.2)$$

$$I^L = 0.37(E_0{}^L - E_0{}^{S2-})^2 + 14.5\text{eV} \quad (4.3)$$

$$I^C = I^L + \text{slope}(\Delta E^{L\rightarrow m}) \quad (4.4)$$

In this chapter, we report a detailed analysis of S K-edge spectra of free and coordinated dtc ligands to Zn, Cu, Ni, Fe, and Mo ions. The crystal structures of $Ni(dtc)_2$,[171] $Cu(dtc)_2$,[153] $Zn_2(dtc)_4$,[153] $Fe_2(dtc)_4$,[172] $Fe(dtc)_3$,[173] and $Mo(dtc)_4$[174] that were examined with S K-edge are displayed in Figure 4.1. As can be seen in Table 4.2, the distances of the S-C and C-N sp^2 atoms retain their bond lengths from the free ligand salt to the various complexes. Detailed studies of these crystal structures are described in the literature.[172-175]

$Ni(dtc)_2$ has rigid square planar geometry and is monomeric both in solution and crystalline phases. The point group for $Ni(dtc)_2$ corresponds to C_{2v} in regards to the whole complex, including the ethyl ligands. However, the complex has D_{2h} symmetry with respect to the Ni and S atoms. The electronic structure of $Ni(dtc)_2$ has been studied in literature using UV-Vis of both solution[176] and as a single crystal in literature.[177] According to the single crystal study, from lowest to highest energy the low spin Ni(II)

square planar complexes have an d-orbital arrangement of: z^2, xz, yz, x^2-y^2, and xy with the xy orbital as the LUMO containing b_{1g} symmetry.[177]

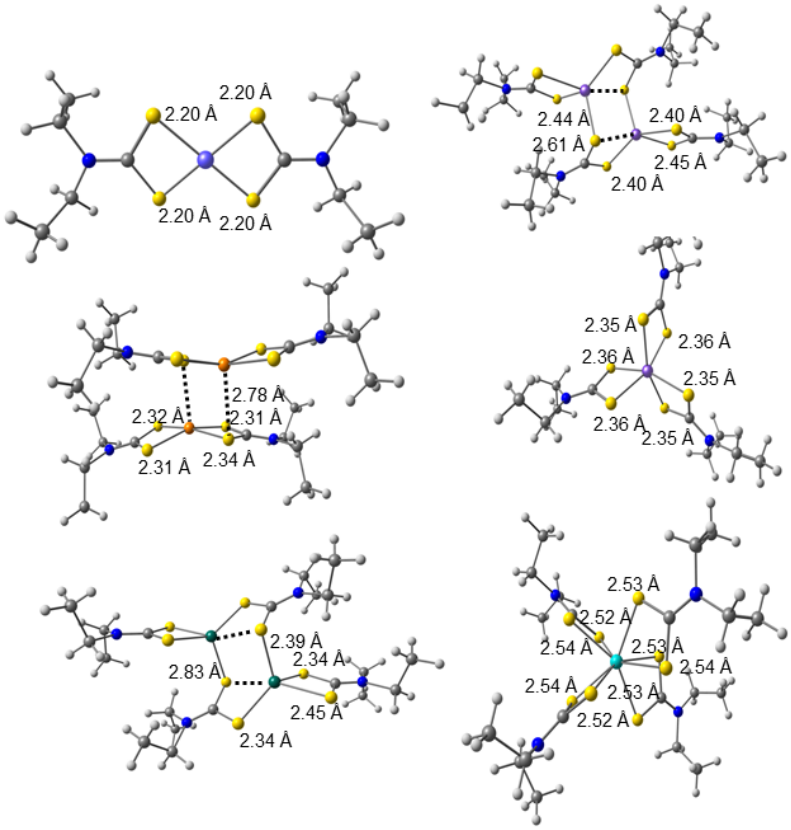


Figure 4.1: The crystal structures of $Ni(dtc)_2$ (top left), $Cu(dtc)_2$ (middle left), $Zn_2(dtc)_4$ (bottom left), $Fe_2(dtc)_4$ (top right), $Fe(dtc)_3$ (middle right), and $Mo(dtc)_4$ (bottom right).

$Cu(dtc)_2$ crystallizes as a weak dimer with an effective formula of $Cu_2(dtc)_4$. The $Cu_2(dtc)_4$ complex can be thought of as two monomers magnetically linked together by a weak ferromagnetic exchange pathway.[178] There is only a slight deviation of the Cu from the plane of the four sulfur atoms of about 0.29 Å. The distance between the two copper monomers is 2.78 Å away as shown in Table 4.2. In solution phase however, $Cu(dtc)_2$ is monomeric. $Cu(dtc)_2$ has a point group of C_{2v}, but has approximately D_{2h} symmetry with respect to the Cu and S atoms.

Table 4.2: Distances in Å between different atoms in the crystal structures from Figure 4.1.

Bond	Na(dtc)	$Zn_2(dtc)_4$	$Cu(dtc)_2$	$Ni(dtc)_2$	$Fe_2(dtc)_4$	$Fe(dtc)_3$	$Mo(dtc)_4$
M-S	-	2.34	2.31	2.20	2.45	2.35	2.52
		2.39	2.34		2.40	2.36	2.53
		2.35	2.78		2.41		2.54
		2.45			2.44		
		2.83			2.61		
S-C	1.74	1.73	1.72	1.72	1.72	1.71	1.72
	1.71	1.74	1.73		1.77	1.70	1.70
		1.75			1.73	1.72	1.69
C-N	1.34	1.32	1.32	1.32	1.32	1.32	1.33
					1.33	1.35	
						1.34	
M…C*	-	2.79	2.77	2.68	2.97	2.84	3.08
		3.01	2.75		2.85	2.83	3.06
						2.81	
M…N*	-	4.11	4.09	4.00	4.29	4.16	4.41
		4.32	4.07		4.18	4.18	

*The M…C and M…N are distances from the central metal to sp^2 C and N of the dtc ligands.

Unlike $Ni/Cu(dtc)_2$ complexes, $Zn_2(dtc)_4$ is a binuclear dithiocarbamate molecule. There are only three S atoms effectively bonding to it, where as there are four with $Ni/Cu(dtc)_2$ compounds. Additionally, the Zn(II)dtc complex has a full d-manifold and the S 3p mixing will not be able to donate electron density to the Zn d-manifold.

The $Fe_2(dtc)_4$ dimer complex is isostructural to $Zn_2(dtc)_4$. There is significant deviation of the Fe from the plane of the four sulfur atoms, which increases the covalent interaction between the Fe(II) site and the axial S atoms. In addition, there are three S atoms bonding to each Fe(II) center as seen in the $Zn_2(dtc)_4$ molecule. There is also an anti-ferromagnetic coupling of the two high spin (S = 2) irons that was studied with

Mossbauer and UV-Vis.[179]

The molecule, $Fe(dtc)_3$, is a mononuclear compound, unlike its Fe(II) counterpart. The point group of $Fe(dtc)_3$ is D_3, but is typically described as O_h in literature with respect to the S and Fe atoms. It's 10 Dq splitting was determined to be 15700 cm^{-1} or 1.95 eV.[180] $Fe(dtc)_3$ complexes are well known to have a mixed spin state at different temperatures.[173,180-182] The mixed spin system needs to be considered when determining the ground state electronic structure.[180] The room temperature mixed spin system needs to be used since the S K-edge measurements were collected at room temperature. It's magnetic moment is 4.24 in solid form and 4.41 in solution phase (benzene and chloroform) at room temperature.[181,182] According to ligand field theory, the two ground states that are accessible to this complex are the $^2T_2$-$^6A_1$ states. Tsipis *et al.* concluded that there is 43% low spin and 57% high spin for the observed spin of $Fe(dtc)_3$ at room temperature.[180] Additionally, $Fe(dtc)_3$ was studied previously at the S K-edge.[183] The rising edge features were assigned to the t_{2g} and e_g orbitals of the approximately octahedral S atoms mixing into the Fe d-manifold.[183] However, the S character was not determined from the rising edge features.

$Mo(dtc)_4$ has four bidentate ligands coordinating to a single metal site. This complex is best described as a square-anti-prismatic molecule with D_{2d} symmetry. The magnetic moment has varied in the literature from 0.68, 1.0, 1.3, and 1.4 BM for $Mo(R_2dtc)_4$.[184,185] It was concluded by Nieuwpoort and Steggerda that $Mo(dtc)_4$ is diamagnetic and that the magnetic susceptibility measurements had paramagnetic impurities present when conducted.[186] In fact, NMR and powder EPR measurements

showed that there were not any peaks present.[184,185] Therefore, the complex is diamagnetic with the Mo in the plus four oxidation state with eight holes in the d-manifold. The 10 Dq value for this system is 2000-2500 cm^{-1} or 0.25-0.31 eV.[186]

Experimental Techniques and Computational Methods

Preparation of Compounds

$NaEt_2dtc$ was purchased from Fisher Scientific and dehydrated under vacuum for 3 hours, where the OH stretch disappeared in FT-IR at 3000-3700 cm^{-1}. $Ni(dtc)_2$,[187] $Cu(dtc)_2$,[188] $Fe(dtc)_3$,[181] and $Mo(dtc)_4$[184] were synthesized by following literature procedures. $Zn_2(dtc)_4$ was synthesized from the same procedure as $Cu(dtc)_2$. $Fe_2(dtc)_4$ was synthesized using glovebox and Schlenk line techniques by mixing 2:1 $NaEt_2dtc$:$FeCl_2$ in degassed MeCN for 12 hours. The solution was filtered and washed thoroughly with cold degassed H_2O to remove the NaCl. The product was dark red and was stored in the glovebox.

Sulfur K-edge X-ray Absorption Spectroscopy

All measurements were collected at beamline 4-3 of the Stanford Synchrotron Radiation Lightsource. Repeated measurements of the same samples did not reveal any significant variation among data sets from the different collection periods. All XAS measurements were carried out at room temperature, and the sample cells were prepared in a nitrogen or argon gas filled glovebox. During the mounting of the samples at the beamline, the sample cell was protected with a few μm thick Mylar window to eliminate sample degradation due to oxidation or exposure to moisture. The solid samples were

ground with boron nitride and pasted onto a Kapton tape. The only exception to this was $Mo(dtc)_4$, which had a low concentration of sulfur and yielded the highest intensity for the Mo L_{III} and L_{II}-edges. Any excess sample was scraped off from the tape to minimize the distortion of peak intensities due to self-absorption effects. The beamline was optimized to maximize incident beam intensity at the end of the scan. All data presented was collected with fluorescence detection using a nitrogen gas purged and a passivated implanted planar silicon detector (PIPS, CANBERRA). Importantly for fluorescence emission data, the pre-edge intensity analysis and the transition dipole integral presented here are limited to reasonably thin samples.

XAS Data Normalization and Fitting

All data was background subtracted and normalized using the Automated Data Reduction Protocol (ADRP) developed by D. Gardenghi.[90] The S K-edge was calibrated to sodium thiosulfate pentahydrate at 2472.02 eV. The data scans were averaged, and a smooth background of a second-order polynomial was removed from the spectrum. Normalization of the data was accomplished by fitting a flattened second-order polynomial to the post edge region and normalizing the fit spline function to 1.0 at 2490 eV. To account for the Mo L_{III} and L_{II}-edges in $Mo(dtc)_4$, the following steps were taken. First, the raw data was normalized at 2600 eV in ADRP without calibrating the data, and the L_{II} edge was fit. The Mo L_{III}-edge was subtracted from the S K and Mo L_{III}-edge normalized data by shifting and scaling the L_{II}-edge fit to the L_{III}-edge height. The spectrum was calibrated to thiosulfate pentahydrate, followed by background subtraction of a second-order polynomial function. Subsequently the data was fit to a flattened

second-order polynomial to the post-edge region and normalizing the spline function to 1.0 at 2490 eV. The error introduced by data reduction and normalization procedures was at most 3% in regards to the peak amplitudes.[189]

The normalized data were fit using Peak Fit v4.12 (SeaSolve). The details of all fits are shown in the supporting information. Due to the comprehensive set of spectra for both the complexes and the free ligand salt, we were able to employ the following common protocol. In order to avoid unreasonable distortion and large variations in intensities for ill-resolved features, additional fits were obtained in consecutive steps by gradually allowing for the amplitudes, energy positions, line-widths, and lastly allowing the Gaussian/Lorentzian mixing ratio to deviate from the pseudo-Voigt line. For $Cu(dtc)_2$, $Ni(dtc)_2$, $Fe(dtc)_3$ and $Mo(dtc)_4$, the final fits were obtained by relaxing all fit parameters except the Gaussian/Lorentzian mixing which were held at 0.5 and the linewidths shared for the M-S and S-C-N π^*. The edge jump was simulated with a Lorentzian ascending curve fixed to 1, a peak at the same energy position as the edge jump to account for the S 4p transition, and additional peaks afterwards to compensate for the EXAFS region. The $Fe_2(dtc)_4$ and $Zn_2(dtc)_4$ spectra were not fitted since the metal-ligand features are jammed against the edge jump and are not resolvable. Only chemically reasonable fits were considered.

Electronic Structure Calculations

All the dtc structures coordinates were obtained from the Cambridge Crystallographic Database and used without modification. Density functional calculations were performed using Amsterdam density function theory program package 2012

(ADF),[137-139] Gaussian09 Revision C.02[102] and ORCA.[140] A triple-ξ basis set with a polarization function was utilized both in ADF and in Gaussian ensuring convergence of the ground state wavefunctions. The basis set used in all ADF single point calculations was TZ2P,[149] and in Gaussian and ORCA was def2-TZVP[106] from EMSL Gaussian basis set exchange.[109,110] Single point calculations were conducted using BP86,[56,57] B3LYP,[53,111] and B(38HF)LYP[55,57,111] functionals in all programming packages. All electronic structure calculations were performed using the presence of a polarizable dielectric environment in Gaussian[127-132] using acetonitrile with a dielectric constant of 35.6 and a solvent radius of 1.81 Å. A conductor like screening model (COSMO)[128,144-146] was utilized for acetonitrile with a dielectric constant of 37.5 and a solvent radius of 2.76 Å in ADF. Optimizations were conducted by doping a single Cu atom in $Zn_2(dtc)_4$ complex and Zn into $Cu_2(dtc)_4$ in Gaussian with the tight convergence criterion. This was necessary to determine the structure of $Cu/Zn(dtc)_4$ since there is no X-ray crystal structure for this system. A single point calculation was carried out on the optimized geometry in ADF. All single point calculations were with the tight convergence criterion. In ADF, all calculations were performed by creating individual fragments of the dtc ligand and merging in with Cu(II), Ni(II), Fe(III), and Mo(IV) metal fragments. Population analysis was conducted in Gaussian using "Atoms-in-Molecules"[64,133-135] from the AIMAll[136] program. Crystallographic coordinates and optimized coordinates are available in Appendix C for all complexes.

TD-DFT calculations were conducted to predict the S K-edge pre-edge region of the XAS spectra using ORCA. The S 1s orbitals were localized since they are

symmetrically equivalent in all complexes. Only excitations were computed from the localized S 1s orbital were allowed. The excitation energies were corrected by a constant to line up the calculated spectra with the experimental spectra. The TD-DFT calculations were performed using the def2-TZVP basis set for all complexes examined. The B3LYP functional was used for the Ni(II), Fe(III) and Mo(IV) dtc complexes, while B(38HF)P86[55-57] was used for $Cu(dtc)_2$. Additionally, the zero order regular approximation[147,148] and COSMO using acetonitrile were also utilized in the TD-DFT calculations.

Results and Analysis

Energy Positions of S K-edge Spectral Features

Na, Cu(II), Ni(II) dtc Complexes. In the S K-edge of the free ligand, there are two distinct transitions, the S-C-N π* and S-C σ* peaks separated by 1.5 eV. The intensities are approximately 1:1.8 due to one double bond and two sigma bonds. Its edge position is at 2474.3 eV as displayed in Figure 4.2 and Table 4.3.

The $Cu(dtc)_2$ S K-edge spectrum has the same S-C-N π* and S-C σ* peaks as well an additional feature, which belongs to the Cu-S σ* bond in the b_{1g} orbital of this complex. This orbital is a singly occupied MO, which supports the spin 1/2 state of this complex. The edge position of the complex is 2474.4 eV based on the first local maxima of the first derivative plot after the white line. In the first derivative plot of the complex, there is an additional bump at 2475.1 in the spectrum directly after the local maximum. This indicates that there are two distinct sulfur environments, and therefore, two distinct

edges. The edge at 2474.4 eV is due to the Cu atoms that lie near two axial sulfur atoms (see Figure 4.2). The edge at 2475.1 is due to the equatorial S donation to the Cu atom.

$Ni(dtc)_2$ contains the similar bonding motif as $Cu(dtc)_2$ and Na(dtc) where its S K-edge spectrum contains the characteristic S-C-N π^* and S-C σ^* peaks. The edge position is located at 2474.9 eV where there is only maximum in the first derivative spectrum in Figure 4.2, which is due to the equatorial S mixing into the Ni d-manifold. This is consistent with $Cu(dtc)_2$ where there is a local maximum of 2475.1 eV. Furthermore, there is large feature that pertains to the Ni-S σ^* bond of the b_{1g} orbital that is shifted higher in energy with respect to the $Cu(dtc)_2$.

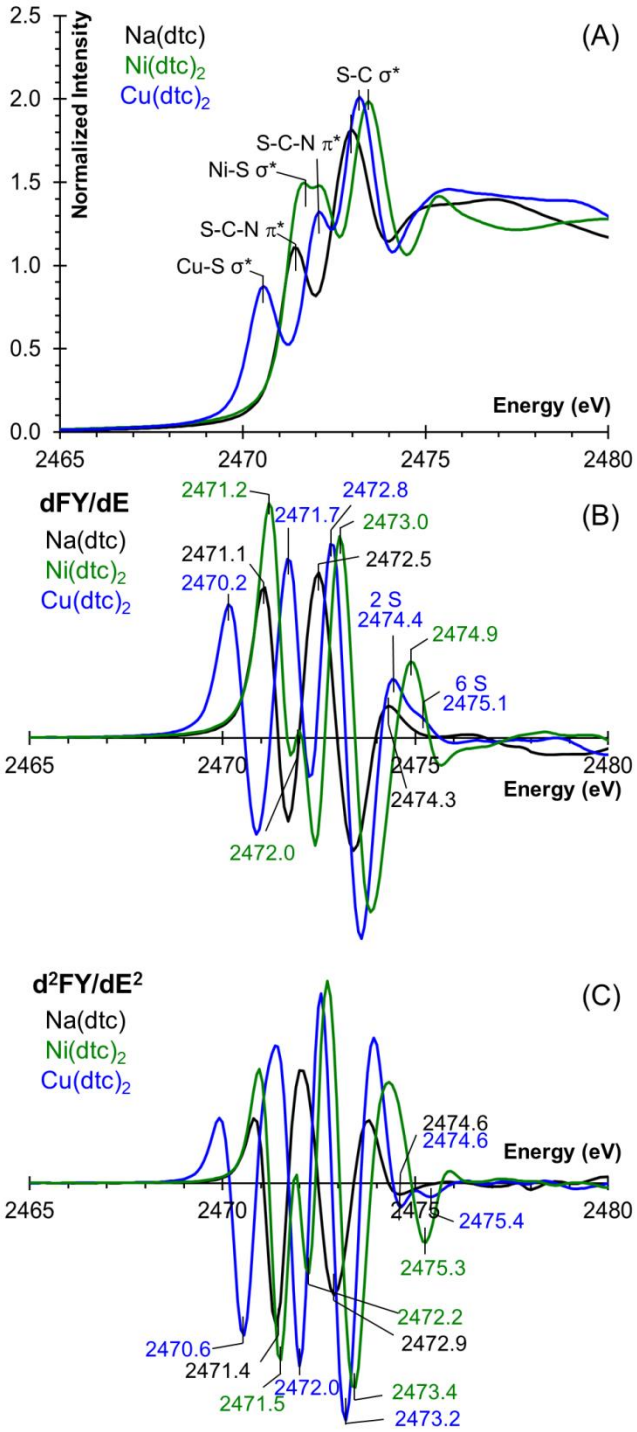


Figure 4.2: Energy position analysis of the XANES region of the normalized S K-edge spectra (A), first derivative spectra (B), and second derivative spectra (C) of Na(dtc), $Ni(dtc)_2$, and $Cu(dtc)_2$.

Na, Fe(III), and Mo(IV) dtc Complexes. The $Fe(dtc)_3$ S K-edge spectrum is more convoluted than the four coordinate dtc complexes described above. There are two shoulders jammed against rising edge S-C-N π* peak as seen in Figure 4.3. Presumably, these shoulders are the t_{2g} and e_g orbitals of the approximately octahedral S atoms mixing into the Fe d-manifold. In addition to the shoulders and the S-C-N π* features, there is also the S-C σ* peak just before the edge position at 2474.9 eV.

The $Mo(dtc)_4$ spectrum (Figure 4.3) is structurally the most complicated complex investigated with XAS in this study. There are only two resolvable features in this spectrum that contain many transitions to the Mo d and ligand orbitals. The first feature contains the Mo-S bonding to the vacant Mo d-orbitals and the S-C-N π* orbitals. The second resolvable contains two peaks as well, which possibly corresponds to the S-C σ* orbitals. The edge position of this complex is also very peculiar since the first local maximum after the most intense peak in the first derivative plot is below the x-axis unlike the other spectra. This indicates the spectrum has a negative slope for several eV into the EXAFS spectrum.

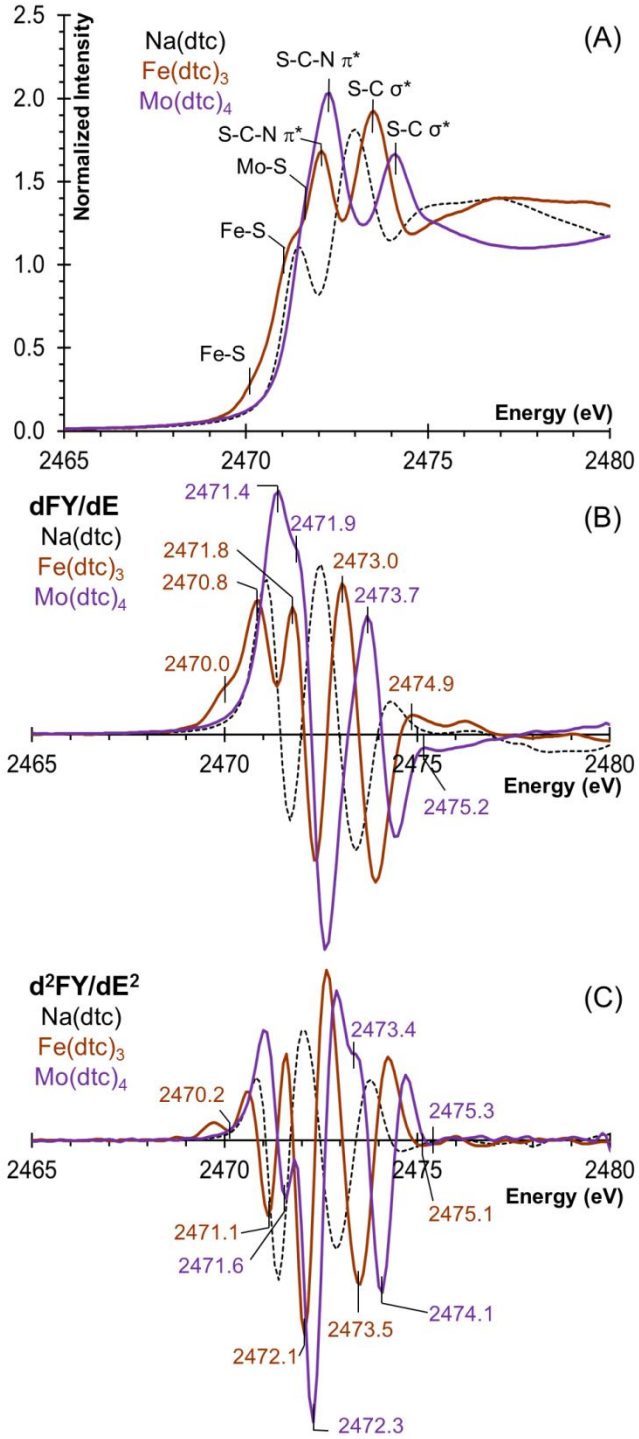


Figure 4.3: Energy position analysis of the XANES region of the normalized S K-edge spectra (A), first derivative spectra (B), and second derivative spectra (C) of Na(dtc), $Fe(dtc)_3$, and $Mo(dtc)_4$.

Na, Fe(II), and Zn(II) dtc Complexes. The $Fe_2(dtc)_4$ complex spectrum is more complicated than its $Fe(dtc)_3$ counterpart (Figure 4.4). Similarly to $Ni(dtc)_2$ and $Cu(dtc)_2$ d-orbitals discussed above, the splitting of the Fe(II) d-manifold is higher in energy than the Fe(III) complex. The energy difference results in an unresolvable pre-edge feature in the rising edge portion of the spectrum. The spectrum does contain a S-C-N π* pushed up against the S-C σ* peak. There are three distinct S environments resulting in three edges. Due to the lack of pre-edge features, this spectrum cannot be fit to extract the amount of S 3p mixing into the F(II) d-manifold.

Zn(II) complexes do not exhibit a pre-edge feature in ligand K-edge spectroscopy. Their 3d-manifold is completely full, and the S atoms mix with Zn 4s/4p orbitals. $Zn_2(dtc)_4$ is very similar to the $Fe_2(dtc)_4$ complex spectrum with no resolvable pre-edge feature and the S-C-N π* is jammed against the S-C σ* peak as displayed in Figure 4.4. Similarly to $Fe_2(dtc)_4$, are three unique sulfurs, which results in three edge jumps. These edge jumps can be seen in the first derivative plots because the local maximum after the white line is very broad. In addition, the lack of pre-edge features results in the inability to determine the amount of S 3p mixing.

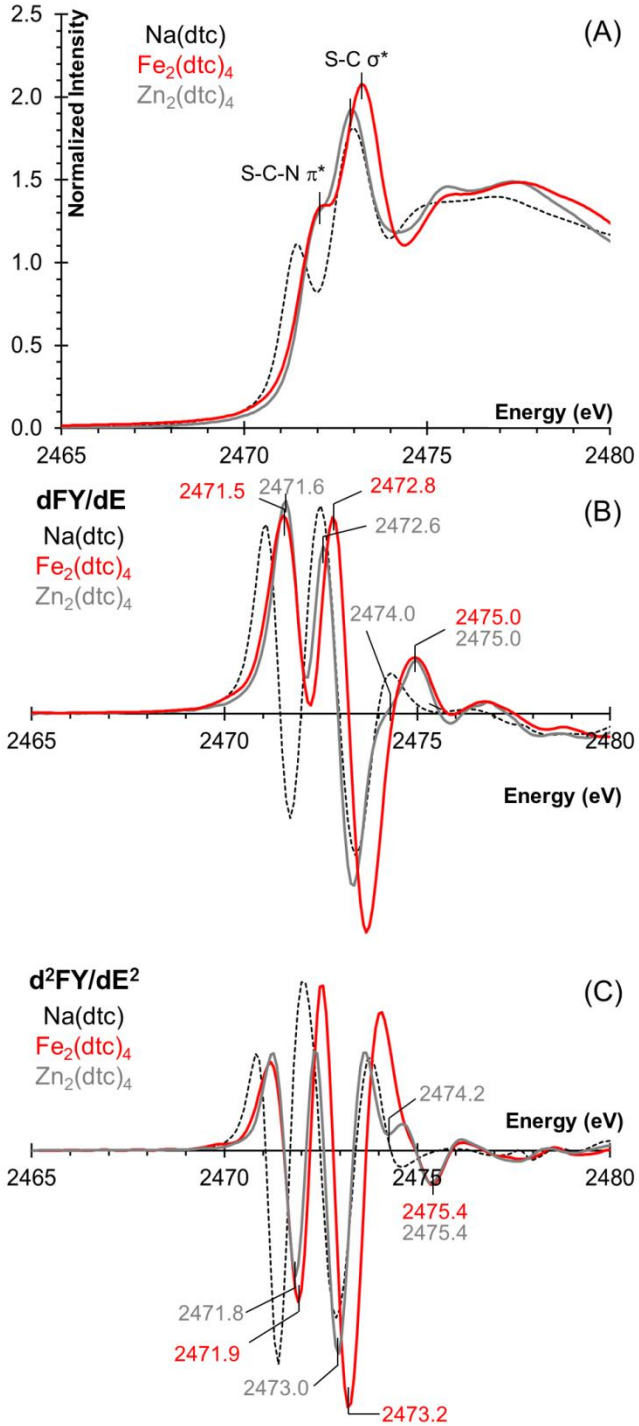


Figure 4.4: Energy position analysis of the XANES region of the normalized S K-edge spectra (A), first derivative spectra (B), and second derivative spectra (C) of Na(dtc), $Fe_2(dtc)_4$, and $Zn_2(dtc)_4$.

Table 4.3. Postulated S K-edge peak positions in eV.

	Edge Position (E_0^C)	Relative Edge Position ($\Delta E_0^{L->M}$)	M-S σ^*/π^* positions	S-C-N π^* Peak positions	S-C σ^* Peak positions	π^*/σ^* gap
Na(dtc)	2474.3	0.0	-	2471.4	2472.9	1.5
Cu(dtc)2	2474.4 2475.1	0.1 0.8	2470.6	2472.0	2473.2	1.2
$Zn_2(dtc)_4$	2474.0 2475.0	-0.3 0.7	-	2471.8	2473.0	1.2
Ni(dtc)2	2474.9	0.6	2471.5	2472.2	2473.4	1.2
$Fe_2(dtc)_4$	2474.9	0.7	-	2471.9	2473.2	1.3
Fe(dtc)3	2474.9	0.6	2470.2 2471.1	2472.1	2473.5	1.4
Mo(dtc)4	2475.2	0.9	2471.6 2472.3	2473.4	2474.1	1.8

Calculated Ground State Orbital Energy Levels

The Na(dtc) ligand has extensive delocalization from the two sulfur atoms into the carbon and the nitrogen. This delocalization provides metal to ligand back bonding that helps stabilize transition metal dtc complexes. There are two holes per ligand in the out of plane π bonding network.

Due to the back bonding capabilities of the dtc ligand, $Ni(dtc)_2$ forms a square planar low spin complex with D_{2h} symmetry. The LUMO of this complex is the b_{1g} orbital which contains two holes in this orbital. When examining the molecular orbital contributions with DFT, it is apparent the d-manifold is arranged in a different order as illustrated in Figure 4.5 than described from literature.[177] The x^2-y^2 orbital is actually

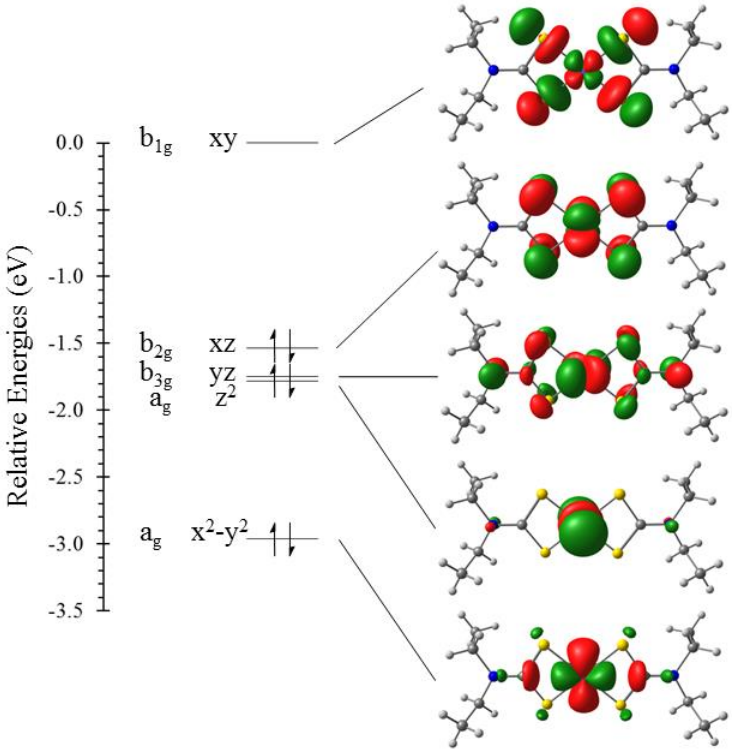


Figure 4.5: $Ni(dtc)_2$ d-manifold orbitals. The orbitals were generated from BP86/def2-TZVP. Notice the back bonding of the x^2-y^2 orbital into the C-N σ orbital.

the lowest in energy due to back bonding into the C-N σ bond. This back bonding is able to overcome the repulsion of the S lone pairs, which destabilizes the orbital. Also shown in Figure 4.5, the LUMO is entirely S and Ni based. The symmetry of the system allows for mixing of the S 3p orbital into the metal d_{xy} LUMO. Two symmetry allowed excitations can occur from the S 1s orbital due to the a_g symmetry in the excited state, which corresponds to the S 3p-M d_{xy} orbital in using the S K-edge. We can consider this as one excitation since the four sulfur atoms are at degenerate energies. In Figure 4.6, the LUMOs are displayed with respect to the uncoordinated free dtc ligand. After exciting to the d-manifold, the next orbitals that are populated are the S-C-N π* and then the S-C σ* orbitals. Interestingly, there is excited state mixing of unoccupied orbitals of two dtc

ligands centered on a +2 point charge. However, this mixing vanishes when the Ni(II) metal takes the place of the point charge.

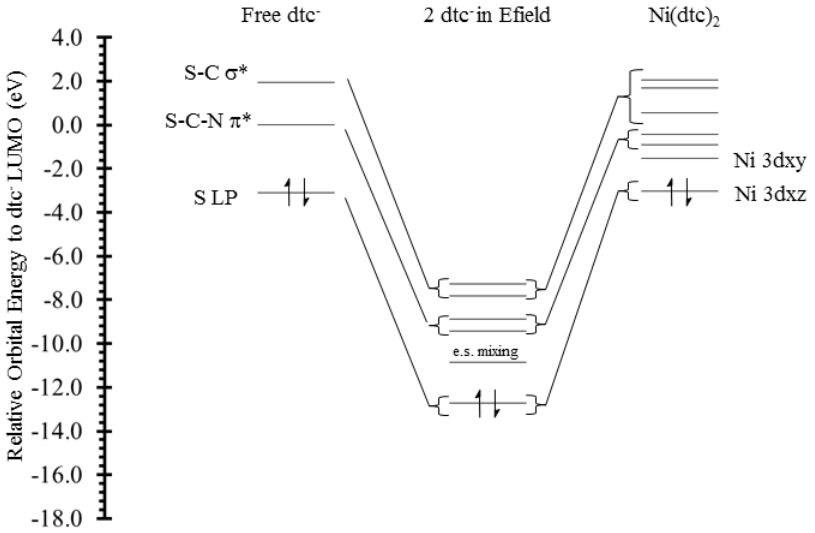


Figure 4.6: The MOs of $Ni(dtc)_2$ starting from the free ligand, two ligands around a 2+ point charge, and on the far right the ligands chelating onto Ni generated from ADF using BP86/TZ2P.

A similar bonding picture is seen for $Cu(dtc)_2$ when compared to $Ni(dtc)_2$ as depicted in Figure 4.7. When comparing the Figures 4.6 and 4.7, the d-manifold splitting between the HOMO and the LUMO is smaller for $Cu(dtc)_2$ than for $Ni(dtc)_2$. This supports the S K-edge spectrum shown in Figure 4.4 where the $Ni(dtc)_2$ b_{1g} orbital is higher in energy with respect to $Cu(dtc)_2$. This shift in the M-S (M = Ni, Cu) σ* peak is due to the splitting of the metal d-manifold. The Cu(II) HOMO is stabilized by the single electron due to Jahn Teller effects in the b_{1g} orbital. The Ni(II) complex doesn't exhibit this stabilization causing a greater splitting of the b_{1g} orbital. Additionally, the MO picture is very similar between the monomer and dimer. The main difference is the dimer contains twice as many orbitals as the monomer. Assuming the same symmetry as

$Ni(dtc)_2$, there are two symmetry allowed excitations occurring from the S 1s to the to the S 3p-M d_{xy} orbital.

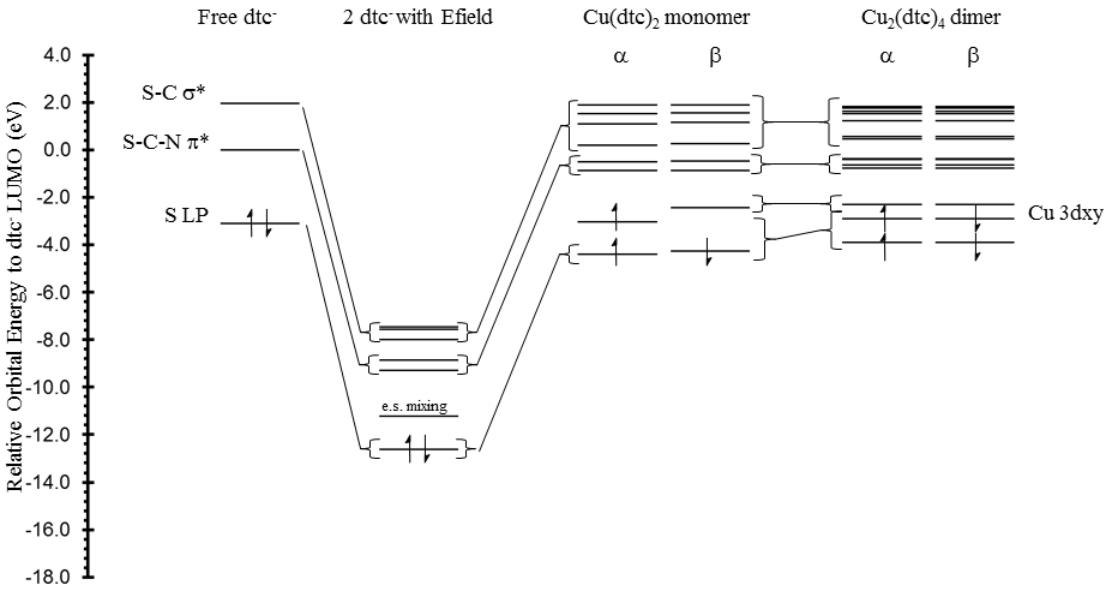


Figure 4.7: The MOs of $Cu(dtc)_2$ starting from the free ligand, two ligands around a 2+ point charge, monomer complex of both spins, and also the $Cu_2(dtc)_4$ dimer computed in ADF using BP86/TZ2P.

The energy decomposition of the Ni, Cu, and Zn dtc complexes in Table 4.4 were computed in ADF to compare to EPR results list in Table 4.1. When examining $Cu_2(dtc)_4$ interactions by using two $Cu(dtc)_2$ molecules, the Pauli repulsion is compensated by the orbital overlap and the electrostatic interactions leaving the solvation energy to make up the binding energy. Additionally, there is less than 0.5% electron density shared between the two monomers as computed by ADF using BP86/TZ2P. When $Cu(dtc)_2$ is doped into a Zn lattice in an optimized structure, there is a greater covalent interaction between the $Zn(dtc)_2$ and $Cu(dtc)_2$ monomers as shown in Table 4.4. Additionally, the total energy of these complexes consists of the solvation energy, the Pauli repulsion, the electrostatic

interaction, and orbital interaction energies. The energy holding the $Cu/Zn(dtc)_4$ dimer together is 0.7 eV, and is not considered for EPR analysis of the bonding parameters. The $Cu_2(dtc)_4$ complex only leaves 0.1 eV unaccounted for, which is most consistent with $Ni(dtc)_2$. This is consistent with the differences in the metal hyperfine values between Zn and Ni host lattices.

Table 4.4: Energy Decomposition Analysis for Zn/Cu/Ni dithiocarbamate complexes (in eV) as implemented in ADF.

Structural Source	Reference Fragments	Pauli Repulsion	Electrostatic Interaction	Orbital Interactions	Solvation	Binding Energy
$Zn(dtc)_2$	Zn^{2+}, 2 dtc^-	16.9	-6.8	-10.2	-0.8	-0.9
$Cu(dtc)_2$ in $Zn(dtc)_2$	Cu^{2+}, 2 dtc^-	16.0	-5.9	-11.6	-0.7	-2.2
$Cu(dtc)_2$ in $Cu(dtc)_2$	Cu^{2+}, 2 dtc^-	9.6	-30.4	-11.2	-0.6	-32.7
$Cu(dtc)_2$ in $Ni(dtc)_2$	Cu^{2+}, 2 dtc^-	30.2	-13.6	-18.9	-0.7	-2.9
$Ni(dtc)_2$	Ni^{2+}, 2 dtc-	30.8	-13.7	-22.0	-0.7	-5.6
$(Cu/Cu)(dtc)_4$	2 $Cu(dtc)_2$	2.9	-1.7	-1.3	-1.3	-1.4
$(Cu/Zn)(dtc)_4$	$Cu(dtc)_2$ & $Zn(dtc)_2$	6.0	-4.5	-2.6	-1.3	-2.4
$(Zn/Zn)(dtc)_4$	2 $Zn(dtc)_2$	6.0	-4.7	-2.7	-1.2	-2.7
$(Cu/Zn)(dtc)_4$ opt[a]	$Cu(dtc)_2$ & $Zn(dtc)_2$	3.8	-2.8	-1.9	-1.1	-1.8
$(Zn/Cu)(dtc)_4$ opt[b]	$Cu(dtc)_2$ & $Zn(dtc)_2$	3.8	-2.8	-1.9	-1.1	-1.8

a) Optimized in Gaussian using $Cu(dtc)_2$ dimer doped with a zinc atom in place of a copper. b) Optimized in Gaussian using $Zn_2(dtc)_4$ doped with one copper atom.

The orbital picture of $Fe(dtc)_3$ is composed of five holes in the 3d manifold regardless of the symmetry and spin state. The hexa-coordinate arrangement of the S atoms is mixed into the Fe 3d-orbitals in an approximate octahedral environment. This is

supported by relative energies of the d-orbitals displayed in Figure 4.8 of both spin 1/2 and 5/2 systems. In a pure, spin 5/2 environment, there would be three holes in the t_{2g} orbital and two holes in the e_g orbital. In the 1/2 spin state, there would be one hole in the t_{2g} orbital and four holes in the e_g orbitals. There is mixing of the S 3p orbitals into all of the Fe 3d orbitals and are thus probed using S K-edge XAS.

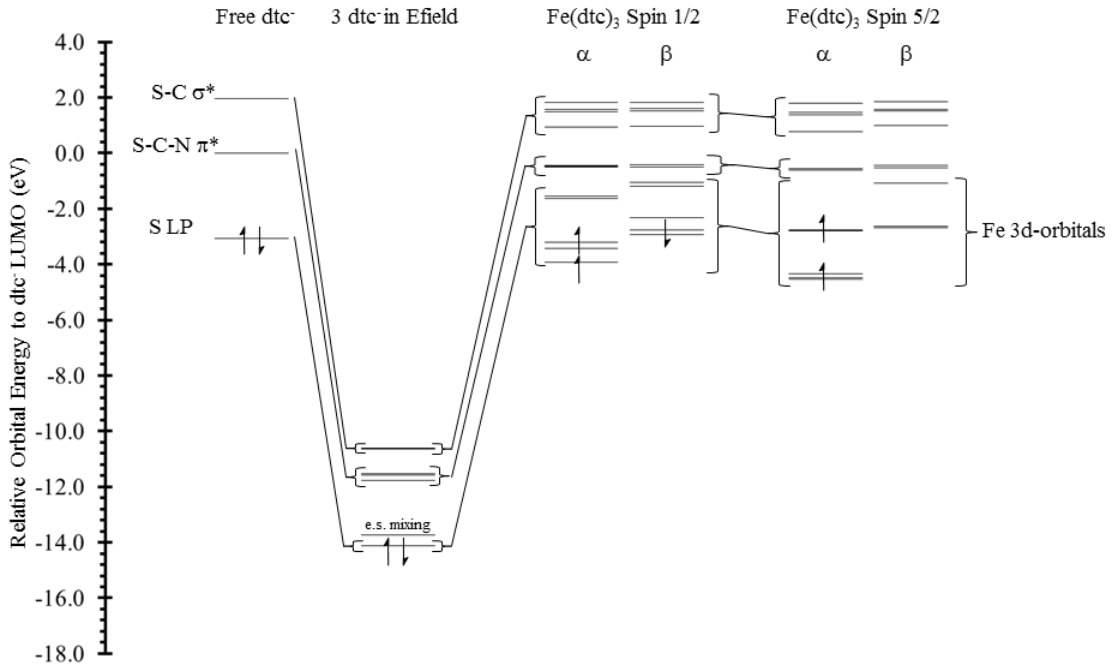


Figure 4.8: The MOs of the crystal structure of room temperature $Fe(dtc)_3$ starting from the free ligand, three ligands around a 3+ point charge, monomer complex of both spin 1/2 and 5/2 states generated from ADF using BP86/TZ2P.

As described in the Introduction, $Mo(dtc)_4$ is a low spin, diamagnetic complex with D_{2d} symmetry. Thus the d-orbitals are split into a_1, b_1, b_2, and e symmetry, which allows for S 3p mixing. The lone pair in this complex presides on the predominately z^2 orbital. Figure 4.9 shows the MO picture of $Mo(dtc)_4$, and illustrates the symmetry mixing of the Mo d-orbitals and the ligand π* orbitals. The small splitting of the Mo d-

and the ligand S-C-N π* orbitals shown in Figure 4.9 is supported by the convoluted rising edge feature in Figure 4.3. There is however, a clear separation of the S-C σ* orbitals from the Mo/S-C-N π* bonding network.

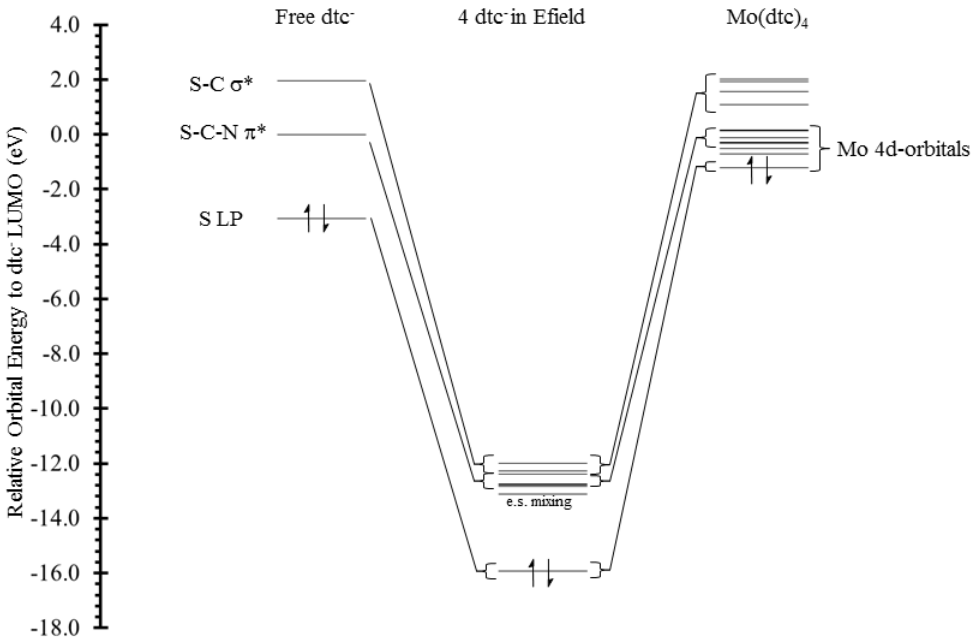


Figure 4.9: The MOs of $Mo(dtc)_4$ starting from the free ligand (left), four ligands around a 4+ point charge (middle), and on the far right the $Mo(dtc)_4$ generated from ADF using BP86/TZ2P.

Ground State Orbital Composition

The Ni, Cu, Fe(III), and Mo dtc complexes were examined with AIM using B3LYP and B(38HF)LYP/def2-TZVP level as shown in Figure 4.10 to compare our interpretation of the XAS S covalencies. Figure 4.10 only shows the mixing into the d-manifold before the S-C-N π* on the free ligand. The general trend produced from B3LYP is that these dtc complexes exhibit normal, innocent bonding between the dtc ligand and the metal center except for $Cu(dtc)_2$. More HF mixing is needed for

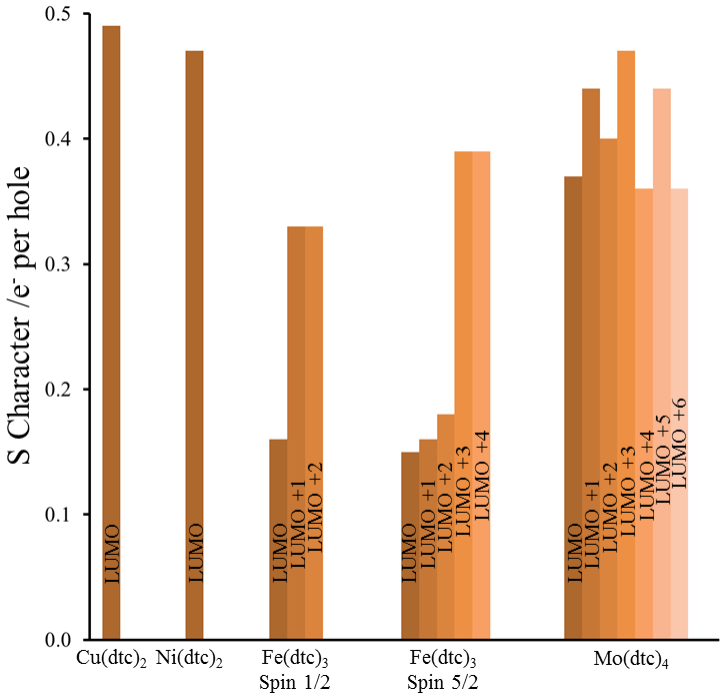


Figure 4.10: The AIM per hole S character of transition metal dtc complexes using def2-TZVP basis set and B3LYP functional for all the complexes except for $Cu(dtc)_2$, for which the B(38HF)LYP functional was used.

comparable results to EPR.[55] The B(38HF)LYP functional gives 0.49 e^- per hole S character vs 0.47 e^- per hole derived from EPR. The S character determined for $Ni(dtc)_2$ was 0.47 e^- per hole indicating a very covalent bond between the sulfurs and the Ni(II) center. Population analysis were also conducted on $Fe(dtc)_3$ for pure spin 1/2 and spin 5/2 states. A weighted average of the two spin systems will give the most accurate representation of the S 3p character mixed into the Fe d-manifold. The t_{2g} orbitals in both spin systems have approximately the same S character of 0.16 e^- per hole. The e_g orbitals are more affected by the change in spin state. The spin 5/2 is more covalent than the spin 1/2 system with 0.39 vs 0.33 e^- per hole S character, respectively in the e_g orbitals. The AIM population analysis of $Mo(dtc)_4$, is also rather covalent with an average of 0.40 e^-

per hole for the orbitals corresponding to the rising edge feature in the S K-edge XAS spectrum. However, only seven LUMOs are present instead of eight (four for the Mo d- and four for the ligand π* orbitals) for $Mo(dtc)_4$ when calculated in Gaussian.

Excited State Orbital Energy Levels

TD-DFT was applied to simulate the S K-edge excitations in ORCA for Cu(II) and Ni(II) dtc complexes in Figure 4.11 using B(38HF)P86 and B3LYP respectively with the def2-TZVP basis set. The TD-DFT calculation does a good job reproducing the intensities and energy spacing of the Ni-S bonding feature and the overall trend of the S K-edge spectrum for $Ni(dtc)_2$. For $Cu(dtc)_2$, the Cu-S peak is reproduced and the S-C-N π* orbitals, but the S-C σ* orbital is lower in energy than the experimental spectrum. The $Ni(dtc)_2$ calculated pre-edge excitation is larger than $Cu(dtc)_2$ due to the additional hole in the b_{1g} orbital in Ni(II) d-manifold, which is to be expected. Additionally, there are two π* features present in the TD-DFT simulation.

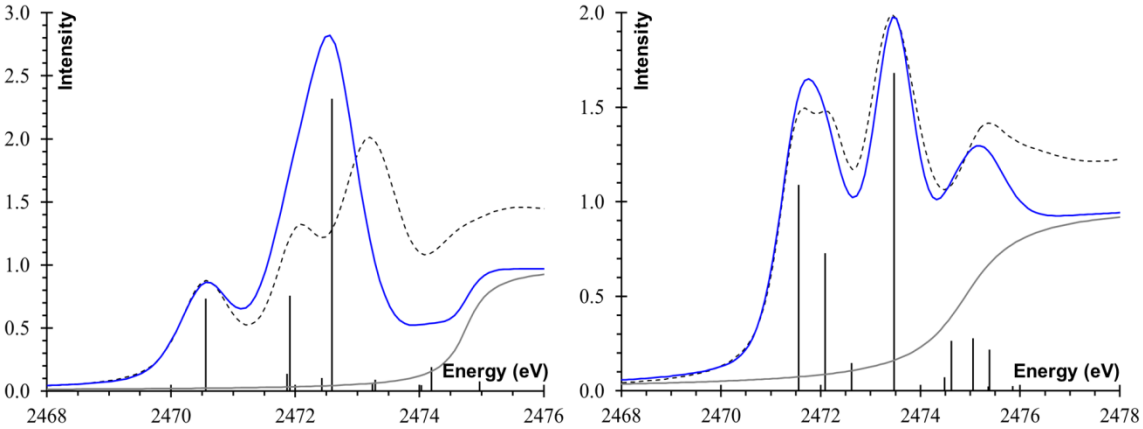


Figure 4.11: TD-DFT of $Cu(dtc)_2$ (left) and $Ni(dtc)_2$ (right) of the M-S, π*, and σ* transitions computed in ORCA compared to their respective S K-edge XAS spectrum.

The mixed spin $Fe(dtc)_3$ is more complicated to analyze with TD-DFT of the S K-

edge. Neither of the pure spin states could reproduce the S K-edge spectrum. Only one system can be computed at a time with TD-DFT. The calculation was computed using B3LYP/def2-TZVP for both spin systems. For the spin 1/2 and 5/2 systems, two excitations are present to the Fe d-orbitals, the e_g and t_{2g} orbitals. In the 5/2 system, the slight shoulder at approximately 2470 eV is present. This small shoulder is gone in the spin 1/2 system, but is replaced with a more predominate shoulder before the S-C-N π* at 2471 eV. The low spin and high spin TD-DFT calculations from ORCA were weighted at 43% and 57% respectively and merged together in Figure 4.12. This qualitatively reproduces the excitations to the t_{2g}, e_g, and π* orbitals. The S-C σ* transitions were not computed to save on computational costs.

TD-DFT was also computed in ORCA for $Mo(dtc)_4$ in Figure 4.12 using B3LYP/def2-TZVP. The simulated spectrum reproduces the excitations in the experimental spectrum. The broad rising edge feature corresponds to excitations to the Mo-S, and S-C-N π* orbitals. The S-C σ* orbitals are shifted higher in energy than in the experimental spectrum.

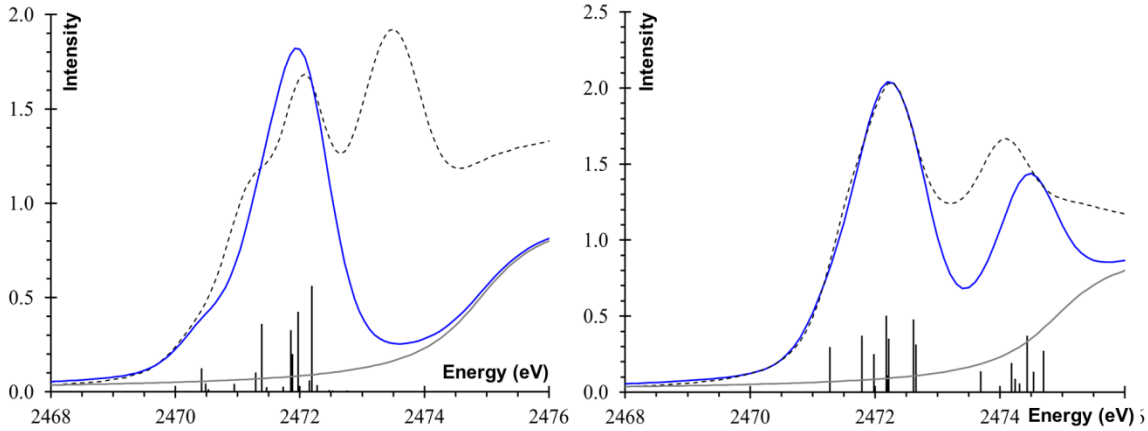


Figure 4.12: TD-DFT calculated in ORCA of Fe-S and π* for $Fe(dtc)_3$ containing 57% spin 5/2 and 43% spin 1/2 (left) and the Mo-S, π*, and σ* for $Mo(dtc)_4$ (right).

Intensity of the S K-edge Spectral Features

The subtractions of the C-S σ* feature and edge jump are displayed in Figure 4.13 for $Cu(dtc)_2$, $Ni(dtc)_2$, $Fe(dtc)_3$, and $Mo(dtc)_4$ leaving the M-S and S-C-N π* peaks. Since the π* peaks are more resolved than the M-S bonds for $Ni(dtc)_2$, $Fe(dtc)_3$, and $Mo(dtc)_4$ spectra, they are displayed in Figure 4.13 for clarity of the fits. Additionally for $Mo(dtc)_4$, there is M-S character in the rising edge region, but is not discernable from the S-C-N π*

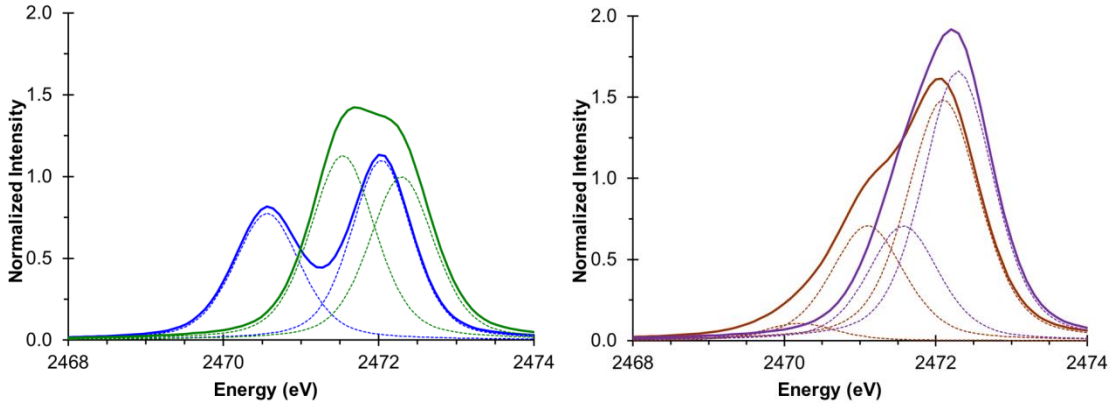


Figure 4.13: The M-S and the π* fits of $Ni(dtc)_2$ (green), $Cu(dtc)_2$ (blue) on the left, $Fe(dtc)_3$ (brown), and $Mo(dtc)_4$ (purple) on the right.

feature. Treatment of the M-S and S-C-N π* features as single transitions gives consistent, reproducible fits for the more resolvable pre-edge and rising edge regions. The details of the average fits of the M-S features are shown in Table 4.5. $Fe(dtc)_3$ and $Mo(dtc)_4$ have multiple M-S peaks due the ill-resolved pre-edge and rising edge features for these compounds. The $Cu(dtc)_2$ and $Ni(dtc)_2$ M-S b_{1g} anti-bonding orbital was fit with one feature with 3% error. The $Fe(dtc)_3$ and $Mo(dtc)_4$ are spectra are more convoluted due to the more complicated MO pictures from Figures 4.8 and 4.9. For $Fe(dtc)_3$, the e_g and t_{2g} orbitals were both fit with single peaks. The fit peaks are separated by 0.9 eV, or

Table 4.5: Numerical fitting results corresponding to pre-edge features from Figure 4.13.

Complex	E, eV	A, -	FWHM	D_0, eV
$Cu(dtc)_2$	2470.6	0.78	0.99	0.98±0.03
$Ni(dtc)_2$	2471.5	1.13	0.98	1.42±0.03
$Fe(dtc)_3$	2470.2	0.11	1.05	0.14±0.04
	2471.1	0.72	1.08	0.99±0.09
$Mo(dtc)_4$	2471.6	0.81	1.08	1.23±0.29
	2472.3	1.59	1.04	1.99±0.30

7,300 cm^{-1} for $Fe(dtc)_3$. This is approximately half the 10 Dq splitting than reported in literature for the mixed spin system.[180] This is due to the mix spin system and also the ill-resolved features of the pre-edge/rising edge features, which increases the error in the fitting. The $Mo(dtc)_4$ MO picture is complicated since the Mo-S σ bonds are close in energy to the Mo-dtc π bonds from back donation. Two peaks were used to fit the broad pre-edge feature for $Mo(dtc)_4$. The error in the fitting of $Mo(dtc)_4$ was much higher than the other spectra due to the small energy gap of the MOs.

In order to determine a dipole integral for any dtc complex, it was necessary to calculate the free-ligand based dipole integral. Using Equation 4.2, an I^L value for Na(dtc) of 17.0 eV was derived. The energy shift between Cu(II) complex and free ligand edge positions are between 0.1 and 0.8 eV due to the slightly different S environments. Since there are two local maxima in the 1st derivative plot in Figure 4.2B, the average of the complex dipole integrals was used to arrive at a dipole integral of 27.8 eV. Moving onto the other complexes, the edge shifts are 0.6, 0.6, and 0.9 eV for the Ni, Fe(III), and Mo complexes, respectively. The slope and the free ligand dipole integral was applied to determine the Ni, Cu, Fe, and Mo complex dipole integrals, which are listed in Table 4.6

along with the S 3p per hole character for all the complexes. The error in the S 3p covalency was 0.03 for $Cu(dtc)_2$. Moving to a multiple hole systems, the per hole covalency error decreases, except for $Mo(dtc)_4$. The large uncertainty associated with $Mo(dtc)_4$ was due to the propagation of the error from fitting the rising edge feature. Due to the lack of pre-edge features and the lack of resolving power of S K-edge, there is a large uncertainty in determining the per hole covalency for $Fe(dtc)_3$ and $Mo(dtc)_4$. Therefore, the per hole covalency was determined for the two lowest energy fit peaks for the Fe and Mo dtc complexes. For $Fe(dtc)_3$, these features correspond to the splitting of the d-orbitals in a mix spin system. Additionally, the two lowest energy peaks correspond to the Mo d-orbitals and the low lying ligand π^* orbitals in $Mo(dtc)_4$. Since Gaussian only produced seven of the eight orbitals expected for the rising edge feature for $Mo(dtc)_4$, 14 holes $Mo(dtc)_4$ were considered for the per hole covalency in Table 4.6. The S character of the per hole average was also shown in Table 4.6 using AIM/B3LYP/def2-TZVP for $Ni(dtc)_2$, $Fe(dtc)_3$, and $Mo(dtc)_4$ and AIM/ B(38HF)LYP /def2-TZVP for $Cu(dtc)_2$. Since $Fe(dtc)_3$ has a mix spin system, the weighted average according to percentages of low spin versus high spin S contribution in the Fe d-orbitals was calculated.

Table 4.6: Quantitative Analysis of Cu(II), Ni(II), Fe(III) and Mo(IV) dtc compounds.

Complex	D_0, eV	# of Absorbers	# of Holes	I^C, eV	Total S 3p per hole, e^-	DFT Total S per hole, e^-
$Cu(dtc)_2$	0.98±0.03	4	1	27.8	0.47±0.03	0.49**
$Ni(dtc)_2$	1.42±0.03	4	2	31.4	0.27±0.01	0.47*
$Fe(dtc)_3$	1.12±0.08	6	5	31.4	0.13±0.01	0.13*
$Mo(dtc)_4$	3.22±0.17	8	14	38.5	0.14±0.03	0.40*

*B3LYP/def2-TZVP
**B(38HF)LYP/def2-TZVP

Discussion

$Zn_2(dtc)_4$

Zn(II) dtc does not exhibit a pre-edge feature in ligand K-edge spectroscopy. Zn(II) complexes are typically thought as the free ligand spectrum when compared to their Cu(II) analogues. The dtc ligand bonds to the Zn 4s and 4p orbitals, which leads to its geometric structure. There are two local maxima in the first derivative plot in Figure 4.4B of 2474.0 and 2475.0 eV for $Zn_2(dtc)_4$. This indicates that there is more than one S environment. In addition, the local maximum at 2474.0 eV is the lowest edge jump in this dtc series. The shift to lower energy is a result of the lowest Z_{eff} of the dtc complexes. The differences in the coordination geometry of $Cu(dtc)_2$ and $Zn_2(dtc)_4$ are reflected in the gap between the S-C-N π^* and the S-C σ^* peaks and thus the $Zn_2(dtc)_4$ cannot be used as a free ligand spectrum.

$Cu(dtc)_2$

The $Cu(dtc)_2$ complex electronic structure has been studied extensively in literature and now it was analyzed with S K-edge spectroscopy. $Cu(dtc)_2$ crystallizes as a dimer similar to $Zn_2(dtc)_4$, but the distance between the two monomers is larger for $Cu(dtc)_2$. According to the EPR and DFT results, the electron density is donated to the Cu(II) center, and not between the two monomers. Therefore, there is strong σ donation to the Cu(II) site which was quantified by EPR 0.47 e^- per hole. Coupling the area of the S K-edge pre-edge feature with previous EPR data, the EPR based dipole integral was 25.0 eV using Equation 4.1. This compound was crucial to develop dipole integral

expressions for N containing sulfur ligands by Queen *et al*.[93] The $Cu(dtc)_2$ dimer has two local maxima in the first derivative plot similar to $Zn_2(dtc)_4$. The first maximum at 2474.4 eV has more electron density on the sulfurs, resulting in a lower Z_{eff} than the second maximum at 2475.1 eV. Applying Equations 4.2-4.4 and using the average of the two edge jumps, a complex dipole integral of 27.8 eV was derived. The covalency of b_{1g} from this complex dipole integral was 0.42 e^- per hole, which is reasonable considering our S K-edge interpretation. However, the complex dipole integral was averaged for $\Delta E^{L\rightarrow m}$ of 0.1 and 0.8 eV. If one of these dipole integrals were used, the dipole integral would be too high or too low to reproduce the EPR covalency. Using the average of the local maxima reliably reproduced the EPR covalency. This covalency is a demonstration of the classical, yet very covalent bonding description.

There are other interpretations of S K-edge used to extract the S 3p mixing in XAS. When we apply the lower curve from Figure 4C of Queen *et al.* we get a per hole covalency value of 0.66 e^-. This shows that this lower curve cannot be applied to S ligands that contain a nitrogen atom since an inverted bonding picture is not chemically feasible. Applying the linear curve from Queen *et al.*,[93] a very unreasonable covalency of 1.98 e^- was derived. The ground state electronic structure was also studied computationally where the B(38HF)LYP/def2-TZVP functional reproduced the EPR covalency with AIM population analysis in Gaussian. This validates the use of equations 4.2-4.4 in obtaining accurate dipole integral for dtc ligands.

Ni(dtc)$_2$

The Ni(dtc)$_2$ complex exhibits a similar electronic picture to the Cu(dtc)$_2$ complex. However, this complex is not ferromagnetically bonded to another Ni(II) monomer. Ni(dtc)$_2$ has one effective sulfur environment due to its rigid square planar structure with only one edge jump. This is seen in the first derivative plot in Figure 4.2B with a clear edge position at 2474.9 eV. The pre-edge feature exhibited by Ni(dtc)$_2$ is higher in energy than Cu(dtc)$_2$. This is supported by the MO diagrams in Figures 4.6 and 4.7. Since Cu(dtc)$_2$ contains an additional electron, it undergoes Jahn-Teller distortion, lowering the energy of the SUMO by 0.9 eV. Due to the increase in energy of Ni-S peak with respect to the Cu-S peak, the π^* is barely resolvable for the Ni(dtc)$_2$ complex. When the π^* is treated as a single excitation when fitting, the Ni-S does not vary substantially. Our group published a fit of Ni(dtc)$_2$ that was obtained by just subtracting the C-S σ^* and the edge jump, which resulted in larger a Ni-S peak and a small π^* that is not chemically feasible as supported by Table 4.5.[93] The pre-edge feature is expected to be more intense than Cu(dtc)$_2$ because the S K-edge is probing two holes in the b_{1g} orbital. The 0.27 e^- S/per hole covalency was not supported by any functionals tested using the AIM population analysis of its ground state. Ni(II) compounds have traditionally been problematic to model their computational ground state electronic structure.[55,190,191]

$Fe_2(dtc)_4$

The $Fe_2(dtc)_4$ complex has a similar structure as $Zn_2(dtc)_4$, but does have four holes on each Fe(II) metal. This high spin complex contains an irresolvable pre-edge feature jammed against the S-C-N π^* feature as seen in Figure 4.4. This bonding motif is

consistent with Fe(II)-S(thiolate)$_4$ complex described in literature where it's pre-edge is not resolvable because it is smeared into the rising edge.[88] The Fe(II) complex is expected to have less S 3p mixing than the Fe(III) complex. The radius of Fe(II) is larger than Fe(III) resulting in larger metal-ligand distances (Figure 4.1 and Table 4.2), and therefore, weaker bonding interactions. The edge position for this complex is located at 2475.0 eV, which is represented as a broad peak in the first derivative plot in Figure 4.4B. The broad peak most likely represents the three different sulfur environments in this complex.

Fe(dtc)$_3$

The Fe(dtc)$_3$ complex has a different bonding picture than the other compounds described above. It has two shoulders just below the S-C-N π^* peak, which corresponds to the t_{2g} and e_g orbitals assuming O_h symmetry of the S and Fe atoms. The separation of the two fit peaks corresponding the S mixed Fe d-orbitals is 0.9 eV, which represents the 10 Dq splitting observed with S K-edge XAS. This value is significantly less than the UV-Vis value of 1.95 eV for the mixed spin system,[180] which could be due to the resolving power of the S K-edge. The determined 57% high spin and 43% low spin states[180] were used to determine a weighted average of the experiment per hole S covalency of 0.13 e^- per hole. The weighted average of the mix spin Fe(dtc)$_3$ TD-DFT reproduced the shoulders below the S-C-N π^* feature in the simulation in Figure 4.11. The B3LYP/def2-TZVP/AIM population analysis in Figure 4.10 shows that the three t_{2g} orbitals and two e_g orbitals have similar S character in both spin systems. Not surprisingly, the S character in the low spin system is less than the high spin state due to

the longer bond lengths associated with the low spin state. The 0.13 e^- per hole covalency was substantiated by the weighted average of the high spin and low spin $Fe(dtc)_3$ using the B3LYP/def2-TZVP/AIM population analysis. The S character in the Fe-S bond has low covalency and high ionic character in this complex.

$\underline{Mo(dtc)_4}$

The $Mo(dtc)_4$ complex also has a complicated bonding picture. The pre-edge feature consists of both the Mo-S and S-C-N π* features. This is supported by the TD-DFT simulation, which reproduced the pre-edge feature with both the Mo-S and S-C-N π* under the same peak. Using the second derivative spectrum in Figure 4.3, the energy positions of these features were resolved at 2471.6 and 2472.3 eV. There was variability in the peak intensities under the pre-edge feature accounting for the larger error associated with the fits. Additionally, there was symmetry mixing of the S-C-N π* with the Mo-S bonding in the same orbitals. This is very evident in the MO diagram in Figure 4.9. In order to extract the amount of S mixed into the Mo 4 d-orbitals, the total area of Mo-S and S-C-N π* features and the numbers of total holes were taken into account in the per hole covalency. Similarly to $Ni(dtc)_2$, the 0.14 e^- per hole S character was substantially lower than any of the functionals tested using the AIM population analysis. All the functionals produced a higher covalent picture than the experimental interpretation. The developed transition dipole integral of 38.5 eV for $Mo(dtc)_4$ determined from the edge position of 2475.1 eV, has the largest transition dipole integral in this dtc series. The large dipole integral is the reason for the low experimental covalent picture. The high Z_{eff} is due to donating electron density to four vacant orbitals into the

Mo 4d-orbitals. Due to the low covalency, the ionic interactions are the dominant force holding this compound together based on our interpretation of the $Mo(dtc)_4$ dipole integral.

Concluding Remarks

We applied a new dipole integral that is applicable to dialkyldithiocarbamate ligands for the S K-edge whose bonding parameters were determined by complex transition dipole integrals first described in Queen *et al*.[93] Using determined complex transition dipole integrals, a wide variety of dtc transition metal complexes with vacant d-orbitals can be investigated at the S K-edge to determine their ground state electronic structures. The more holes the metal contains in its d-manifold, the more electron density is donated, but the covalency decreases as a result. The bonding picture of homoleptic dtc compounds range from simple to very complicated electronic and geometric complexes depending on the transition metal and its oxidation state. In addition to the covalent interactions, the ionic attractions are also important in the stability of these complexes. All of the dtc complexes exhibit classical, non-inverted bonding with these transition metals. These dtc systems are best modeled typically with the B3LYP functional with the exception of Cu(II) dtc complexes, where the best results are obtained with 38% HF mixing B88 exchange functional. The dtc ligand possesses very unique properties because it can stabilize high oxidation state metals that are generally unstable due to back bonding into S-C-N $\pi*$ network. Due to the presence of a nearby N atom, the intensities of the ligand K-edge spectrum are more intense than S containing ligands with C and H

atoms. Therefore, a larger dipole integral is needed to compensate for the larger area of the pre-edge features when studied with S K-edge XAS.[93]

The dtc ligands' ability to bind many transition metals makes it an ideal candidate for waste water treatment.[192] Addition of halogens can be added either by photolysis or haloalkanes, aliphatic ammines, and nitrosyl radicals are also known to bind to dtc complexes.[152] Dtc ligands can be removed through oxidation to form a disulfide bond between two dtc ligands yielding tetraethylthiuram disulfide.[152] This shows the robustness of dtc ligands, which relates back to its electronic structure. The Na(dtc) ligand is a unique S ligand in that it contains two sulfurs, but only a minus one charge. This means it is more oxidized than electron rich sulfides, dithiolates, and thiolates. This promotes the formation of stable complexes with transition metals, even at high oxidation states.[93] In fact it can bind Fe-S biomimetic clusters of nitrogenase at high oxidation states that are not feasible with thiolate ligands to stabilize single cubane clusters.[44]

CHAPTER 5

ELECTRONIC STRUCTURE DETERMINATION OF COPPER AND SODIUM DIETHYLDITHIOCARBAMATE COMPLEXES USING S K-EDGE X-RAY ABSORPTION SPECTROSCOPY AND DENSITY FUNCTIONAL THEORY

Introduction

For over three decades X-ray absorption spectroscopy (XAS) has been employed to analyze quantitatively the electronic structure of bioinorganic systems, biomimetic analogues, and organometallic catalysts using metal K, L_{III} and L_{II}-edges, and ligand K-edge. XAS is a reliable technique for probing ground state electronic structure from core orbital excitations. One of the most studied elements with ligand K-edge XAS is sulfur. XAS is the only technique available that can provide comparable electronic and geometric structural information for sulfur based ligands. The X-ray absorption near-edge structure (XANES) is well defined in literature for sulfides,[87] thiolates,[88] dithiolenes,[62] MetSO and $MetSO_2$ ligands.[154,155] A common sulfur based ligand that is not well defined in the XANES region is the family of dialkyldithiocarbamates. Diethyldithiocarbamate (dtc) ligands are bidentate and their formal charge lies between -1 and 0 of thiolates and thioethers respectively.

The intensity of features probed at the S K-edge in XAS measurements is proportional to the amount of S character contributing to each unoccupied or semi-unoccupied molecular orbital (SUMO) of the chelated metal center. Predominately, the sulfur character originates from the S 3p orbitals. Equation 5.1 expresses the relationship

of the S 3p character (α^2), to the area of the XANES features (D_0). This relationship is also dependent on the number of holes (h) in the unoccupied orbital(s), the number of absorbing atoms (n), the complex transition dipole integral (I(S1s→3p), eV/hole), and the1/3 ratio corresponds to the x, y, and z dependence of the transition dipole integral expression.

$$D_0 = \frac{1}{3}\alpha^2 \frac{h}{n} I(S1s \rightarrow 3p) \quad (5.1)$$

To determine the transition dipole integrals, supplementary experimental data describing the electronic structure is needed. For example, the super hyperfine structure was analyzed with electron paramagnetic resonance (EPR) for bis(creatininium)$CuC1_4$ at the Cl K-edge when dipole integrals were first being developed.[92] The experimentally determined Cl covalency was applied to the intensity of pre-edge feature in the Cl K-edge.[92] Once this dipole integral was determined, it was applied to extract the Cl 3p character of transition metal chloride complexes.[157,158] Similarly, transition dipole integrals were developed for S^{2-}, SR^-, and dithiolenes using X-ray photoelectron spectroscopy[87] and EPR.[87,92,156]

Recently, the interpretation of the sulfur transition dipole integrals was expanded to include the dtc ligand.[93] The paramagnetic $Cu(dtc)_2$ complex was examined using the S K-edge to study the sigma donation of the dtc ligand into the Cu^{2+} $3d_{xy}$ SUMO. The bonding parameters of $Cu(dtc)_2$ have been studied extensively using EPR.[159-163] The spin on the Cu^{2+} center in $Cu(dtc)_2$ measured from the Cu hyperfine coupling was 0.54±0.03.[159-161] This corresponds to 48% Cu 3d and 47% S 3p character in the SUMO. The corresponding transition dipole integral from the 47% S 3p character, was

incorporated as an additional data point in a recent study of Ni(II)S_4 complexes for the development of Equations 5.2-5.4.[93] Utilizing Equation 5.2-5.4, transition dipole integrals can now be determined without the aid of other experimental data. These equations are second order polynomials due to the Bohr and Moseley models that consider shielding, and therefore, effective nuclear charge.[193] The effective nuclear charge is proportional to the binding energies of both the donor core and acceptor valence electrons.[93] The slope in Equation 5.2 refers to the tangential line to the polynomial in regards to the difference between the edge position of the free ligand and sodium sulfide. The ligand transition dipole integral, I^L, in Equation 5.3 is also calculated in reference to S^{2-} anion and the free ligand. The complex dipole integral (I^C) in Equation 5.4 is dependent on Equations 5.2 and 5.3, in addition to, the energy difference of the edge positions of the free ligand and complexed ligand.

$$\text{slope}=3.2(E_0{}^{L}-E_0{}^{S2-})^2+2.3 \quad (5.2)$$

$$I^L=0.37(E_0{}^{L}-E_0{}^{S2-})^2+14.5\text{eV} \quad (5.3)$$

$$I^C=I^L+\text{slope}(\Delta E^{L\rightarrow m}) \quad (5.4)$$

The method for normalization of the XAS K-edge spectra is discussed extensively in literature.[45,189,194] The procedure includes 2nd order background subtraction of the raw data, followed by a constrained fit of a spline function to the post-edge region, which is used to normalize the spectrum to 1.00 at 2490 eV. However, this method of normalization can artificially inflate the XANES region resulting in larger peak areas and thus larger calculated S contributions to the bonding character. Therefore, we explored two additional normalization methods in order to test the sensitivity of our findings to

those when we used traditional normalization methods prescribed by the literature. One method is a quick normalization that simply shifts and scales the data to 0 and 1 at defined points without conducting a background subtraction. This approach minimizes the effect of background subtraction of the raw data. The second method employed performs a background subtraction of the shifted and scaled data using an arctangent function to simulate the edge jump for the photoelectron.

$Cu(dtc)_2$ complexes have been the subjected to many studies of its geometric and electronic structure, making it an excellent candidate for the development and understanding of the dtc ligand at the S K-edge due to the paramagnetic nature of the Cu(II) center. $Cu(dtc)_2$ is monomeric in solution but crystallizes as a dimer by weak ferromagnetic interactions.[178] Figure 5.1 shows that the dimerization of $Cu(dtc)_2$ results in slight deviation of the Cu(II) ion from the plane of the four sulfurs.[153] Electronic structure information such as d-orbital splitting, and orbital energies were described in literature using UV-Vis, angular overlap method,[195,196] X-ray photoelectron spectroscopy,[188] and density functional theory (DFT).[192] Orbital coefficients were examined not only with EPR, but with Cu K-edge XAS,[193] and extend Hückel MO calculations.[197] The complex dipole integral, I^C, was recently developed using Equation 5.1 for the S K-edge XAS based on the coefficient for the $3d_{xy}$ orbital I^C for $Cu(dtc)_2$.[93]

Using both established and alternative data analysis methods and quantitative procedures to measure uncertainty of fit areas for ligand XAS, we describe the I^C for the $Cu\text{-}S_4$ d_{xy} anti-bonding orbital. Furthermore, the I^C calculated for $Cu(dtc)_2$ was then used to obtain the corresponding sodium diethyldithiocarbamate (Na(dtc)) ligand transition

dipole integral (I^L). The resulting transition dipole integrals were applied to the quantification of the S 3p character in the rising edge spectra of both $Cu(dtc)_2$ and Na(dtc). In order to determine what effects of different detectors at various beamlines contributed to the data subsequent analysis, we collected S K-edge data at the Stanford Synchrotron Radiation Lightsource (SSRL), Advanced Light Source (ALS), the Canadian Light Source (CLS), and the Synchrotron Radiation Center (SRC). A similar approach was utilized for $[PdCl_4]^{2-}$, $[PdCl_6]^{2-}$, and $PdCl_2$ complexes where different complex dipole integrals were needed for the interpretation of the Cl K-edge.[194]

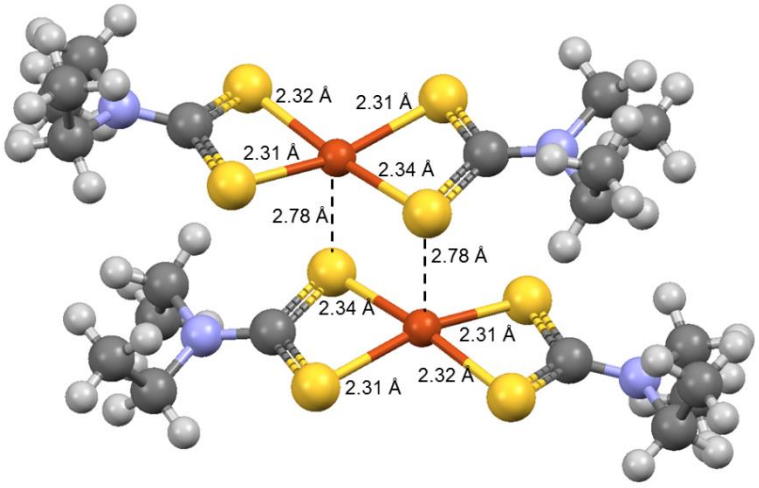


Figure 5.1: The crystal structure of $Cu(dtc)_2$ dimer from the Cambridge Crystallographic Database Code CETCAM12.

Experimental Techniques and Computational Methods

Sample Preparation

Na(dtc) was purchased from Fisher Scientific and dehydrated under vacuum for 3 hours. This procedure led to the OH stretch in the FT-IR spectrum at 3000-3700 cm^{-1} disappearing and the resulting material was assumed to be suitably pure. $Na_2S_2O_3 \bullet 5H_2O$

was purchased from Sigma Aldrich and used without further modification. $Cu(dtc)_2$ was synthesized following a procedure from literature.[188]

Sulfur K-edge X-ray Absorption Spectroscopy

SSRL. The S K-edge X-ray absorption spectra were measured at beamline 4-3 under storage ring (SPEAR 3) condition of 300-80 mA current and 3 GeV energy. BL 4-3 has a 20-pole, 2.0 T Wiggler beamline equipped with a liquid N_2 cooled Si(111) double-crystal monochromator. All XAS measurements were carried out at room temperature and the samples were prepared in a nitrogen or argon gas filled gloveboxes. The solid samples were ground with boron nitride and pasted onto a Kapton tape. Any excess sample was scraped off from the tape to minimize the distortion of peak intensities due to self-absorption effects. The sample cell was protected with a few μm thick Mylar polypropylene window to eliminate possible sample degradation due to oxidation or exposure to moisture. The beamline was optimized to maximize incident beam intensity at the high energy end of the scan. The data presented were either collected with partial electron yield or fluorescence detection methods. Partial electron yield was collected using a multi-element Lytle (EXAFS Co) detector equipped with nickel grid at a 45 V collector potential. Fluorescence detection methods utilized were the Lytle or a nitrogen gas purged and a passivated implanted planar silicon detector (PIPS, CANBERRA).

CLS. S K-edge measurements were collected on Soft X-ray Microcharacterization Beamline (SXRMB) 06B1-1 at CLS. This facility's beam current was 250-130 mA with a 2.9 GeV storage ring energy. The SXRMB beamline utilizes a water cooled Si(111) or

InSb(111) double crystal monochromator with a collimating mirror up field from the monochromator and a toroidal focusing mirror. The measurements were conducted at room temperature with all the samples prepared in a nitrogen filled glovebag. The solid samples were ground with boron nitride and pasted onto carbon tape. Silicon tape was not used because the Kα emission from silicon saturated the detector (>30% detector deadtime) during fluorescence measurements. Excess sample was scraped off from the tape to minimize self-absorption. The sample cell was protected with a polypropylene window. The data was collected using total electron yield, Kα, and total fluorescence yield detection methods. Total electron yield was collected in ultrahigh vacuum chamber (UHV) with a positive bias. The fluorescence data presented was collected with a four element silicon drift detector in a helium purged or UHV sample chamber.

ALS. Beamline 9.3.1 was utilized for the S K-edge data. The beam current was 500 mA from a 1.9 GeV storage ring. The beamline utilizes a Si(III) double crystal monochromator. Fluorescence and direct current measurements were carried out at room temperature for sample that were prepared in air. The samples were mixed with boron nitride and pasted onto a carbon tape, while excess sample was scraped off. Direct current and fluorescence measurements were conducted in UHV and collected simultaneously. Direct current was collected using a positive bias. Fluorescence measurements were collected using a Si photodiode detector. Photo-damage was observed for two different collections of the same sample. For the first data collection, the data was extrapolated backwards to time zero using a linear method. In the second data collection, the beam was spot moved after each scan to eliminate radiation damage in the XANES region.

SRC. All XAS measurements were carried out at beamline 093 at SRC with an Aladdin storage ring energy of 800 MeV and 250 mA current. The monochromator was an air cooled InSb(111), with a focusing mirror down field from the monochromator. The measurements were conducted at room temperature for sample cells that were prepared in air, ground with boron nitride and pasted onto carbon tape. Direct current was collected using a positive bias, and fluorescence measurements were collected using a micro-channel plate (MCP) detector simultaneously in UHV.

XAS Data Normalization, Fitting, and Error Analysis

All the S K-edge data averaged and calibrated to sodium thiosulfate pentahydrate at 2472.02 eV. The following three normalization procedures were utilized to determine the differences in the normalized data. The error introduced by data reduction and normalization procedures was at most 3% in the peak amplitudes.[189]

Shift and Scale (1). One method of normalization used for all calibrated spectra by setting the x-axis to zero at 2465 eV and scaling the data to one at 2480 eV. This normalization technique is method 1. The benefit of the shift and scale normalization is that it allows for quick and consistent normalization of all data of the XANES region. In addition, it shows how the pre-edge feature features varies with detector type, and the post-edge region is consistent with all scans from different detectors up to 2480 eV. The drawback to this method is the intensities of the pre-edge and rising edge features are smaller and cannot directly be compared to complexes normalized using different methods.

Arctangent Fit to Shift and Scale (2). Normalization technique 2 is fitting an arctangent to 1 of the shift and scaled data. Figure 5.2 illustrates an example of how data are manipulated with the background correction and normalization procedures. A second order polynomial was fit to the subtracted data points before and after the XANES region. The data were subtracted from the second order polynomial. The line shape of the arctangent function was allowed to vary between 0.8 and 1.2, the approximate shape of the XAS data. Due to the curvature of the arctangent function at the pre-edge region, a linear fit is needed to keep the pre-edge from rising too soon. The linear fit of the

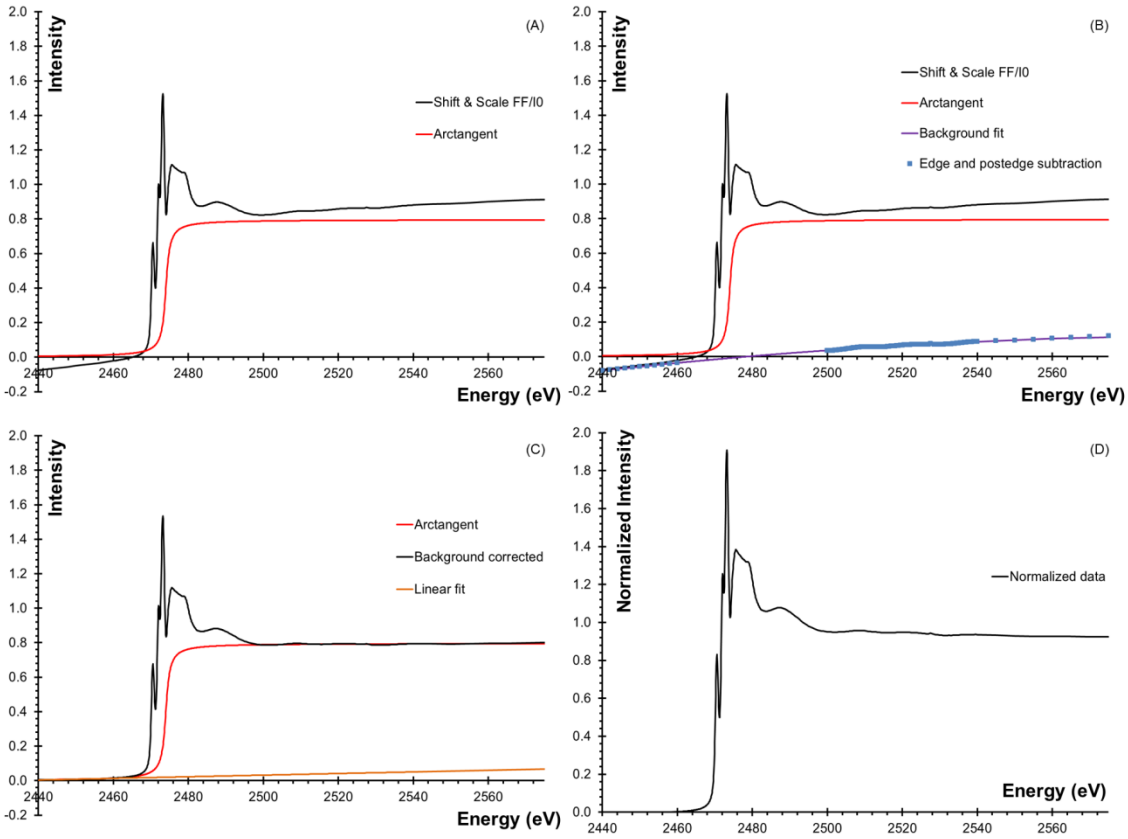


Figure 5.2: Data treatment 2 by fitting an arctangent function to shift and scale data (A), subtracting the data (B), subtracting pre-edge linear fit (C), and normalization (D).

pre-edge region lowers the EXAFS region slightly and the spectrum is normalized to 1 at the last data point. The criterion for acceptable normalization was determined by the maximum value given by the least squares fit of the 2nd order fit of the subtracted data as shown in Figure 5.2B. Unlike the shift and scale normalization, the pre-edge features become similar when comparing the different detectors. Both the S-C-N π^* and the post edge-regions start to vary between the various detectors.

Automated Data Reduction Protocol (ADRP, 3). ADRP consists of three steps to analyze the XAS data: (1) baseline subtraction, (2) background correction, and (3) normalization. The baseline subtraction and background subtraction are performed in a single step. The background is fit with a smooth second-order polynomial, that is then subtracted from the spectrum. Normalization of the data was accomplished by fitting a flattened second-order polynomial to the post edge region and normalizing the fit spline function to 1.0 at 2490 eV. A detailed analysis using ADRP was conducted earlier and is not discussed further.[189,194] The pre-edge regions from this normalization become very consistent, while the post edge region becomes more divergent between the different detectors.

XANES Fitting. The normalized data were fit using Peak Fit v4.12 (SeaSolve Software, Inc.). The details of all fits are shown in Appendix C. Due to the comprehensive set of spectra for both $Cu(dtc)_2$ and the free ligand salt, we were able to employ the following common protocol: for the anhydrous Na(dtc) salt, the S-C-N π^* absorption was fit as a single transition using the Gaussian+Lorentzian Amplitude

Function in Peak Fit with the Gaussian/Lorentzian mixing ratio held constant at 0.5. The white line containing S-C σ* orbitals, was fit as an envelope of transitions using the Gaussian+Lorentzian Amplitude Function with unrestricted Gaussian/Lorentzian mixing ratio. The edge jump was simulated with a Lorentzian ascending curve was normalized to one. Additionally, a peak fixed at the same energy position as the edge jump was used to account for the S 4p transition and an additional peak was allowed to float at higher energies to compensate for the EXAFS region. The S-C-N π* and S-C σ* features were taken out of the free ligand to obtain a reasonable edge position and utilized as the background for the $Cu(dtc)_2$ complex as a user defined function. The user defined function was used to subtract the edge-jump by aligning the maximum peak of the first derivative spectrum of the complex immediately after the white line. After the subtraction of the free ligand spectrum without the edge jump, the remaining peak intensities were refit. In order to avoid unreasonable distortion and large variations in intensities for ill-resolved features, additional fits were obtained in consecutive steps by gradually allowing for the amplitudes, energy positions, line-widths, and lastly allowing the Gaussian/Lorentzian mixing ratio to deviate from the pseudo-Voigt line. The final fits for the Cu-S peak evaluation were obtained by relaxing all fit parameters except the Gaussian/Lorentzian mixing which were held at 0.5 and the linewidths were shared between the Cu-S σ* and S-C-N π* peaks. The S-C-N π* peak was obtained by locking the Cu-S fitting parameters and fitting the π* with two peaks separated by about 0.3 eV due to the splitting of these orbitals in the ground state. The final fits obtained held the

Gaussian/Lorentzian mixing at 0.5, the linewidths were shared between the two π* peaks, and the energy positions fixed. Only chemically reasonable fits were considered.

Error Analysis. We collected S K-edge data for $Cu(dtc)_2$ at four different beamlines using three different detection methods. An earlier paper of chloropalladium complexes supports the need of different complex transition dipole integrals for data gathered at different beamlines.[194] At SSRL, we collected fluorescence yield (FY) from PIPS and Lytle detectors along with partial electron yield (EY). Two independent collections of $Cu(dtc)_2$ using the PIPS detector were gathered. Data from the two collections showed no real systematic differences. However, there is a substantial difference in the pre-edge areas, where the Lytle FY detection method produced a larger pre-edge area than the PIPS detector. EY is a surface technique that was collected simultaneously with PIPS FY. The amplitude of the pre-edge feature is lower for the EY vs. the PIPS detector. The FY amplitude was lower for the most intense feature than for EY indicating the slight presence of self-absorption. At CLS, total fluorescence yield (TFY), windowed Kα, and total electron yield (TEY) detection methods were utilized. The TFY data and Kα pre-edge intensities were approximately identical and very similar to the PIPS data from SSRL at the pre-edge feature. The signal was saturated at the rising edge and white line features resulting in truncated peaks. The TEY CLS data also experienced this dead time issue. The amplitude of the TEY and FY data gathered at ALS was also very similar to that at CLS and SSRL TEY and FY data, but the linewidths were noticeably smaller. The TEY and FY ALS data collected simultaneously experiences the same trend as the SSRL PIPS and partial EY. The data measured at SRC was less

resolved than SSRL, CLS, and ALS. The poorer resolving power resulted in flattened, and widen features. This distortion leads to larger uncertainty in the interpreted fit areas, and therefore, the per hole covalency (α^2).

The dependence of results on the different normalization techniques was examined in this chapter to assess the consistency of the interpreted fits and extracted covalencies. As shown in overlay in Figures C.2 and C.3 in Appendix C, the post-edge region of the CLS data is not as intense as SSRL using normalization techniques 2 &3. Using normalization 1, the post-edges intensities are not as separated, but the pre-edge features vary. The ALS data follows the same trends as the SSRL data for all three normalization methods. The impact of these normalization techniques are presented in Table 5.3. The uncertainty was calculated by propagating the standard deviations of the EPR, normalizations, and fits using equation 5.1.

Electronic Structure Calculations

Na(dtc) and $Cu(dtc)_2$ structures coordinates were obtained from the Cambridge Crystallographic Database. Density functional calculations were performed using Gaussian09 Revision C.02[102] and ORCA.[140] The 6-31G**,[198-200] a combination of 6-311+G* for Cu(II)[102] and 6-31++G** for S, C, N, H[198,199] atoms is referred to as A, def2-SVP,[106] def2-TZVP,[106] def2-QZVP,[106] and cc-pVTZ-DK[107,108] basis sets from the EMSL basis set exchange[109,110] were utilized for the description of the electronic ground state structure. All electronic structure calculations were performed using the presence of a polarizable dielectric environment (PCM)[127-132] in Gaussian using acetonitrile with a dielectric constant of 35.6 and a solvent radius of 1.81 Å. A conductor like screening

model (COSMO)[128,144-146] was utilized in ORCA for acetonitrile with a dielectric constant of 36.6 and a solvent radius of 1.344 Å. $Cu(dtc)_2$ and Na(dtc) were optimized in Gaussian with a tight convergence criteria using def2-TZVP. $Cu(dtc)_2$ was optimized using B3LYP[53,111] and Na(dtc) was optimized using B(38HF)P86[55-57] functional with acetonitrile PCM to shield the electrostatic interaction between dtc^- and Na^+ ions. Single point calculations were conducted using B3LYP and B(38HF)P86 functionals in both programming packages. Population analysis were conducted in Gaussian using "Atoms-in-Molecules"[64,133-135] from the AIMAll program.[136] Additionally, the hole covalencies were determined by utilizing Mulliken Population Analysis (MPA)[58] and Weinhold's Natural Population Analysis (NPA) in Gaussian.[59] In ORCA, the Löwdin population analysis[60] was utilized as well for the covalencies. Crystallographic coordinates and optimized coordinates are available in Appendix C.

TD-DFT calculations were conducted to simulate the S K-edge pre-edge region of the XAS spectra using ORCA. The S 1s orbitals were localized since they are symmetry equivalent in the $Cu(dtc)_2$ and Na(dtc) molecules. Only excitations computed from the localized S 1s orbital were allowed. The excitation energies were corrected by a constant to line up the calculated spectra with the experimental spectra. The TD-DFT calculations were performed using B3LYP and B(38HF)P86 functionals in ORCA. The RIJCOSX approximation[141-143] for hybrid functionals was employed along with standard integration grids, COSMO, and the Tamm-Dancoff approximation.[201] Only the def2-TZVP basis set was utilized along with the Zero Order Regular Approximation (ZORA), which uses uncontracted Gaussian basis sets.[147,148]

Results and Analysis

Analysis of Energy Positions of XANES Features

Figure 5.3 summarizes the normalized, first and second derivative spectra of the most representative data from $Cu(dtc)_2$ and the free ligand salt, Na(dtc). The free ligand has two distinct features: the S-C-N π^* at the rising edge, and the S-C σ^* located under the white line. When dtc chelates to a Cu(II) ion, the Cu-S σ^* orbital is accessible with S K-edge due to the one hole present in the d-manifold corresponding to the pre-edge feature for $Cu(dtc)_2$. This result corresponds to the Cu $3d_{xy}$ anti-bonding orbital located at 2470.6 eV. The inflection point of the rising edge feature for $Cu(dtc)_2$ is located at the maximum of the first derivative spectrum in Figure 5.3 at 2474.4 eV corresponding to the Z_{eff} of the S 1s core orbital. The free ligand inflection point is slightly reduced at 2474.3 eV. The rising edge feature of $Cu(dtc)_2$ is composed of a S-C-N π^* system that is 1.4 eV higher in energy at 2472.0 eV. This π^* system is perpendicular to the S-C-N plane of the molecule and should contain considerable S 3pz character. The first orbital probed in the free ligand spectrum is also the S-C-N π^* orbital. In the free ligand however, it lies lower in energy at 2471.4 eV. The energy difference of the π^* features is due to the change of Z_{eff} of the S oxidation state when chelated to Cu(II). The white line of the free ligand is located at 2472.9 eV, which corresponds mostly to the S-C σ^* located on the ligand. For $Cu(dtc)_2$, the white line feature is at 2473.2 eV indicating the presence of a more oxidized S compared to its free ligand salt. The smaller ΔE values of the rising edge feature through the first inflection point after the white line for both the free ligand and complex

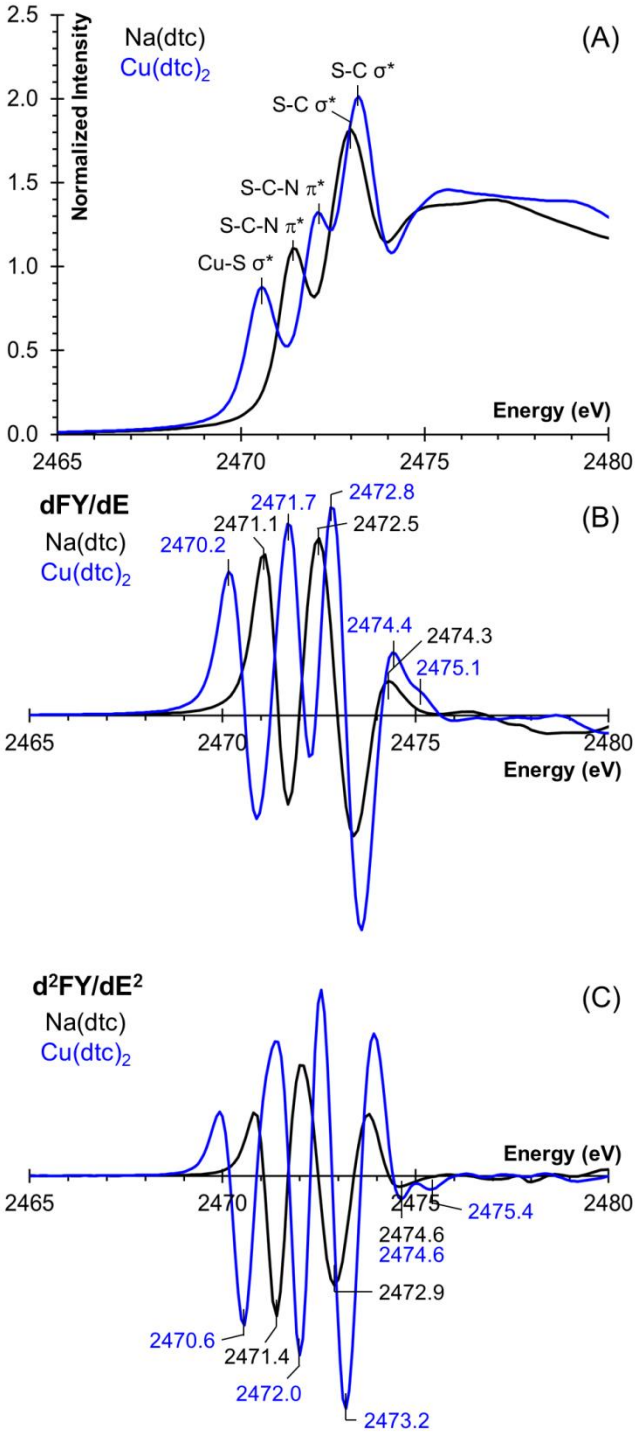


Figure 5.3: Energy position analysis of the XANES region of the normalized S K-edge spectra (A), first derivative spectra (B), and second derivative spectra (C) of Na(dtc) and $Cu(dtc)_2$.

is indicative of the smaller energy spacing between MOs just under the continuum.

Ground State Orbital Composition

DFT was used to model the ground state of $Cu(dtc)_2$ and Na(dtc). Previous studies utilized B3LYP as an appropriate functional for optimization of $Cu(dtc)_2$ monomer.[192] This optimization was carried out to simplify the monomer's electronic structure due to the deviation of the Cu of the four sulfur plane as seen in the crystal structure in Figure 5.1. Past success of modeling Cu based proteins used 38% HF mixing into the BP86 functional.[202] Figure 5.4 displays the expected MOs probed using S K-edge XAS of $Cu(dtc)_2$ and Na(dtc) including the Cu-S dxy, S-C-N π*, and C-S σ* orbitals. The two π*

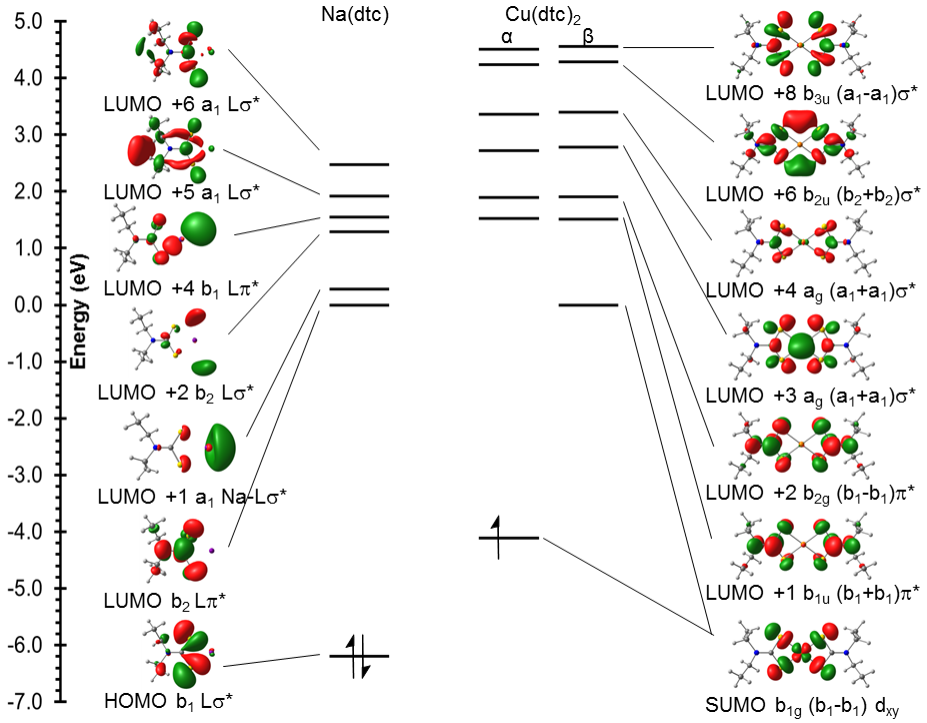


Figure 5.4: MO diagram of Na(dtc) and $Cu(dtc)_2$ generated from B(38HF)P86/def2-TZVP. Mulliken symbols derived assuming C_{2v} symmetry for Na(dtc) and D_{2h} for $Cu(dtc)_2$.

orbitals are split by approximately 0.4 eV and can account for broad rising edge feature for $Cu(dtc)_2$. The S-C σ* feature is composed of four different MOs within about 1.8 eV range. For Na(dtc), there are two π* orbitals separated by approximately 0.6 eV. There are three S-C σ* orbitals probed by XAS that are grouped together in a ~1.2 eV range.

The quantitative ground state analysis was examined for $Cu(dtc)_2$ and Na(dtc) and results are reported in Table 5.1. The incorporation of 38% HF mixing into BP86 was utilized for the D_{4h} $CuCl_4^{2-}$ compound that reproduced the Cl superhyperfine EPR analysis of 29%.[55] The Cu hyperfine spin evaluated from EPR was 0.54±0.03 for $Cu(dtc)_2$.[159-161] The B(38HF)P86 functional does a remarkably good job at reproducing the Cu spin from EPR of about 0.51 using the AIM total spin densities. Using B3LYP/AIM, the Cu spin was calculated at 0.38, which results in a much larger S contribution in the SUMO. A comparison of the first three LUMOs using B(38HF)P86 and the B3LYP functionals are reported in Table 5.1 using AIM, NPA, Mulliken and Löwdin population analyses. The results from the B3LYP functional indicate that the bonds are too covalent for the sulfurs in the SUMO, which also supports the need for more HF mixing. However, the S character is nearly identical for both of these functionals in the LUMO +1 and LUMO +2.

Using the B(38HF)P86 functional, the ground state description of the first three LUMOs for optimized $Cu(dtc)_2$ is shown in Figure 5.5. Figure 5.6 shows similar results optimized for Na(dtc) by varying the number of basis functions. Approximately 95% of the electron density is located in the $3d_{xy}$ orbital of the SUMO. This lowers the amount of Cu contribution to the SUMO. Even though the calculated spin is approximately 0.51, the

Table 5.1: Comparison of S character using B3LYP and B(38HF)P86 functionals using different population analyses of $Cu(dtc)_2$ and Na(dtc).

Functional/ def2-TZVP	Compound	Orbital	AIM	Löwdin	NPA	MPA
B(38HF)P86	$Cu(dtc)_2$	LUMO	0.48	0.45	0.55	0.53
B(38HF)P86	$Cu(dtc)_2$	LUMO +1	0.31	0.31	0.21	0.29
B(38HF)P86	$Cu(dtc)_2$	LUMO +2	0.35	0.37	0.29	0.33
B(38HF)P86	Na(dtc)	LUMO	0.38	0.31	0.26	0.30
B3LYP	$Cu(dtc)_2$	LUMO	0.56	0.53	0.65	0.62
B3LYP	$Cu(dtc)_2$	LUMO +1	0.30	0.31	0.22	0.29
B3LYP	$Cu(dtc)_2$	LUMO +2	0.35	0.36	0.30	0.34
B3LYP	Na(dtc)	LUMO	0.37	0.31	0.27	0.31

Cu character is 0.47 e^- in the SUMO giving about 0.48 e^- S character. To test these results, equivalent calculations were performed with AIM and these additional calculations produced consistent results indicating that AIM is not greatly affected by the basis set selection. Basis set saturation was achieved with the A basis set used earlier in literature for $Cu(dtc)_2$ when compared to def2-QZVP/AIM. The amount of S character increases approximately 5% from LUMO +1 to LUMO +2 π^* system. Löwdin population analysis is affected by the basis set and can vary from def2-QZVP, but generally produces similar results to AIM. NPA is too covalent in the SUMO, and is also not greatly affected by the basis set. Similar to NPA, MPA is too covalent in the SUMO, and it tends to vary between basis sets. All population-based methods show non-negligible Cu contribution in the LUMO +1 orbital corresponding to π back donation into the S-C-N π^* system. At LUMO +2, the amount of Cu character becomes negligible signifying that

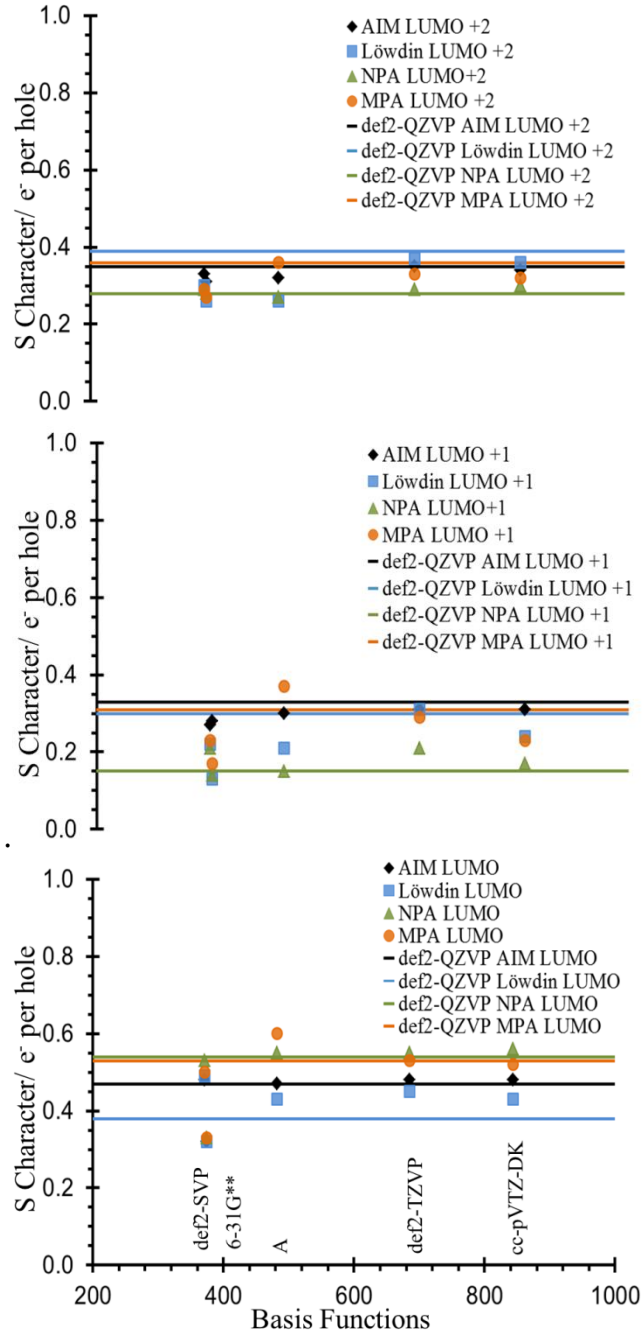


Figure 5.5: Per hole S character in the first three LUMOs of $Cu(dtc)_2$ with different basis sets and population analyses using the B(38HF)P86 functional.

there is no back donation in this orbital. The complexation of dtc ligands to Cu(II) results in a slight decrease of S character in the S-C-N π^* LUMOs compared to the

uncoordinated free ligand salt. The crystal structure produces nearly an identical electronic structure when compared to optimized structure, even though the copper atom deviates from planarity from the four sulfur atoms.

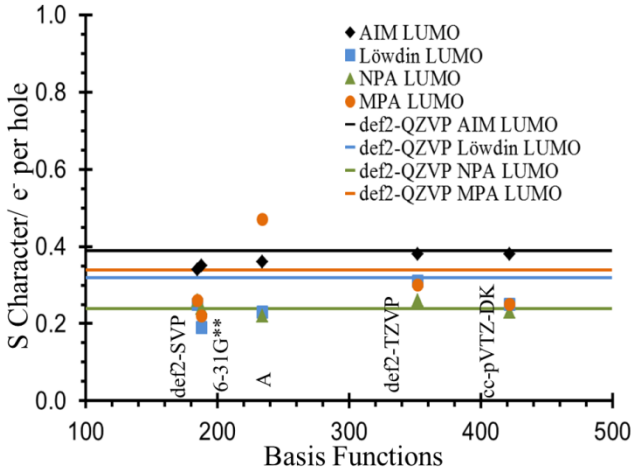


Figure 5.6: Per hole S character in the LUMO of Na(dtc) using different basis sets and population analyses with the B(38HF)P86 functional.

S K-edge measurements probe the ground state electronic structure of the sulfur MOs in covalently bonded systems. Applying line broadening to the AIM analysis and the energy splitting of the calculated MOs, the S K-edge of $Cu(dtc)_2$ and Na(dtc) is reproduced qualitatively in Figure 5.7. For the $Cu(dtc)_2$ AIM simulation, the splitting between the Cu-S and S-C-N π* features is close to the experimental spectrum. However, the S-C-N π* feature is noticeably broader than experimental S K-edge data. The AIM broadening of the S-C σ* feature is also more pronounced than is observed in the experimental spectrum, which is comprised of two intense transitions to the S-C σ* orbitals. For Na(dtc), the rising edge feature is composed of two transitions: one assigned to the S-C-N π* network and the second to a peculiar Na-S bond as seen in Figure 5.7.

The S-C σ* is an envelope of features underneath the white line. The splitting of the rising edge and white line is smaller that of the experimental S K-edge spectrum.

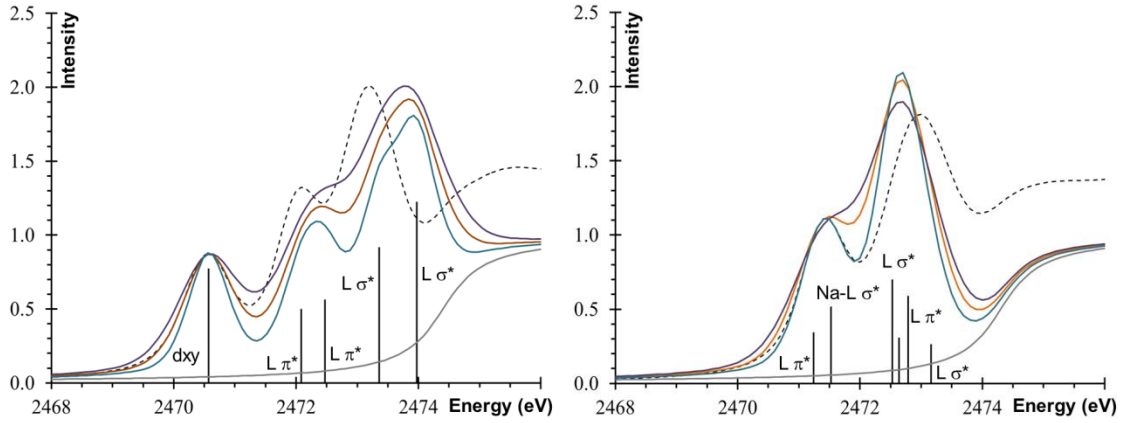


Figure 5.7: Ground state S K-edge simulation of $Cu(dtc)_2$ (left) and Na(dtc) (right) using B(38HF)P86/def2-TZVP/AIM. The line widths range from 0.8 (light blue), 1.0 (brown) and 1.2 (purple) eV. An arctangent function was used to simulate the edge jump at 2474.4 eV.

Excited State Energy Analysis

TD-DFT calculations were performed with $Cu(dtc)_2$ to simulate the S K-edge spectrum with the def2-TZVP basis set. Assuming D_{2h} symmetry, two transitions are allowed from the b_{2u} and b_{3u} S 1s orbitals to the S 3p mixed b_{1g} SUMO. Additionally, there is one allowed symmetry transition to both the b_{1u} and b_{2g} S-C-N π* orbitals from the S 1s orbitals. Figure 5.8 shows the TD-DFT spectrum of 38% HF mixing into the BP86 functional. B(38HF)P86 qualitatively reproduces the ground state electronic

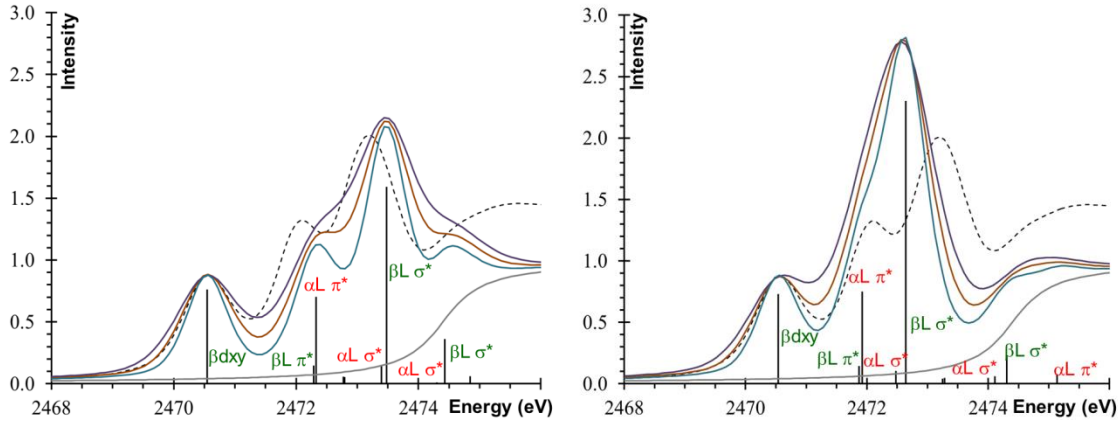


Figure 5.8: TD-DFT S K-edge simulation of $Cu(dtc)_2$ using B3LYP (left) and B(38HF)P86 (right). The line widths vary from 0.8 (light blue), 1.0 (brown) and 1.2 (purple) eV. An arctangent function was used for the edge jump at 2474.4 eV.

structure, but the ΔE of Cu-S transition to the π* and σ* is not reproduced well. The B(30HF)P86 does a satisfactory job at mapping the S K-edge spectrum in Figure C.7 in Appendix C. The two S-C-N π* orbitals become degenerate when the excited state was evaluated. However, there are only two excitations, split by ~0.05 eV, from the spin polarization of the unrestricted system. The S-C-N π* feature corresponds to single excitations to both orbitals (four holes) simultaneously as shown in Table 5.3. Based on the TD-DFT calculations, the white line feature is a combination of many orbitals, including the S-C σ*. Therefore, this feature is not a single transition, but an envelope of transitions.

The dissimilarity of the alpha and beta transitions influences the calculated oscillator strengths in the rising edge and white line features. The pre-edge feature is a pure beta transition to the SUMO of the b_{1g} d_{xy} orbital since the unpaired electron is spin up. The π* orbitals are mostly alpha transitions. This finding suggests that the "trip-doublet" exchange coupling is favored of the excited electron with the unpaired electron

including the core 1s electron.[203] The "trip-doublet" state maximizes the number of states at four resulting in loss of total intensity since the beta transitions only account for two spin states. The white line feature, however, is predominately composed of beta transitions that favor the "sing-doublet" coupling. These effects are only crudely simulated by TD-DFT in spin unrestricted systems and are not fully taken into account in the calculation.[70]

One symmetry allowed transition occurs from the a_2 S 1s orbitals to the S-C-N π* b_2 orbital of Na(dtc), using C_{2v} point group to describe the S-C-N motif with the exclusion of the ethyl groups. This symmetry allowed transition accounts for the pre-edge feature shown in the free ligand spectra. The excited state spectrum was simulated for Na(dtc) using the B(38HF)P86 functional in Figure 5.9. The S-C-N π* rising edge feature is well reproduced and accounts for one orbital. The ΔE of from the π* rising edge to the white line feature is best reproduced by B(30HF)P86 as can be seen in Appendix C (Figure C.7). Although, the simulated S-C σ* intensity is higher than what is

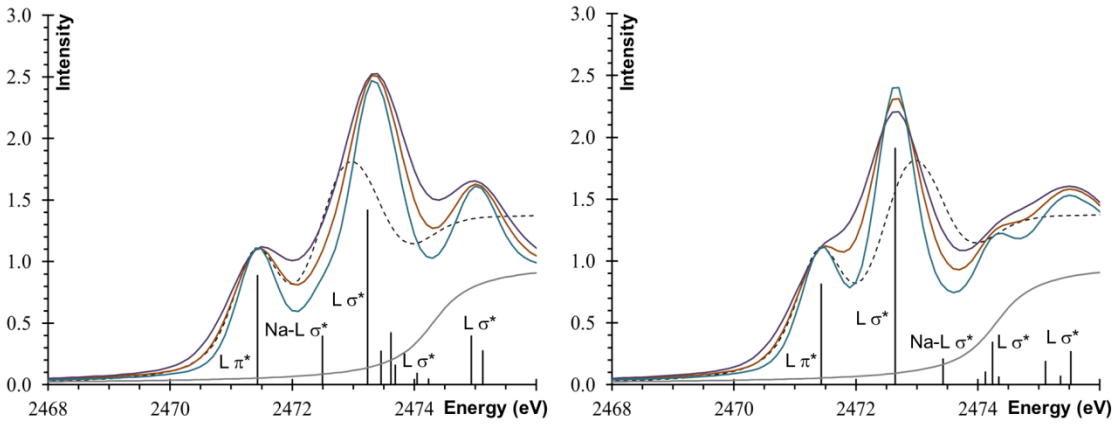


Figure 5.9: Calculated S K-edge of Na(dtc) using B3LYP (left) and B(38HF)P86 (right). The line widths range from 0.8 (light blue), 1.0 (brown), and 1.2 (purple) eV. The edge jump was mimicked with an arctangent function at 2474.3 eV.

experimentally observed. Similarly to $Cu(dtc)_2$ TD-DFT calculations, the white line is a mixture of orbitals and is an envelope of transitions as pictured in Table 5.2. There is a Na-L excitation around the white line, which could be due to limitations of DFT.

Table 5.2. TD-DFT S K-edge excitations, oscillator strengths, excitation energies and LUMOs populated (>10%) of $Cu(dtc)_2$ and Na(dtc).

Compound	Excitation	Energy (eV)	Oscillator Strength ($x10^4$)	LUMO(s)
$Cu(dtc)_2$	1	2448.1	13	0
	2	2449.5	3	1, 2
	3	2449.5	13	1, 2
	4	2450.1	2	3, 8
	5	2450.2	40	3, 8
	6	2450.8	1	1, 2
	7	2450.9	1	1, 2
	8	2451.7	1	3, 4, 6
	9	2451.9	4	3, 4, 6
	10	2452.7	1	4, 6
Na(dtc)	1	2448.9	17	0
	2	2450.1	39	5, 6, 10
	3	2450.9	4	1, 2, 4
	4	2451.6	2	1, 2, 4
	5	2451.7	7	3
	6	2451.8	1	2, 4, 5
	7	2452.6	4	5, 6
	8	2453.0	6	5, 8, 9, 10
	9	2452.8	2	7
	10	2453.5	5	8, 9, 10, 13

Intensity of S K-edge Spectral Features

Table 5.3 summarizes the S K-edge extracted areas, covalencies and transition dipole integrals from differing synchrotron facilities, detection techniques, and normalization methods. Using Equations 5.2-5.4 and assuming a constant slope value of 23.93, the ligand transition dipole integrals were determined from the complex dipole integrals from the set of data collected, and similar values were obtained for I^L as compared to literature (17 eV).[93] $Cu(dtc)_2$ has two local maxima in the first derivative spectrum after the white line, and therefore, the average energy position was utilized as the edge jump. I^L was evaluated by using the ΔE value of 0.45 eV of the inflection points on the rising edge of $Cu(dtc)_2$ and Na(dtc). The areas of the pre-edge and rising edge features are the most sensitive to normalization methods. The normalization technique 1 typically yielded the smallest areas compared to fitting an arctangent function and ADRP. The complex dipole integral is directly proportional to the areas. Normalization 1 produced the smallest transition dipole integrals for both the complex and the free ligand, while normalization 3 gave the largest. Data from different beamline facilities and the detection techniques led to substantial variability in the analysis as seen in Table 5.3. SRC detectors had the least resolvable features resulting in a larger error bars from fitting. ALS, CLS, and SSRL yielded similar results since their spectra were very similar. The fluorescence Lytle detector produced the largest pre-edge feature of 1.13 eV for the Cu-S orbital, yielding a complex transition dipole integral of approximately 30 eV using normalizations 2 and 3. Since the error bars don't deviate much for the different normalization methods, normalization 1 introduces the most uncertainty due to the

Table 5.3: Summary of $Cu(dtc)_2$ normalizations, areas, complex transition dipole integrals, and ligand transition dipole integrals.

Facility	Detector	Norm.	D_0 Cu-S σ*, eV	I^C Cu-S σ*, eV	I^L Cu-S σ*, eV
SSRL	PIPS[a]	1	0.74 ± 0.03	18.61 ± 1.39	7.84 ± 1.39
SSRL	PIPS[a]	2	0.93 ± 0.03	23.31 ± 1.65	12.54 ± 1.65
SSRL	PIPS[a]	3	0.98 ± 0.03	24.57 ± 1.72	13.80 ± 1.72
SSRL	PIPS[b]	1	0.83 ± 0.03	20.80 ± 1.51	10.03 ± 1.51
SSRL	PIPS[b]	2	1.01 ± 0.03	25.36 ± 1.76	14.59 ± 1.76
SSRL	PIPS[b]	3	1.03 ± 0.03	25.88 ± 1.79	15.11 ± 1.79
SSRL	Lytle	1	0.95 ± 0.03	23.82 ± 1.67	13.05 ± 1.67
SSRL	Lytle	2	1.12 ± 0.03	28.12 ± 1.92	17.35 ± 1.92
SSRL	Lytle	3	1.13 ± 0.03	28.39 ± 1.93	17.62 ± 1.93
SSRL	EY	1	0.74 ± 0.03	18.53 ± 1.39	7.76 ± 1.39
SSRL	EY	2	0.93 ± 0.03	23.22 ± 1.65	12.45 ± 1.65
SSRL	EY	3	0.94 ± 0.03	23.56 ± 1.67	12.79 ± 1.67
CLS	Ka	1	0.87 ± 0.03	21.80 ± 1.56	11.03 ± 1.56
CLS	Ka	2	0.93 ± 0.03	23.40 ± 1.65	12.63 ± 1.65
CLS	Ka	3	1.02 ± 0.03	25.61 ± 1.78	14.84 ± 1.78
CLS	TFY	1	0.86 ± 0.03	21.69 ± 1.56	10.92 ± 1.56
CLS	TFY	2	0.93 ± 0.03	23.39 ± 1.65	12.62 ± 1.65
CLS	TFY	3	1.02 ± 0.03	25.50 ± 1.77	14.73 ± 1.77
CLS	TEY	1	0.86 ± 0.03	21.69 ± 1.56	10.92 ± 1.56
CLS	TEY	2	0.93 ± 0.03	23.38 ± 1.65	12.61 ± 1.65
CLS	TEY	3	1.10 ± 0.03	27.72 ± 1.90	16.95 ± 1.90
ALS	FY[c]	1	0.79 ± 0.03	19.94 ± 1.46	9.17 ± 1.46
ALS	FY[c]	2	0.90 ± 0.03	22.49 ± 1.60	11.72 ± 1.60
ALS	FY[c]	3	1.00 ± 0.03	25.08 ± 1.74	14.31 ± 1.74
ALS	FY[d]	1	0.79 ± 0.03	19.91 ± 1.46	9.14 ± 1.46
ALS	FY[d]	2	0.88 ± 0.03	22.13 ± 1.58	11.36 ± 1.58
ALS	FY[d]	3	1.00 ± 0.03	25.04 ± 1.74	14.27 ± 1.74
ALS	TEY	1	0.74 ± 0.03	18.48 ± 1.38	7.71 ± 1.38
ALS	TEY	2	0.83 ± 0.03	20.80 ± 1.51	10.03 ± 1.51
ALS	TEY	3	0.97 ± 0.03	24.28 ± 1.70	13.51 ± 1.70
SRC	FY	1	0.92 ± 0.06	23.12 ± 2.08	12.35 ± 2.08
SRC	FY	2	1.12 ± 0.05	28.01 ± 2.23	17.24 ± 2.23
SRC	FY	3	1.15 ± 0.05	28.98 ± 2.25	18.21 ± 2.25
SRC	TEY	1	0.80 ± 0.05	20.06 ± 1.75	9.29 ± 1.75
SRC	TEY	2	0.97 ± 0.05	24.28 ± 2.02	13.51 ± 2.02
SRC	TEY	3	1.00 ± 0.05	25.23 ± 2.07	14.46 ± 2.07

[a,b]Two independent collections. [c]Exhibited radiation damage and data was extrapolated backwards. [d]Beam position moved after each scan.

smaller areas from the fit features. Consequently, the uncertainty is the smallest for normalization 3. The different detection and normalizations methods yield similar fits of the Cu-S σ* $3d_{xy}$ orbital with a range of approximately 0.2 eV in the fit areas. This wide range indicates that separate dipole integrals are necessary for extracting S contributions from experimental data.

From Equation 5.1, the area (D_0) of the S-C-N π* feature has a larger uncertainty due to a less resolved feature than the Cu-S σ* peak. When linked to the Cu-S σ* feature during fitting procedures, this π* feature had a line width of approximately 1.00 eV. This line width is indicative of a single transition and supports the TD-DFT calculations but not ground state DFT calculations. XAS probes the electronic ground state and the ground state description needs to be considered. Table 5.4 examines the S character of the rising edge S-C-N π* feature of $Cu(dtc)_2$ using SSRL PIPS data. Using the ground state electronic structure determined from DFT, the π* was treated with two peaks split by 0.3 eV. Figure 5.10 shows an example of $Cu(dtc)_2$ fit to the ground state description. The total area was used for the determination of the S character due to the limited resolving power of the rising edge and the presence of the C-S σ* peak. The lower resolving power from the detectors of the S-C-N π* results in slightly higher uncertainty in the fit areas. This error was carried through to the extracted covalencies. Even though the three normalization techniques produce different areas, the amount of sulfur character was not affected due to the proportionality of the rising edge feature versus the pre-edge. The experimental S contribution to the S-C-N π* orbitals was 0.18 e^- per hole, 0.36 e^- per orbital, and 0.72 e^- per molecule. Using the per hole method from the population analyses

with DFT from Figure 5.5 and Table 5.1, approximately half of the electron density is not observed. As discussed above, the alpha electrons transition more often to the S-C-N π* from the S 1s, which would account for the missing electron density. The reason for this phenomenon is not currently understood to us, however, a correction factor 3/2 was implemented for three spin states for the alpha orientation of the electrons and two for the beta. The corrected intensity of π* feature is still less than the B(38HF)P86/def2-TZVP/AIM covalency. The total intensity of the transitions at the S K-edge when spin orbit coupling is present is only partially observed. For the neighboring Mo, Ru, and Pd

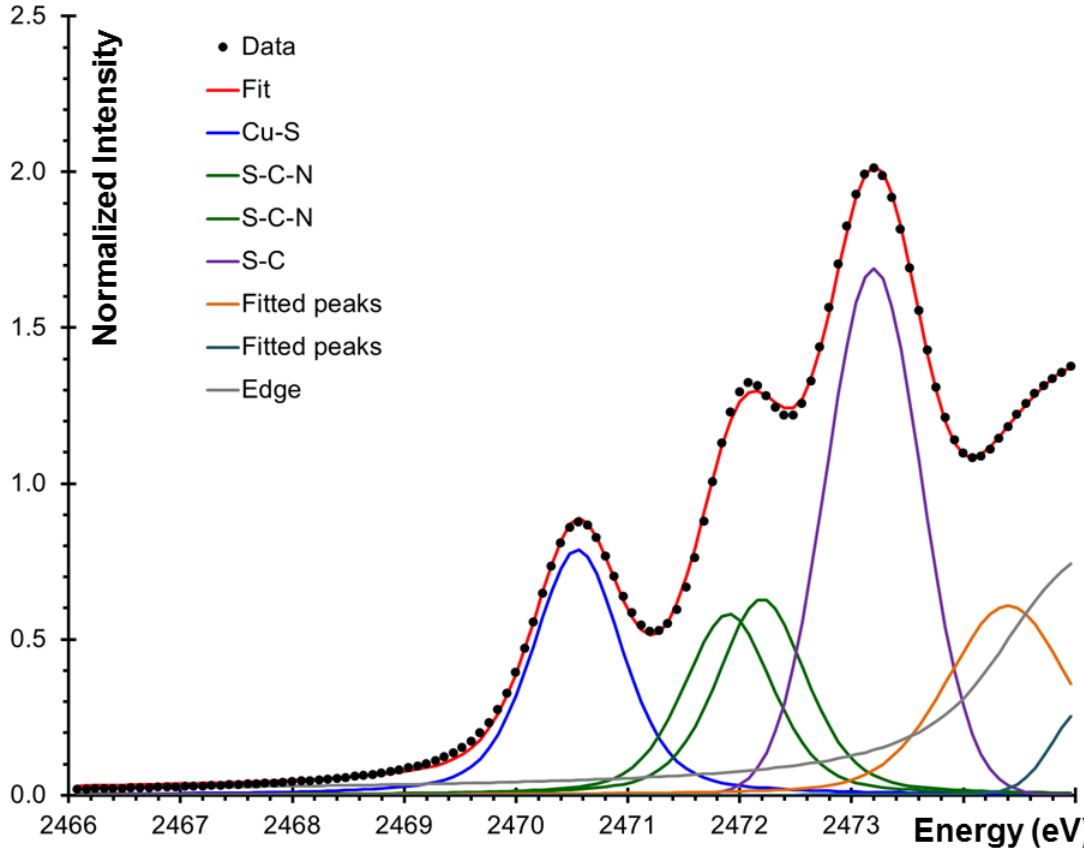


Figure 5.10: Ground state fit of $Cu(dtc)_2$ that utilizes one peak for the Cu-S bond, two fits for the S-C-N π* orbitals, and one fit for the C-S σ*.

L-edges Mo L-edges, the ratio of the L_{III}:L_{II} is approximately 3:2 instead of the theoretical ratio of 2:1. Therefore, the experimentally corrected covalency should be less than the covalency calculated from B(38HF)P86/def2-TZVP/AIM.

Table 5.4. S character per hole of $Cu(dtc)_2$ rising edge π* feature using SSRL PIPS FY.

Norm.	D_0 Cu-S σ*, eV	I^C Cu-S σ*, eV	π* ΣD_0, eV	α^2	α^2 correction[c]
1[a]	0.71 ± 0.03	17.82 ± 1.35	1.09 ± 0.03	0.18 ± 0.02	0.28 ± 0.02
2[a]	0.89 ± 0.03	22.28 ± 1.61	1.36 ± 0.04	0.18 ± 0.01	0.27 ± 0.02
3[a]	0.94 ± 0.03	23.54 ± 1.67	1.43 ± 0.04	0.18 ± 0.01	0.27 ± 0.02
1[b]	0.81 ± 0.03	20.26 ± 1.48	1.16 ± 0.03	0.17 ± 0.01	0.26 ± 0.02
2[b]	1.00 ± 0.03	25.16 ± 1.75	1.47 ± 0.03	0.18 ± 0.01	0.26 ± 0.02
3[b]	1.02 ± 0.03	25.71 ± 1.78	1.50 ± 0.04	0.18 ± 0.01	0.26 ± 0.02

[a,b]Two independent collections. [c]3/2 correction was used (see text).

The Na(dtc) π* feature was evaluated and the results are presented in Table 5.5. Using the I^C determined from the complex dipole integral in equation 5.3, the ligand transition dipole integrals were determined. The experimentally determined S character of the S-C-N π* feature is approximately 0.31 e^- and slightly less than the calculated B(38HF)P86/def2-TZVP/AIM covalency at about 0.38 e^-. However, the experimental covalency is close to the MPA, NPA and Löwdin population analyses. The normalization technique affects the fit area with normalization 1 yielding the lowest, and normalization 3 producing the largest fit areas. The smaller the fit area (D_0) of the rising edge feature, the higher the propagated uncertainty is in the determined S 3p character (α^2) of the S-C-N π* orbital. However, the covalency of the π* feature in the free ligand is influenced by both the fit area of the Cu-S σ* and S-C-N π* peaks of Na(dtc). Therefore, larger uncertainties are associated with this result due to the propagation of error from $Cu(dtc)_2$

to the free ligand. The propagation of this error for the determination of the S character is about 10-15%. The limited resolving power at SRC does not yield chemically reasonable fits and is not considered in Table 5.5. The SSRL and CLS facilities and detectors produced similar areas for their respective normalizations.

Table 5.5: Summary of Na(dtc) normalizations, areas, and per hole covalencies of the S-C-N π* feature.

Synchrotron	Detection	Normalization	D_0 S-C-N π*, eV	α^2 S S-C-N π*
SSRL	PIPS[a]	1	1.15 ± 0.03	0.44 ± 0.08
SSRL	PIPS[a]	2	1.36 ± 0.03	0.32 ± 0.04
SSRL	PIPS[a]	3	1.39 ± 0.03	0.30 ± 0.04
SSRL	PIPS[b]	1	1.03 ± 0.03	0.31 ± 0.05
SSRL	PIPS[b]	2	1.21 ± 0.03	0.25 ± 0.03
SSRL	PIPS[b]	3	1.27 ± 0.03	0.25 ± 0.03
CLS	Kα	1	1.19 ± 0.03	0.32 ± 0.05
CLS	Kα	2	1.30 ± 0.03	0.31 ± 0.04
CLS	Kα	3	1.31 ± 0.03	0.26 ± 0.03
CLS	TFY	1	1.19 ± 0.03	0.33 ± 0.05
CLS	TFY	2	1.30 ± 0.03	0.31 ± 0.04
CLS	TFY	3	1.31 ± 0.03	0.27 ± 0.03

[a,b]Two independent collections

Conclusions

The experimental S 3p character of $Cu(dtc)_2$ was determined for the pre-edge and rising edge features in the S K-edge XANES region. Past EPR analysis of $Cu(dtc)_2$ was utilized to develop the ligand transition dipole integral to quantify the S character in Na(dtc) pre-edge feature. Additionally, ground state DFT computations were calibrated to the EPR covalency and were applied to model the S K-edge spectrum using excited state DFT. The complex transition dipole integral was determined based on the S covalency of 0.47 e^- per hole for the Cu-S $3d_{xy}$ orbital. Compared to the Cu-S(Cys) π* bond to the $3d_{xy}$

SUMO in plastocyanin has a covalency of 45%.[84,85,93,202] Maleonitriledithiolate ligands sigma donation to the 3 d_{xy} SUMO of Cu(II) metal center is very covalent with 54% S 3p character.[93,156,204] Using the complex dipole integral from $Cu(dtc)_2$, the ligand transition dipole integrals were determined. The S character of Na(dtc) S-C-N π* LUMO was determined using the respective ligand transition dipole integrals. The B(38HF)P86/def2-TZVP/AIM reproduced the spin observed on Cu(II) site from the metal hyperfine coupling of EPR in the ground state. The excited state DFT picture of the S K-edge mimics the spectral features observed experimentally with B(38HF)P86/def2-TZVP. However, other functionals may give a better representation of the energy splitting of these features. Application of the transition dipole integral to the rising edge S-C-N π* feature in the $Cu(dtc)_2$ spectrum proved challenging. The interpreted S 3p character of $Cu(dtc)_2$ was significantly less than the ground state DFT population analyses for the S-C-N π* LUMOs. Using TD-DFT, the transitions of the alpha electrons are favored over the beta electrons. If the alpha and beta transitions were equivalent, then the isotropic intensity would be more intense than experimentally observed. Na(dtc) does not exhibit loss of intensity since it is a spin restrictive system. Qualitatively for $Cu(dtc)_2$ and Na(dtc), the ground state and excited state DFT produced similar S K-edge spectra when line broadening was applied to the ground state AIM covalency and excited state oscillator strengths.

Additionally, we conducted a detailed analysis to extract S character and transition dipole integrals from the XANES region for both $Cu(dtc)_2$ and Na(dtc). These results were achieved using different detectors, beamline stations, and normalization

techniques. The amount of S character in the rising edge was 0.27 e^- per hole for $Cu(dtc)_2$ and 0.31 e^- per hole for Na(dtc). This correlates well with loss of ligand character when coordinated to metal centers due to the donation of electron density from the ligand to metal and back donation pathways. The experimental electronic structure information determined from the rising edge feature has never been quantified, even for the well-studied sulfur based systems. In summary, different complex and ligand dipole integrals are needed for different facilities, detection techniques, and normalization methods for the most accurate results. The Cu-S σ* pre-edge feature varied the most amongst the three normalization procedures. This pre-edge feature didn't significantly vary for normalizations 2 and 3 with the exception of the SRC data. However, the S-C σ* features had a wider range for normalizations 2 and 3. Using chemically reasonable fits, the error from normalization and fitting was 0.03 eV for Cu-S σ* pre-edge feature for all three normalization procedures. The propagation of error from the normalization, fits, and the EPR data yielded an error of about 7-9% for the complex transition dipole integral. The error in normalization and the fit area of the S-C-N π* peak of $Cu(dtc)_2$ and Na(dtc) was 2-3%. However, the propagation of error in the covalency of the rising edge feature for $Cu(dtc)_2$ and Na(dtc) was 7-8% and 12-18%, respectively.

CHAPTER 6

REDUCTIVE AMINATION OF DIMETHYLHYDRAZONES USING AMINE-BORANE COMPLEXES

Introduction

The reduction of 1,1-dimethylhydrazones have been performed in the literature in obtaining the corresponding hydrazines. LAH, $NaBH_4$, pyridine borane (PB), sodium cyanoborohydride ($NaBH_3CN$) have been commonly used for the reduction of C=N π systems.[74,75,205] $NaBH_3CN$ and PB are more selective towards the C=N π system than LAH and $NaBH_4$.[74] However, one drawback to the use of PB and $NaBH_3CN$ is that these reagents are toxic. There have been a few examples discussed in literature of the success of other amine-boranes as substitutes to $NaBH_3CN$ and PB for the reduction of hydrazones.[81,82,205] On example is Casarini *et al.* use of dimethylamine borane with *p*-toluenesulfonic acid for the reduction of α,β unsaturated hydrazones to successfully render allyl hydrazines.[81] Another example is by Perdicchia *et al*. where they utilized trimethylamine borane and HCl gas for their reductions of hydrazones.[82]

However, some amine-boranes are expensive, but are easily synthesized using the free amine and either dimethylsulfide borane (BMS) or THF-borane.[206-208] The objective of this study was to find amine-boranes that could be synthesized *in situ* just prior to the reduction of dimethylhydrazones resulting in high yields. The different amine-boranes examined in this chapter are *tert*-butylamine borane, diethylamine borane, triethylamine borane, morpholine borane, and pyridine borane. Aqueous solutions of alkylamines were

not considered due the fast hydrolysis of BMS in the presence of water. The reactivities of the various amine-boranes were measured with respect to their reduction capabilities towards the syntheses of 2-heptylidene-1,1-dimethylhydrazine and 2-benzyl-1,1-dimethylhydrazine. The chosen optimal amine-borane was utilized for the reduction of hydrazones by making the amine-borane *in situ*. The hydrazines synthesized are illustrated in Figure 6.1.

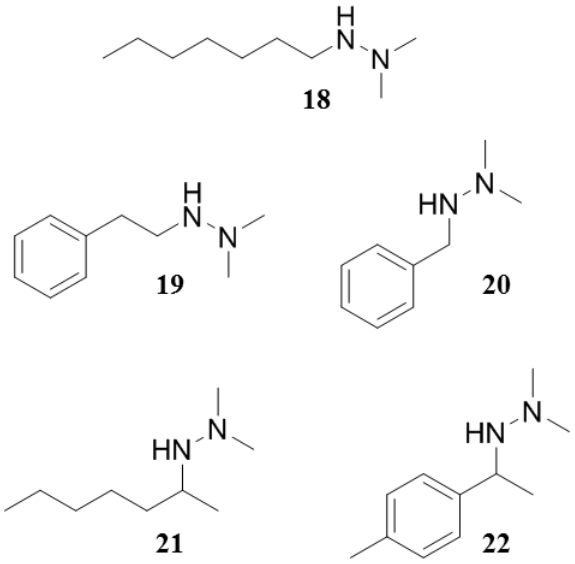


Figure 6.1: The hydrazines synthesized were **18**) 2-heptyl-1,1-dimethylhydrazine, **19**) 1,1-dimethyl-2-phenethylhydrazine, **20**) 2-benzyl-1,1-dimethylhydrazine, **21**) 2-(heptan-2-yl)-1,1-dimethylhydrazine, and **22**) 1,1-dimethyl-2-(1-*p*-tolylethyl)hydrazine.

Experimental Procedures

Materials and Methods

Reactions employed oven- or flame-dried glassware under nitrogen unless otherwise noted. Diethyl ether was distilled from sodium/benzophenone ketyl under nitrogen. Dichloromethane, toluene, *tert*-butylamine, morpholine, diethylamine,

triethylamine, and pyridine were distilled from CaH_2 under nitrogen. 2-(Heptan-2-ylidene)-1,1-dimethylhydrazine,[209] 1,1-dimethyl-2-(2-phenylethylidene)hydrazine,[210] and (*E*)-2-benzylidene-1,1-dimthylhydrazine[211] were prepared as previously reported. All other materials were used as received from commercial sources. Thin-layer chromatography (TLC) employed 0.25 mm glass silica gel plates with UV indicator and visualized with UV light (254 nm) or potassium permanganate staining. Nuclear magnetic resonance (NMR) data were obtained from Bruker DRX-500 (500 MHz). Infrared spectra (IR) were obtained from JASCO FTIR-4100. High-resolution mass spectra (HRMS) were obtained from Bruker MicroTOF with a Dart 100 – SVP 100 ion source (Ionsense Inc., Saugus, MA).

Synthesis of Amine-Boranes

Tert-butylamine borane. A 100 mL round-bottomed flask equipped with a stirring bar, and an N_2 outlet was charged with *tert*-butylamine (5.00 mL, 47.6 mmol), and 30 mL of dichloromethane. The reaction vessel was cooled to 0 °C and BMS (4.10 mL, 43.3 mmol) was added, the reaction was warmed to room temperature and stirred for 30 min. The resulting mixture was filtered through a pad of Celite followed by concentration *in vacuo* yielded 3.56 g (95%) of the title compound as a white solid. **^{1}H NMR** (500 MHz, Chloroform-*d*) δ 3.50 (s), 1.72 (s), 1.37 (s), 1.31 (s), 1.18 (s).

Diethylamine borane. Diethylamine borane compound was prepared by the general procedure described for *tert*-butylamine borane employing diethylamine (4.00 mL, 38.7 mmol), dichloromethane (20 mL), and BMS (3.40 mL, 35.2 mmol) to yield

diethylamine borane (3.13 g, 99% yield) as a clear to pale yellow liquid. **^{1}H NMR** (500 MHz, Chloroform-*d*) δ 3.44 (s), 2.83 – 2.75 (m), 1.52 (s), 1.32 (s), 1.21 (t, *J* = 7.3 Hz).

Triethylamine borane. The title compound was prepared by the general procedure described for *tert*-butylamine borane subjecting triethylamine (1.54 mL, 11.0 mmol), dichloromethane (10 mL), and BMS (0.945 mL, 10.0 mmol) to yield triethylamine borane (1.04 g, 91% yield) as a clear liquid. **^{1}H NMR** (500 MHz, Chloroform-*d*) δ 2.78 (q, *J* = 7.3 Hz), 1.75 (s), 1.56 (s), 1.36 (s), 1.18 (t, *J* = 7.3 Hz).

Pyridine borane. Pyridine borane was prepared by the general procedure described for *tert*-butylamine borane using pyridine (4.70 mL, 58.0 mmol), dichloromethane (30 mL), and BMS (5.00 mL, 52.7 mmol) to render pyridine borane (4.50 g, 92% yield) as yellow liquid. **^{1}H NMR** (500 MHz, Chloroform-*d*) δ 8.58 (d, *J* = 5.6 Hz), 7.93 (t, *J* = 7.8 Hz), 7.51 (s), 7.51 (d, *J* = 13.7 Hz), 2.70 (s), 2.31 (s).

Morpholine borane. The morpholine borane compound was prepared by the general procedure described for *tert*-butylamine borane employing morpholine (3.00 mL, 34.7 mmol), dichloromethane (20 mL), and BMS (2.99 mL, 31.5 mmol) that provided morpholine borane (2.90 g, 91% yield) as a white solid. **^{1}H NMR** (500 MHz, Chloroform-*d*) δ 3.99 (d, *J* = 11.5 Hz), 3.84 (s), 3.57 (t, *J* = 12.3 Hz), 3.13 (d, *J* = 13.7 Hz), 2.90 – 2.81 (m), 2.05 – 1.16 (m).

Synthesis of Hydrazones

2-Heptylidene-1,1-dimethylhydrazine. A 100 mL round-bottomed flask equipped with a magnetic stirring bar, and an N_2 inlet was charged with heptanal (4.20 mL, 29.8 mmol), dichloromethane (20 mL), followed by unsym-dimethylhydrazine (4.60 mL, 60.5 mmol) were subsequently added. The reactant mixture was stirred at room temperature for 12 h. The resulting mixture was dried with $MgSO_4$ and filtered through a pad of Celite. Concentration *in vacuo* followed by bulb to bulb distilled from CaH_2 afforded 4.09 g (88%) of the title compound as a clear liquid. **^{1}H NMR** (500 MHz, Chloroform-*d*) δ 6.66 (t, *J* = 5.6 Hz, 1H), 2.71 (s, 6H), 2.22 (td, *J* = 7.7, 5.6 Hz, 2H), 1.51 – 1.41 (m, 2H), 1.36 – 1.23 (m, 6H), 0.87 (t, *J* = 6.5 Hz, 3H). **^{13}C NMR** (126 MHz, Chloroform-*d*) δ 140.27, 43.79, 33.46, 32.04, 29.24, 28.12, 22.90, 14.40. **IR** (Film): 2954, 2926, 2854, 2820, 2781, 1469, 1444, 1255, 1139, 1027, cm^{-1}. **HRMS** (ESI): Calcd for $C_9H_{20}N_2$ $[M+H]^+$: 157.1699, found: 157.1723.

(*E*)-1,1-Dimethyl-2-(1-p-tolylethylidene)hydrazine.[212] A 100 mL round- bottomed flask equipped with a magnetic stirring bar, an N_2 inlet and fitted with a reflux condenser was charged with 4-methylacetphenone (2.00 g, 14.9 mmol), toluene (7 mL), 1.0 mg of *p*-TsOH, followed by unsym-dimethylhydrazine (4.55 mL, 60.6 mmol) were subsequently added. The reaction was stirred for 12 h at 85 °C. The resulting mixture was dried with $MgSO_4$ and filtered through a pad of Celite. Concentration *in vacuo* followed by bulb to bulb distilled from CaH_2 afforded 2.38g (90%) of the title compound as a

yellow liquid. **^{1}H NMR** (500 MHz, Chloroform-*d*) δ 7.64 (d, *J* = 8.2 Hz, 2H), 7.17 (d, *J* = 7.9 Hz, 2H), 2.59 (s, 6H), 2.36 (s, 3H), 2.34 (s, 3H).

Synthesis of Hydrazines: General Procedure
for 1,2-Reductions of Hydrazones

2-Heptyl-1,1-dimethylhydrazine (**18**). In a 50-mL round-bottomed flask equipped with a magnetic stirring bar, an N_2 inlet was charged with 2-heptylidene-1,1-dimethylhydrazine (0.078 M in methanol), methanol, the reducing agent in a 1:1.1-3 mole ratio to the hydrazone, and methyl orange as an indicator. A 1:5 HCl:methanol (v/v) was titrated dropwise at room temperature until the solution had maintained a pink/red color for 30 min. The reaction was determined finished with the disappearance of the hydrazone spot (rf=0.26) according to TLC (10% EtOAc:hexanes).

2-Benzyl-1,1-dimethylhydrazine (**20**). The title compound was prepared by the general procedure described for compound 2-heptyl-1,1-dimethylhydrazine employing *(E)*-2-benzylidene-1,1-dimethylhydrazine in a 1:3 mole ratio of the reducing agent. The reaction was completed with the disappearance of the hydrazone peak (rf=0.40) using TLC (10% EtOAc:hexanes).

Synthesis of Hydrazines: General Procedure
for *In Situ* 1,2-Reductions of Hydrazones

2-Heptyl-1,1-dimethylhydrazine (**18**). A 25 mL round-bottomed flask equipped with a magnetic stirring bar, and an N_2 inlet was added *tert*-butylamine (1.60 mL, 15.3 mmol), and 10 mL of dichloromethane. The reaction vessel was cooled to 0 °C and BMS

(1.42 mL, 15.0 mmol) was added. The reaction was warmed to room temperature and stirred for 30 min. In a separate 100-mL round-bottomed flask equipped with a magnetic stirring bar and N_2 inlet was charged with 2-heptylidene-1,1-dimethylhydrazine (0.782 g, 5.00 mmol), methyl orange dye as an indicator, and 20 mL of methanol were subsequently added. The contents of the 25 mL flask were transferred to the 100 mL flask, and rinsed with five milliliters of methanol. A 1:5 HCl:methanol (v/v) was titrated dropwise at room temperature until the solution had maintained a pink/red color for 30 min. Aqueous sodium hydroxide (25% w/w) was added dropwise with stirring until a pH greater than 10 was achieved according to litmus paper. The solution of the resulting mixture was removed *in vacuo* and the remaining oil was diluted with diethyl ether (25 mL). The resulting mixture was dried with $MgSO_4$, washed with distilled diethyl ether, and filtered through a pad of Celite. Concentration *in vacuo* followed by bulb to bulb distilled from CaH_2 afforded 0.551g (70%) of the title compound as a clear liquid. **^{1}H NMR** (500 MHz, Chloroform-*d*) δ 2.72 (t, *J* = 7.3 Hz, 2H), 2.41 (s, 6H), 1.94 (s, 1H), 1.43 (p, *J* = 7.1 Hz, 2H), 1.30 – 1.23 (m, 6H), 0.84 (d, *J* = 7.5 Hz, 3H). **^{13}C NMR** (126 MHz, Chloroform-*d*) δ 49.20, 48.10, 32.13, 29.58, 28.96, 27.71, 22.93, 14.39. **IR** (Film): 3178, 2927, 2854, 2807, 2764, 1469, 1377, 1092, 1014, 885, 725, cm^{-1}. **HRMS** (ESI): Calcd for $C_9H_{22}N_2$ $[M+H]^+$: 159.1856, found: 159.1916.

1,1-Dimethyl-2-phenethylhydrazine (**19**). The title compound was prepared by the general procedure described for 2-heptyl-1,1-dimethylhydrazine employing 1,1-dimethyl-2-(2-phenylethylidene)hydrazine (0.810 g, 4.99 mmol), *tert*-butylamine (1.60 mL, 15.3 mmol), and BMS (1.42 mL, 15.0 mmol) to furnish 1,1-dimethyl-2-phenethylhydrazine

(0.694 g, 85%) as a clear liquid. **^{1}H NMR** (500 MHz, Chloroform-*d*) δ 7.37 – 7.15 (m, 5H), 3.04 (t, *J* = 7.4 Hz, 2H), 2.81 (t, *J* = 7.4 Hz, 2H), 2.42 (s, 6H), 2.07 (s, 1H).

2-Benzyl-1,1-dimethylhydrazine (**20**). The title compound was prepared by the general procedure described for 2-heptyl-1,1-dimethylhydrazine employing *(E)*-2-benzylidene-1,1-dimethylhydrazine (0.741 g, 5.00 mmol), *tert*-butylamine (1.60 mL, 15.3 mmol), and BMS (1.42 mL, 15.0 mmol) to yield 2-benzyl-1,1-dimethylhydrazine (0.572 g, 76%) as a clear liquid. **^{1}H NMR** (500 MHz, Chloroform-*d*) δ 7.41 – 7.28 (m, 4H), 7.25 (d, *J* = 6.8 Hz, 1H), 3.94 (s, 2H), 2.50 (s, 6H), 2.22 (s, 1H).

1,1-Dimethyl-2-(1-*p*-tolylethyl)hydrazine (**22**). The title compound was prepared by the general procedure described for 2-heptyl-1,1-dimethylhydrazine employing (*E*)-1,1-dimethyl-2-(1-p-tolylethylidene)hydrazine (0.881 g, 5.00 mmol), *tert*-butylamine (1.60 mL, 15.3 mmol), and BMS (1.42 mL, 15.0 mmol) to yield 1,1-dimethyl-2-(1-*p*-tolylethyl)hydrazine (0.752 g, 84%) as a light yellow liquid. **^{1}H NMR** (500 MHz, Chloroform-*d*) δ 7.24 (d, *J* = 7.8 Hz, 2H), 7.12 (d, *J* = 7.7 Hz, 2H), 3.97 (q, *J* = 6.6 Hz, 1H), 2.42 (s, 6H), 2.32 (s, 3H), 2.13 (s, 1H), 1.28 (d, *J* = 6.4 Hz, 3H). **^{13}C NMR** (126 MHz, Chloroform-*d*) δ 142.61, 136.75, 129.39, 126.93, 57.06, 48.51, 22.95, 21.42. **IR** (Film): 3193, 2976, 2946, 2840, 2807, 2765, 1515, 1473, 1446, 1362, 1106, 1091, 1017, 895, 818, 777, 733, cm^{-1}. **HRMS** (ESI): Calcd for $C_{11}H_{18}N_2$ $[M+H]^+$: 179.1543, found: 179.1566.

2-(Heptan-2-yl)-1,1-dimethylhydrazine (**21**). A 25 mL round-bottomed flask equipped with a magnetic stirring bar and an N_2 inlet was added *tert*-butylamine (1.28 mL, 12.2 mmol), and 8 mL of dichloromethane. The reaction vessel was cooled to 0 °C and BMS (1.14 mL, 12.0 mmol) was added. The reaction was warmed to room temperature and stirred for 30 min. In a separate 100-mL round-bottomed flask equipped with a magnetic stirring bar and an N_2 inlet was charged with 2-(heptan-2-ylidene)-1,1-dimethylhydrazine (0.623 g, 3.99 mmol), 1.0 mg of methyl orange dye, and 15 mL of methanol were subsequently added. The contents of the 25 mL flask were transferred to the 100 mL flask, and rinsed with five milliliters of methanol. A 1:5 HCl:methanol (v/v) was titrated dropwise at room temperature until the solution had maintained a pink/red color for 30 min. The solution of the resulting mixture was removed *in vacuo* and the remaining pink solid was dissolved in a minimum amount of $NaOH_{(aq)}$ (25% w/w). The solution of the resulting mixture was diluted with diethyl ether (25 mL) and subsequently dried with $MgSO_4$, washed with distilled diethyl ether, and filtered through a pad of Celite. Concentration *in vacuo* followed by bulb to bulb distilled from CaH_2 afforded 0.538g (85%) of the title compound as a clear liquid. **^{1}H NMR** (500 MHz, Chloroform-*d*) δ 2.75 (h, *J* = 6.0 Hz, 1H), 2.39 (s, 6H), 1.95 (s, 1H), 1.41 (td, *J* = 10.6, 5.2 Hz, 1H), 1.31 – 1.17 (m, 7H), 0.98 (d, *J* = 6.3 Hz, 3H), 0.85 (t, *J* = 6.7 Hz, 3H). **^{13}C NMR** (126 MHz, Chloroform-*d*) δ 52.80, 48.65, 36.09, 32.48, 26.08, 22.98, 20.01, 14.37. **IR** (Film): 3189, 2955, 2928, 2857, 2807, 2764, 1477, 1461, 1374, 1137, 1015, 895, 772, cm^{-1}. **HRMS** (ESI): Calcd for $C_9H_{22}N_2$ $[M+H]^+$: 159.1856, found: 159.1893.

Results and Discussion

To test the reducing capability of different amine-boranes, we examined the 1,2-reduction of the C=N π system of an aliphatic and conjugated dimethylhydrazones as displayed in Table 6.1. All the amine-boranes were successfully able to reduce both the

Table 6.1: Reduction of dimethylhydrazones from different amine-boranes in HCl/MeOH.

2-heptylidene-1,1-dimethylhydrazine		
Amine-borane	Time (min)	Equiv
tert-butylamine	30	3
diethylamine	30	1.1
triethylamine	30	3
morpholine	30	1.1
PB	30	1.1
2-benzylidene-1,1-dimethylhydrazine		
tert-butylamine	60	3
diethylamine	60	3
triethylamine	240	3
morpholine	150	3
PB	30	1.1

aliphatic and conjugated systems. The amine-boranes in Table 6.1 differ structurally and electronically. The *tert*-butylamine, diethylamine, triethylamine consist of electron donating alkyl groups, whereas, PB and morpholine contain electron withdrawing groups. The reactivities towards the aliphatic hydrazones seem to be dictated by the size of the R groups on the amine due to steric hindrance. The *tert*-butylamine borane and triethylamine borane are bulkier and required about two more equivalents to shift the equilibrium towards the products than the smaller amine-boranes. However, steric hindrance and electronic groups influence the reactivity of the conjugated system of 2-

benzylidene-1,1-dimethylhydrazine. PB was the most reactive towards the synthesis of **20**. The electron withdrawing group helps facilitate the reaction thus only needing slightly more than one equivalent for the reaction to go to completion in 30 min. *Tert*-butylamine borane and diethylamine borane took 60 min with three equivalents towards the synthesis of **20**. Interestingly, morpholine borane took longer than *tert*-butylamine borane and diethylamine borane with three equivalents, even though morpholine's oxygen has an electron withdrawing effect. Triethylamine borane was the least efficient, probably due to it having the largest steric hindrance of the reducing agents.

The order of addition is important in the case of these reductions. The hydrazone was always added first, followed by degassed MeOH and the indicator. Most importantly, the 1/5 HCl/MeOH solution has to be titrated slowly. If too much of the hydrochloric methanol solution was added too fast, the amine-borane could hydrolyze before the delivery of the hydride to the hydrazone.

The workup after the reaction was an important aspect for which amine-borane that would be used for the *in situ* reductions of hydrazones. The hydrolysis of excess triethylamine borane is very slow in hydrochloric methanol solution,[207] resulting in contamination of the product. Although PB was successfully used in these reductions, the byproduct of PB, pyridine, was difficult to remove from the product. Diethylamine borane was more reactive than triethylamine borane due to the less steric hindrance, but does not readily hydrolyze in acidic media. Similarly to diethylamine borane and PB, morpholine borane is slow to hydrolyze and difficult to remove during the workup. *Tert*-butylamine borane is the fastest of these amine-boranes to hydrolyze in acidic media. The

free *tert*-butylamine is very volatile and easily removed during the *in vacuo* in the workup. These 1,1-dimethylhydrazines are oxygen sensitive and oxidize back to the hydrazone in air. The workups commonly used in the literature of column purification or B-N bond cleavage via refluxing sodium carbonate solution of excess amine-borane complex were not successfully exploited in this study. Instead the workup utilized in this study limited the amount of water during the workup and conducted using Schlenk line techniques.

The ideal amine-borane is cheap, reactive, and easy to work with, especially during the workup and purification of the desired dimethylhydrazines. Using the data from Table 6.1 and the ease of workup, *tert*-butylamine borane was viewed as the best candidate for the 1,2 reduction of hydrazones. Even though *tert*-butylamine was not the most active reducing agent, three equivalents always reduced the hydrazones to completion. The use of three equivalents was not an issue due to the fast hydrolysis of the reducing agent, and the ease of the removal of the *tert*-butylamine during the workup. The results using the *tert*-butylamine borane to react with various hydrazones containing different functionalities are listed in Table 6.2. The results in Table 6.2 show the efficient

Table 6.2: Reduction of dimethylhydrazones using 3 equivalents of *tert*-butylamine borane.

Dimethylhydrazine	Time (min)	% Yield
18	30	70
19	30	85
20	60	76
21	30	85
22	30	84

reduction of the hydrazones in 30-60 min obtained in good yields. The most difficult to reduce was **20**, whereas **22** reduced in 30 min. It seems the C=N π system is stabilized by the additional methyl group in **22**, thus speeding up the reaction. In addition, the *tert*-butylamine borane is effective against breaking the conjugation to yield molecules **20** and **22**. The synthesis of **18** and **19** proceeded with no troubles and finished in 30 min. The synthesis of **21** utilized a slightly different workup, due to its higher volatility. Therefore, the HCl salt was formed prior to the removal of the solution, which resulted in high yield before purifying the product by distillation.

Conclusion

We investigated the use of designer amine-boranes for the reduction of dimethylhydrazones. The optimal amine-borane was determined based on reactivity and ease of workup towards the syntheses of **18** and **20**. We then determined a novel way for 1,2 reductions of dimethylhydrazones by synthesizing the reducing agent *in situ* using the optimal amine-borane, *tert*-butylamine borane. *Tert*-butylamine borane was effective in the reduction of the C=N π system of the hydrazone and easy to purify during the workup resulting in good yields of molecules **18-22**.

CHAPTER 7

CONCLUSION

Using XAS and computational theory together helps elucidate the description of the ground state electronic structure of inorganic coordination compounds. In Chapter 2, we experimentally examined a biomimetic model of FeMo-co of nitrogenase. Due to the convoluted spectrum pertaining to the different sulfur environments, the exact bonding description could not be quantified. The peak assignments could only be assigned based on Slater's rules for effective oxidation states. However, qualitative assessments of the intensity of the S K-edge XANES region are consistent with the bonding nature of μ_3 Fe-S clusters. To quantitate the bonding description of the sulfur based ligands in [Mo-3Fe-4S] cluster and to the Mo site, we investigated simpler models in Chapters 3-5.

Chapter 3 focused on the Mo-S bond through S K-edge XAS and computational theory. The literature analysis for the experimental bonding description for Fe-S clusters proved fruitless for the MoS_4^{2-} anion. Therefore, *ab initio* WFN theory was utilized to elucidate the covalent nature of Mo-S bond. The application of the WFN results to the innocent $(PPh_4)_2MoS_4$ salt provided a new transition dipole integral used for Na_2MoS_4 and $(NH_4)_2MoS_4$ compounds. The experimental covalencies for the Na_2MoS_4 and $(NH_4)_2MoS_4$ salts showed the electron donation and hydrogen bonding interactions towards the cations. The DFT functionals examined were too covalent for the MoS_4^{2-} anion. However, TD-DFT qualitatively reproduced the S K-edge spectrum. This showed that the excited state description is reliable, while the ground state description was

inaccurate. In summary, the sulfides donate about five electrons to the formally empty Mo d-orbitals, producing a very covalent bond in MoS_4^{2-}.

The bonding description of the dtc ligand was quantified experimentally in different transition metal complexes. The transition dipole integral was determined for the one hole system using past literature EPR data of $Cu(dtc)_2$. A new methodology developed in the Szilagyi lab that was recently published determined the transition dipole integral for coordination complexes based on S oxidation state, and utilized $Cu(dtc)_2$ as a data point.[93] This methodology was applied to extract the S covalency of these complexes. WFN calculations could not be utilized due to the size of these systems. Therefore, DFT was implemented to complement the experimental covalencies. The Ni(II) and Mo(IV) systems proved to be too covalent by DFT. The covalency of a chemical bond is inversely proportional to the amount of holes present in the transition metal d-manifold. Therefore, the Cu(II) dtc system should be the most covalent. Simply altering the amounts of HF exchange into the functionals did not improve the electronic structure either for Ni(II) and Mo(IV) dtc complexes. Hybrid GGA functionals utilized in literature successfully complemented the Cu(II) and Fe(III) dtc systems. Qualitatively piecing these models together from chapters 3 and 4, the $MoFe_3S_4(dtc)_5$ cluster contains a covalent [Mo-3Fe-4S] core, which is stabilized by the ionic interactions of the surrounding dtc ligands.

$Cu(dtc)_2$ was used a model complex in Chapter 5 for evaluating the uncertainty of the S K-edge spectrum when measured at different beamline facilities and subjected to different measuring techniques. The transition dipole integrals were statistically different

at different synchrotron facilities, and when comparing fluorescence versus electron yield detection methods. The application of the $Cu(dtc)_2$ allowed us to determine the free ligand transition of Na(dtc) assuming the same detectors and facilities were utilized of both the compounds. The free ligand dipole integral allowed us to extract the rising edge features of the S K-edge spectrum. The transition dipole integral was applied to the $Cu(dtc)_2$ to the rising feature to extract the S covalency, although a correction factor was necessary. The experimental covalency of the Cu $3d_{xy}$ orbital was close to the DFT covalency using the B(38HF)P86 functional. The spin density on the Cu(II) was very similar to the EPR measurements. Even with the success of the B(38HF)P86 functional reproducing the electronic ground state picture, it did not give as accurate of an excited state description as other functionals.

In Chapter 6, a new synthetic methodology was developed in regards to the reduction of the carbon-nitrogen π system of dimethylhydrazones. The *tert*-butylamine borane complex was chosen as the optimal borane for this system due to its ability to reduce the π system with different functionalities, and for its easy removal during workup. The reactions were completed in 30-60 min according to TLC. The final products were recovered in high yield with high purity according to ^{1}H NMR and high resolution mass spectroscopy.

Outlook

As the world's population increases, the demand for bioavailable nitrogen in the form of ammonia increases. Currently 1.4% of the world's energy is used in the Haber-

Bosch process for fixing nitrogen at high temperatures and pressures. The biomimetic models hold the secrets of how the FeMo-co can reduce nitrogen at ambient temperatures and pressures. XAS correlated with DFT is a very powerful combination in probing these complicated iron-sulfur clusters to understand their reactivity. The development of the individual donations of the ligands to the Mo and Fe sites using simpler models is the template to build up to actual [Mo-3Fe-4S] clusters. With the aid of the Fe and Mo L_{III} and L_{II}-edges, the ligand donation to these sites will reveal approximately how much metal character there is in the metal ligand bond. This proves useful in biomimetic complexes, especially to complexes **4** and **9** in the Introduction in Chapter 1. DFT functionals could be calibrated to the ligand covalency from the XAS data of the simpler models discussed in this thesis and used further for mapping the potential energy surface for the *in silico* reduction of dinitrogen, and the intermediate substrates. Once the potential energy surface has been determined, new synthetic models could be designed and synthesized based on the *in silico* models.

Laboratory scale reactions, if profitable and useful, are scaled up in industry. With the scale up process, large amounts of chemicals are needed to keep the reaction stoichiometries consistent. The scale up process potentially means working with very toxic molecules in more than lethal quantities. Therefore, we developed a synthetic method that works around toxic cyanide based reagents using amine-boranes. We synthesized amine-boranes *in situ* without the need for isolation towards the selective reduction of the carbon-nitrogen π systems. This reaction methodology saves time and is more efficient, and can hopefully be successfully applied to an industrial setting.

REFERENCES CITED

(1) Seefeldt, L. C.; Hoffman, B. M.; Dean, D. R. In *Annual Review of Biochemistry* 2009; Vol. 78, p 701-722.

(2) Vitousek, P. M.; Howarth, R. W. *Biogeochemistry* **1991**, *13*, 87-115.

(3) Peters, J. W.; Szilagyi, R. K. *Current Opinion in Chemical Biology* **2006**, *10*, 101-108.

(4) Igarashi, R. Y.; Seefeldt, L. C. *Critical Reviews in Biochemistry and Molecular Biology* **2003**, *38*, 351-384.

(5) Schindelin, H.; Kisker, C.; Schlessman, J. L.; Howard, J. B.; Rees, D. C. *Nature (London)* **1997**, *387*, 370-376.

(6) Spatzal, T.; Aksoyoglu, M.; Zhang, L.; Andrade, S. L. A.; Schleicher, E.; Weber, S.; Rees, D. C.; Einsle, O. *Science* **2011**, *334*, 940-940.

(7) Lancaster, K. M.; Roemelt, M.; Ettenhuber, P.; Hu, Y.; Ribbe, M. W.; Neese, F.; Bergmann, U.; DeBeer, S. *Science* **2011**, *334*, 974-977.

(8) Harris, T. V.; Szilagyi, R. K. *Inorganic Chemistry* **2011**, *50*, 4811-4824.

(9) Venters, R. A.; Nelson, M. J.; McLean, P. A.; True, A. E.; Levy, M. A.; Hoffman, B. M.; Ormejohnson, W. H. *Journal of the American Chemical Society* **1986**, *108*, 3487-3498.

(10) Hedman, B.; Frank, P.; Gheller, S. F.; Roe, A. L.; Newton, W. E.; Hodgson, K. O. *Journal of the American Chemical Society* **1988**, *110*, 3798-3805.

(11) Corbett, M. C.; Tezcan, F. A.; Einsle, O.; Walton, M. Y.; Rees, D. C.; Latimer, M. J.; Hedman, B.; Hodgson, K. O. *Journal of Synchrotron Radiation* **2005**, *12*, 28-34.

(12) Conradson, S. D.; Burgess, B. K.; Holm, R. H. *Journal of Biological Chemistry* **1988**, *263*, 13743-13749.

(13) Odonnell, M. J.; Smith, B. E. *Biochemical Journal* **1978**, *173*, 831-839.

(14) Seefeldt, L. C.; Dance, I. G.; Dean, D. R. *Biochemistry* **2004**, *43*, 1401-1409.

(15) Hidai, M.; Mizobe, Y. *Chemical Reviews* **1995**, *95*, 1115-1133.

(16) Yandulov, D. V.; Schrock, R. R. *Science* **2003**, *301*, 76-78.

(17) Barriere, F. *Coordination Chemistry Reviews* **2003**, *236*, 71-89.

(18) Pickett, C. J. *Journal of Biological Inorganic Chemistry* **1996**, *1*, 601-606.

(19) Lee, S. C.; Holm, R. H. *Chemical Reviews* **2004**, *104*, 1135-1157.

(20) Wolff, T. E.; Berg, J. M.; Hodgson, K. O.; Frankel, R. B.; Holm, R. H. *Journal of the American Chemical Society* **1979**, *101*, 4140-4150.

(21) Wolff, T. E.; Power, P. P.; Frankel, R. B.; Holm, R. H. *Journal of the American Chemical Society* **1980**, *102*, 4694-4703.

(22) Armstrong, W. H.; Holm, R. H. *Journal of the American Chemical Society* **1981**, *103*, 6246-6248.

(23) Mascharak, P. K.; Armstrong, W. H.; Mizobe, Y.; Holm, R. H. *Journal of the American Chemical Society* **1983**, *105*, 475-483.

(24) Mascharak, P. K.; Papaefthymiou, G. C.; Armstrong, W. H.; Foner, S.; Frankel, R. B.; Holm, R. H. *Inorganic Chemistry* **1983**, *22*, 2851-2858.

(25) Palermo, R. E.; Holm, R. H. *Journal of the American Chemical Society* **1983**, *105*, 4310-4318.

(26) Palermo, R. E.; Singh, R.; Bashkin, J. K.; Holm, R. H. *Journal of the American Chemical Society* **1984**, *106*, 2600-2612.

(27) Armstrong, W. H.; Mascharak, P. K.; Holm, R. H. *Journal of the American Chemical Society* **1982**, *104*, 4373-4383.

(28) Zhang, Y. P.; Bashkin, J. K.; Holm, R. H. *Inorganic Chemistry* **1987**, *26*, 694-702.

(29) Ciurli, S.; Holm, R. H. *Inorganic Chemistry* **1989**, *28*, 1685-1690.

(30) Huang, J. S.; Mukerjee, S.; Segal, B. M.; Akashi, H.; Zhou, J.; Holm, R. H. *Journal of the American Chemical Society* **1997**, *119*, 8662-8674.

(31) Tyson, M. A.; Coucouvanis, D. *Inorganic Chemistry* **1997**, *36*, 3808-3809.

(32) Han, J.; Koutmos, M.; Al Ahmad, S.; Coucouvanis, D. *Inorganic Chemistry* **2001**, *40*, 5985-5999.

(33) Coucouvanis, D. *Accounts of Chemical Research* **1991**, *24*, 1-8.

(34) Han, J.; Coucouvanis, D. *Inorganic Chemistry* **2002**, *41*, 2738-2746.

(35) Koutmos, M.; Georgakaki, I. P.; Tsiolis, P.; Coucouvanis, D. *Zeitschrift Fur Anorganische Und Allgemeine Chemie* **2008**, *634*, 255-261.

(36) Coucouvanis, D.; Alahmad, S.; Salifoglou, A.; Dunham, W. R.; Sands, R. H. *Angewandte Chemie-International Edition in English* **1988**, *27*, 1353-1355.

(37) Demadis, K. D.; Chen, S. J.; Coucouvanis, D. *Polyhedron* **1994**, *13*, 3147-3151.

(38) Demadis, K. D.; Coucouvanis, D. *Inorganic Chemistry* **1994**, *33*, 4195-4197.

(39) Demadis, K. D.; Coucouvanis, D. *Inorganic Chemistry* **1995**, *34*, 436-448.

(40) Demadis, K. D.; Malinak, S. M.; Coucouvanis, D. *Inorganic Chemistry* **1996**, *35*, 4038-4046.

(41) Laughlin, L. J.; Coucouvanis, D. *Journal of the American Chemical Society* **1995**, *117*, 3118-3125.

(42) Coucouvanis, D.; Mosier, P. E.; Demadis, K. D.; Patton, S.; Malinak, S. M.; Kim, C. G.; Tyson, M. A. *Journal of the American Chemical Society* **1993**, *115*, 12193-12194.

(43) Malinak, S. M.; Simeonov, A. M.; Mosier, P. E.; McKenna, C. E.; Coucouvanis, D. *Journal of the American Chemical Society* **1997**, *119*, 1662-1667.

(44) Liu, Q. T.; Huang, L. G.; Liu, H. Q.; Lei, X. J.; Wu, D. X.; Kang, B. S.; Lu, J. X. *Inorganic Chemistry* **1990**, *29*, 4131-4137.

(45) Solomon, E. I.; Hedman, B.; Hodgson, K. O.; Dey, A.; Szilagyi, R. K. *Coordination Chemistry Reviews* **2005**, *249*, 97-129.

(46) Foresman, J. B.; Frisch, A. *Exploring Chemistry with Electronic Structure Methods.*; 2nd ed.; Gaussian, Inc, 1993.

(47) Cramer, C., J. *Essentials of Computational Chemistry: Theories and Models*; 2nd ed.; John Wiley & Sons, 2004.

(48) Hohenberg, P.; Kohn, W. *Physical Review B* **1964**, *136*, B864-+.

(49) Kohn, W.; Sham, L. J. *Physical Review* **1965**, *140*, 1133-&.

(50) Perdew, J. P.; Burke, K.; Ernzerhof, M. *Physical Review Letters* **1996**, *77*, 3865-3868.

(51) Perdew, J. P.; Schmidt, K. *Density Functional Thoery and Its Application to Materials* **2000**, 1-20.

(52) Tao, J. M.; Perdew, J. P.; Staroverov, V. N.; Scuseria, G. E. *Physical Review Letters* **2003**, *91*.

(53) Becke, A. D. *Journal of Chemical Physics* **1993**, *98*, 1372-1377.

(54) Becke, A. D. *Journal of Chemical Physics* **1993**, *98*, 5648-5652.

(55) Szilagyi, R. K.; Metz, M.; Solomon, E. I. *Journal of Physical Chemistry A* **2002**, *106*, 2994-3007.

(56) Perdew, J. P. *Physical Review B* **1986**, *33*, 8822-8824.

(57) Becke, A. D. *Physical Review A* **1988**, *38*, 3098-3100.

(58) Mulliken, R. S. *Journal of Chemical Physics* **1955**, *23*, 1833-1840.

(59) Foster, J. P.; Weinhold, F. *Journal of the American Chemical Society* **1980**, *102*, 7211-7218.

(60) Löwdin, P.-O.; Per-Olov, L. In *Advances in Quantum Chemistry*; Academic Press: 1970; Vol. Volume 5, p 185-199.

(61) Bader, R. F. W.; Oxford University Press: Oxford, 1990.

(62) Szilagyi, R. K.; Lim, B. S.; Glaser, T.; Holm, R. H.; Hedman, B.; Hodgson, K. O.; Solomon, E. I. *Journal of the American Chemical Society* **2003**, *125*, 9158-9169.

(63) Szilagyi, R. K.; Winslow, M. A. *Journal of Computational Chemistry* **2006**, *27*, 1385-1397.

(64) Corts-Guzman, F.; Bader, R. F. W. *Coordination Chemistry Reviews* **2005**, *249*, 633-662.

(65) Jablonski, M.; Palusiak, M. *Journal of Physical Chemistry A* **2010**, *114*, 12498-12505.

(66) Stener, M.; Fronzoni, G.; de Simone, M. *Chemical Physics Letters* **2003**, *373*, 115-123.

(67) George, S. D.; Petrenko, T.; Neese, F. *Inorganica Chimica Acta* **2008**, *361*, 965-972.

(68) George, S. D.; Petrenko, T.; Neese, F. *Journal of Physical Chemistry A* **2008**, *112*, 12936-12943.

(69) Ray, K.; George, S. D.; Solomon, E. I.; Wieghardt, K.; Neese, F. *Chemistry-a European Journal* **2007**, *13*, 2783-2797.

(70) George, S. D.; Neese, F. *Inorganic Chemistry* **2010**, *49*, 1849-1853.

(71) Chandrasekaran, P.; Stieber, S. C. E.; Collins, T. J.; Que, L., Jr.; Neese, F.; DeBeer, S. *Dalton Transactions* **2011**, *40*, 11070-11079.

(72) Kozimor, S. A.; Yang, P.; Batista, E. R.; Boland, K. S.; Burns, C. J.; Clark, D. L.; Conradson, S. D.; Martin, R. L.; Wilkerson, M. P.; Wolfsberg, L. E. *Journal of the American Chemical Society* **2009**, *131*, 12125-12136.

(73) Minasian, S. G.; Keith, J. M.; Batista, E. R.; Boland, K. S.; Clark, D. L.; Conradson, S. D.; Kozimor, S. A.; Martin, R. L.; Schwarz, D. E.; Shuh, D. K.; Wagner, G. L.; Wilkerson, M. P.; Wolfsberg, L. E.; Yang, P. *Journal of the American Chemical Society* **2012**, *134*, 5586-5597.

(74) Hutchins, R. O.; Hutchins, M. K. *Reduction of C=N to CHNH by Metal Hydrides*; Pergamon Press, 1991; Vol. 8.

(75) Seyden-Penne, J. *Reductions by the Alumino- and Borohydrides in Organic Synthesis*; 2nd ed.; Wiley-VCH, 1997.

(76) Sunsdahl, B.; Smith, A. R.; Livinghouse, T. *Angewandte Chemie* **2014**, n/a-n/a.

(77) Heydari, A.; Tavakol, H.; Aslanzadeh, S.; Azarnia, J.; Ahmadi, N. *Synthesis-Stuttgart* **2005**, 627-633.

(78) Dion, I.; Vincent-Rocan, J.-F.; Zhang, L.; Cebrowski, P. H.; Lebrun, M.-E.; Pfeiffer, J. Y.; Bedard, A.-C.; Beauchemin, A. M. *Journal of Organic Chemistry* **2013**, *78*, 12735-12749.

(79) Hutchins, R. O.; Learn, K.; Nazer, B.; Pytlewski, D.; Pelter, A. *Organic Preparations and Procedures International* **1984**, *16*, 337-372.

(80) Kikugawa, Y.; Kawase, M. *Synthetic Communications* **1979**, *9*, 49-52.

(81) Casarini, M. E.; Ghelfi, F.; Libertini, E.; Pagnoni, U. M.; Parsons, A. F. *Tetrahedron* **2002**, *58*, 7925-7932.

(82) Perdicchia, D.; Licandro, E.; Maiorana, S.; Baldoli, C.; Giannini, C. *Tetrahedron* **2003**, *59*, 7733-7742.

(83) Haung, L.; Yang, Y.; Liu, Q.; Lu, J. *Jiegou Huaxue* **1986**, *5*, 61.

(84) Shadle, S. E.; Pennerhahn, J. E.; Schugar, H. J.; Hedman, B.; Hodgson, K. O.; Solomon, E. I. *Journal of the American Chemical Society* **1993**, *115*, 767-776.

(85) George, S. D.; Metz, M.; Szilagyi, R. K.; Wang, H. X.; Cramer, S. P.; Lu, Y.; Tolman, W. B.; Hedman, B.; Hodgson, K. O.; Solomon, E. I. *Journal of the American Chemical Society* **2001**, *123*, 5757-5767.

(86) Glaser, T.; Rose, K.; Shadle, S. E.; Hedman, B.; Hodgson, K. O.; Solomon, E. I. *Journal of the American Chemical Society* **2001**, *123*, 442-454.

(87) Rose, K.; Shadle, S. E.; Glaser, T.; de Vries, S.; Cherepanov, A.; Canters, G. W.; Hedman, B.; Hodgson, K. O.; Solomon, E. I. *Journal of the American Chemical Society* **1999**, *121*, 2353-2363.

(88) Williams, K. R.; Hedman, B.; Hodgson, K. O.; Solomon, E. I. In *Inorganica Chimica Acta* 1997; Vol. 263, p 315-321.

(89) So, J.-H.; Boudjouk, P.; Hong, H.; Weber, W. *Inorganic Syntheses* **1992**, *29*, 30-32.

(90) Gardenghi, D. J. In *Automated Data Reduction Protocol, Version 1.1* http://computational.chemistry.montana.edu/ADRP/ Bozeman MT, 2011.

(91) Bernholc, J.; Stiefel, E. I. *Inorganic Chemistry* **1985**, *24*, 1323-1330.

(92) Hedman, B.; Hodgson, K. O.; Solomon, E. I. *Journal of the American Chemical Society* **1990**, *112*, 1643-1645.

(93) Queen, M. S.; Towey, B. D.; Murray, K. A.; Veldkamp, B. S.; Byker, H. J.; Szilagyi, R. K. *Coordination Chemistry Reviews* **2013**, *257*, 564-578.

(94) Wittneben, V.; Sprafke, A.; Diemann, E.; Muller, A.; Kuetgens, M.; Chauvistre, R.; Hormes, J. *Journal of Molecular Structure* **1989**, *198*, 525-529.

(95) Muller, A.; Wittneben, V.; Diemann, E.; Hormes, J.; Kuetgens, U. *Chemical Physics Letters* **1994**, *225*, 359-363.

(96) Muller, A.; Diemann, E.; Jostes, R.; Bogge, H. *Angewandte Chemie-International Edition in English* **1981**, *20*, 934-955.

(97) George, S. J.; Drury, O. B.; Fu, J.; Friedrich, S.; Doonan, C. J.; George, G. N.; White, J. M.; Young, C. G.; Cramer, S. P. *Journal of Inorganic Biochemistry* **2009**, *103*, 157-167.

(98) Kutzler, F. W.; Natoli, C. R.; Misemer, D. K.; Doniach, S.; Hodgson, K. O. *Journal of Chemical Physics* **1980**, *73*, 3274-3287.

(99) Jostes, R.; Muller, A.; Diemann, E. *Theochem-Journal of Molecular Structure* **1986**, *30*, 311-328.

(100) Manthiram, A.; Sarode, P. R.; Madhusudan, W. H.; Gopalakrishnan, J.; Rao, C. N. R. *Journal of Physical Chemistry* **1980**, *84*, 2200-2203.

(101) Takagi, H.; Mikata, Y.; Ichimura, A.; Yano, T.; Kinoshita, I.; Hori, M.; Collins, T. J.; Gottschaldt, M.; Yano, S. *Electrochimica Acta* **2009**, *54*, 1286-1291.

(102) Gaussian 09, R. C., M. J. Frisch, G. W. Trucks, H. B. Schlegel, G. E. Scuseria, M. A. Robb, J. R. Cheeseman, G. Scalmani, V. Barone, B. Mennucci, G. A. Petersson, H. Nakatsuji, M. Caricato, X. Li, H. P. Hratchian, A. F. Izmaylov, J. Bloino, G. Zheng, J. L. Sonnenberg, M. Hada, M. Ehara, K. Toyota, R. Fukuda, J. Hasegawa, M. Ishida, T. Nakajima, Y. Honda, O. Kitao, H. Nakai, T. Vreven, J. A. Montgomery, Jr., J. E. Peralta, F. Ogliaro, M. Bearpark, J. J. Heyd, E. Brothers, K. N. Kudin, V. N. Staroverov, R. Kobayashi, J. Normand, K. Raghavachari, A. Rendell, J. C. Burant, S. S. Iyengar, J. Tomasi, M. Cossi, N. Rega, J. M. Millam, M. Klene, J. E. Knox, J. B. Cross, V. Bakken, C. Adamo, J. Jaramillo, R. Gomperts, R. E. Stratmann, O. Yazyev, A. J. Austin, R. Cammi, C. Pomelli, J. W. Ochterski, R. L. Martin, K. Morokuma, V. G. Zakrzewski, G. A. Voth, P. Salvador, J. J. Dannenberg, S. Dapprich, A. D. Daniels, Ö. Farkas, J. B. Foresman, J. V. Ortiz, J. Cioslowski, and D. J. Fox, Gaussian, Inc., Wallingford CT **2009**.

(103) Hay, P. J.; Wadt, W. R. *Journal of Chemical Physics* **1985**, *82*, 270-283.

(104) Wadt, W. R.; Hay, P. J. *Journal of Chemical Physics* **1985**, *82*, 284-298.

(105) Hay, P. J.; Wadt, W. R. *Journal of Chemical Physics* **1985**, *82*, 299-310.

(106) Weigend, F.; Ahlrichs, R. *Physical Chemistry Chemical Physics* **2005**, *7*, 3297-3305.

(107) Woon, D. E.; Dunning, T. H. *Journal of Chemical Physics* **1993**, *98*, 1358-1371.

(108) Peterson, K. A.; Figgen, D.; Dolg, M.; Stoll, H. *Journal of Chemical Physics* **2007**, *126*.

(109) Feller, D. *Journal of Computational Chemistry* **1996**, *17*, 1571-1586.

(110) Schuchardt, K. L.; Didier, B. T.; Elsethagen, T.; Sun, L. S.; Gurumoorthi, V.; Chase, J.; Li, J.; Windus, T. L. *Journal of Chemical Information and Modeling* **2007**, *47*, 1045-1052.

(111) Lee, C. T.; Yang, W. T.; Parr, R. G. *Physical Review B* **1988**, *37*, 785-789.

(112) Adamo, C.; Barone, V. *Journal of Chemical Physics* **1998**, *108*, 664-675.

(113) Molawi, K.; Cohen, A. J.; Handy, N. C. *International Journal of Quantum Chemistry* **2002**, *89*, 86-93.

(114) Hoe, W. M.; Cohen, A. J.; Handy, N. C. *Chemical Physics Letters* **2001**, *341*, 319-328.

(115) Perdew, J. P.; Chevary, J. A.; Vosko, S. H.; Jackson, K. A.; Pederson, M. R.; Singh, D. J.; Fiolhais, C. *Physical Review B* **1992**, *46*, 6671-6687.

(116) Perdew, J. P.; Burke, K.; Wang, Y. *Physical Review B* **1996**, *54*, 16533-16539.

(117) Zhao, Y.; Truhlar, D. G. *Journal of Chemical Physics* **2006**, *125*.

(118) Dahlke, E. E.; Truhlar, D. G. *Journal of Physical Chemistry B* **2005**, *109*, 15677-15683.

(119) Becke, A. D. *Journal of Chemical Physics* **1996**, *104*, 1040-1046.

(120) Lynch, B. J.; Fast, P. L.; Harris, M.; Truhlar, D. G. *Journal of Physical Chemistry A* **2000**, *104*, 4811-4815.

(121) Zhao, Y.; Truhlar, D. G. *Journal of Physical Chemistry A* **2004**, *108*, 6908-6918.

(122) Schultz, N. E.; Zhao, Y.; Truhlar, D. G. *Journal of Physical Chemistry A* **2005**, *109*, 11127-11143.

(123) Cohen, A. J.; Handy, N. C. *Molecular Physics* **2001**, *99*, 607-615.

(124) Zhao, Y.; Truhlar, D. G. *Theoretical Chemistry Accounts* **2008**, *120*, 215-241.

(125) Zhao, Y.; Truhlar, D. G. *Journal of Physical Chemistry A* **2006**, *110*, 13126-13130.

(126) Zhao, Y.; Truhlar, D. G. *Journal of Physical Chemistry A* **2006**, *110*, 5121-5129.

(127) Miertus, S.; Scrocco, E.; Tomasi, J. *Chemical Physics* **1981**, *55*, 117-129.

(128) Pascualahuir, J. L.; Silla, E.; Tunon, I. *Journal of Computational Chemistry* **1994**, *15*, 1127-1138.

(129) Tomasi, J. *Wiley Interdisciplinary Reviews-Computational Molecular Science* **2011**, *1*, 855-867.

(130) Tomasi, J.; Mennucci, B.; Cammi, R. *Chemical Reviews* **2005**, *105*, 2999-3093.

(131) Mennucci, B.; Tomasi, J. *Journal of Chemical Physics* **1997**, *106*, 5151-5158.

(132) Cossi, M.; Barone, V.; Cammi, R.; Tomasi, J. *Chemical Physics Letters* **1996**, *255*, 327-335.

(133) Bader, R. F. W. *Accounts of Chemical Research* **1985**, *18*, 9-15.

(134) Bader, R. F. W. *Journal of Physical Chemistry A* **2010**, *114*, 7431-7444.

(135) Giles, L. J.; Grigoropoulos, A.; Szilagyi, R. K. *European Journal of Inorganic Chemistry* **2011**, 2677-2690.

(136) Kieth, T. A. **2012**.

(137) ADF 2012.01, T. C., Vrije Universiteit: Amsterdam,; The Netherlands, h. w. s. c.

(138) Guerra, C. F.; Snijders, J. G.; te Velde, G.; Baerends, E. J. *Theoretical Chemistry Accounts* **1998**, *99*, 391-403.

(139) te Velde, G.; Bickelhaupt, F. M.; Baerends, E. J.; Guerra, C. F.; Van Gisbergen, S. J. A.; Snijders, J. G.; Ziegler, T. *Journal of Computational Chemistry* **2001**, *22*, 931-967.

(140) Neese, F. *e. a.* **2010**.

(141) Neese, F.; Wennmohs, F.; Hansen, A.; Becker, U. *Chemical Physics* **2009**, *356*, 98-109.

(142) Kossmann, S.; Neese, F. *Chemical Physics Letters* **2009**, *481*, 240-243.

(143) Neese, F. *Journal of Computational Chemistry* **2003**, *24*, 1740-1747.

(144) Klamt, A. *Journal of Physical Chemistry* **1995**, *99*, 2224-2235.

(145) Klamt, A.; Schuurmann, G. *Journal of the Chemical Society-Perkin Transactions 2* **1993**, 799-805.

(146) Pye, C. C.; Ziegler, T. *Theoretical Chemistry Accounts* **1999**, *101*, 396-408.

(147) Vanlenthe, E.; Baerends, E. J.; Snijders, J. G. *Journal of Chemical Physics* **1993**, *99*, 4597-4610.

(148) van Wullen, C. *Journal of Chemical Physics* **1998**, *109*, 392-399.

(149) Baerends, E. J.; Branchadell, V.; Sodupe, M. *Chemical Physics Letters* **1997**, *265*, 481-489.

(150) Che, L.; Gardenghi, D. J.; Szilagyi, R. K.; Minton, T. K. *Langmuir* **2011**, *27*, 6814-6821.

(151) Oneal, S. C.; Kolis, J. W. *Journal of the American Chemical Society* **1988**, *110*, 1971-1973.

(152) Hogarth, G. In *Progress in Inorganic Chemistry, Vol 53* 2005; Vol. 53, p 71-561.

(153) Cvek, B.; Milacic, V.; Taraba, J.; Dou, Q. P. *Journal of Medicinal Chemistry* **2008**, *51*, 6256-6258.

(154) Martin-Diaconescu, V.; Kennepohl, P. *Inorganic Chemistry* **2009**, *48*, 1038-1044.

(155) Karunakaran-Datt, A.; Kennepohl, P. *Journal of the American Chemical Society* **2009**, *131*, 3577-3582.

(156) Sarangi, R.; George, S. D.; Rudd, D. J.; Szilagyi, R. K.; Ribas, X.; Rovira, C.; Almeida, M.; Hodgson, K. O.; Hedman, B.; Solomon, E. I. *Journal of the American Chemical Society* **2007**, *129*, 2316-2326.

(157) Shadle, S. E.; Hedman, B.; Hodgson, K. O.; Solomon, E. I. *Inorganic Chemistry* **1994**, *33*, 4235-4244.

(158) Shadle, S. E.; Hedman, B.; Hodgson, K. O.; Solomon, E. I. *Journal of the American Chemical Society* **1995**, *117*, 2259-2272.

(159) Pettersson, R.; Vanngard, T. *Arkiv for Kemi* **1961**, *17*, 249-&.

(160) Gersmann, H. R.; Swalen, J. D. *Journal of Chemical Physics* **1962**, *36*, 3221-&.

(161) Weeks, M. J.; Fackler, J. P. *Inorganic Chemistry* **1968**, *7*, 2548-&.

(162) Kirmse, R.; Solovev, B. V. *Journal of Inorganic & Nuclear Chemistry* **1977**, *39*, 41-44.

(163) Reddy, T. R.; Srinivas.R *Journal of Chemical Physics* **1965**, *43*, 1404-&.

(164) Savino, P. C.; Bereman, R. D. *Inorganic Chemistry* **1973**, *12*, 173-176.

(165) Hurd, C. M.; Coodin, P. *Journal of Physics and Chemistry of Solids* **1967**, *28*, 523-&.

(166) Morton, J. R. *Chemical Reviews* **1964**, *64*, 453-&.

(167) Schmitt, R. D.; Maki, A. H. *Journal of the American Chemical Society* **1968**, *90*, 2288-&.

(168) Maki, A. H.; McGarvey, B. R. *Journal of Chemical Physics* **1958**, *29*, 31-34.

(169) Kivelson, D.; Neiman, R. *Journal of Chemical Physics* **1961**, *35*, 149-&.

(170) Kuska, H. A.; Rogers, M. T. *Journal of Chemical Physics* **1965**, *43*, 1744-&.

(171) Husain, A.; Nami, S. A. A.; Singh, S. P.; Oves, M.; Siddiqi, K. S. *Polyhedron* **2011**, *30*, 33-40.

(172) Ileperuma, O. A.; Feltham, R. D. *Inorganic Chemistry* **1975**, *14*, 3042-3045.

(173) Leipoldt, J. G.; Coppens, P. *Inorganic Chemistry* **1973**, *12*, 2269-2274.

(174) Beurskens, J. G. M. v. d. A. a. P. T. *Crystal Structure Communications* **1974**, *3*, 653-656.

(175) Bonamico, M.; Mazzone, G.; Vaciago, A.; Zambonel.L *Acta Crystallographica* **1965**, *19*, 898-&.

(176) Jorgensen, C. K. *Journal of Inorganic & Nuclear Chemistry* **1962**, *24*, 1571-1585.

(177) Dingle, R. *Inorganic Chemistry* **1971**, *10*, 1141-&.

(178) Vansanten, J. A.; Vanduyneveldt, A. J.; Carlin, R. L. *Inorganic Chemistry* **1980**, *19*, 2152-2153.

(179) Vries, J. L. K.; Trooster, J. M.; Boer, E. D. *Inorganic Chemistry* **1973**, *12*, 2730-2733.

(180) Tsipis, C. A.; Hadjikostas, C. C.; Manoussakis, G. E. *Inorganica Chimica Acta* **1977**, *23*, 163-171.

(181) White, A. H.; Martin, R. L.; Roper, R.; Kokot, E.; Waterman, H. *Australian Journal of Chemistry* **1964**, *17*, 294-&.

(182) Ewald, A. H.; Martin, R. L.; Sinn, E.; White, A. H. *Inorganic Chemistry* **1969**, *8*, 1837-&.

(183) Milsmann, C.; Sproules, S.; Bill, E.; Weyhermuller, T.; George, S. D.; Wieghardt, K. *Chemistry-a European Journal* **2010**, *16*, 3628-3645.

(184) Varadi, Z. B.; Nieuwpoo.A *Inorganic & Nuclear Chemistry Letters* **1974**, *10*, 801-804.

(185) Brown, D. A.; Glass, W. K.; Toma, H. J.; Waghorne, W. E. *Journal of the Chemical Society-Dalton Transactions* **1987**, 2531-2536.

(186) Nieuwpoort, A.; Steggerda, J. J. *Recueil Des Travaux Chimiques Des Pays-Bas-Journal of the Royal Netherlands Chemical Society* **1976**, *95*, 294-298.

(187) Hendrickson, A. R.; Martin, R. L.; Rohde, N. M. *Inorganic Chemistry* **1975**, *14*, 2980-2985.

(188) Chang, H.; Cheng, K. L. *Spectroscopy Letters* **1981**, *14*, 795-807.

(189) Giles, L. J.; Grigoropoulos, A.; Szilagyi, R. K. *Journal of Physical Chemistry A* **2012**, *116*, 12280-12298.

(190) Solomon, E. I.; Szilagyi, R. K.; George, S. D.; Basumallick, L. *Chemical Reviews* **2004**, *104*, 419-458.

(191) Szilagyi, R. K.; Solomon, E. I. *Current Opinion in Chemical Biology* **2002**, *6*, 250-258.

(192) Georgieva, I.; Trendafilova, N. *Journal of Physical Chemistry A* **2007**, *111*, 13075-13087.

(193) Katare, R. K.; Joshi, S. K.; Shrivastava, B. D.; Pandeya, K. B.; Mishra, A. *X-Ray Spectrometry* **2000**, *29*, 187-191.

(194) Boysen, R. B.; Szilagyi, R. K. *Inorganica Chimica Acta* **2008**, *361*, 1047-1058.

(195) Nikolov, G. S. *Journal of Inorganic & Nuclear Chemistry* **1977**, *39*, 249-253.

(196) Nikolov, G. S.; Atanasov, M. A. *Journal of Inorganic and Nuclear Chemistry* **1981**, *43*, 1201-1206.

(197) Keijzers, C. P.; Vanderav.A; Vries, H. *Inorganic Chemistry* **1972**, *11*, 1338-&.

(198) Harihara.Pc; Pople, J. A. *Theoretica Chimica Acta* **1973**, *28*, 213-222.

(199) Francl, M. M.; Pietro, W. J.; Hehre, W. J.; Binkley, J. S.; Gordon, M. S.; Defrees, D. J.; Pople, J. A. *Journal of Chemical Physics* **1982**, *77*, 3654-3665.

(200) Rassolov, V. A.; Pople, J. A.; Ratner, M. A.; Windus, T. L. *Journal of Chemical Physics* **1998**, *109*, 1223-1229.

(201) Hirata, S.; Head-Gordon, M. *Chemical Physics Letters* **1999**, *314*, 291-299.

(202) George, S. D.; Basumallick, L.; Szilagyi, R. K.; Randall, D. W.; Hill, M. G.; Nersissian, A. M.; Valentine, J. S.; Hedman, B.; Hodgson, K. O.; Solomon, E. I. *Journal of the American Chemical Society* **2003**, *125*, 11314-11328.

(203) Cory, M. G.; Zerner, M. C. *Chemical Reviews* **1991**, *91*, 813-822.

(204) Kirmse, R.; Stach, J.; Dietzsch, W.; Hoyer, E. *Inorganica Chimica Acta* **1978**, *26*, L53-L55.

(205) Pelter, A.; Rosser, R. M.; Mills, S. *Journal of the Chemical Society-Perkin Transactions 1* **1984**, 717-720.

(206) Kelly, H. C.; Underwoo.Ja *Inorganic Chemistry* **1969**, *8*, 1202-&.

(207) Brown, H. C.; Murray, L. T. *Inorganic Chemistry* **1984**, *23*, 2746-2753.

(208) Jaska, C. A.; Temple, K.; Lough, A. J.; Manners, I. *Journal of the American Chemical Society* **2003**, *125*, 9424-9434.

(209) Corey, E. J.; Enders, D. *Chemische Berichte-Recueil* **1978**, *111*, 1337-1361.

(210) Clarke, L. F.; Osullivan, F.; Hegarty, A. F. *Journal of the Chemical Society-Perkin Transactions 2* **1991**, 1649-1652.

(211) Petroski, R. J. *Synthetic Communications* **2006**, *36*, 1727-1734.

(212) Newkome, G. R.; Fishel, D. L. *Journal of Organic Chemistry* **1966**, *31*, 677-&.

APPENDICES

APPENDIX A

SUPPORTING INFORMATION FOR CHAPTER 3

Coordinates

XYZ file for MoS_4^{2-} anion symmetrized in ChemCraft to Td:

S	-1.257215839	-1.257215839	1.257215835
S	1.257215834	-1.257215834	-1.257215838
S	-1.257215834	1.257215834	-1.257215838
S	1.257215839	1.257215839	1.257215835
Mo	0.000000000	0.000000000	0.000000002

XYZ file for $(NH_4)_2MoS_4$ crystal structure 5 Å out from MoS_4^{2-} anion:

Mo	11.9441	8.6814	11.3135
S	14.0915	8.6814	10.8292
S	11.6555	8.6814	13.4767
S	10.9931	10.4447	10.4607
S	10.9931	6.9180	10.4607
N	12.7887	8.6814	7.4667
H	12.0217	8.6814	7.8693
H	13.5172	8.6814	7.9669
H	12.7982	7.9869	6.9177
H	12.7982	9.3759	6.9177
N	7.9953	8.6814	10.8340
H	7.2284	8.6814	10.4314
H	8.7239	8.6814	10.3338
H	8.0049	7.9869	11.3831
H	8.0049	9.3759	11.3831
N	17.5820	8.6814	10.8340
H	16.8151	8.6814	10.4314
H	18.3106	8.6814	10.3338
H	17.5916	7.9869	11.3831
H	17.5916	9.3759	11.3831
N	11.1781	5.2088	13.5670
H	11.9450	5.2088	13.9696
H	10.4495	5.2088	14.0672
H	11.1685	5.9033	13.0179
H	11.1685	4.5143	13.0179
N	11.1781	12.1539	13.5670
H	11.9450	12.1539	13.9696
H	10.4495	12.1539	14.0672
H	11.1685	12.8484	13.0179
H	11.1685	11.4594	13.0179
N	9.1352	5.2088	8.0633
H	9.5675	5.2088	8.8210
H	9.6155	5.2088	7.3203

H 8.6568 4.4726 8.0035
H 8.6568 5.9450 8.0035
N 9.1352 12.1539 8.0633
H 9.5675 12.1539 8.8210
H 9.6155 12.1539 7.3203
H 8.6568 11.4177 8.0035
H 8.6568 12.8901 8.0035
N 10.0382 8.6814 16.3377
H 9.6059 8.6814 15.5800
H 9.5579 8.6814 17.0807
H 10.5166 9.4176 16.3975
H 10.5166 7.9452 16.3975
N 14.8316 8.6814 14.1636
H 14.3992 8.6814 14.9212
H 14.3513 8.6814 13.4206
H 15.3100 9.4176 14.1038
H 15.3100 7.9452 14.1038
N 13.9285 5.2088 10.2374
H 14.3609 5.2088 9.4798
H 14.4088 5.2088 10.9804
H 13.4501 4.4726 10.2972
H 13.4501 5.9450 10.2972
N 13.9285 12.1539 10.2374
H 14.3609 12.1539 9.4798
H 14.4088 12.1539 10.9804
H 13.4501 11.4177 10.2972
H 13.4501 12.8901 10.2972

XYZ file for Na_2MoS_4 crystal structure 7 Å out from MoS_4^{2-} anion:

Na 9.1491 8.6938 16.3508
Na 14.8089 5.2162 22.4637
Na 14.8089 12.1713 22.4637
Na 10.0173 5.2162 20.3266
Na 10.0173 12.1713 20.3266
Na 13.9407 8.6938 14.2137
Na 6.3594 8.6938 19.6933
Na 15.9426 8.6938 19.6933
Na 12.8070 5.2162 16.9841
Na 12.8070 12.1713 16.9841
Na 11.1510 8.6938 23.0970
Mo 12.0038 1.7387 19.2291
S 12.9465 3.4977 20.0872
S 12.3154 8.6938 17.0781
S 12.9465 6.9348 20.0872
S 9.8609 8.6938 19.6939

APPENDIX B

SUPPORTING INFORMATION FOR CHAPTER 4

Spectral Fits

Documentation of employment of the fits of dtc complexes along with the free ligand spectrum for quantitative analysis of the pre-edge features:

- hallow circles indicate normalized data points for the spectra of complexes
- hollow triangles indicate normalized data points for the spectra of free ligands
- thin continuous lines are the proposed edge jumps of the complexes
- thin dashed lines represent rising-edge, white line, and EXAFS features that changed upon coordination
- shaded areas indicate pre-edge features
- thick continuous lines are the sum of pre-edge features and shifted ligand spectra

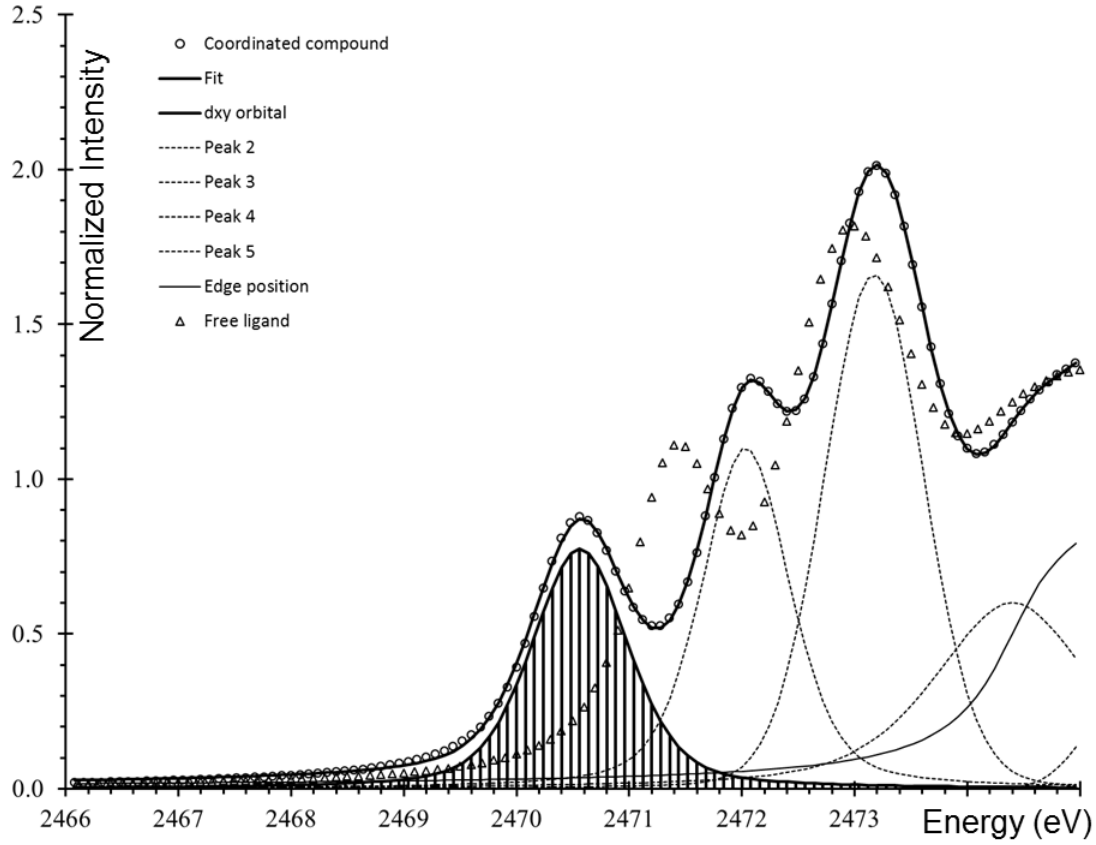


Figure B.1: $Cu(dtc)_2$ and Na(dtc).

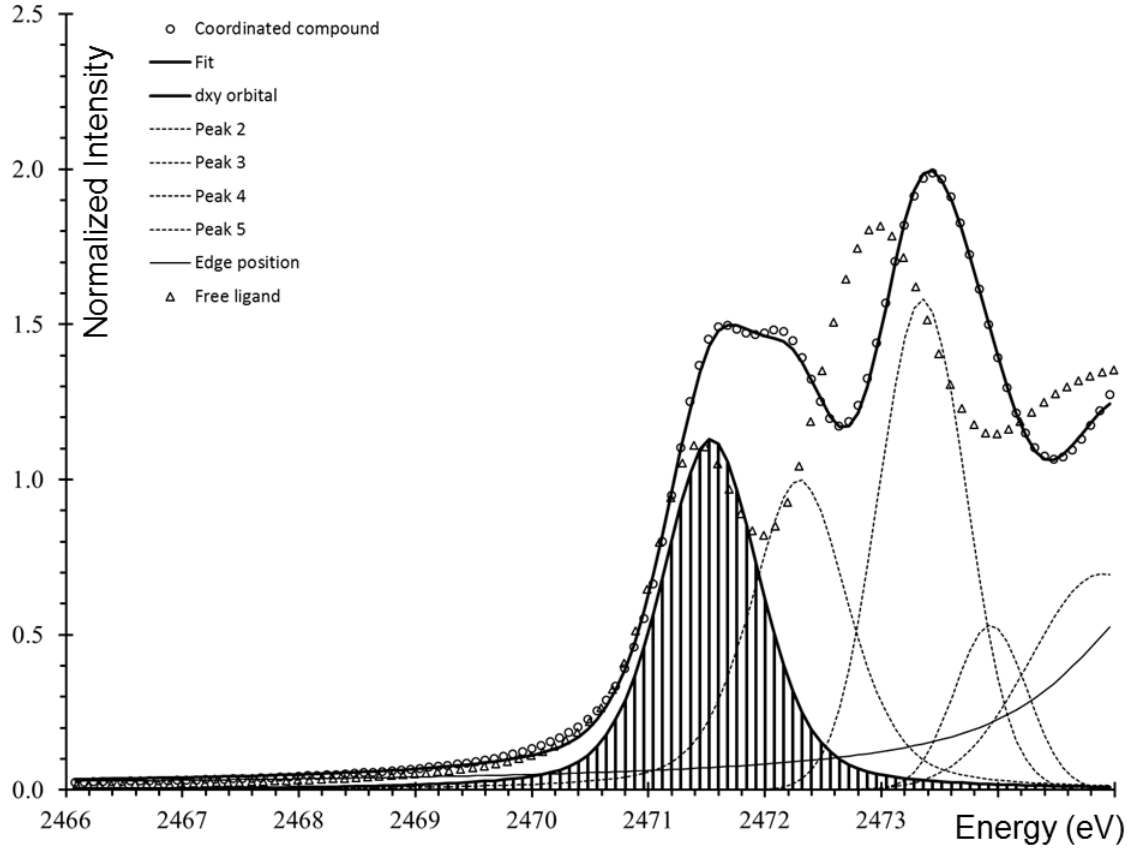


Figure B.2: $Ni(dtc)_2$ and Na(dtc).

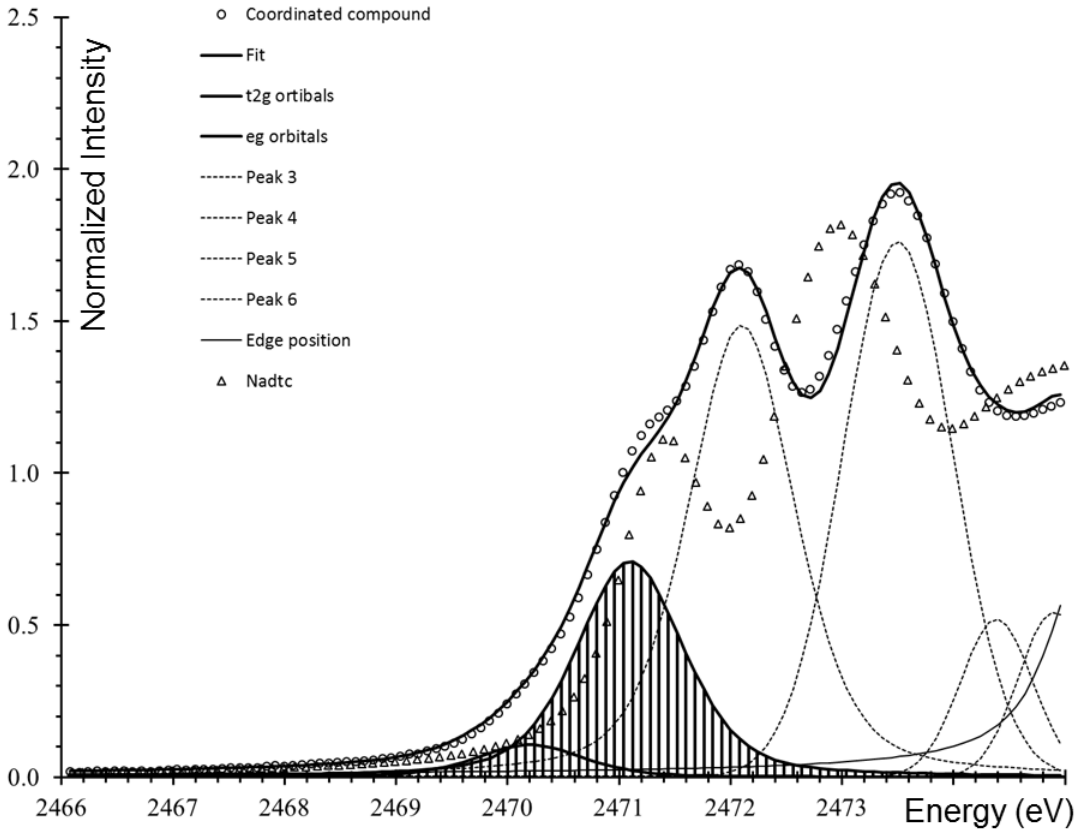


Figure B.3: $Fe(dtc)_3$ and Na(dtc).

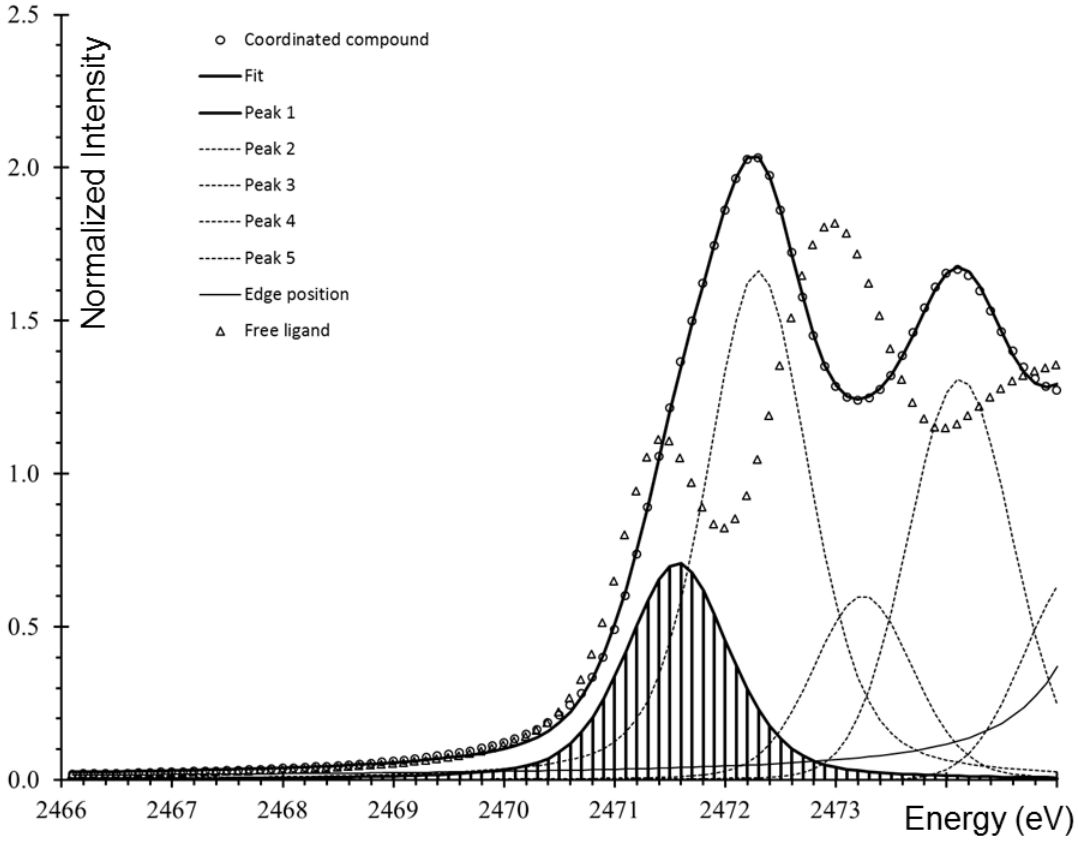


Figure B.4: $Mo(dtc)_4$ and Na(dtc).

Atomic Coordinates for Computational Models of Transition Metal dtc Complexes

$Ni(dtc)_2$

Ni	0.000000000	0.000000000	0.000000000
S	1.696900000	1.403700000	-0.093400000
S	1.691800000	-1.410400000	0.000000000
N	3.998700000	0.008200000	0.064900000
C	4.757500000	-1.231400000	0.259700000
H	5.607400000	-1.165400000	-0.203400000
H	4.264100000	-1.974500000	-0.122500000
C	5.007200000	-1.496900000	1.740100000
H	5.511700000	-0.771600000	2.114600000
H	5.499300000	-2.315300000	1.839600000
H	4.167000000	-1.571400000	2.198300000
C	4.764800000	1.271700000	0.015600000
H	5.588200000	1.166900000	0.516500000
H	4.247700000	1.977000000	0.434600000

C	5.092800000	1.670500000	-1.408500000
H	5.589600000	0.966400000	-1.831700000
H	5.617000000	2.473800000	-1.403400000
H	4.278100000	1.823000000	-1.893300000
C	2.683600000	0.000000000	0.000000000
S	-1.696900000	-1.403700000	0.093400000
S	-1.691800000	1.410400000	0.000000000
N	-3.998700000	-0.008200000	-0.064900000
C	-4.757500000	1.231500000	-0.259700000
H	-5.607400000	1.165400000	0.203400000
H	-4.264100000	1.974500000	0.122500000
C	-5.007200000	1.496900000	-1.740100000
H	-5.511700000	0.771600000	-2.114600000
H	-5.499300000	2.315300000	-1.839600000
H	-4.167000000	1.571400000	-2.198300000
C	-4.764800000	-1.271700000	-0.015600000
H	-5.588200000	-1.166900000	-0.516500000
H	-4.247700000	-1.977000000	-0.434600000
C	-5.092800000	-1.670500000	1.408500000
H	-5.589600000	-0.966400000	1.831700000
H	-5.617000000	-2.473800000	1.403400000
H	-4.278100000	-1.823000000	1.893300000
C	-2.683600000	0.000000000	0.000000000

$Cu(dtc)_2$ dimer

Cu	0.000000000	0.000000000	0.000000000
S	1.764000000	1.420700000	-0.441500000
S	1.829800000	-1.445300000	-0.166700000
C	2.728600000	0.000000000	-0.481700000
N	4.019700000	-0.000400000	-0.755600000
C	4.739800000	1.237700000	-1.111300000
H	4.093100000	1.904500000	-1.453100000
H	5.386800000	1.043100000	-1.834400000
C	5.482900000	1.824300000	0.080100000
H	4.847000000	2.005000000	0.804500000
H	5.920600000	2.660000000	-0.186000000
H	6.158800000	1.185800000	0.390100000
C	4.835800000	-1.227700000	-0.711400000
H	4.407100000	-1.881300000	-0.103500000
H	5.728500000	-1.011000000	-0.342100000
C	5.003700000	-1.858000000	-2.081700000
H	4.129000000	-2.143300000	-2.418700000
H	5.596500000	-2.635300000	-2.012300000
H	5.393200000	-1.202900000	-2.696300000

S	-1.819100000	1.436300000	-0.172400000
S	-1.768100000	-1.448400000	-0.342800000
C	-2.718900000	-0.012200000	-0.415500000
N	-4.019700000	-0.017500000	-0.659800000
C	-4.807400000	1.231600000	-0.658400000
H	-5.596400000	1.125200000	-1.246400000
H	-4.254300000	1.970600000	-1.016600000
C	-5.265600000	1.576400000	0.745500000
H	-5.816400000	0.845900000	1.098100000
H	-5.792100000	2.401700000	0.723600000
H	-4.482900000	1.703500000	1.322500000
C	-4.767800000	-1.265000000	-0.898300000
H	-5.678500000	-1.178900000	-0.518900000
H	-4.314100000	-2.013500000	-0.435200000
C	-4.868200000	-1.579300000	-2.384200000
H	-5.265400000	-0.816000000	-2.852100000
H	-5.431400000	-2.371400000	-2.512900000
H	-3.972700000	-1.753900000	-2.742100000
Cu	1.829800000	-1.445300000	2.611900000
S	0.065800000	-2.866000000	3.053300000
S	0.000000000	0.000000000	2.778600000
C	-0.898800000	-1.445300000	3.093600000
N	-2.189900000	-1.444900000	3.367500000
C	-2.910000000	-2.683100000	3.723200000
H	-2.263300000	-3.349900000	4.065000000
H	-3.557000000	-2.488400000	4.446300000
C	-3.653100000	-3.269700000	2.531800000
H	-3.017200000	-3.450400000	1.807400000
H	-4.090800000	-4.105300000	2.797900000
H	-4.329000000	-2.631200000	2.221800000
C	-3.006000000	-0.217700000	3.323200000
H	-2.577300000	0.436000000	2.715300000
H	-3.898600000	-0.434400000	2.954000000
C	-3.173900000	0.412700000	4.693600000
H	-2.299200000	0.697900000	5.030500000
H	-3.766700000	1.189900000	4.624200000
H	-3.563400000	-0.242500000	5.308200000
S	3.648900000	-2.881700000	2.784200000
S	3.597900000	0.003000000	2.954600000
C	4.548700000	-1.433100000	3.027300000
N	5.849500000	-1.427800000	3.271700000
C	6.637200000	-2.676900000	3.270300000
H	7.426200000	-2.570500000	3.858300000
H	6.084100000	-3.415900000	3.628500000

C	7.095400000	-3.021700000	1.866400000
H	7.646200000	-2.291300000	1.513800000
H	7.622000000	-3.847000000	1.888200000
H	6.312700000	-3.148800000	1.289300000
C	6.597600000	-0.180300000	3.510200000
H	7.508400000	-0.266500000	3.130700000
H	6.144000000	0.568100000	3.047000000
C	6.698000000	0.133900000	4.996100000
H	7.095200000	-0.629300000	5.464000000
H	7.261200000	0.926000000	5.124800000
H	5.802500000	0.308500000	5.353900000

$Cu(dtc)_2$ monomer

Cu	0.000000000	0.000000000	0.000000000
S	1.764000000	1.420700000	-0.441500000
S	1.829800000	-1.445300000	-0.166700000
C	2.728600000	0.000000000	-0.481700000
N	4.019700000	-0.000400000	-0.755600000
C	4.739800000	1.237700000	-1.111300000
H	4.093100000	1.904500000	-1.453100000
H	5.386800000	1.043100000	-1.834400000
C	5.482900000	1.824300000	0.080100000
H	4.847000000	2.005000000	0.804500000
H	5.920600000	2.660000000	-0.186000000
H	6.158800000	1.185800000	0.390100000
C	4.835800000	-1.227700000	-0.711400000
H	4.407100000	-1.881300000	-0.103500000
H	5.728500000	-1.011000000	-0.342100000
C	5.003700000	-1.858000000	-2.081700000
H	4.129000000	-2.143300000	-2.418700000
H	5.596500000	-2.635300000	-2.012300000
H	5.393200000	-1.202900000	-2.696300000
S	-1.819100000	1.436300000	-0.172400000
S	-1.768100000	-1.448400000	-0.342800000
C	-2.718900000	-0.012200000	-0.415500000
N	-4.019700000	-0.017500000	-0.659800000
C	-4.807400000	1.231600000	-0.658400000
H	-5.596400000	1.125200000	-1.246400000
H	-4.254300000	1.970600000	-1.016600000
C	-5.265600000	1.576400000	0.745500000
H	-5.816400000	0.845900000	1.098100000
H	-5.792100000	2.401700000	0.723600000
H	-4.482900000	1.703500000	1.322500000
C	-4.767800000	-1.265000000	-0.898300000

H	-5.678500000	-1.178900000	-0.518900000
H	-4.314100000	-2.013500000	-0.435200000
C	-4.868200000	-1.579300000	-2.384200000
H	-5.265400000	-0.816000000	-2.852100000
H	-5.431400000	-2.371400000	-2.512900000
H	-3.972700000	-1.753900000	-2.742100000

Cu doped $Ni(dtc)_2$ monomer

Cu	0.000000000	0.000000000	0.000000000
S	1.696900000	1.403700000	-0.093400000
S	1.691800000	-1.410400000	0.000000000
N	3.998700000	0.008200000	0.064900000
C	4.757500000	-1.231400000	0.259700000
H	5.607400000	-1.165400000	-0.203400000
H	4.264100000	-1.974500000	-0.122500000
C	5.007200000	-1.496900000	1.740100000
H	5.511700000	-0.771600000	2.114600000
H	5.499300000	-2.315300000	1.839600000
H	4.167000000	-1.571400000	2.198300000
C	4.764800000	1.271700000	0.015600000
H	5.588200000	1.166900000	0.516500000
H	4.247700000	1.977000000	0.434600000
C	5.092800000	1.670500000	-1.408500000
H	5.589600000	0.966400000	-1.831700000
H	5.617000000	2.473800000	-1.403400000
H	4.278100000	1.823000000	-1.893300000
C	2.683600000	0.000000000	0.000000000
S	-1.696900000	-1.403700000	0.093400000
S	-1.691800000	1.410400000	0.000000000
N	-3.998700000	-0.008200000	-0.064900000
C	-4.757500000	1.231500000	-0.259700000
H	-5.607400000	1.165400000	0.203400000
H	-4.264100000	1.974500000	0.122500000
C	-5.007200000	1.496900000	-1.740100000
H	-5.511700000	0.771600000	-2.114600000
H	-5.499300000	2.315300000	-1.839600000
H	-4.167000000	1.571400000	-2.198300000
C	-4.764800000	-1.271700000	-0.015600000
H	-5.588200000	-1.166900000	-0.516500000
H	-4.247700000	-1.977000000	-0.434600000
C	-5.092800000	-1.670500000	1.408500000
H	-5.589600000	-0.966400000	1.831700000
H	-5.617000000	-2.473800000	1.403400000
H	-4.278100000	-1.823000000	1.893300000

C	-2.683600000	0.000000000	0.000000000

$Zn_2(dtc)_4$ dimer

Zn	0.000000000	0.000000000	0.000000000
C	1.952600000	1.718400000	-1.000100000
N	2.929500000	2.516100000	-1.397900000
C	2.753500000	3.979100000	-1.468600000
H	1.834800000	4.188400000	-1.774800000
H	3.390600000	4.359000000	-2.123500000
C	2.990900000	4.608900000	-0.103700000
H	2.337900000	4.256700000	0.536800000
H	2.891700000	5.581600000	-0.170900000
H	3.897300000	4.393900000	0.201600000
C	4.282000000	2.016900000	-1.735300000
H	4.459800000	1.185000000	-1.228800000
H	4.955800000	2.689500000	-1.464500000
C	4.417400000	1.738100000	-3.226300000
H	3.806400000	1.016100000	-3.480500000
H	5.339600000	1.472000000	-3.426400000
H	4.195200000	2.547900000	-3.731500000
S	2.182200000	0.000000000	-0.869900000
S	0.389400000	2.342000000	-0.596100000
S	-2.153200000	-0.565000000	-0.717700000
C	-1.895300000	-2.267600000	-0.590900000
N	-2.867100000	-3.130000000	-0.798600000
C	-4.245000000	-2.696800000	-1.139100000
H	-4.634800000	-3.329100000	-1.793700000
H	-4.213200000	-1.801500000	-1.559900000
C	-5.128900000	-2.641300000	0.096900000
H	-5.192900000	-3.534700000	0.493600000
H	-6.023000000	-2.330500000	-0.155100000
H	-4.739500000	-2.021200000	0.749200000
C	-2.697100000	-4.598700000	-0.685800000
H	-3.509200000	-4.992600000	-0.280300000
H	-1.931100000	-4.795300000	-0.088900000
C	-2.453700000	-5.234100000	-2.047100000
H	-3.173500000	-4.977800000	-2.661800000
H	-2.435000000	-6.209600000	-1.954500000
H	-1.595200000	-4.924700000	-2.404200000
S	-0.261700000	-2.806500000	-0.256700000
Zn	-0.261728563	-2.806479964	2.134288032
C	-2.214334431	-4.524915720	3.134411970
N	-3.191266055	-5.322595179	3.532185813
C	-3.015217954	-6.785536131	3.602899745

H	-2.096528181	-6.994906476	3.909054807
H	-3.652283924	-7.165451771	4.257744043
C	-3.252636171	-7.415378386	2.238032216
H	-2.599661475	-7.063173889	1.597446103
H	-3.153424159	-8.388033529	2.305188259
H	-4.159022009	-7.200379488	1.932700125
C	-4.543724075	-4.823386237	3.869580625
H	-4.721521983	-3.991484051	3.363128495
H	-5.217536183	-5.495980710	3.598773682
C	-4.679158819	-4.544612284	5.360540613
H	-4.068116191	-3.822573655	5.614758545
H	-5.601288775	-4.278445354	5.560731721
H	-4.456910801	-5.354400177	5.865828383
S	-2.443879115	-2.806479964	3.004183889
S	-0.651173612	-5.148520726	2.730392979
S	0.000000000	0.000000000	2.391036257
S	1.891512375	-2.241498201	2.852027426
C	1.633545965	-0.538855732	2.725233207
N	2.605337033	0.323559988	2.932864702
C	3.983270560	-0.109649878	3.273415043
H	4.373117474	0.522618148	3.927949683
H	3.951478514	-1.004957169	3.694158199
C	4.867168084	-0.165208266	2.037405757
H	4.931203147	0.728262432	1.640638914
H	5.761228841	-0.476013223	2.289400245
H	4.477734071	-0.785248075	1.385060528
C	2.435363846	1.792231095	2.820053160
H	3.247515637	2.186116370	2.414564122
H	1.669388811	1.988780341	2.223189975
C	2.191962104	2.427601715	4.181340107
H	2.911759640	2.171312721	4.796102938
H	2.173252245	3.403118997	4.088791038
H	1.333423898	2.118251107	4.538455869

Cu doped $Zn(dtc)_2$ monomer

Cu	0.000000000	0.000000000	0.000000000
C	1.952600000	1.718400000	-1.000100000
N	2.929500000	2.516100000	-1.397900000
C	2.753500000	3.979100000	-1.468600000
H	1.834800000	4.188400000	-1.774800000
H	3.390600000	4.359000000	-2.123500000
C	2.990900000	4.608900000	-0.103700000
H	2.337900000	4.256700000	0.536800000
H	2.891700000	5.581600000	-0.170900000

H	3.897300000	4.393900000	0.201600000
C	4.282000000	2.016900000	-1.735300000
H	4.459800000	1.185000000	-1.228800000
H	4.955800000	2.689500000	-1.464500000
C	4.417400000	1.738100000	-3.226300000
H	3.806400000	1.016100000	-3.480500000
H	5.339600000	1.472000000	-3.426400000
H	4.195200000	2.547900000	-3.731500000
S	2.182200000	0.000000000	-0.869900000
S	0.389400000	2.342000000	-0.596100000
S	-2.153200000	-0.565000000	-0.717700000
C	-1.895300000	-2.267600000	-0.590900000
N	-2.867100000	-3.130000000	-0.798600000
C	-4.245000000	-2.696800000	-1.139100000
H	-4.634800000	-3.329100000	-1.793700000
H	-4.213200000	-1.801500000	-1.559900000
C	-5.128900000	-2.641300000	0.096900000
H	-5.192900000	-3.534700000	0.493600000
H	-6.023000000	-2.330500000	-0.155100000
H	-4.739500000	-2.021200000	0.749200000
C	-2.697100000	-4.598700000	-0.685800000
H	-3.509200000	-4.992600000	-0.280300000
H	-1.931100000	-4.795300000	-0.088900000
C	-2.453700000	-5.234100000	-2.047100000
H	-3.173500000	-4.977800000	-2.661800000
H	-2.435000000	-6.209600000	-1.954500000
H	-1.595200000	-4.924700000	-2.404200000
S	-0.261700000	-2.806500000	-0.256700000

Cu doped $Zn_2(dtc)_4$ dimer

Cu	0.000000000	0.000000000	0.000000000
C	1.952605868	1.718435756	-1.000123938
N	2.929537492	2.516115215	-1.397897781
C	2.753489391	3.979056167	-1.468611713
H	1.834799618	4.188426512	-1.774766775
H	3.390555361	4.358971807	-2.123456012
C	2.990907608	4.608898422	-0.103744184
H	2.337932912	4.256693925	0.536841928
H	2.891695596	5.581553565	-0.170900227
H	3.897293446	4.393899524	0.201587907
C	4.281995512	2.016906273	-1.735292593
H	4.459793420	1.185004086	-1.228840463
H	4.955807620	2.689500746	-1.464485650
C	4.417430256	1.738132320	-3.226252581

H	3.806387627	1.016093691	-3.480470514
H	5.339560212	1.471965390	-3.426443689
H	4.195182238	2.547920213	-3.731540351
S	2.182150552	0.000000000	-0.869895857
S	0.389445049	2.342040762	-0.596104947
S	-2.153240939	-0.564981763	-0.717739394
C	-1.895274528	-2.267624233	-0.590945175
N	-2.867065596	-3.130039952	-0.798576670
C	-4.244999123	-2.696830086	-1.139127011
H	-4.634846037	-3.329098112	-1.793661652
H	-4.213207078	-1.801522795	-1.559870167
C	-5.128896647	-2.641271698	0.096882275
H	-5.192931710	-3.534742396	0.493649117
H	-6.022957404	-2.330466741	-0.155112214
H	-4.739462635	-2.021231889	0.749227504
C	-2.697092409	-4.598711059	-0.685765128
H	-3.509244200	-4.992596334	-0.280276090
H	-1.931117374	-4.795260305	-0.088901943
C	-2.453690667	-5.234081679	-2.047052075
H	-3.173488204	-4.977792685	-2.661814906
H	-2.434980808	-6.209598962	-1.954503006
H	-1.595152461	-4.924731071	-2.404167838
S	-0.261728563	-2.806479964	-0.256748225
Zn	-0.261728563	-2.806479964	2.134288032
C	-2.214334431	-4.524915720	3.134411970
N	-3.191266055	-5.322595179	3.532185813
C	-3.015217954	-6.785536131	3.602899745
H	-2.096528181	-6.994906476	3.909054807
H	-3.652283924	-7.165451771	4.257744043
C	-3.252636171	-7.415378386	2.238032216
H	-2.599661475	-7.063173889	1.597446103
H	-3.153424159	-8.388033529	2.305188259
H	-4.159022009	-7.200379488	1.932700125
C	-4.543724075	-4.823386237	3.869580625
H	-4.721521983	-3.991484051	3.363128495
H	-5.217536183	-5.495980710	3.598773682
C	-4.679158819	-4.544612284	5.360540613
H	-4.068116191	-3.822573655	5.614758545
H	-5.601288775	-4.278445354	5.560731721
H	-4.456910801	-5.354400177	5.865828383
S	-2.443879115	-2.806479964	3.004183889
S	-0.651173612	-5.148520726	2.730392979
S	0.000000000	0.000000000	2.391036257
S	1.891512375	-2.241498201	2.852027426

C	1.633545965	-0.538855732	2.725233207
N	2.605337033	0.323559988	2.932864702
C	3.983270560	-0.109649878	3.273415043
H	4.373117474	0.522618148	3.927949683
H	3.951478514	-1.004957169	3.694158199
C	4.867168084	-0.165208266	2.037405757
H	4.931203147	0.728262432	1.640638914
H	5.761228841	-0.476013223	2.289400245
H	4.477734071	-0.785248075	1.385060528
C	2.435363846	1.792231095	2.820053160
H	3.247515637	2.186116370	2.414564122
H	1.669388811	1.988780341	2.223189975
C	2.191962104	2.427601715	4.181340107
H	2.911759640	2.171312721	4.796102938
H	2.173252245	3.403118997	4.088791038
H	1.333423898	2.118251107	4.538455869

Cu doped $Zn_2(dtc)_4$ dimer optimized structure from Gaussian

Cu	0.000000000	0.000000000	0.000000000
S	-1.871956532	1.446532906	-0.199131353
C	-2.845741866	0.035335213	-0.288173278
N	-4.164884892	0.046245391	-0.482018880
C	-4.901137319	1.314306951	-0.658114865
H	-5.704386770	1.117723597	-1.382897376
H	-4.211002031	2.040886810	-1.109207119
C	-5.473350634	1.852884564	0.653352443
H	-6.179626947	1.142900941	1.106737136
H	-6.013559755	2.790099934	0.456745717
H	-4.671192823	2.060143792	1.375031501
C	-4.966622435	-1.193397588	-0.559377799
H	-5.942944905	-0.963948633	-0.108248089
H	-4.484350877	-1.953159357	0.070682905
C	-5.137334903	-1.697414812	-1.992876839
H	-5.623660698	-0.947151594	-2.632723660
H	-5.768127440	-2.597972688	-1.988210689
H	-4.165650058	-1.959181724	-2.434479958
S	-1.931478299	-1.462877825	-0.153685237
C	2.601634309	0.000000000	-1.109915800
N	3.826323064	-0.007873090	-1.649654441
C	4.548690370	1.241730395	-1.951695160
H	3.800396850	2.020016176	-2.157540883
H	5.114231798	1.070481260	-2.879566575
C	5.482441481	1.677304847	-0.821366109
H	4.914620881	1.886565708	0.095777480

H	6.012235952	2.594510779	-1.116661952
H	6.235947080	0.907515588	-0.600403929
C	4.519444231	-1.267323880	-1.979047968
H	4.153136187	-2.040916325	-1.290062048
H	5.587684956	-1.111936623	-1.767333041
C	4.312969745	-1.697186502	-3.432437144
H	3.250040726	-1.885999713	-3.637683250
H	4.871784009	-2.624879565	-3.622884318
H	4.676251727	-0.933318570	-4.134990006
S	1.709473447	-1.440417525	-0.756332237
S	1.750114594	1.449141250	-0.701423446
Zn	-1.946525942	-1.864512682	2.341984303
C	-4.433925399	-2.454796340	3.638921015
N	-5.564874514	-2.700524083	4.321934346
C	-6.300450233	-3.972997061	4.189400472
H	-5.574542056	-4.753449891	3.926436038
H	-6.708819670	-4.211837844	5.182753542
C	-7.420972608	-3.907063030	3.150305572
H	-7.014903436	-3.702908010	2.149837168
H	-7.949376808	-4.871055999	3.118581952
H	-8.156107129	-3.127113300	3.396891344
C	-6.143571400	-1.723639788	5.265242970
H	-5.890343202	-0.716471384	4.908734361
H	-7.236635612	-1.832704288	5.207632202
C	-5.658481088	-1.924651372	6.701987520
H	-4.571303854	-1.779961627	6.770737172
H	-6.146915059	-1.191820553	7.360691559
H	-5.903706444	-2.930163555	7.073590627
S	-3.577081444	-0.948890418	3.854026452
S	-3.768603221	-3.602851460	2.526097991
S	0.000000000	0.000000000	2.586689211
S	0.076646516	-2.960801281	2.956942248
C	0.877240872	-1.417272861	3.077430116
N	2.133400107	-1.338583204	3.546634496
C	2.875219131	-2.523831163	4.019712379
H	3.496253103	-2.195270010	4.866190302
H	2.144905895	-3.248993849	4.402529265
C	3.743566066	-3.158074838	2.932316133
H	4.488339310	-2.447717975	2.545395824
H	4.283123722	-4.020211032	3.350785603
H	3.125451513	-3.509321530	2.094542034
C	2.855138225	-0.053969644	3.652728529
H	3.915967429	-0.268354576	3.457003580
H	2.489735048	0.604618648	2.854934791

C	2.682930660	0.610549861	5.019395986
H	3.035953289	-0.038830843	5.833659018
H	3.268022479	1.541249992	5.051102853
H	1.627836724	0.859291094	5.199857258

Zn doped $Cu_2(dtc)_4$ dimer optimized from Gaussian.

Cu	0.000000000	0.000000000	0.000000000
S	1.773690756	1.448588548	-0.646444803
S	1.697796164	-1.437585178	-0.772853989
C	2.610728261	0.000000000	-1.084102442
N	3.839580634	-0.009412019	-1.613955803
C	4.582574183	1.238155846	-1.871924342
H	5.146884922	1.089607777	-2.804498236
H	3.846959166	2.034867963	-2.050965688
C	5.521844351	1.618060337	-0.725890365
H	6.262363460	0.828638517	-0.532551338
H	6.066938873	2.536444544	-0.987696284
H	4.957128884	1.803166692	0.198387679
C	4.519786454	-1.267466672	-1.973954874
H	5.587963808	-1.131518425	-1.748861039
H	4.138510788	-2.056752037	-1.311448080
C	4.320730733	-1.651439808	-3.441236692
H	4.698517508	-0.871213982	-4.117671519
H	4.870661554	-2.579368494	-3.654777938
H	3.257556652	-1.821574845	-3.661030232
S	-1.856038863	1.452488768	-0.219831898
S	-1.949230906	-1.455300961	-0.103175058
C	-2.849607666	0.052331845	-0.235527392
N	-4.176463739	0.080464287	-0.363374258
C	-4.902510712	1.357741032	-0.517517409
H	-4.235245142	2.063142594	-1.032119974
H	-5.757745020	1.159022865	-1.179210297
C	-5.372709612	1.934531517	0.818348687
H	-4.517384828	2.170899182	1.466068357
H	-5.935745648	2.861265261	0.636655111
H	-6.032271070	1.233466301	1.349059815
C	-4.998976710	-1.147173108	-0.380521572
H	-4.489256177	-1.909808423	0.224170473
H	-5.942742978	-0.900691159	0.127526595
C	-5.263305945	-1.657179854	-1.797782136
H	-4.324047986	-1.937993004	-2.294338537
H	-5.908269138	-2.546301630	-1.750381455
H	-5.773297372	-0.901552638	-2.412445313
Zn	-1.931903082	-1.815100912	2.394761779

S	-3.718471009	-3.623069800	2.633111584
S	-3.592955432	-0.928984414	3.886971049
C	-4.421824211	-2.455434197	3.697146563
N	-5.562541512	-2.698489311	4.365548497
C	-6.280677809	-3.982494806	4.248271159
H	-6.720630522	-4.194312872	5.234078346
H	-5.540138354	-4.764424895	4.035124460
C	-7.365140876	-3.960453973	3.169778918
H	-8.115438091	-3.180729758	3.366211643
H	-7.883278839	-4.930342342	3.149600785
H	-6.925504491	-3.783563432	2.178355751
C	-6.171584255	-1.707611105	5.274059607
H	-7.262406713	-1.821501304	5.187639723
H	-5.911210428	-0.706034992	4.907273309
C	-5.726274134	-1.881573762	6.727128404
H	-5.980186161	-2.880621173	7.110380024
H	-6.233480374	-1.137935725	7.358966801
H	-4.641472803	-1.734140762	6.823288688
S	0.100823576	-2.957043675	2.940224815
S	0.000000000	0.000000000	2.598501837
C	0.899743604	-1.416178040	3.057423996
N	2.165709095	-1.334534427	3.497445894
C	2.923163380	-2.522645114	3.937836953
H	2.205266752	-3.252593706	4.335274871
H	3.568425347	-2.200174503	4.768229025
C	3.760015877	-3.145967030	2.819710567
H	3.118510762	-3.486928450	1.995381840
H	4.309404905	-4.013650955	3.213299353
H	4.495061866	-2.432463376	2.419958506
C	2.879538841	-0.046807347	3.614064701
H	2.481223193	0.629534926	2.847788730
H	3.935062377	-0.245630219	3.377038883
C	2.746183368	0.577425653	5.004015255
H	1.695971460	0.814831754	5.224061830
H	3.327710904	1.509907204	5.044696492
H	3.126746764	-0.092931549	5.788338671

$Fe(dtc)_3$ crystal structure at 298 K

Fe	0.000000000	0.000000000	0.000000000
C	-1.061000000	-1.321900000	2.240700000
C	-2.424500000	-3.143000000	3.118400000
C	-3.203600000	-3.527400000	3.613500000
C	-1.217100000	-1.491400000	4.682000000
C	-2.238600000	-0.507900000	5.222200000

N	-1.562900000	-1.955800000	3.312200000
S	-1.410000000	-1.775500000	0.633700000
S	0.000000000	0.000000000	2.354200000
H	-2.788600000	-3.008100000	2.196800000
H	-1.768600000	-3.897800000	3.111000000
H	-3.515100000	-4.358300000	3.152500000
H	-3.947800000	-2.859800000	3.635000000
H	-2.928000000	-3.749100000	4.549000000
H	-1.177800000	-2.283400000	5.291100000
H	-0.322300000	-1.045700000	4.655600000
H	-1.971300000	-0.220400000	6.141800000
H	-3.136900000	-0.945800000	5.258200000
H	-2.281800000	0.291500000	4.622900000
C	2.778300000	0.000000000	-0.534200000
C	4.871800000	1.308300000	-0.838900000
C	5.699800000	1.479500000	0.467000000
C	4.795700000	-1.265000000	-1.101900000
C	4.963800000	-1.411100000	-2.614800000
N	4.101300000	-0.013800000	-0.799300000
S	1.890400000	1.406800000	-0.161400000
S	1.817900000	-1.415500000	-0.501600000
H	4.224900000	2.066300000	-0.922700000
H	5.489700000	1.308200000	-1.625200000
H	6.200100000	2.344600000	0.434000000
H	6.348300000	0.723000000	0.552600000
H	5.083900000	1.480800000	1.254900000
H	5.696100000	-1.258400000	-0.667000000
H	4.261300000	-2.034200000	-0.751500000
H	5.438800000	-2.267600000	-2.816700000
H	5.498500000	-0.642900000	-2.967000000
H	4.064200000	-1.418500000	-3.051500000
C	-1.710300000	1.396100000	-1.782800000
C	-3.402200000	3.149400000	-2.118400000
C	-3.471200000	4.326600000	-3.028100000
C	-2.579200000	1.630900000	-4.058700000
C	-3.865700000	0.861700000	-4.292900000
N	-2.462300000	2.076700000	-2.627100000
S	-1.547200000	1.780500000	-0.113200000
S	-0.766400000	0.039600000	-2.222400000
H	-3.083500000	3.455800000	-1.221500000
H	-4.318300000	2.757800000	-2.031300000
H	-4.102000000	5.004100000	-2.650100000
H	-3.796000000	4.034700000	-3.927700000
H	-2.561600000	4.732500000	-3.118200000

H	-1.802400000	1.041700000	-4.280700000
H	-2.568300000	2.435600000	-4.652200000
H	-3.915800000	0.578900000	-5.250700000
H	-4.648100000	1.445900000	-4.077000000
H	-3.882500000	0.052400000	-3.705600000

$Mo(dtc)_4$

Mo	0.000000000	0.000000000	0.000000000
C	-2.916400000	5.197900000	0.021600000
C	-2.158100000	2.099600000	-0.524000000
C	-3.928700000	2.955800000	-2.056600000
C	-3.280800000	3.778500000	-3.145700000
C	-3.531100000	3.977300000	0.303000000
N	-3.107900000	3.003300000	-0.766200000
S	-1.666000000	0.936000000	-1.650900000
S	-1.285900000	1.984500000	0.913400000
H	-3.176600000	5.870300000	0.714400000
H	-3.208100000	5.518700000	-0.879600000
H	-1.923300000	5.080800000	0.027900000
H	-4.843200000	3.317300000	-1.875100000
H	-3.999800000	2.006600000	-2.363300000
H	-3.836300000	3.730300000	-3.975800000
H	-2.366700000	3.420100000	-3.335700000
H	-3.209900000	4.730500000	-2.847600000
H	-3.240100000	3.647100000	1.200900000
H	-4.525200000	4.084900000	0.293100000
C	0.248100000	-2.103300000	-2.231700000
C	1.554700000	-3.058700000	-4.059200000
C	2.497100000	-4.103300000	-3.572000000
C	-0.784500000	-3.917500000	-3.512500000
C	-1.716800000	-3.316400000	-4.532600000
N	0.306500000	-2.985100000	-3.231600000
S	1.406300000	-0.904600000	-1.886600000
S	-1.085400000	-1.983000000	-1.154200000
H	1.301900000	-3.269500000	-5.003500000
H	2.014300000	-2.171300000	-4.026800000
H	3.311400000	-4.115300000	-4.152400000
H	2.050900000	-4.997600000	-3.606100000
H	2.763100000	-3.899700000	-2.629700000
H	-0.407500000	-4.772100000	-3.869600000
H	-1.289100000	-4.102100000	-2.669100000
H	-2.461400000	-3.956300000	-4.722200000
H	-1.213400000	-3.131700000	-5.376700000
H	-2.094900000	-2.461900000	-4.176500000

S	-1.406400000	-0.904600000	1.886400000
S	1.085000000	-1.983400000	1.153900000
C	-0.248400000	-2.103500000	2.231400000
N	-0.307100000	-2.985300000	3.231200000
C	-1.555200000	-3.058900000	4.058800000
C	0.783700000	-3.918100000	3.511900000
C	-2.497900000	-4.103300000	3.571500000
C	1.716100000	-3.317200000	4.532100000
H	-1.302600000	-3.269700000	5.003000000
H	-2.014700000	-2.171300000	4.026500000
H	0.406600000	-4.772700000	3.869100000
H	1.288400000	-4.102700000	2.668600000
H	-3.312100000	-4.115100000	4.152000000
H	-2.051800000	-4.997600000	3.605500000
H	-2.763800000	-3.899500000	2.629200000
H	2.460600000	-3.957300000	4.721800000
H	1.212900000	-3.132500000	5.376300000
H	2.094500000	-2.462700000	4.176100000
S	1.666300000	0.935400000	1.651000000
S	1.286300000	1.984300000	-0.913200000
C	2.158700000	2.099200000	0.524200000
N	3.108400000	3.002700000	0.766500000
C	3.929400000	2.954800000	2.056900000
C	3.532000000	3.976700000	-0.302600000
C	3.281500000	3.777500000	3.146100000
C	2.917500000	5.197300000	-0.021100000
H	4.000300000	2.005600000	2.363400000
H	4.844000000	3.316100000	1.875300000
H	4.526100000	4.084100000	-0.292700000
H	3.240800000	3.646500000	-1.200500000
H	3.837000000	3.729100000	3.976200000
H	2.367400000	3.419300000	3.336000000
H	3.210800000	4.729500000	2.848000000
H	3.177900000	5.869700000	-0.713900000
H	3.209300000	5.517900000	0.880100000
H	1.924300000	5.080400000	-0.027400000

APPENDIX C

SUPPORTING INFORMATION FOR CHAPTER 5

XAS Workups of $Cu(dtc)_2$ and Na(dtc)

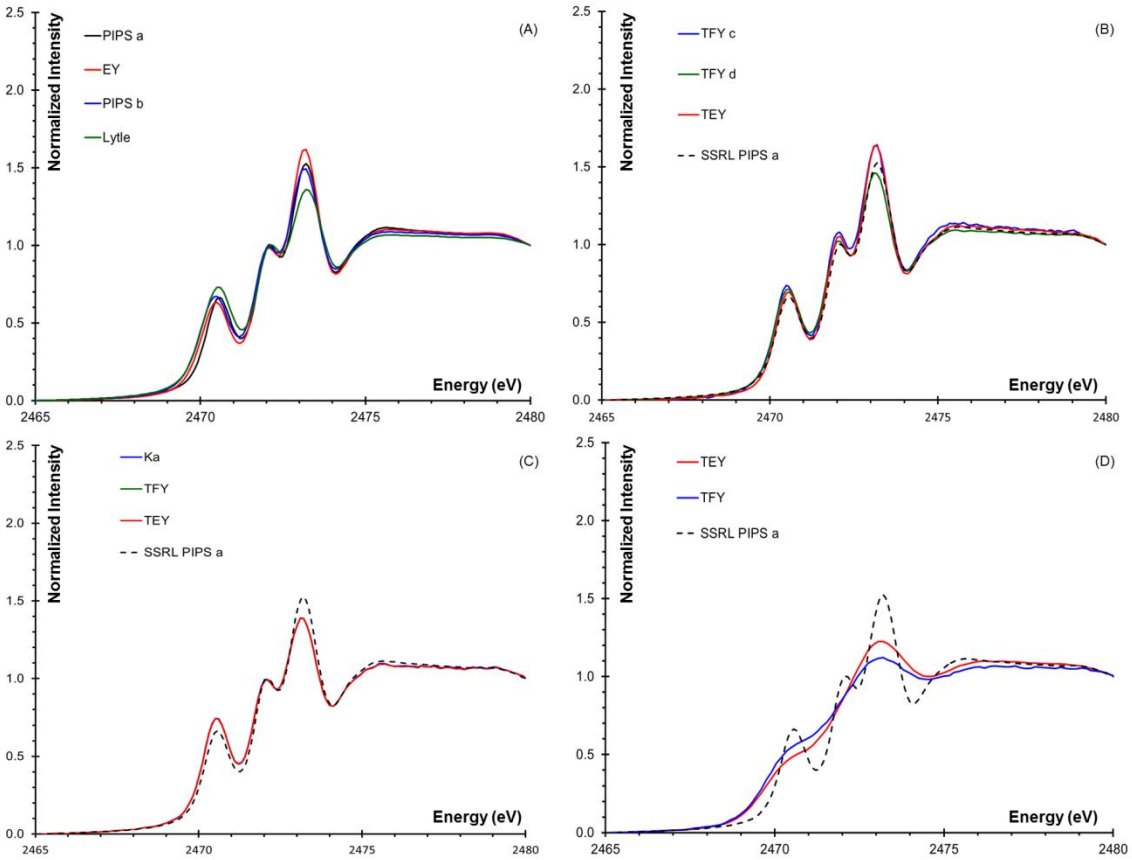


Figure C.1: Shift and scale workups of $Cu(dtc)_2$ at SSRL (A), ALS (B), CLS (C), and SRC (D).

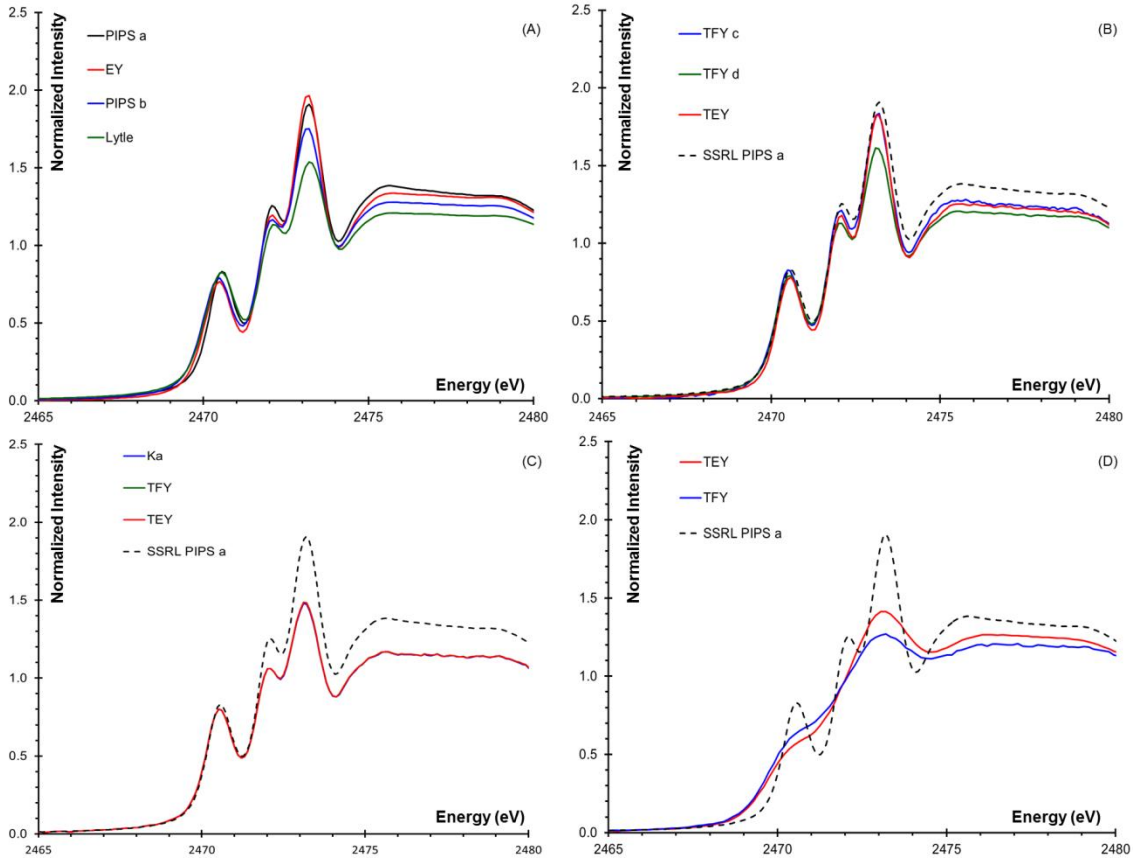


Figure C.2: Arctangent fit to shift and scale workups of $Cu(dtc)_2$ at SSRL (A), ALS (B), CLS (C), and SRC (D).

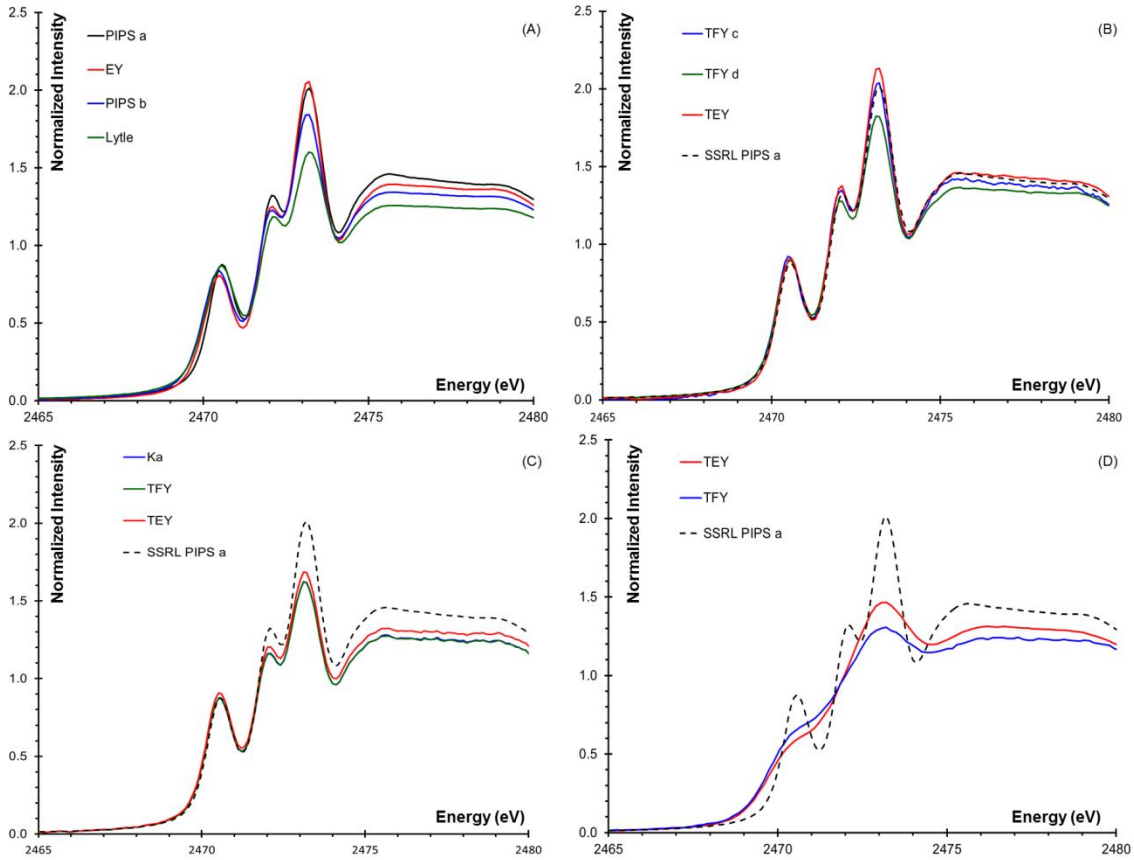


Figure C.3: ADRP workups of $Cu(dtc)_2$ at SSRL (A), ALS (B), CLS (C), and SRC (D).

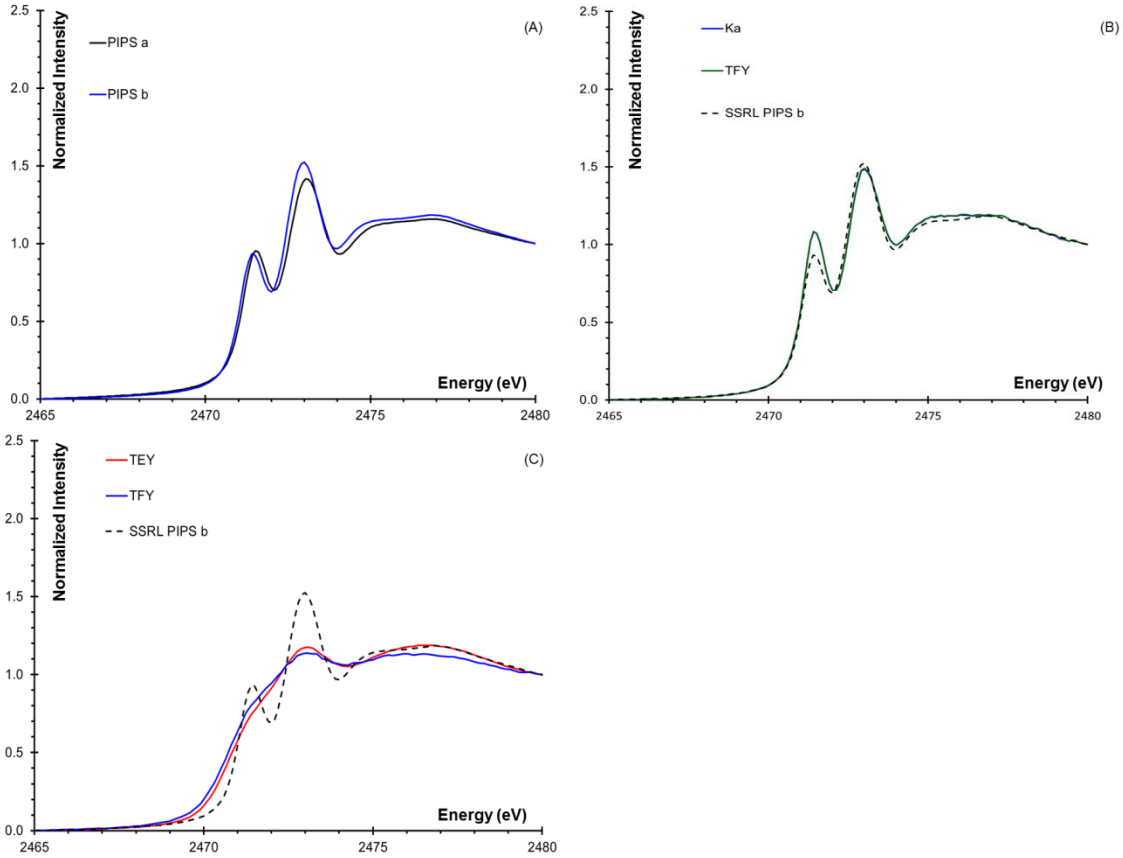


Figure C.4: Shift and scale workups of Na(dtc) at SSRL (A), CLS (B), and SRC (C).

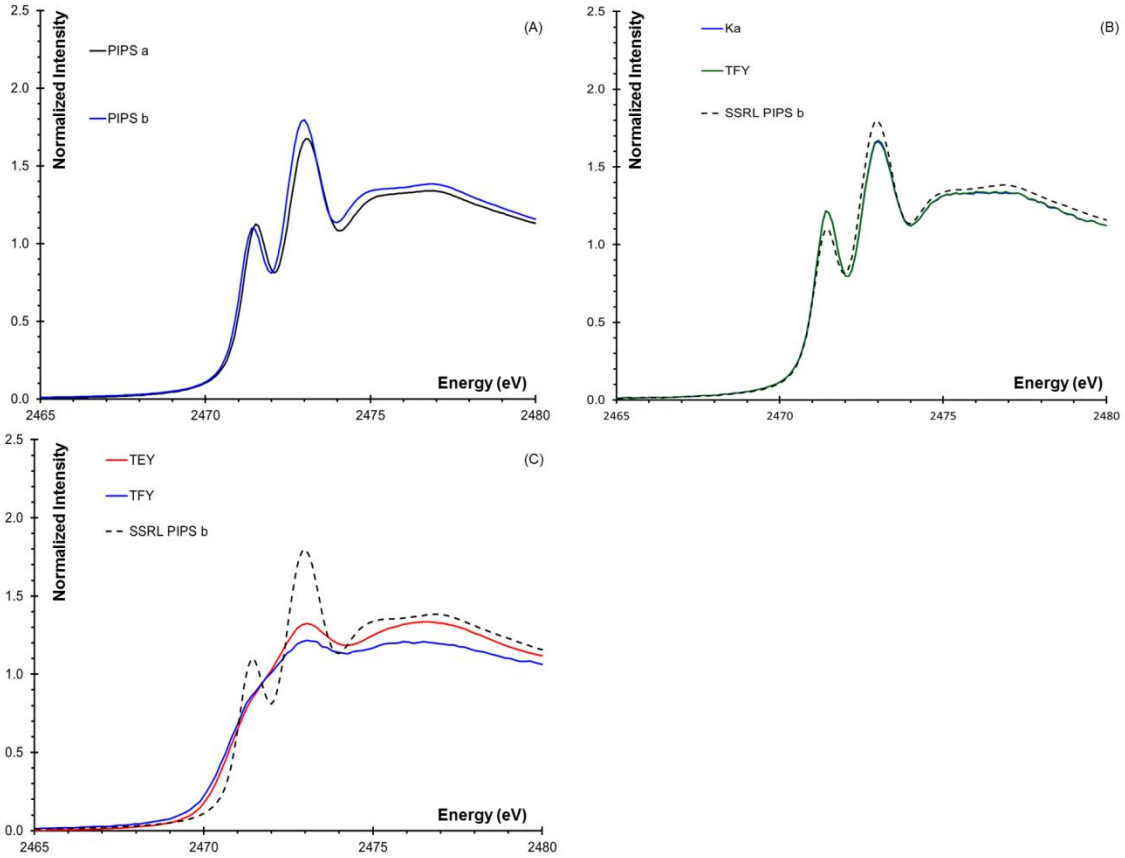


Figure C.5: Arctangent fit of shift and scale workups of Na(dtc) at SSRL (A), CLS (B), and SRC (C).

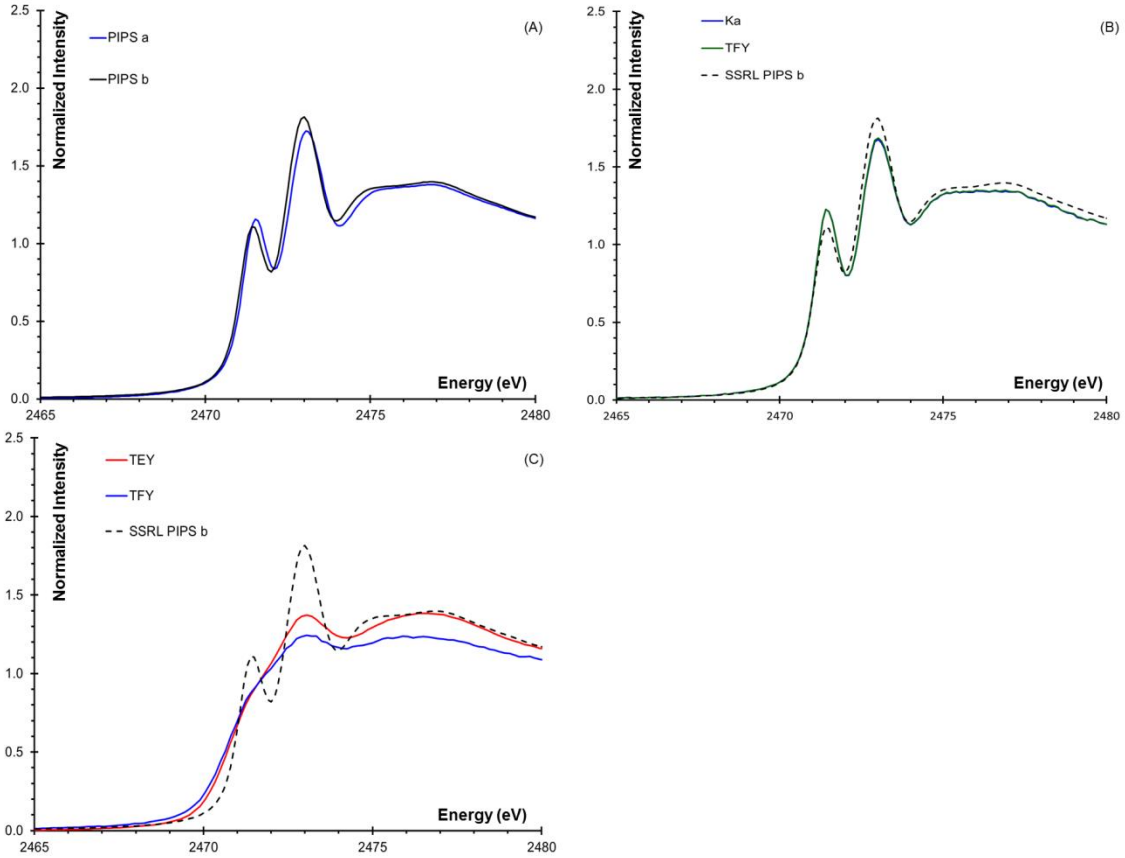


Figure C.6: ADRP workups of Na(dtc) at SSRL (A), CLS (B), and SRC (C).

TD-DFT of $Cu(dtc)_2$ and Na(dtc)

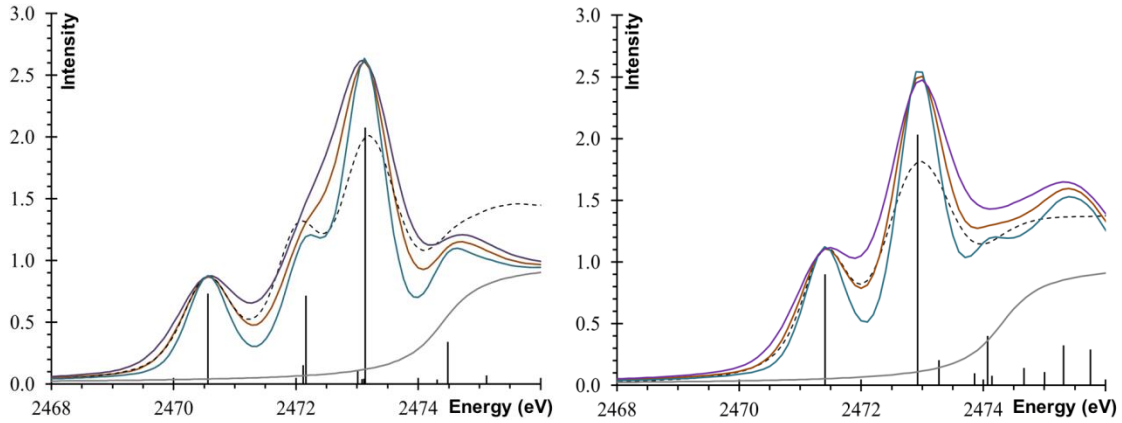


Figure C.7: Calculated S K-edge of $Cu(dtc)_2$ (left) and Na(dtc) (right) using B(30HF)P86/def2-TZVP. The line widths range from 0.8 (light blue), 1.0 (brown), and 1.2 (purple) eV. The edge jump was mimicked with an arctangent function.

Ground State Description of S K-edge XAS of Na(dtc)

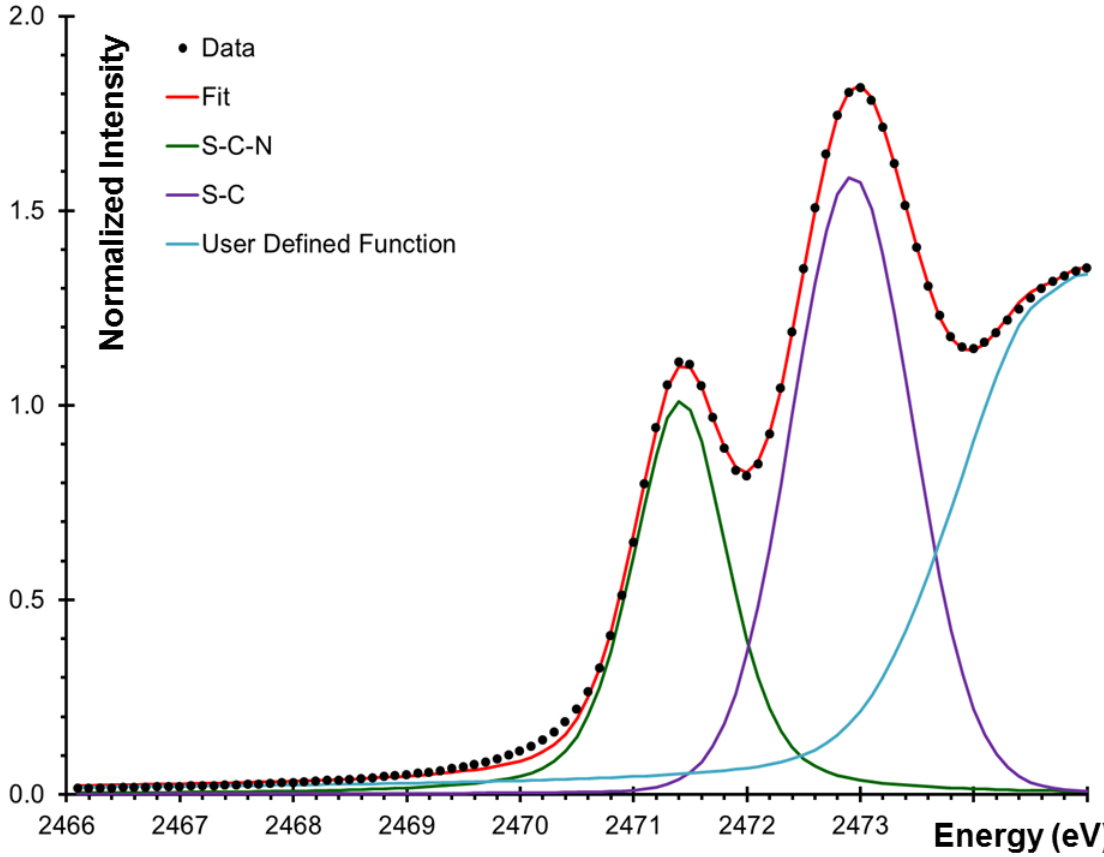


Figure C.8: Ground state fit of Na(dtc) collected from SSRL that utilizes one peak for the S-C-N π^* and C-S σ^* orbitals, and a user defined function to fit the edge jump and neighboring EXAFS features.

Atomic Coordinates for Computational Models of $Cu(dtc)_2$ and Na(dtc) Complexes

$Cu(dtc)_2$ monomer from $Cu_2(dtc)_4$ dimer crystal structure

Cu	-0.026232000	-0.166403000	-0.470676000
S	1.743163000	-1.382585000	0.375053000
S	1.807924000	1.244264000	-0.803709000
C	2.710064000	-0.030074000	-0.056503000
N	4.005569000	0.049546000	0.182832000
C	4.729978000	-1.014347000	0.905009000
H	4.088231000	-1.532383000	1.452243000
H	5.389235000	-0.602691000	1.517654000
C	5.452308000	-1.956256000	-0.047242000
H	4.804141000	-2.355133000	-0.665742000
H	5.893332000	-2.665595000	0.465598000
H	6.123673000	-1.454998000	-0.555695000
C	4.822326000	1.192709000	-0.264575000
H	4.384310000	1.620161000	-1.043052000
H	5.708407000	0.863372000	-0.558763000
C	5.013964000	2.227370000	0.829073000
H	4.145375000	2.611183000	1.070463000
H	5.606514000	2.937621000	0.505344000
H	5.412879000	1.800876000	1.614953000
S	-1.844027000	-1.460032000	0.180533000
S	-1.786531000	1.327016000	-0.582347000
C	-2.737734000	-0.004045000	-0.039021000
N	-4.034255000	0.087740000	0.210850000
C	-4.823485000	-1.090966000	0.621549000
H	-5.602365000	-0.796765000	1.156632000
H	-4.265403000	-1.680009000	1.188893000
C	-5.305501000	-1.863945000	-0.590815000
H	-5.861253000	-1.281183000	-1.150137000
H	-5.832694000	-2.635360000	-0.297770000
H	-4.532776000	-2.174184000	-1.108823000
C	-4.776771000	1.350772000	0.048905000
H	-5.693812000	1.153705000	-0.268840000
H	-4.329956000	1.908636000	-0.636407000
C	-4.851888000	2.124761000	1.357392000
H	-5.242167000	1.554033000	2.051095000
H	-5.411847000	2.920051000	1.234455000
H	-3.950314000	2.398841000	1.626616000

$Cu(dtc)_2$ optimized in Gaussian from $Ni(dtc)_2$ crystal structure using B3LYP functional, and def2-TZVP basis set.

Cu	0.000000000	0.000000000	0.000000000
S	1.848329000	1.459525000	-0.095271000
S	1.866948000	-1.423421000	0.206808000
N	4.122682000	0.039671000	0.124508000
C	4.904822000	-1.195067000	0.270380000
H	5.823343000	-1.063881000	-0.304755000
H	4.343953000	-2.007200000	-0.188652000
C	5.226893000	-1.528504000	1.724069000
H	5.793901000	-0.728686000	2.203953000
H	5.826896000	-2.439386000	1.769824000
H	4.311109000	-1.693345000	2.291312000
C	4.889086000	1.288824000	0.025751000
H	5.775843000	1.172095000	0.651517000
H	4.288880000	2.089472000	0.454193000
C	5.286720000	1.632474000	-1.406726000
H	5.895287000	0.844961000	-1.855034000
H	5.870635000	2.554826000	-1.416868000
H	4.401473000	1.781291000	-2.024535000
C	2.789296000	0.027055000	0.083967000
S	-1.848329000	-1.459525000	0.095271000
S	-1.866948000	1.423421000	-0.206808000
N	-4.122682000	-0.039671000	-0.124508000
C	-4.904822000	1.195067000	-0.270380000
H	-5.823343000	1.063881000	0.304755000
H	-4.343953000	2.007200000	0.188652000
C	-5.226893000	1.528504000	-1.724069000
H	-5.793901000	0.728686000	-2.203953000
H	-5.826896000	2.439386000	-1.769824000
H	-4.311109000	1.693345000	-2.291312000
C	-4.889086000	-1.288824000	-0.025751000
H	-5.775843000	-1.172095000	-0.651517000
H	-4.288880000	-2.089472000	-0.454193000
C	-5.286720000	-1.632474000	1.406726000
H	-5.895287000	-0.844961000	1.855034000
H	-5.870635000	-2.554826000	1.416868000
H	-4.401473000	-1.781291000	2.024535000
C	-2.789296000	-0.027055000	-0.083967000

Na(dtc) optimized xyz coordinates from Gaussian using the $NaEt_2dtc•3H_2O$ crystal structure, B(38HF)P86 functional, def2-TZVP basis set, and acetonitrile PCM.

Na	3.530384000	0.000020000	0.000712000
S	1.150463000	-1.416819000	0.460545000
S	1.150090000	1.416744000	-0.461544000
C	0.293647000	-0.000036000	-0.000154000
N	-1.040797000	-0.000042000	0.000163000
C	-1.830331000	1.153975000	-0.403109000
C	-1.830254000	-1.154065000	0.403598000
C	-2.199147000	2.045995000	0.764751000
C	-2.199860000	-2.045737000	-0.764307000
H	-1.266534000	1.713050000	-1.143184000
H	-2.730535000	0.771982000	-0.884924000
H	-1.266018000	-1.713441000	1.143094000
H	-2.730085000	-0.772077000	0.886125000
H	-2.821140000	2.871917000	0.420814000
H	-1.303462000	2.458728000	1.225730000
H	-2.758394000	1.497878000	1.522778000
H	-2.821596000	-2.871799000	-0.420247000
H	-1.304467000	-2.458333000	-1.226008000
H	-2.759587000	-1.497434000	-1.521834000

APPENDIX D

NMRs FROM CHAPTER 6

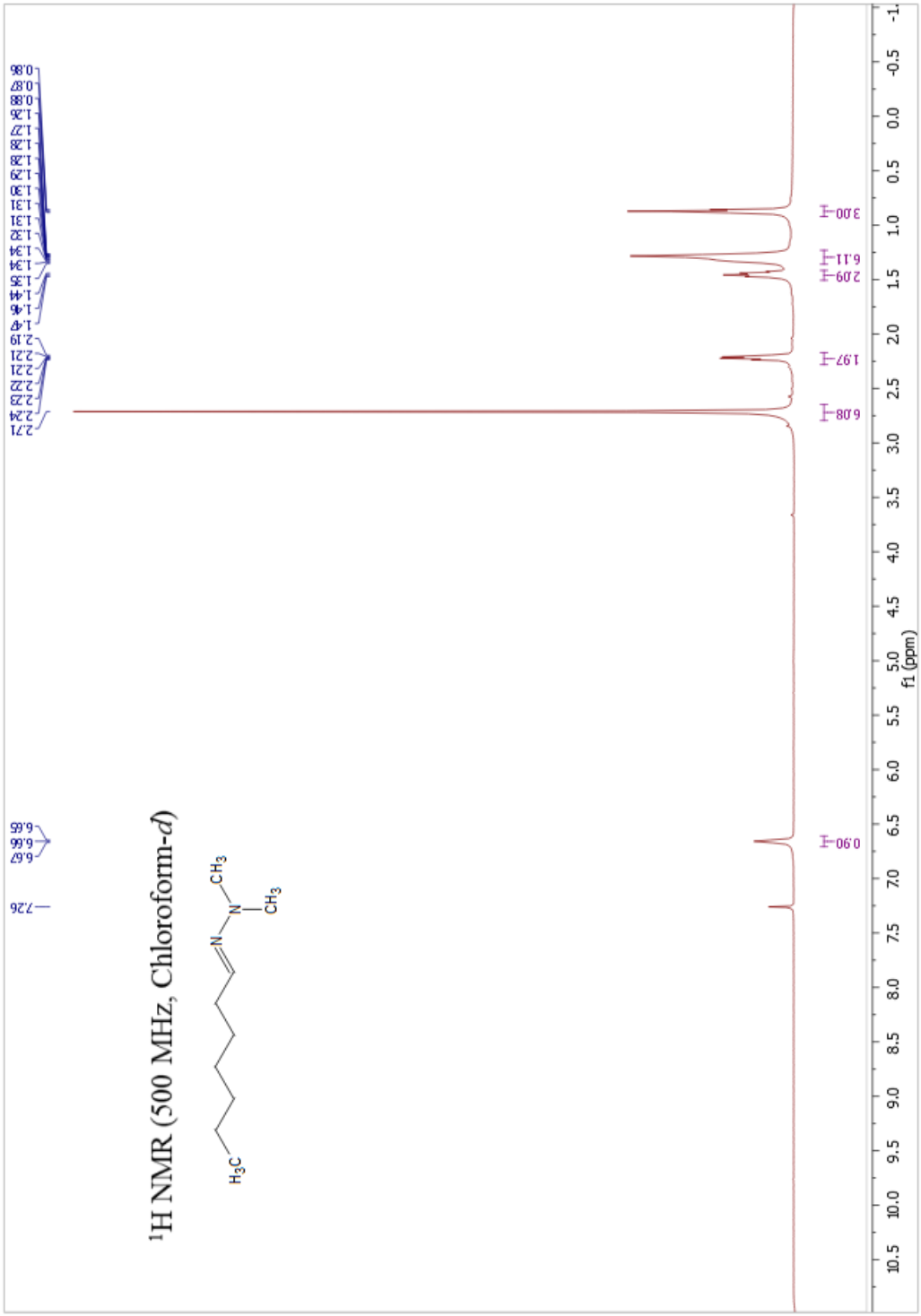


Figure D.1: ^{1}H NMR of 2-heptylidene-1,1-dimethylhydrazine.

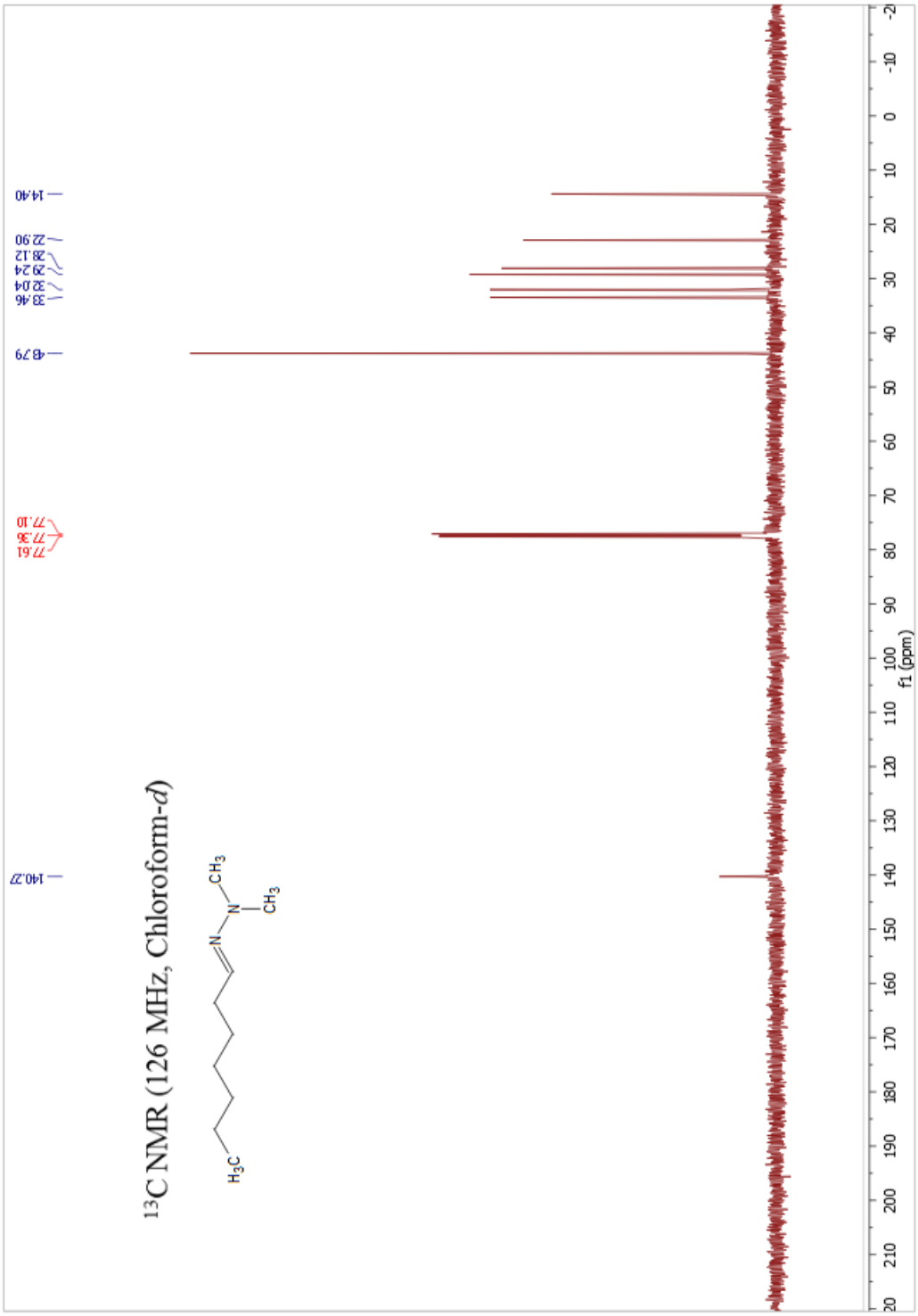


Figure D.2: ^{13}C NMR of 2-heptylidene-1,1-dimethylhydrazine.

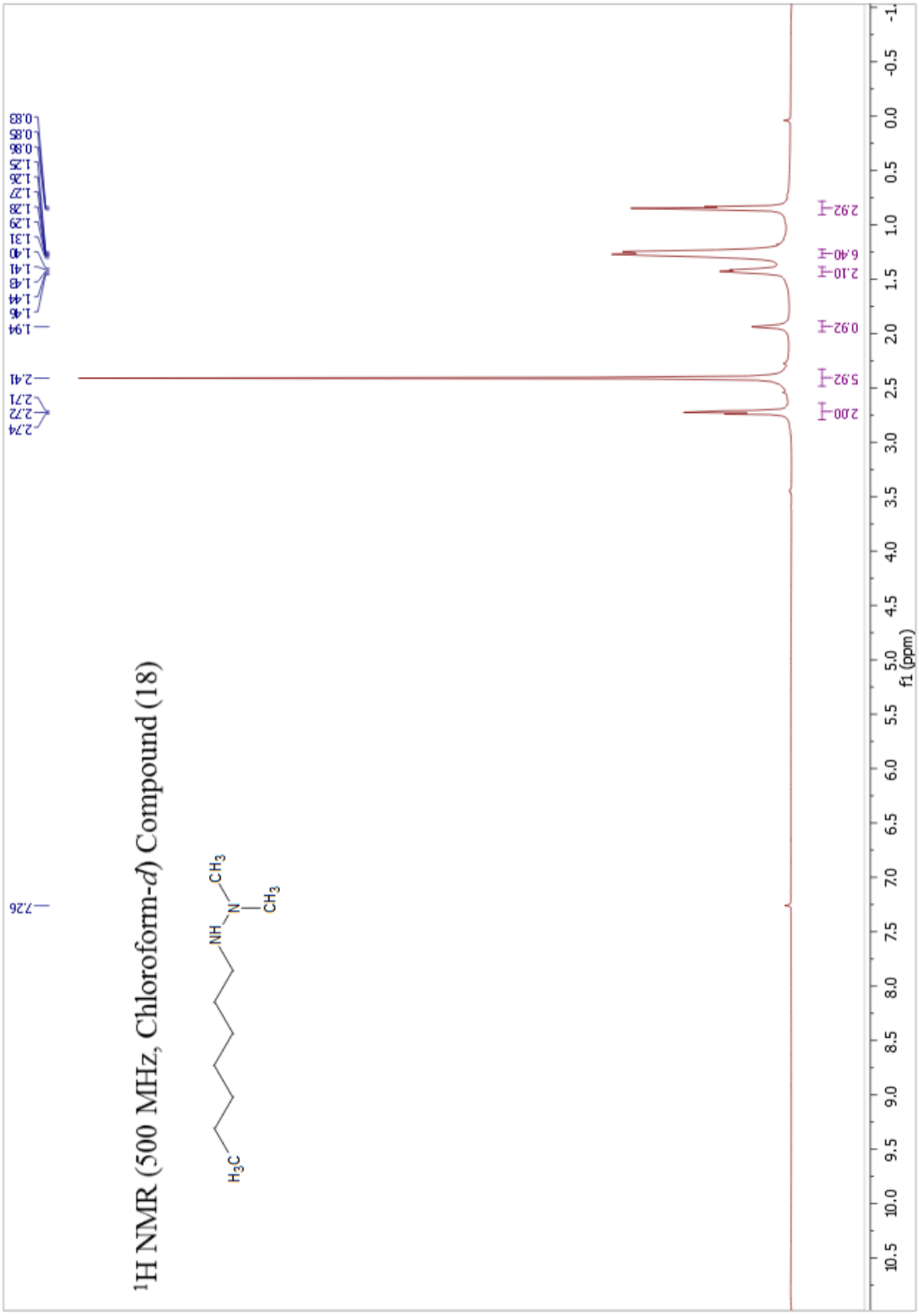


Figure D.3: ^{1}H NMR of 2-heptyl-1,1-dimethylhydrazine (**18**).

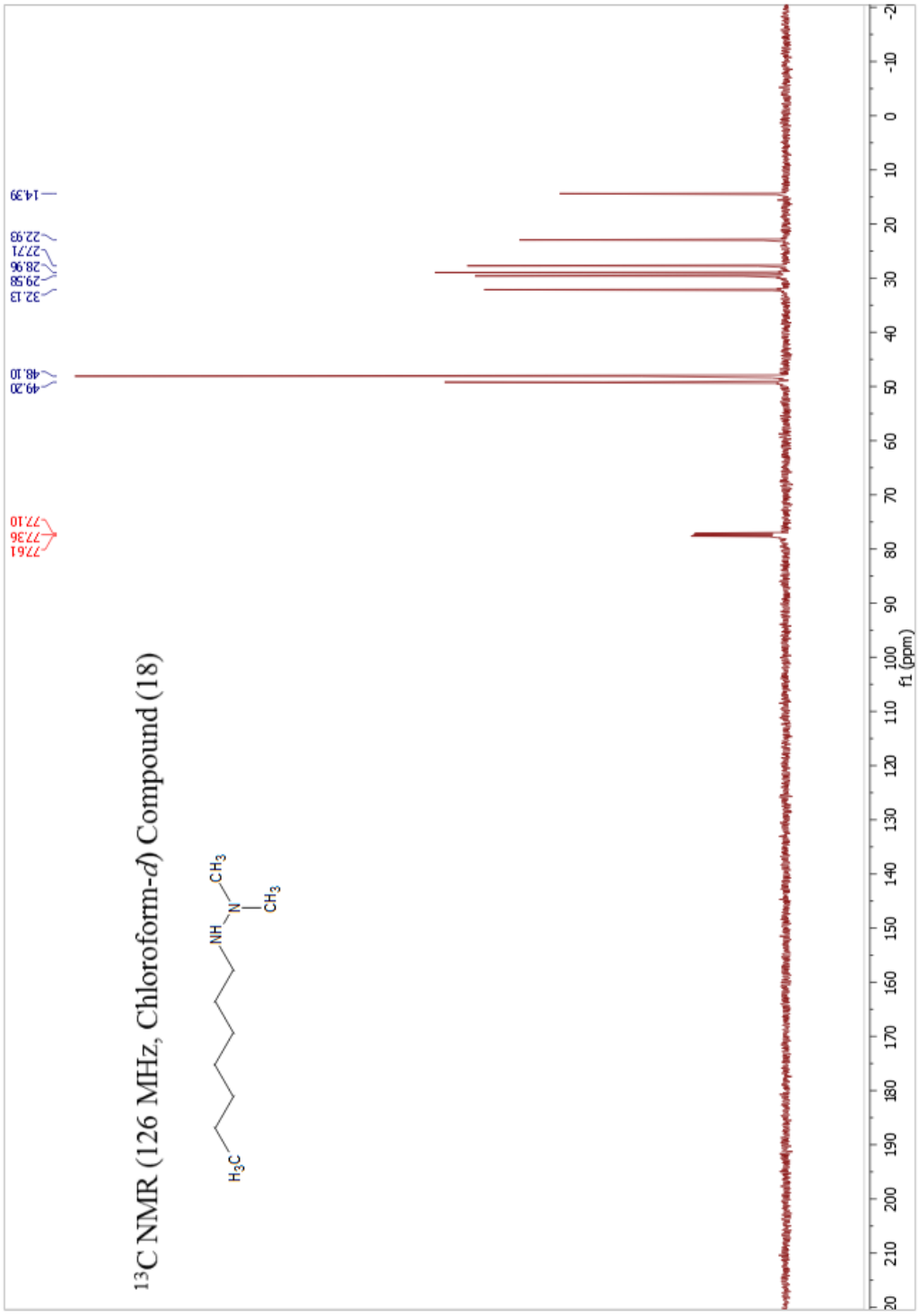


Figure D.4: ^{13}C NMR of 2-heptyl-1,1-dimethylhydrazine (**18**).

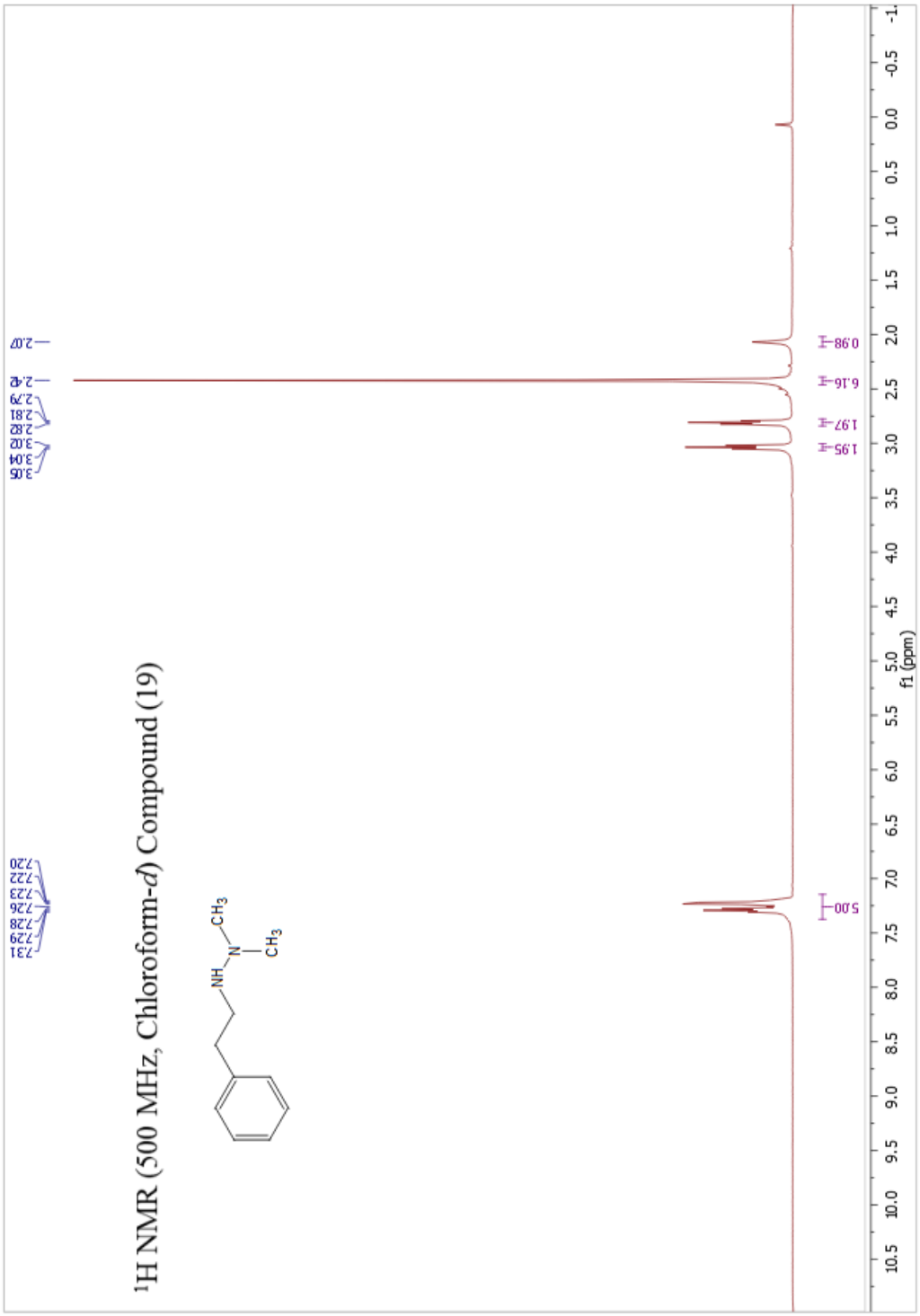


Figure D.5: ^{1}H NMR of 1,1-dimethyl-2-phenethylhydrazine (**19**).

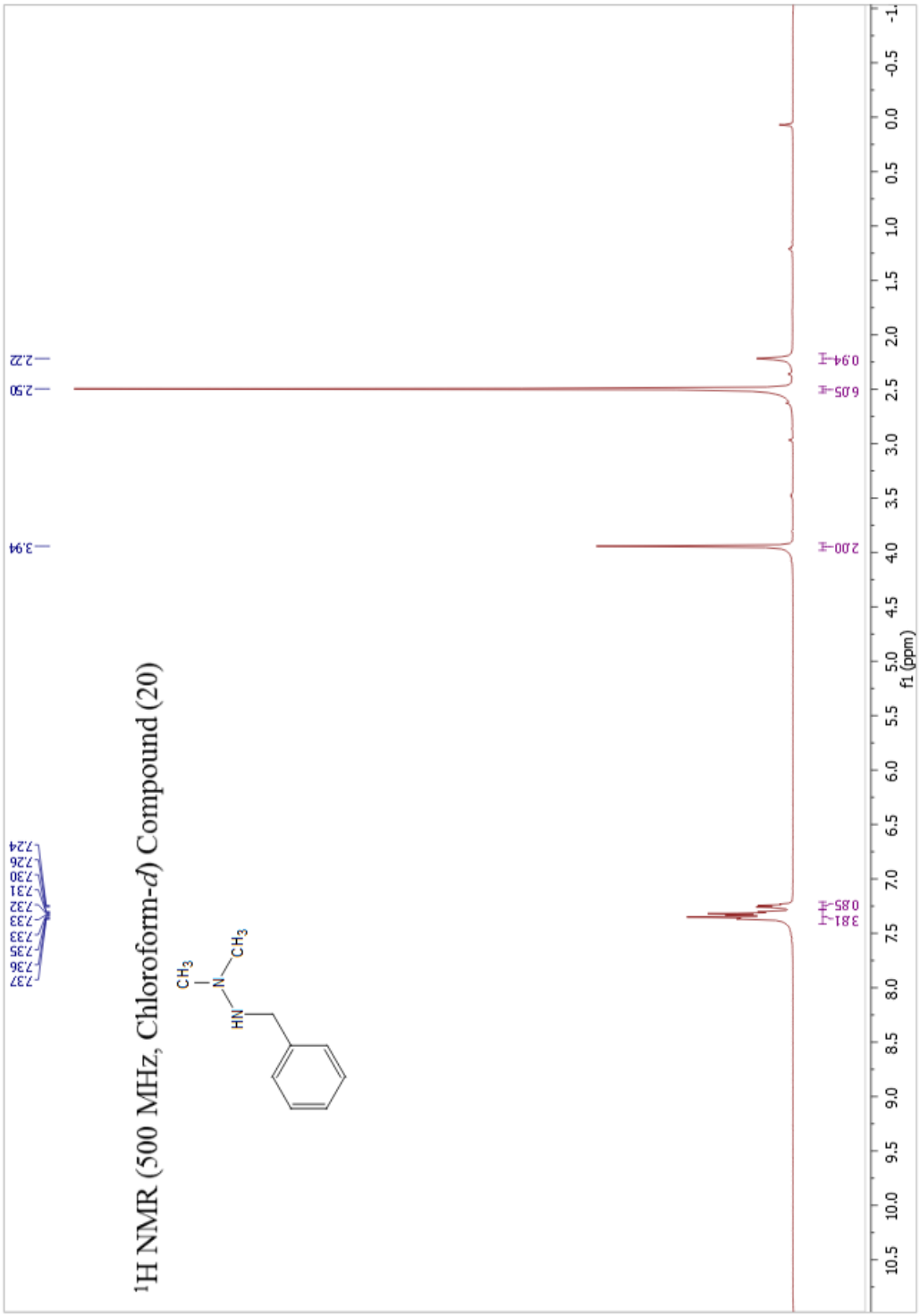


Figure D.6: ^{1}H NMR of 2-benzyl-1,1-dimethylhydrazine (**20**).

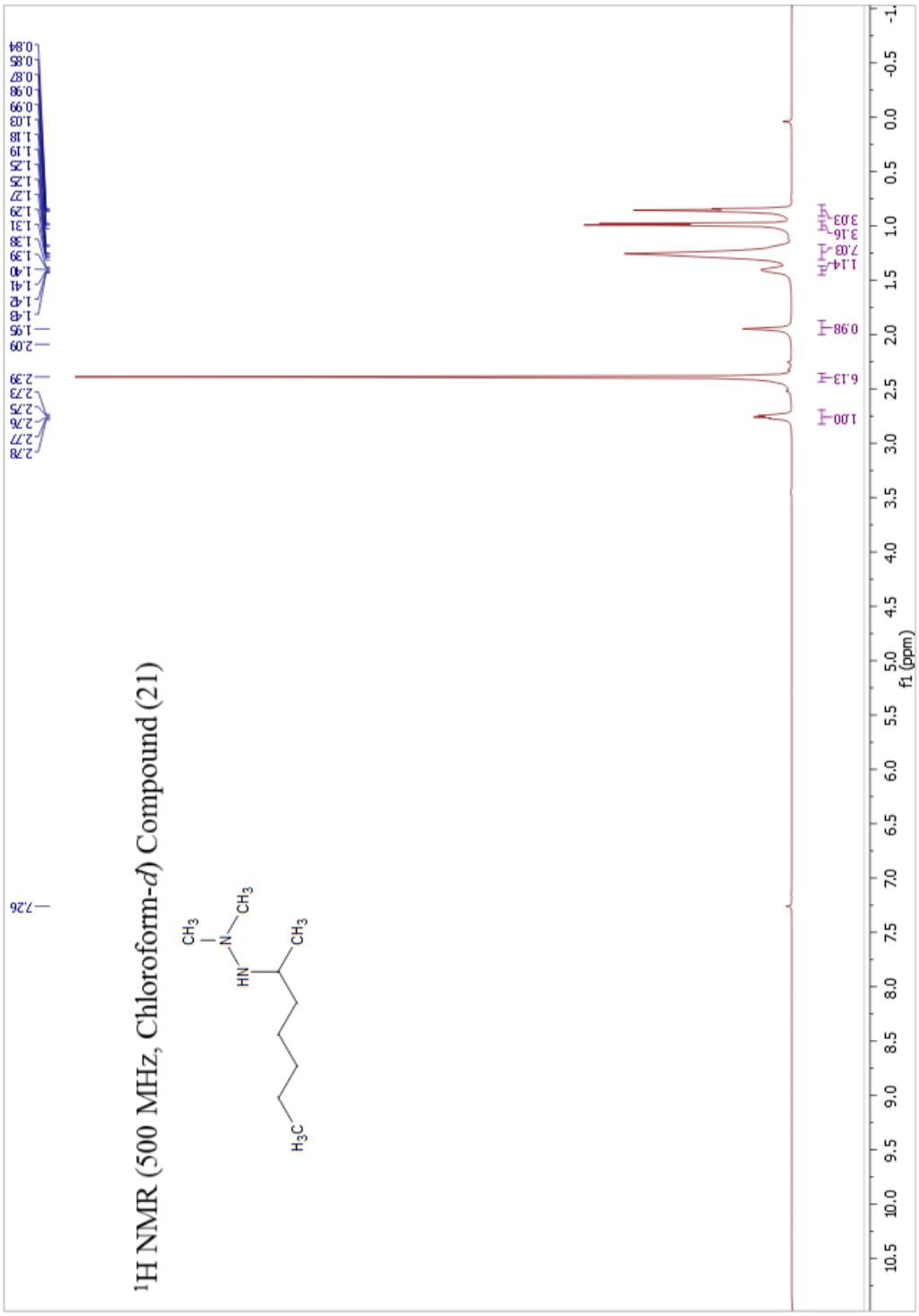


Figure D.7: ^{1}H NMR of 2-(heptan-2-yl)-1,1-dimethylhydrazine (**21**).

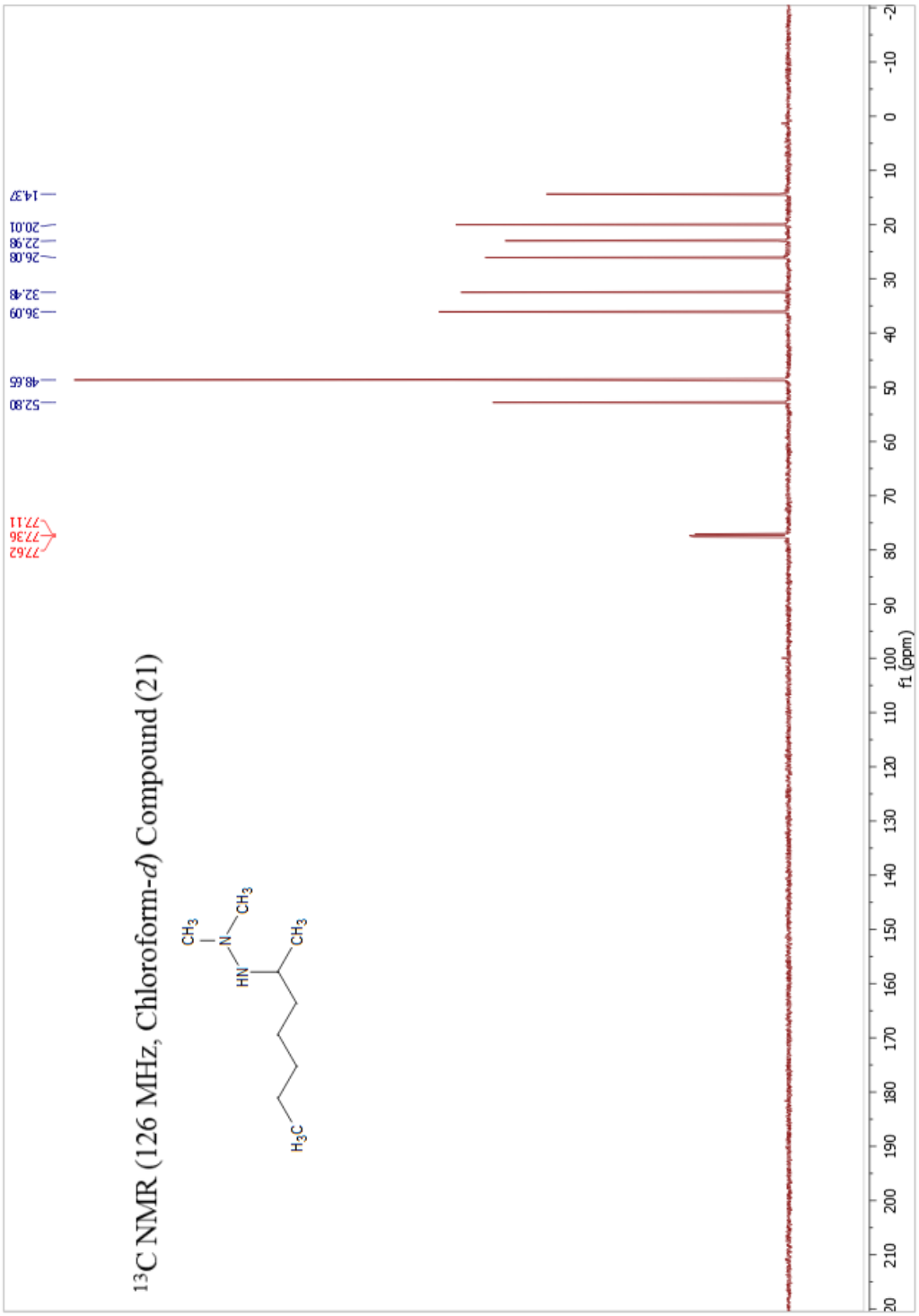


Figure D.8: ^{13}C NMR of 2-(heptan-2-yl)-1,1-dimethylhydrazine (**21**).

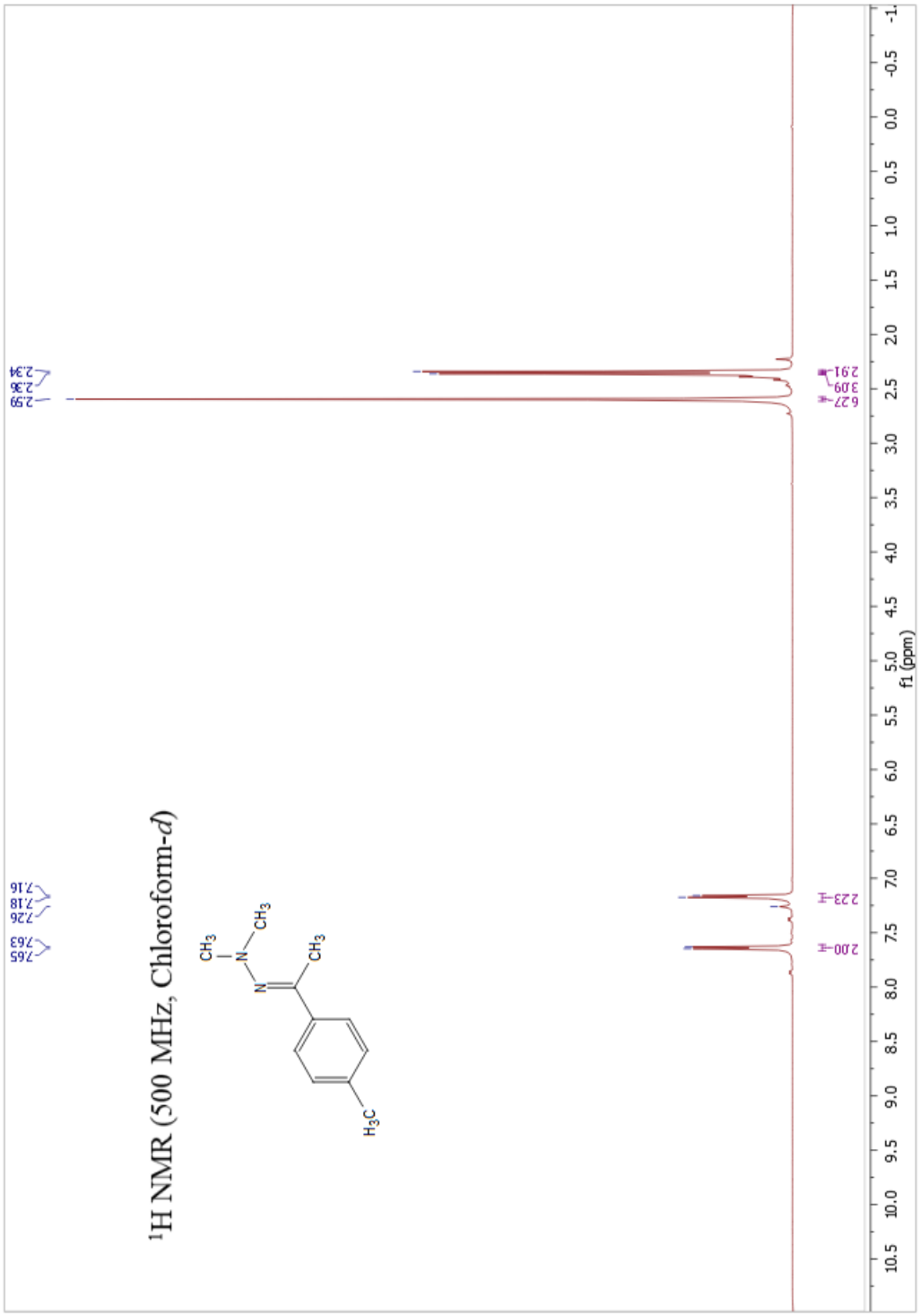


Figure D.9: ^{1}H NMR of (*E*)-1,1-dimethyl-2-(1-p-tolylethylidene)hydrazine.

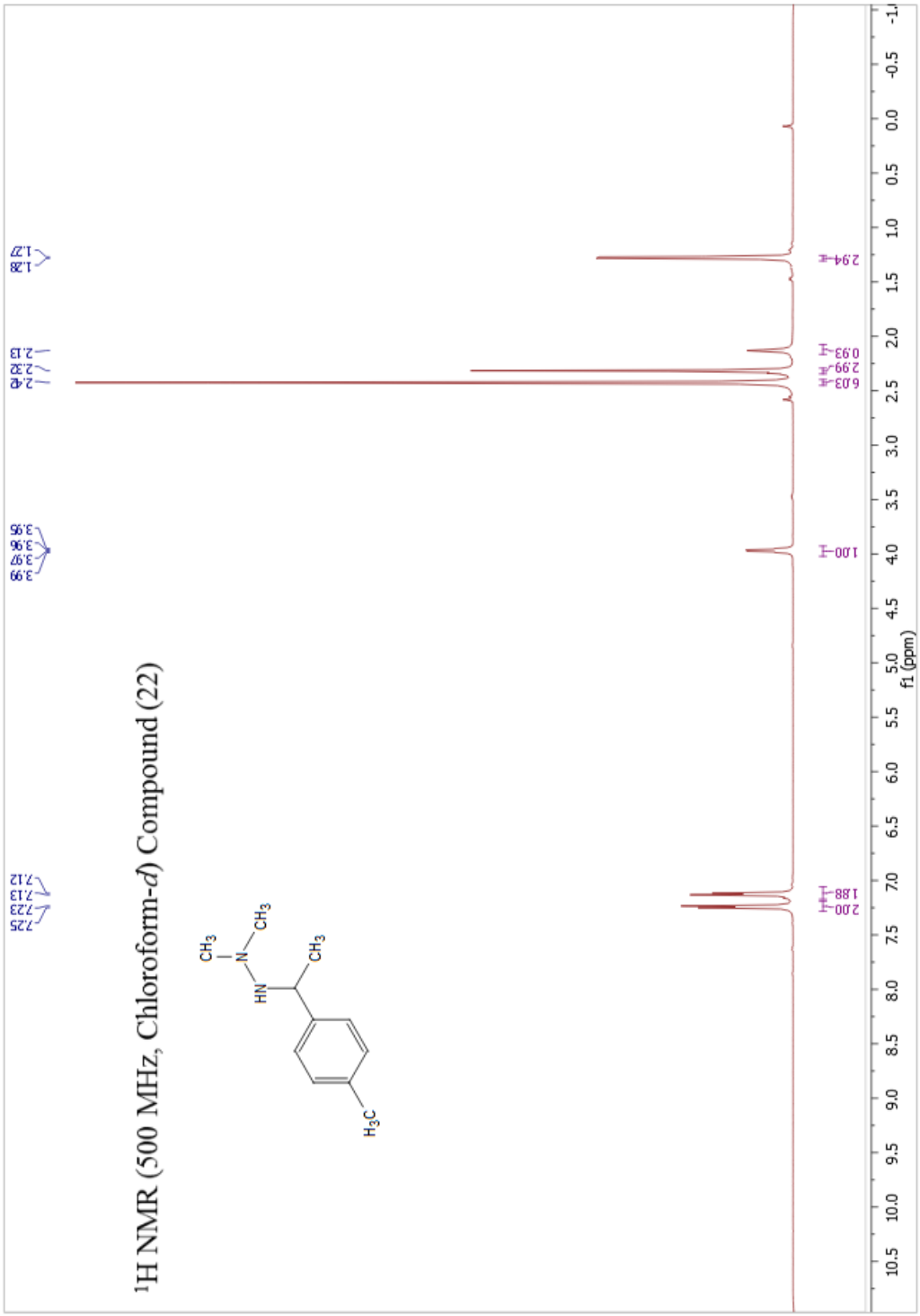


Figure D.10: ^{1}H NMR of 1,1-dimethyl-2-(1-*p*-tolylethyl)hydrazine (**22**).

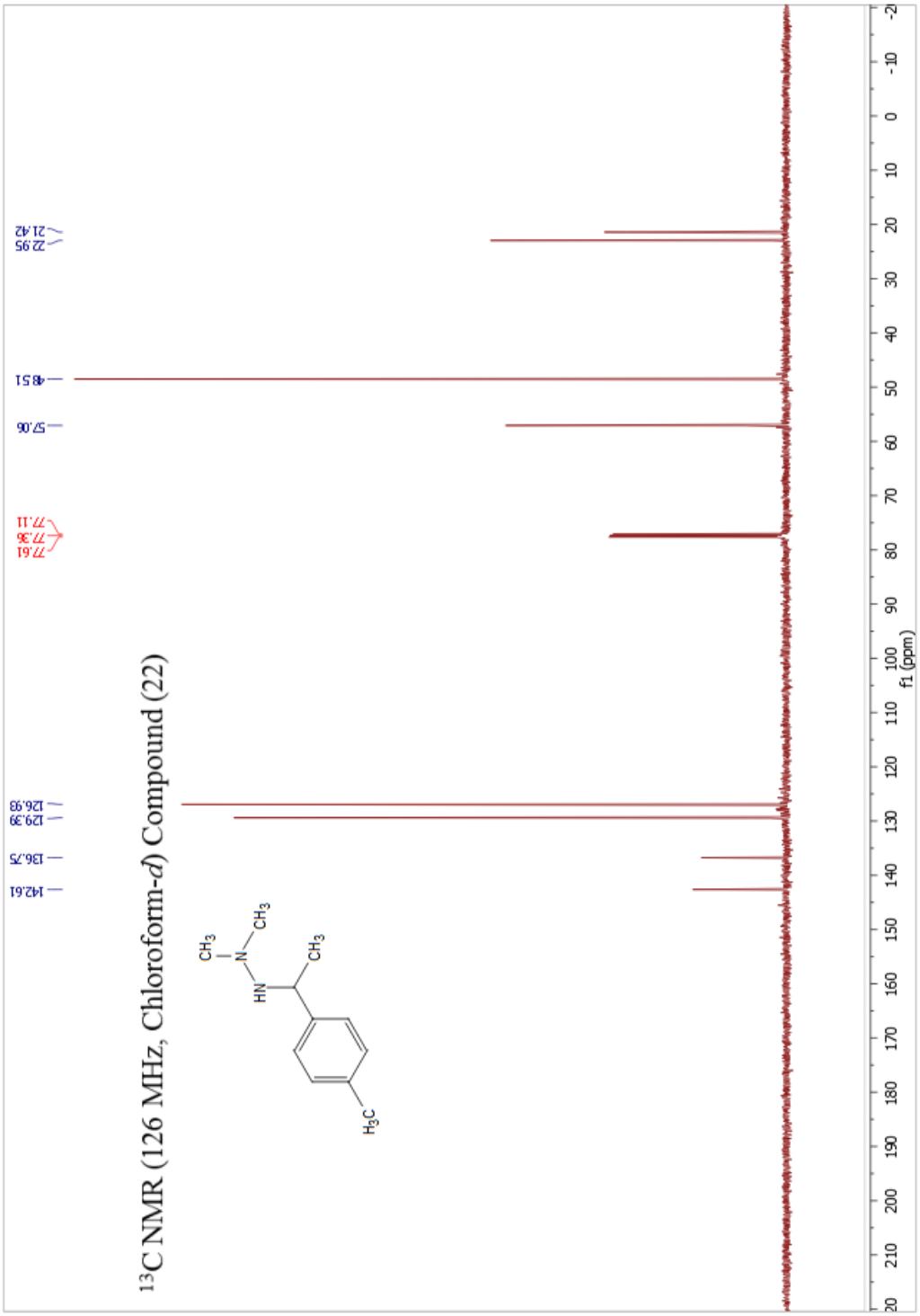


Figure D.11: ^{13}C NMR of 1,1-dimethyl-2-(1-*p*-tolylethyl)hydrazine (**22**).

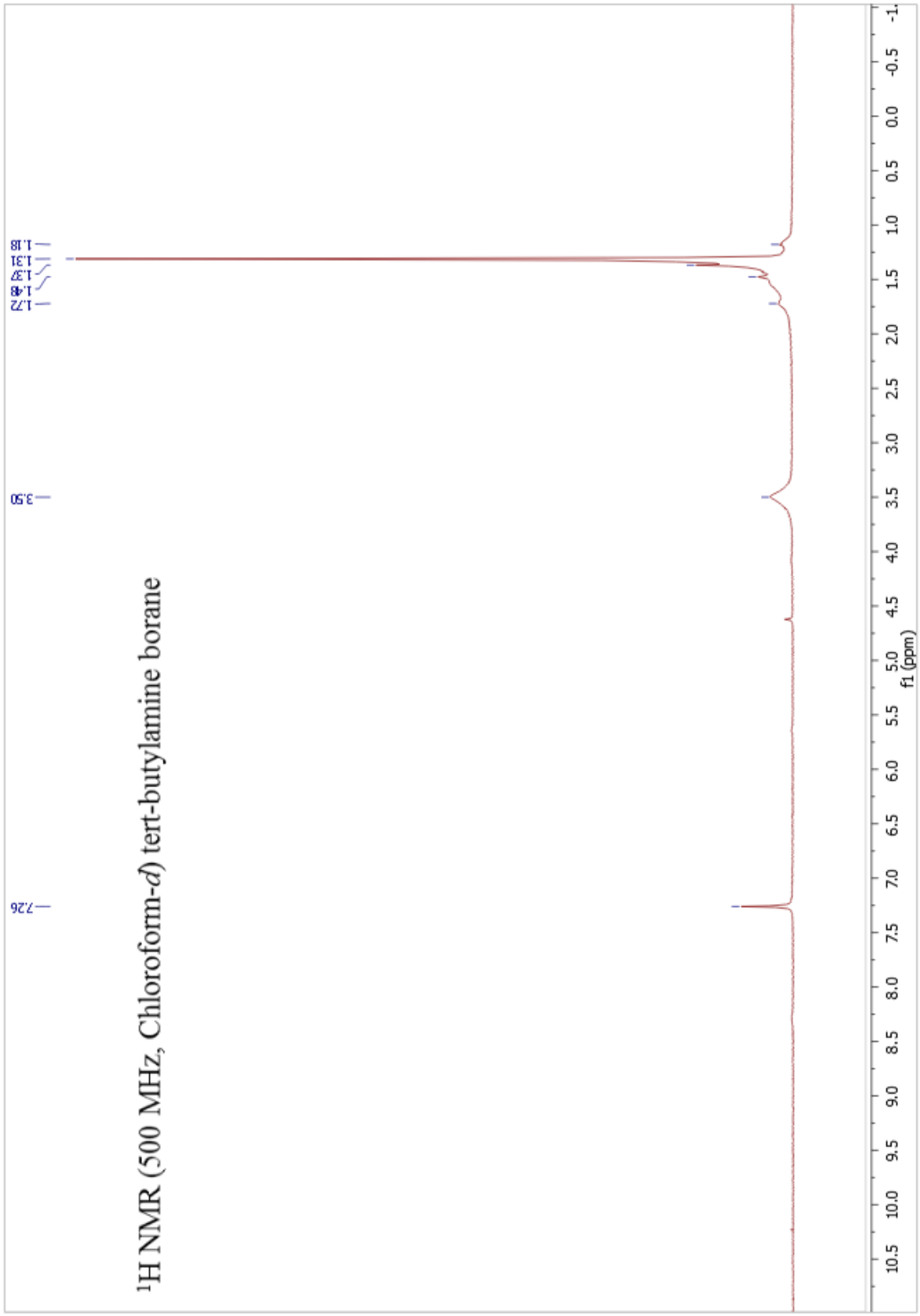


Figure D.12: ^{1}H NMR of *tert*-butylamine borane.

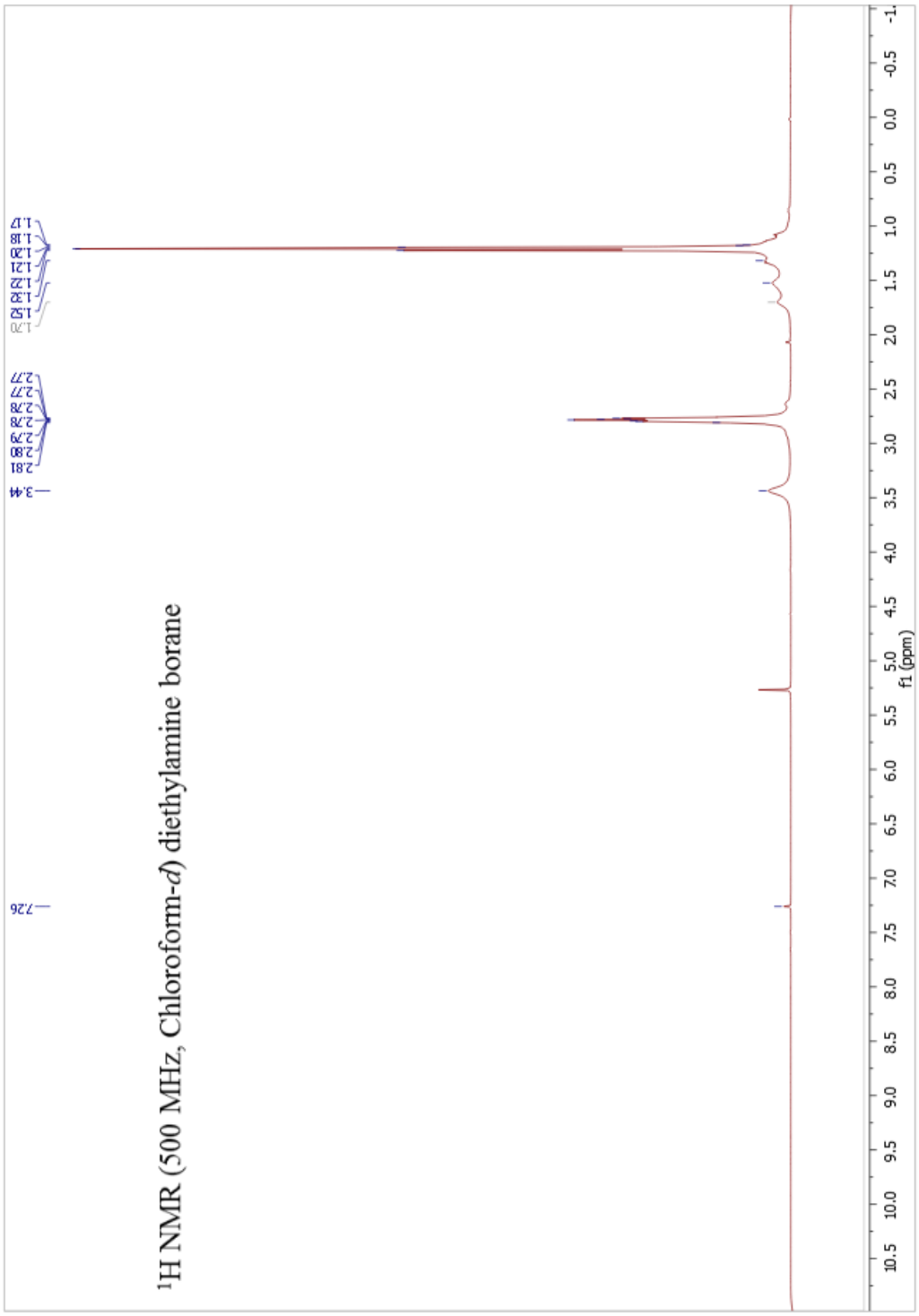


Figure D.13: ^{1}H NMR of diethylamine borane.

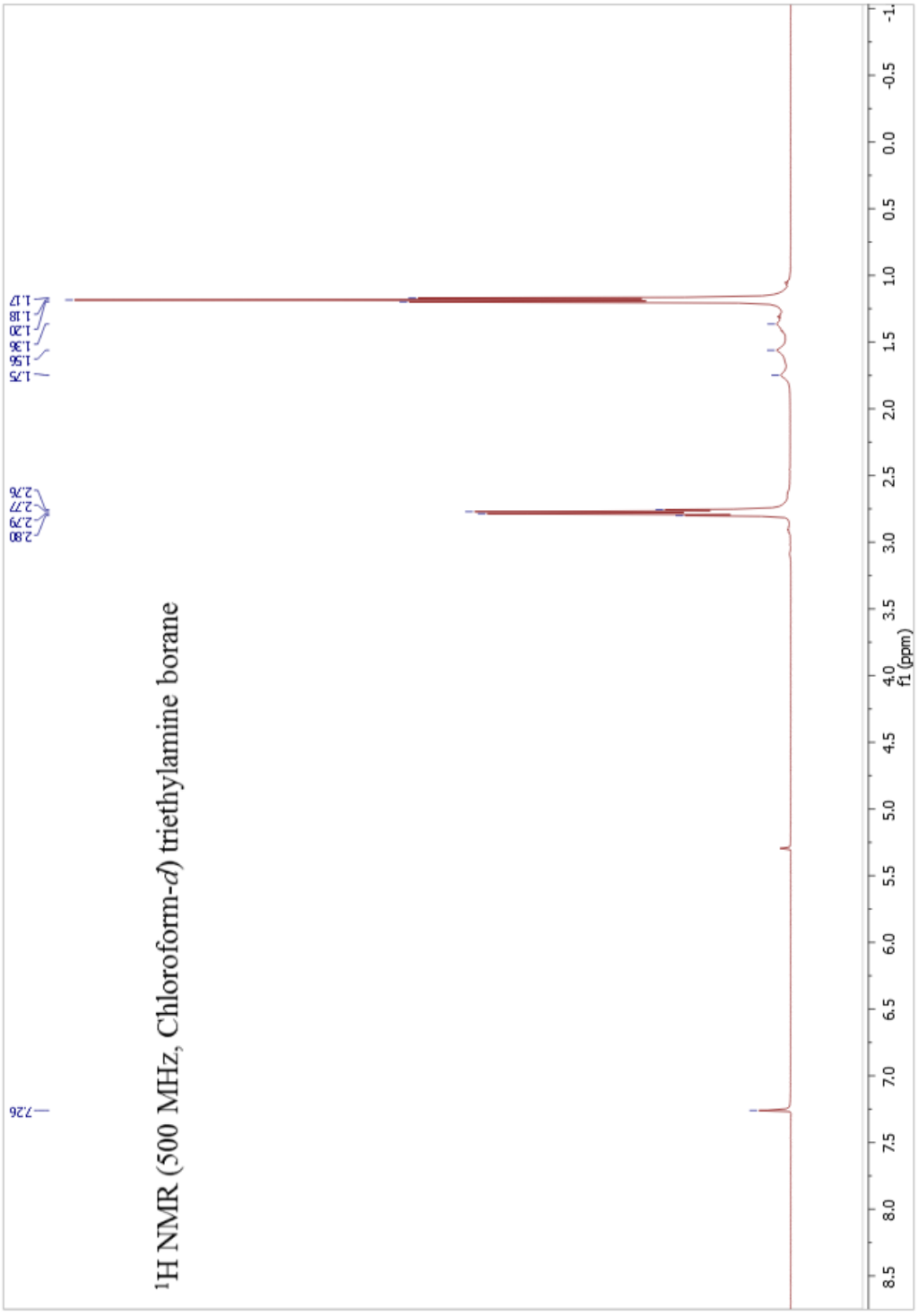


Figure D.14: ^{1}H NMR of triethylamine borane.

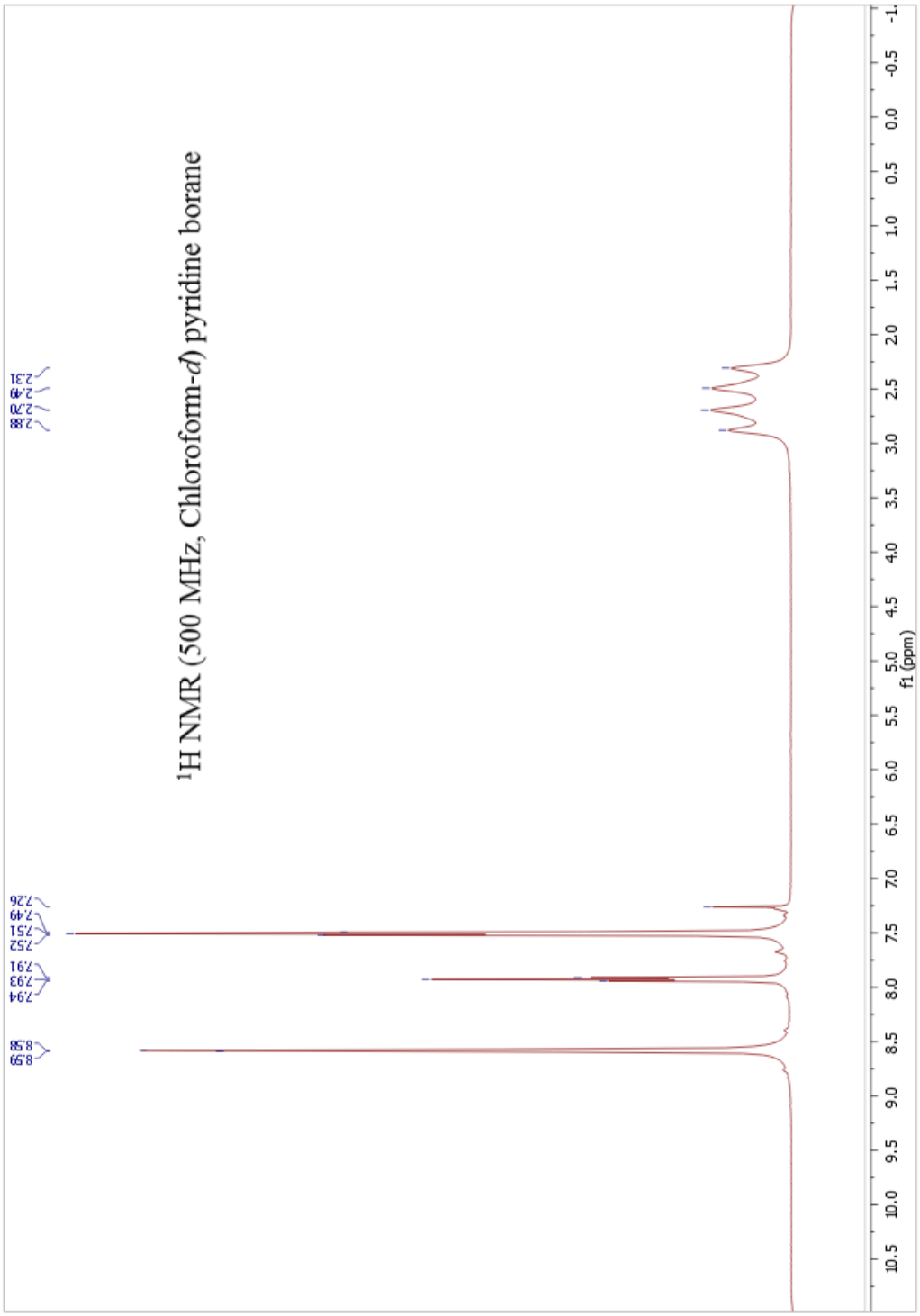


Figure D.15: ^{1}H NMR of pyridine borane.

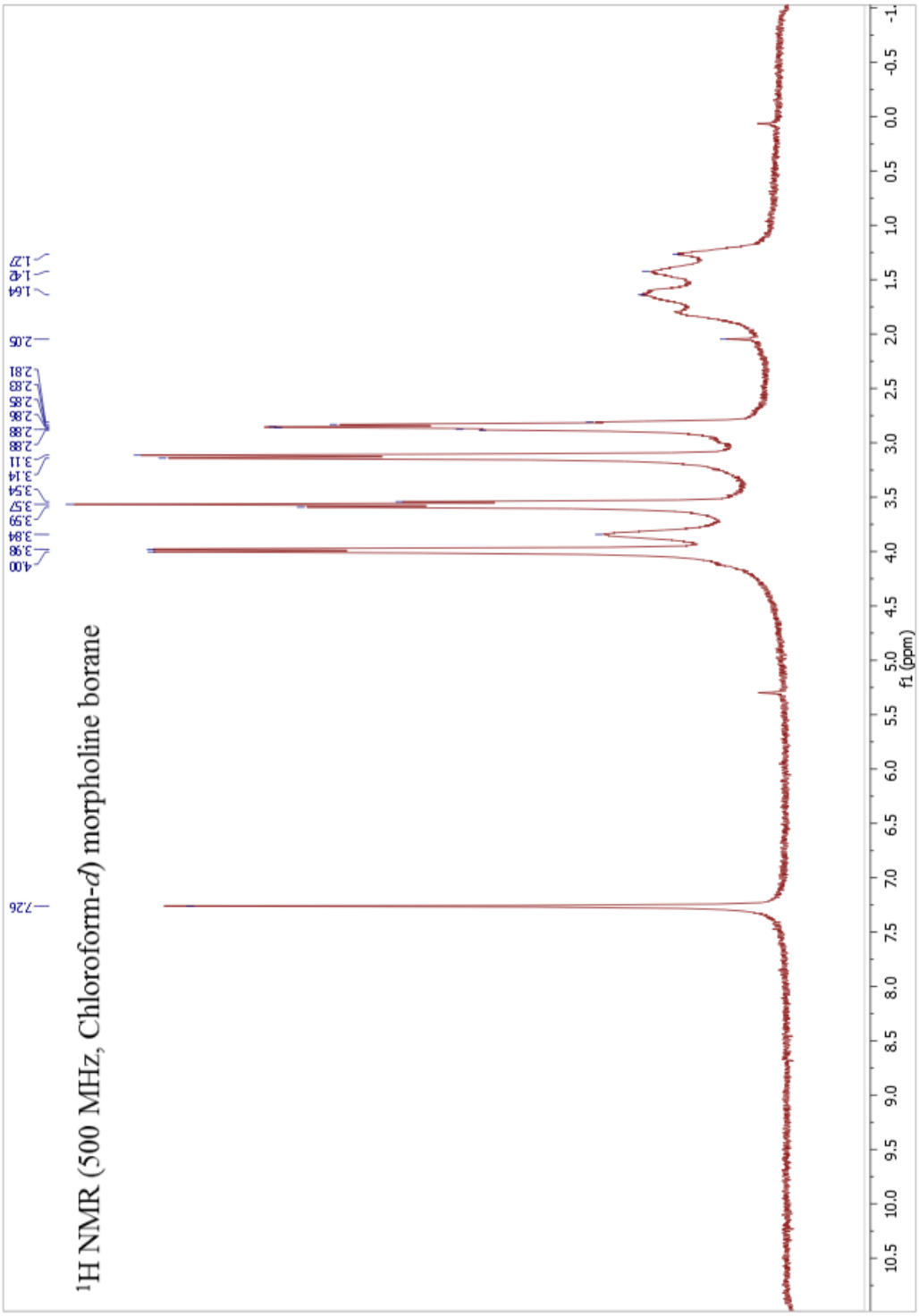


Figure D.16: ^{1}H NMR of morpholine borane.